Interband optical injection and control of electron spin populations and ballistic spin currents in bulk semiconductors.

by

Ravi Dinesh Rama Bhat

A thesis submitted in conformity with the requirements
for the degree of Doctor of Philosophy
Graduate Department of Physics
University of Toronto

Abstract

Interband optical injection and control of electron spin populations and ballistic spin currents in bulk semiconductors.

Ravi Dinesh Rama Bhat
Doctor of Philosophy
Graduate Department of Physics
University of Toronto
2006

This thesis theoretically studies interband optical injection of spin current, carrier spin, current, and carrier population by one-photon absorption, two-photon absorption, and the interference of one- and two-photon absorption ("1+2" excitation) in cubic bulk semiconductors. Novel effects—"1+2" spin-current injection, "1+2" spin control, and one-photon pure spin-current injection—are proposed and studied, and theories of previously known effects—"1+2" current injection, "1+2" carrier-population control, and two-photon spin injection—are extended. Each of the effects is studied phenomenologically from the point of view of crystal symmetry to determine the polarization and crystal orientation dependence, especially for cubic materials. The focus of the thesis is on the optical injection, rather than on the subsequent scattering, transport, and relaxation of the nonequilibrium carrier distributions. A microscopic expression for the injection rate of each effect is derived with the optical field treated as a perturbation. The effects are studied with simple analytical band models, perturbative in the Bloch wave vector $\mathbf{k}$. "1+2" current injection and "1+2" spin-current injection, which are nonzero in isotropic materials, are evaluated using the isotropic, eight-band Kane model. "1+2" population control, "1+2" spin control, and two-photon spin injection which require a lower symmetry model, are evaluated in the parabolic band approximation using a fourteen-band model. Each of these, and one-photon pure spin-current injection are further calculated numerically using the fourteen band $\mathbf{k} \cdot \mathbf{p}$ Hamiltonian. The calculation is nonperturbative in $\mathbf{k}$, and hence shows the limit of validity of the simpler models. Strain is incorporated into the fourteen-band calculation to show that one-photon pure spin-current injection can be increased with the application of strain. It is shown that two-photon spin injection can yield a very high degree spin polarization, but

only due to transitions that do not conserve angular momentum. Excitonic effects on "1+2" excitation are studied using the effective-mass theory of Wannier excitons and accounting for degenerate bands. It is shown that excitonic effects cause a phase shift in the dependence of "1+2" current injection and "1+2" spin-current injection on the optical phases, and cause an enhancement of all four "1+2" effects.

Acknowledgements

First, and most importantly, I would like to acknowledge my parents, who support me unconditionally, and have always encouraged me academically.

I would like to acknowledge John Sipe, my thesis supervisor, whose high standards and enthusiasm for science have motivated me to produce this thesis. He and I have discussed all of the ideas presented in this thesis, and are co-authors on the published papers based on them. I thank him for his mentorship, and for providing me the opportunity to interact with many other talented and engaging scientists. I have learned a lot from his graduate students and post-doctoral fellows, especially Rob Spekkens, Lora Ramunno, Anatoli Shkrebtii, Petr Kral, Oleg Prepelita, and Eugene Sherman. Not only did I share an office with Fred Nastos and Ali Najmaie, but we discussed physics and learned from each other regularly. In particular, I acknowledge Fred's input on issues of computation and *ab initio* techniques, and Ali's assistance with the symmetry calculations for Chapter 5. They are both co-authors on the paper based on Chapter 5. The contents of this thesis have also benefited from my interactions with many experimentalists. I enjoyed numerous discussions with Art Smirl, Marty Stevens, Henry van Driel, James Fraser, Daniel Côté, Yaser Kerachian, Petr Nemec, Wolfgang Rühle, and Jens Hübner. I was inspired to study two-photon spin injection (Chapter 4) by Wolfgang Rühle, and extensively discussed that topic from an experimental perspective with Petr Nemec.

I shared most of my time as a graduate student with my brother Navin. During that time, as roomates and peers, we discussed science, writing, and supported one another through the challenges of graduate student life. I thank him for always being my brother first.

I thank Aaron, Shalini, the rest of my family, and my friends for their support and encouragement. Too often my thesis took priority over spending time with them, and I'm thankful that they are understanding. I'm especially grateful to Julia Radcliffe, who has loved and supported me without wavering. Julia also helped produce Figure 2.1 and Figure 3.1.

Contents

Chapter 1

Introduction

Semiconductors are characteristically photoconductive due to interband optical transitions (from filled valence bands to empty conduction bands), which populate the illuminated material with mobile carriers: electrons and holes. Early studies of interband optical transitions used incoherent, unpolarized light sources and were insensitive to properties of the initial carrier distribution that decay on fast timescales [1]. But modern detection techniques make possible the measurement of such properties, and modern laser systems—capable of coherent, well-tailored light fields—make possible the selection of some interband transitions over others, so that one can photoexcite carrier distributions with interesting and important properties. For example, with circularly polarized light, one can photoexcite conduction band electrons that are partially spin-polarized [2], and with a two-colour light field, one can photoexcite a $\mathbf{k}$-space distribution of carriers with polar asymmetry—i.e., an electrical current—and control the direction of the current by adjusting the phases of the fields [3, 4]. This thesis shows theoretically that various combinations of one- and two-photon interband transitions can generate carrier distributions with net spin and/or a net correlation between velocity and spin, i.e. a spin current.

Spin is a fundamental and characteristic property of the electron, but it is unexploited in typical semiconductor devices, which form the basis of modern electronics. The emerging field of semiconductor spintronics is based on the hope that the control of electron spin in semiconductors will lead to the development of new kinds of data storage and processing devices, and perhaps to the development of a solid state quantum computer [5–8]. Though semiconductor spintronics is mainly focussed on electrical methods of spin-current injection and spin control [9–13], optical methods of spin injection and spin detection have played an important early role [14–16].

The canonical bulk semiconductor for optical studies is GaAs, which is cubic and has zinc-blende symmetry [17]. In this thesis, I focus on typical III-V semiconductors (including GaAs) and cubic II-VI semiconductors, which have band structures similar to GaAs. They feature

a direct band gap between s-like conduction bands, and degenerate, p-like heavy- and light-hole valence bands. The selection rules for interband one-photon excitation with circularly polarized light in such semiconductors, which are reviewed in Chapter 4, are often re-stated in the literature, and are typically attributed to angular momentum conservation. They explain, for excitation close to the band edge, the experimentally observed 3:1 ratio of spin-up to spin-down photoexcited conduction band electrons (or stated alternately, the 50% degree of spin polarization) [2].

This spin selectivity of interband one-photon optical transitions with circularly polarized light has underpinned optical studies in semiconductor spintronics. But what is possible with other types of optical excitation? The initial motivation of this thesis was to study the spin properties of carriers excited by nonlinear optical processes.

Two-photon absorption of circularly polarized light can also excite spin-polarized electrons in the conduction band [18], but there has been some confusion in the literature as to the degree of spin-polarization [19]. A tempting, but erroneous application of angular momentum conservation can lead one to conclude that carriers are fully polarized. Chapter 4 of this thesis presents the first calculation of two-photon spin injection that goes beyond a simple spherical model. It clarifies the selection rules for the transitions responsible for spin-polarization and predicts conditions under which a very high degree of spin-polarization is possible. The material of Chapter 4 was published in 2005 along with experiments on one- and two-photon spin injection [20].

When a semiconductor is simultaneously irradiated by an optical field and its phase-coherent second harmonic, quantum interference between one- and two-photon absorption pathways enables excitation of carrier distributions with interesting properties. This is an example of an "$n+m$" coherent-control scheme, in which a two-colour light field controls a physical or chemical process by interference of n- and m-photon transitions [21–23]. Interference between one- and two-photon transitions, for example, allows controllable polar asymmetry of photoelectrons in atomic ionization [24, 25], and controllable dissociation of HD^+ [26]. In semiconductors, it has been shown that "1+2" excitation can generate a ballistic current, even in the absence of an electrical bias, and that the direction and magnitude of the current can be controlled by the phases of the optical fields [3, 4, 27–35]. This "1+2" current injection has been studied in a variety of configurations: impurity-band absorption [28], free-carrier absorption [27–29], quantum well intersubband transitions [30], asymmetric quantum well interband transitions [31, 32], and quantum well interband transitions [33–35]. Most relevant to this thesis are the works of Atanasov *et al.* and Haché *et al.* [3, 4], which showed that "1+2" current injection is possible for interband transitions in bulk semiconductors.

The total density of photoexcited carriers can also be modulated by quantum interference

in "1+2" excitation, but only for materials that lack a center of inversion [36]. Fraser *et al.* demonstrated such carrier population control for interband transitions in bulk GaAs, which is noncentrosymmetric [36, 37].

Results presented in Chapter 2 of this thesis, published in 2000 [38], were the first to show that "1+2" excitation can generate spin currents. By appropriately choosing the polarization of the fields, one can generate (i) a spin-polarized electrical current (SPEC), in which electrons are photoexcited with a net spin and net velocity, or (ii) a pure spin current (PSC) with *no* associated electrical current, in which electrons traveling in one direction have net spin up while those traveling in the opposite direction have net spin down.

Whereas a SPEC is required for some proposed semiconductor spintronics devices [7, 8, 16, 39, 40], a PSC is somewhat of a novelty. The first observations of pure spin currents were based on the "1+2" scheme presented in this thesis [41, 42]. Pure spin currents can also occur from the spin Hall effect [43–46], and from spin pumping schemes [47–55]. Subsequent calculations of "1+2" spin currents in quantum wells [33, 34, 56–58] and quantum wires [59] have also appeared. Others have proposed that a dc electric field can drive a dissipationless PSC [60–63]. Rashba has shown that such dissipationless PSCs can exist in the ground state of low symmetry materials, and hence a distinction should be made between them and the kind of transport PSC that I present in this thesis [64, 65].

Results in this thesis also show that the net spin of photoexcited carriers can be modulated by quantum interference in "1+2" excitation, but only for noncentrosymmetric materials. Recent experiments have confirmed "1+2" spin control in GaAs/AlGaAs multiple quantum wells [66, 67].

Thus, the picture has emerged over the last ten years that when a bulk semiconductor undergoes "1+2" excitation, modulation of the phases of the fields can modulate: carrier population, ballistic currents, carrier spin, and/or ballistic spin currents. The latter two were first proposed by work presented in this thesis. Which of these four "1+2" effects occur depends on the polarization states of the fields. There have been several experimental observations of "1+2" interband excitation in bulk semiconductors.[1] Such experiments have been performed with either: (a) two fields, typically short pulses, one the generated second harmonic of the other [4, 36, 37, 41, 42, 66–76], or (b) a single ultrashort pulse having at least an octave bandwidth [77, 78].

Previous microscopic calculations of "1+2" processes in bulk semiconductors fall into two categories: *ab initio* density functional methods have been used for current injection [3] and population control [36], while simple analytical band models perturbative in $\mathbf{k}$ (with at most

[1] I include in this category experiments with heterostructures at excess energies greater than the confinement energy, in which the confinement plays a minor role.

eight spherical, parabolic bands) have been used for current injection [3, 79, 80]. The former are best suited for excess energies on the order of eVs, while the latter are only valid for excitation close to the band edge and cannot be applied to population and spin control, which vanish in such centrosymmetric models.

This thesis presents novel calculations of the "1+2" effects. In Chapter 2, I study the effects phenomenologically from the point of view of crystal symmetry to determine their polarization and crystal orientation dependence, and microscopically using simple analytical models, perturbative in the Bloch wave vector $\mathbf{k}$, to determine their magnitude. The band model is perturbative in the Bloch wave vector $\mathbf{k}$, and hence appropriate to excitation close to the band edge. Current injection and spin-current injection, which are nonzero in isotropic materials, are evaluated in Chapter 2 using the isotropic, eight-band Kane model. Population control and spin control, which require a lower symmetry model, are evaluated in the parabolic band approximation using a fourteen-band model in Appendix C. In Chapter 3, a numerical calculation of the fourteen band $\mathbf{k} \cdot \mathbf{p}$ Hamiltonian is used for a microscopic calculation of each "1+2" effect. The calculation is nonperturbative in $\mathbf{k}$, and hence shows the limit of validity of the calculations in Chapter 2 and Appendix C. Chapter 6 accounts for "excitonic effects", which are a consequence of the correlation between the optically excited electron and its hole caused by their Coulomb attraction. Such correlations were neglected in previous theories of "1+2" effects and in Chapters 2–5 of this thesis, which use the independent-particle approximation. Excitonic effects are well-studied in one- and two-photon absorptions, but have not previously been studied in "1+2" excitation. The recently published results of Chapter 6 predict a frequency-dependent phase shift in the dependence of the current and spin current on the optical phases [81].

Figure 1.1 shows, in the red box, my calculated band structure for GaAs with the fourteen band $\mathbf{k} \cdot \mathbf{p}$ Hamiltonian described in Chapter 3. Also shown is its relation to an *ab initio* band structure calculation of GaAs.

Although this thesis is mainly focussed on electron spin properties of nonlinear optical excitation, the finding that a pure spin current can be generated from "1+2" excitation begged the question of whether a PSC can be generated from linear excitation. Chapter 5 shows that, in noncentrosymmetric materials, a ballistic pure spin current can indeed be generated from one-photon absorption alone. This PSC is simpler, but more subtle than the "1+2" spin current discussed in Chapters 2, 3, and 6. The calculation in Chapter 5 of the PSC from one-photon absorption uses the same numerical solution to the fourteen-band $\mathbf{k} \cdot \mathbf{p}$ Hamiltonian used in Chapters 3 and 4, but also accounts for external strain on the crystal. The calculation shows that the PSC can be increased with the application of strain. The results of Chapter 5 were recently published [82], and the one-photon PSC has been confirmed experimentally [83].

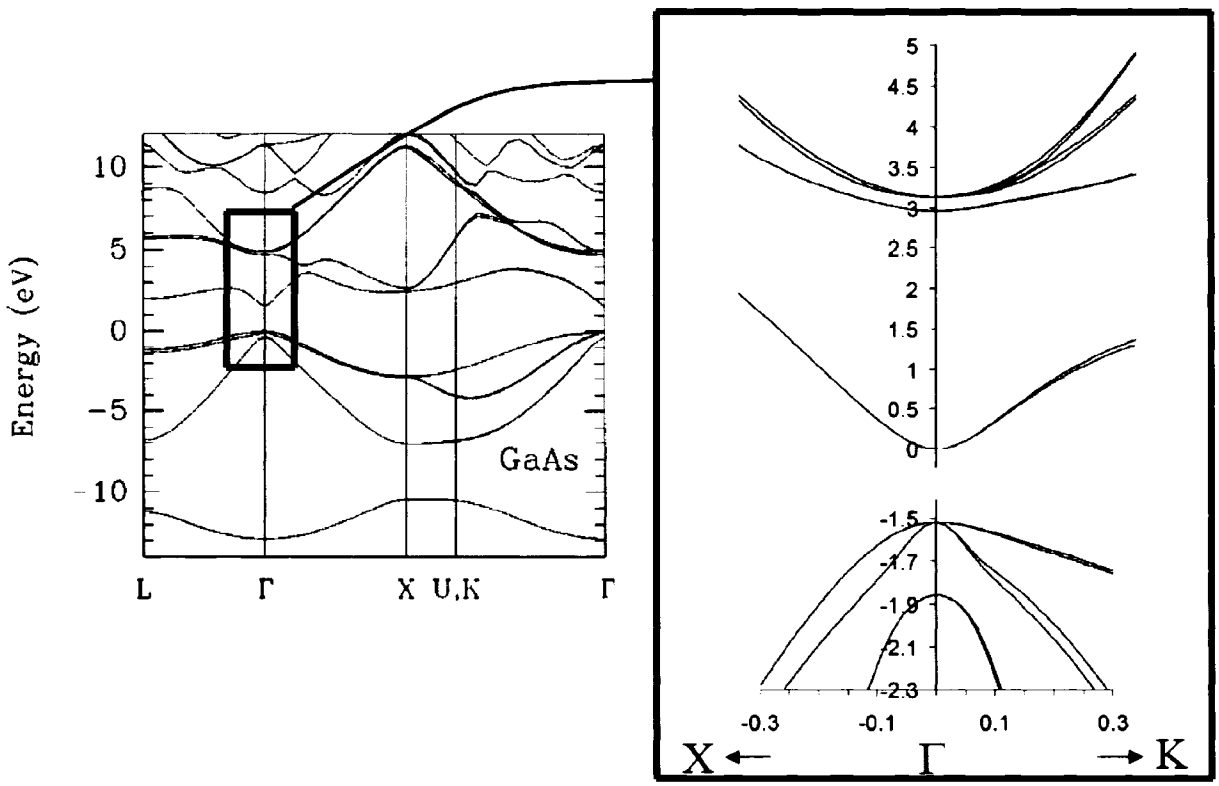

Figure 1.1: Band structures for GaAs: *ab initio* (left) and fourteen band $\mathbf{k}\cdot\mathbf{p}$ (right) calculations. The units for the horizontal ($\mathbf{k}$) axis on the right are Å^{-1}, and the units for the vertical (Energy) axis on the right are eV.

Electromagnetic units are discussed in Appendix A.

1.1 Assumptions and Limitations

The theoretical studies in this thesis share some common assumptions and limitations. Throughout the thesis, I use a framework based on (i) a perturbative expansion in the optical field amplitudes, and (ii) a conceptual separation of the initial carrier photoinjection from the subsequent carrier scattering. I calculate the photoinjection rates for a zero-temperature semiconductor in the Fermi's golden rule (FGR) limit. Also, I use the velocity gauge coupling of light with the material, and treat the light in the long-wavelength limit.

At the low optical intensities characteristic of our natural environment, materials respond to light linearly. At higher intensities, experimentally accessible since the invention of the laser, material response can be nonlinear [84]. Up to intensities of about 10^{14} W/cm^2—typical experiments discussed in this thesis use intensities no more than 10 GW/cm^2 [4, 20, 36, 41, 42, 66, 85]—one can study the material response with a perturbative expansion in the optical fields. In fact, the expansion of the polarization in powers of the incident electric field forms the common language of nonlinear optics [84]. The calculations in this thesis are intended for intensities at which such a perturbative approach is valid, and for light sources that can be treated classically.

Higher intensity optical excitation is experimentally possible, but lies in the realm of strong-field nonlinear optics [86], which is outside the scope of this thesis. Strong-field "1+2" excitation has been studied in atoms and small molecules [87–94]. The observation of strong-field nonlinear optics in semiconductors, without destroying the sample, requires ultrashort optical pulses of only a few cycles [95, 96].

The physical processes initiated by optical excitation naturally separate into distinct timescales. Whereas interband transitions begin with the onset of the optical field, momentum relaxation occurs on a timescale of 100 fs, and other processes—electron spin relaxation, carrier cooling, and carrier recombination—occur on ps timescales or longer [97]. This situation lends itself to a conceptual separation of the initial carrier photoinjection from the subsequent carrier scattering and carrier transport. In this thesis, I focus on microscopic calculations of the initial photoinjection. Thus, one should keep in mind that the effects I calculate here will relax to a steady-state value under continuous illumination, or will decay to zero following pulsed excitation as a result of carrier scattering. The relaxation and transport of the carriers after "1+2" excitation has been studied with an effective circuit model [68], hydrodynamic equations [3, 69, 70], Boltzmann transport in the relaxation time approximation [42], a non-equilibrium Green function formalism [80], and the semiconductor Bloch equations [34, 56, 58]. The results

in this thesis can be input into any of these methods that do not go beyond its limitations. Even the simplest method, the effective circuit model, has given good agreement with room temperature electrical current injection experiments [68, 72, 78], although more sophisticated models are necessary at higher carrier density [34, 56, 58, 70]. Also, the Boltzmann transport model gives good agreement with spin-current injection experiments as shown in Chapter 3.

A consequence of not treating photoinjection and carrier scattering on the same theoretical level is the inability to properly model two-photon transitions that have a one-photon resonance. Thus, the results of all but Chapter 5 of this thesis are limited to excess photon energy ($2\hbar\omega - E_g$) less than the fundamental band gap E_g.

I calculate the photoinjection rates of spin current, spin, current, and carrier population by taking the Fermi's golden rule (FGR) limit of perturbation theory. In this limit, the injection rate (the rate of change in time) of any of these properties is constant for continuous optical fields. Even if scattering and relaxation are neglected, taking the FGR limit eliminates contributions to these properties with other time dependencies. For example, upon excitation with a quasi-monochromatic pulse with electric-field envelope $\mathcal{E}(t)$, there are three distinct contributions to the current: current injection, which is proportional to $\int^t |\mathcal{E}(t')|^2 dt'$; "shift" current, which is proportional to $|\mathcal{E}(t)|^2$; and rectification current, which is proportional to $d|\mathcal{E}(t)|^2/dt$ [98–102]. There will be analogous "shift"-like and rectification-like contributions to the effects studied in this thesis, but they have not been studied in detail. However, the different time dependencies of the three current contributions allow for their separate examination experimentally, at least in principle. And as with the one-photon current, rough order-of-magnitude estimates indicate that the injection contribution will always dominate unless it is forbidden by symmetry. In this thesis, I only study the injection contribution to each effect.

Although typical semiconductor experiments are conducted at room temperature or liquid-nitrogen temperature, in this thesis, I study ideal zero-temperature, undoped semiconductors. At increased temperatures, electron-phonon interactions increase carrier scattering, which affects the relaxation and transport of the carriers. Increased temperature also increases the lattice constant of the material, which can in principle modify the values of all the $\mathbf{k}\cdot\mathbf{p}$ model parameters, but significantly modifies only the band gaps [17]. For example, at zero temperature, the band gap of GaAs is 1.519 eV, but at room temperature it is 1.42 eV [17]. However, theoretical calculations of semiconductor optical properties are commonly made with a zero temperature crystal, and moreover I have checked that using finite temperature values for the band gaps has little influence on the results presented in the thesis. To best aid comparison with experiments conducted at any temperature, I present spectra as a function of excess photon energy (energy relative to the band gap) rather than absolute photon energy. Finally, for undoped semiconductors, typical temperatures will not introduce any significant equilibrium

concentration of free carriers.

Throughout this thesis, I use the long-wavelength limit. In this approximation, the spatial dependence of the electric field is neglected, since it typically varies on a scale much larger than a unit cell of the crystal. As a consequence, the propagation direction of the optical field only matters insofar as the polarization must be perpendicular to the propagation direction. The electric field in the equations in this thesis is the field inside the material. Typically, it is related to the incident optical field in a straightforward manner by Fresnel reflection coefficients [103]. But for complicated material geometries, Maxwell's equations must be solved self-consistently with the optical-injection equations. We undertook such a task to model a "1+2" spin control experiment on a (110)-grown multiple quantum well sample in which propagation effects were important [67]. In this thesis, I neglect local-field effects.

There are two commonly used forms for the optical interaction Hamiltonian: the velocity- and length-gauge couplings. The former takes the form $H_{v\text{-int}}(t) = -(e/c)\,\mathbf{A}(t)\cdot\mathbf{v}+e^2A^2/(2mc^2)$, where $\mathbf{A}(t)$ is the vector potential associated with the Maxwell electric field [$\mathbf{E} = -c^{-1}\dot{\mathbf{A}}(t)$] and $\mathbf{v}$ is the velocity operator associated with the field-free Hamiltonian H_0. In the long-wavelength limit, the position dependence of $\mathbf{A}(t)$ is neglected, and thus the second term in $H_{v\text{-int}}(t)$ can be neglected, since it can be absorbed in an overall time-dependent phase of the full system ket and hence cannot cause any transitions between states of H_0. The length-gauge coupling takes the form $H_{r\text{-int}}(t) = -e\mathbf{E}(t)\cdot\mathbf{r}$, which is also known as the dipole Hamiltonian. The $\mathbf{A}(t)\cdot\mathbf{v}$ coupling is typically favored for semiconductors [103, 104] since the position operator is difficult to deal with for periodic systems [105, 106], although the $\mathbf{E}(t)\cdot\mathbf{r}$ coupling can also be used [101, 106]. The two forms of interaction Hamiltonian are equivalent in theory, being related by a gauge transformation. However, when a nonlocal Hamiltonian is used, there is a correction to the velocity-gauge $H_{v\text{-int}}(t)$ to restore equivalence [106–108]. Many approximate approaches to band structure calculation—including most pseudopotentials, and the truncation to a finite number of bands—implicitly assume an underlying field-free Hamiltonian that is nonlocal and hence require a nonlocal correction to the velocity gauge $H_{v\text{-int}}(t)$ [107]. The correction does not affect one-photon transitions, but it does affect higher-order transitions including the two-photon transitions studied here. However, I neglect such nonlocal corrections, which have been found to be small for a two-band calculation of two-photon absorption [107] and for an *ab initio* calculation of second-harmonic generation [109].

The issues discussed above in this section are not unique to this thesis. They also arise in calculations of nonlinear optical susceptibilities [84]. In fact, the effects calculated in this thesis can be related to nonlinear susceptibilities. Two-photon absorption and "1+2" current injection are related to third-order susceptibilities $\chi^{(3)}$, and "1+2" population control is related to a second-order susceptibility $\chi^{(2)}$. The spin injections—one- and two-photon spin injec-

tion, and "1+2" spin control—and the spin-current injections—"1+2" spin-current injection and one-photon spin injection—can probably be described in the context of a magneto-optical susceptibility, although such a task has not yet been undertaken.

Thus, in a sense, this thesis studies linear and nonlinear optics of electron spin in semiconductors. There are three main kinds of spin in semiconductors that can be optically excited: electron spin, hole spin, and nuclear spin. Optical excitation of nuclear spin is indirect, occurring as a result of angular momentum transfer from spin-polarized carriers to the nuclei [2]; I do not study excitation of nuclear spin in this thesis. Whereas the spins of electrons in the conduction band relax on the order of 100 ps, the spins of holes in the heavy- and light-hole valence bands relax on the order of 100 fs in bulk GaAs [110, 111]. The difference is due to the degeneracy of the heavy- and light-hole bands at the Γ point, and the entanglement of spin and orbital degrees of freedom, which allow the holes to lose their spins rapidly through momentum scattering (the Elliot-Yafet spin-relaxation mechanism) [112, 113]. As a consequence, most of the focus in semiconductor spintronics has been on electron spin rather than hole spin [8], since electron spin lasts long enough to be more easily observed and to have more potential usability in a spintronics device. In this thesis, I focus on electron spin. Hole spin is considered in Chapter 2, but otherwise neglected in the rest of the thesis.

1.2 Relation to published papers

Parts of this thesis are drawn from papers published in the Physical Review [20, 38, 81, 82]. Most of Bhat and Sipe, Phys. Rev. Lett. **85**, 5432 (2000) is in Secs. 2.1, 2.3.3, 2.3.4, and 2.4, although it is corrected to a new notation that displays cubic symmetry. It is augmented in Sec. 2.3.3 with Appendix B of Bhat and Sipe, Phys. Rev. B **72**, 075205 (2005). The rest of that paper is Chapter 6 and Appendix E. Chapter 4 and part of Appendix C is my theoretical work from Bhat, Nemec, Kerachian, van Driel, and Sipe, Phys. Rev. B **71**, 035209 (2005). Chapter 5 is my theoretical work from Bhat, Nastos, Najmaie, and Sipe, Phys. Rev. Lett. **94**, 096603 (2005). It is augmented by Appendix D, which appears here for the first time. Chapter 3, Sec. 2.2, Appendix B, and parts of Appendix C will form a manuscript to be submitted to Phys. Rev. B.

Chapter 2

Two-colour Quantum Interference: Symmetries and the Parabolic Band Approximation

Quantum interference between one- and two-photon absorption pathways allows coherent control of interband transitions in unbiased bulk semiconductors; carrier population, carrier spin polarization, photocurrent injection, and spin-current injection can all be controlled. In this chapter, each of the four effects is studied from two perspectives: macroscopic and microscopic. From a macroscopic, phenomenological perspective, I show how each effect is constrained by the symmetry of the crystal, and can be described by a handful of material-dependent constants. The microscopic calculation of these material-dependent constants is divided into two parts: first, for the effect of interest, one derives a microscopic expression, which is a function of matrix elements and energies of the electron states; second, one uses a model Hamiltonian to evaluate the microscopic expression. In this chapter, I use a simple model Hamiltonian, diagonalized using a perturbative expansion in the Bloch wave vector $\mathbf{k}$, to derive expressions for the material-dependent constants. The model features parabolic energy bands and is applicable to excitation of electrons close to the fundamental band edge. In the next chapter, I use a more accurate model, but within a numerical rather than an analytical approach. The microscopic expressions derived and used in this chapter for the "1+2" effects assume that the energy bands are doubly degenerate (that is, there is no spin-splitting). Noncentrosymmetric semiconductors have a small but nonzero spin-splitting, but it is neglected in the parabolic band model used in this chapter. Generalized microscopic expressions are derived in the next chapter for models that include spin-splitting.

2.1 Microscopic expressions for "1+2" effects

The first microscopic expression derived for interband "1+2" current injection in bulk semiconductors used the independent-particle approximation, used velocity-gauge coupling ($\mathbf{A} \cdot \mathbf{p}$) in the long-wavelength approximation, and took the Fermi's golden rule (FGR) limit of the second-order perturbation in the optical fields [3]. Subsequently, Aversa and Sipe studied the semiconductor response to "1+2" excitation using a perturbative solution to semiconductor optical Bloch equations (SOBEs) derived using length gauge coupling ($\mathbf{E} \cdot \mathbf{r}$) [100]. The two different approaches, which both used the independent-particle approximation, produce formally equivalent microscopic expressions for "1+2" current injection, although the velocity-gauge approach requires modification for nonlocal Hamiltonians as discussed in Sec. 1.1 [100]. However, the SOBEs obscure the quantum interference nature of the "1+2" effects.

Microscopic expressions for the other three "1+2" effects—population control, spin-current injection, and spin control—can be easily derived by generalizing the derivation of the microscopic expression for current control. In fact, this has been done for population control [36]. In the rest of this section, I present a unified derivation of all four "1+2" effects. It is review for current injection [3, 114] and population control [36], but novel for spin-current injection and spin control.

The optical field is modeled as a superposition of monochromatic fields of frequency ω and 2ω:

$$\mathbf{E}(t) = \mathbf{E}_{\omega} \exp(-i\omega t) + \mathbf{E}_{2\omega} \exp(-i2\omega t) + c.c. \tag{2.1}$$

I calculate the injection of each "1+2" process using microscopic expressions derived using velocity gauge ($\mathbf{A} \cdot \mathbf{v}$) coupling in the long-wavelength approximation, treating the field perturbatively in the FGR limit, and using the independent-particle approximation [3, 36].[1] The initial state is an ideal semiconductor in its ground state $|0\rangle$, with filled valence bands v and empty conduction bands c. The light field causes transitions to states $|cv\mathbf{k}\rangle \equiv a^{\dagger}_{c,\mathbf{k}} a_{v,\mathbf{k}} |0\rangle$, where the creation operator $a^{\dagger}_{n,\mathbf{k}}$ creates an electron in the Bloch state $|n\mathbf{k}\rangle$. By introducing "hole" creation operators $b^{\dagger}_{v,\mathbf{k}}$, where $b^{\dagger}_{v,\mathbf{k}} \equiv a_{v,\mathbf{k}}$, one can refer to the state $|cv\mathbf{k}\rangle$ as an electron-hole state.[2] The optically injected electron and hole have the same crystal wave vector $\mathbf{k}$ as a consequence of the long-wavelength approximation. I write the state of the system as $|\psi(t)\rangle = c_0(t)|0\rangle + \sum c_{cv\mathbf{k}}(t)|cv\mathbf{k}\rangle$ and calculate $c_{cv\mathbf{k}}(t)$ to second order in perturbation theory,

[1] Some consequences of relaxing the independent-particle approximation are presented in Chapter 6.

[2] The notation $b^{\dagger}_{v,\mathbf{k}} \equiv a_{v,-\mathbf{k}}$ is more common, since the operator $a_{v,-\mathbf{k}}$ creates a hole with crystal momentum $\hbar\mathbf{k}$, whereas the operator $a_{v,\mathbf{k}}$ creates a hole with crystal momentum $-\hbar\mathbf{k}$ [104]. However, for the purposes of this section, such a notation is unnecessarily cumbersome.

treating the light classically in the long-wavelength limit. The result is

$$c_{cv\mathbf{k}}(t) = \left[\Omega^{(1)}_{c,v,\mathbf{k}} + \Omega^{(2)}_{c,v,\mathbf{k}}\right] \frac{\exp\left[-it\left(2\omega + i\varepsilon\right)\right]}{2\omega - \omega_{cv}(\mathbf{k}) + i\varepsilon}, \tag{2.2}$$

where ε is an infinitesimally small parameter to account for the turn-on of the monochromatic fields, and

$$\Omega^{(1)}_{c,v,\mathbf{k}} = i\frac{e}{2\hbar\omega}\mathbf{E}_{2\omega}\cdot\mathbf{v}_{c,v}(\mathbf{k}), \tag{2.3}$$

$$\Omega^{(2)}_{c,v,\mathbf{k}} = \left(\frac{e}{\hbar\omega}\right)^2 \sum_n \frac{\left[\mathbf{E}_\omega\cdot\mathbf{v}_{c,n}(\mathbf{k})\right]\left[\mathbf{E}_\omega\cdot\mathbf{v}_{n,v}(\mathbf{k})\right]}{\omega_{nv}(\mathbf{k}) - \omega}, \tag{2.4}$$

where $\mathbf{v}_{n,m}(\mathbf{k})$ is a velocity matrix element between Bloch states, $\hbar\omega_n(\mathbf{k})$ is the energy of band n, and $\omega_{nm}(\mathbf{k}) \equiv \omega_n(\mathbf{k}) - \omega_m(\mathbf{k})$. To lowest order, the coefficient $c_0(t) = 1$.

The four "1+2" effects can be generalized as the injection rate of the expectation value in the state $|\psi(t)\rangle$ of a one-body operator $\hat{\Theta}$. In second quantized form [115]

$$\hat{\Theta} = \sum_{n,m,\mathbf{k},\mathbf{k}'} a^\dagger_{n\mathbf{k}} a_{m\mathbf{k}'} \langle n\mathbf{k}|\,\hat{\theta}\,|m\mathbf{k}'\rangle, \tag{2.5}$$

where $\hat{\theta}$ is the associated single-particle operator.[3] For current injection, $\hat{\theta} = e\mathbf{v}$, where $\mathbf{v}$ is the velocity operator. For population control, $\hat{\theta}$ is the projector onto c bands $\sum_{c,\mathbf{k}} |c\mathbf{k}\rangle\langle c\mathbf{k}|$, which gives the number of electron-hole pairs. For spin control, $\hat{\theta}$ is the spin operator $\mathbf{S}$. For spin-current injection, $\hat{\theta}$ is the product $v^i S^j$. However, due to the spin-orbit part of the velocity operator—the so-called "anomalous" velocity, discussed in Sec. 2.3.1—$\mathbf{v}$ and $\mathbf{S}$ do not commute, and thus $v^i S^j$ is not Hermitian. Instead, one should take $(v^i S^j + S^j v^i)/2$ as the operator for spin-current. But since I neglect the anomalous velocity (see Appendix B), this is not necessary.

In what follows, I assume that $\hat{\theta}$ is diagonal in $\mathbf{k}$ (i.e., $\langle n\mathbf{k}|\,\hat{\theta}\,|m\mathbf{k}'\rangle = \langle n\mathbf{k}|\,\hat{\theta}\,|m\mathbf{k}\rangle\,\delta_{\mathbf{k},\mathbf{k}'}$). This property is satisfied by the four important examples of $\hat{\theta}$ above, but note that it is not satisfied by the polarization, since the position operator is not strictly diagonal in $\mathbf{k}$ [105, 106].

In terms of the electron and hole operators, (2.5) becomes

$$\hat{\Theta} = \sum_{c,c',\mathbf{k}} a^\dagger_{c\mathbf{k}} a_{c'\mathbf{k}}\theta_{c,c'}(\mathbf{k}) - \sum_{v,v',\mathbf{k}} b^\dagger{}_{v'\mathbf{k}} b_{v\mathbf{k}}\theta_{v,v'}(\mathbf{k}) + \sum_{c,v,\mathbf{k}}\left(a^\dagger_{c\mathbf{k}} b^\dagger_{v\mathbf{k}}\theta_{c,v}(\mathbf{k}) + h.c.\right) + \sum_{v,\mathbf{k}}\theta_{v,v}(\mathbf{k}),$$

where $\theta_{n,m}(\mathbf{k}) \equiv \langle n\mathbf{k}|\,\hat{\theta}\,|m\mathbf{k}\rangle$. By using the basic anti-commutation relations $\left\{a_{n,\mathbf{k}}, a^\dagger_{m,\mathbf{k}'}\right\} = \delta_{n,m}\delta_{\mathbf{k},\mathbf{k}'}$ and $\left\{a_{n,\mathbf{k}}, a_{m,\mathbf{k}'}\right\} = \left\{a^\dagger_{n,\mathbf{k}}, a^\dagger_{m,\mathbf{k}'}\right\} = 0$, and the properties of the ground state $a_{c,\mathbf{k}}|0\rangle =$

[3]Here, and throughout the thesis, one can make the replacement $\sum_{\mathbf{k}} = \left(L^3/8\pi^3\right)\int d^3k$, where the integral on the right side is over the first Brillouin zone, and L^3 is a normalization volume.

$b_{v,\mathbf{k}}|0\rangle = 0$, one finds

$$\langle 0|\hat{\Theta}|0\rangle = \sum_{v,\mathbf{k}} \theta_{v,v}(\mathbf{k}), \tag{2.6}$$

$$\langle 0|\hat{\Theta}|cv\mathbf{k}\rangle = \theta_{v,c}(\mathbf{k}), \tag{2.7}$$

$$\langle cv\mathbf{k}|\hat{\Theta}|c'v'\mathbf{k}\rangle = \theta_{c,c'}(\mathbf{k})\,\delta_{v,v'} - \theta_{v',v}(\mathbf{k})\,\delta_{c,c'} + \delta_{c,c'}\delta_{v,v'}\sum_{v,\mathbf{k}}\theta_{v,v}(\mathbf{k}). \tag{2.8}$$

Note that while, in general, the expectation value of an observable operator $\hat{\Theta}$ in the ground state can be nonzero, the population of electron-hole pairs is zero (by definition of the ground state), and the current density in the ground state is zero. There can be a net spin in the ground state of a magnetic material, and there can be a net spin current in a material of low enough symmetry to allow a nonzero second-rank pseudotensor. Rashba discussed such equilibrium, non-transport spin currents in materials of $C_{\infty v}$ and C_{2v} symmetry [64]. Neither a net ground-state spin nor spin-current are allowed by symmetry in materials with T_d or O_h symmetry, which are the focus of this thesis.

Using (2.6), (2.7), and (2.8), the injection rate of the expectation value of $\hat{\Theta}$ per unit volume is

$$\frac{d}{dt}\langle\hat{\Theta}\rangle \equiv \frac{1}{L^3}\frac{d}{dt}\langle\psi|\hat{\Theta}|\psi\rangle \tag{2.9}$$

$$= \frac{1}{L^3}\frac{d}{dt}\left\{\left[c_0^*(t)\sum_{cv\mathbf{k}} c_{cv\mathbf{k}}(t)\,\theta_{v,c}(\mathbf{k}) + c.c.\right] + \sum_{c'v'}\sum_{cv\mathbf{k}} c^*_{cv\mathbf{k}}(t)\,c_{c'v'\mathbf{k}}(t)\left[\theta_{c,c'}(\mathbf{k})\,\delta_{v,v'} - \theta_{v',v}(\mathbf{k})\,\delta_{c,c'}\right]\right\} \tag{2.10}$$

$$= \frac{1}{L^3}\sum_{c'v'}\sum_{cv\mathbf{k}}\left[\theta_{c,c'}(\mathbf{k})\,\delta_{v,v'} - \theta_{v',v}(\mathbf{k})\,\delta_{c,c'}\right]\frac{d}{dt}\left[c^*_{cv\mathbf{k}}(t)\,c_{c'v'\mathbf{k}}(t)\right]. \tag{2.11}$$

In the first step, the term from $|c_0|^2$ combines with the term due to the last term of (2.8) to give $|c_0|^2 + \sum|c_{cv\mathbf{k}}|^2$, which is equal to 1 and independent of time. The first term in the square brackets in (2.10) is the coherence between the electron-hole excitation and the ground state. Its $\mathbf{E}_{2\omega}$ piece gives the index of refraction, and the one-photon "shift" and rectification currents, which are more naturally derived in the length gauge and with a density matrix approach [101]. Its injection rate vanishes in the FGR limit. Using (2.2),

$$\frac{d}{dt}c^*_{cv\mathbf{k}}(t)\,c_{c'v'\mathbf{k}}(t) = \left[\left(\Omega^{(1)}_{c,v,\mathbf{k}}\right)^* + \left(\Omega^{(2)}_{c,v,\mathbf{k}}\right)^*\right]\left[\Omega^{(1)}_{c',v',\mathbf{k}} + \Omega^{(2)}_{c',v',\mathbf{k}}\right]\frac{2\varepsilon\exp(2\varepsilon t)}{(2\omega - \omega_{c'v'}(\mathbf{k}) + i\varepsilon)(2\omega - \omega_{cv}(\mathbf{k}) - i\varepsilon)}. \tag{2.12}$$

The FGR limit is the limit $\varepsilon \to 0$. In this limit, terms will only contribute when $\omega_{c'v'}(\mathbf{k}) =$

$\omega_{cv}(\mathbf{k}) = 2\omega$, for then

$$\lim_{\varepsilon\to 0} \frac{2\varepsilon \exp(2\varepsilon t)}{[2\omega - \omega_{cv}(\mathbf{k})]^2 + \varepsilon^2} = 2\pi\delta(2\omega - \omega_{cv}(\mathbf{k})). \tag{2.13}$$

In the parabolic band model, this only occurs when $\omega_{cc'}(\mathbf{k}) = \omega_{vv'}(\mathbf{k}) = 0$.[4] Taking the FGR limit,

$$\begin{aligned}\frac{d}{dt}\langle\hat{\Theta}\rangle =& \frac{2\pi}{L^3}\sum_{cv\mathbf{k}}{\sum_{c'v'}}' \left[\theta_{c,c'}(\mathbf{k})\delta_{v,v'} - \theta_{v',v}(\mathbf{k})\delta_{c,c'}\right] \\ &\times \left[\left(\Omega^{(1)}_{c,v,\mathbf{k}}\right)^* + \left(\Omega^{(2)}_{c,v,\mathbf{k}}\right)^*\right]\left[\Omega^{(1)}_{c',v',\mathbf{k}} + \Omega^{(2)}_{c',v',\mathbf{k}}\right]\delta(2\omega - \omega_{cv}(\mathbf{k})),\end{aligned} \tag{2.14}$$

where the prime on the summation implies the restriction to bands for which $\omega_{cc'}(\mathbf{k}) = \omega_{vv'}(\mathbf{k}) = 0$. Expanding the product of the two terms in square brackets,

$$\frac{d}{dt}\langle\hat{\Theta}\rangle = \dot{\theta}_{(1)} + \dot{\theta}_{(I)} + \dot{\theta}_{(2)}, \tag{2.15}$$

where

$$\dot{\theta}_{(1)} \equiv \frac{2\pi}{L^3}\sum_{cv\mathbf{k}}{\sum_{c'v'}}' \left[\theta_{c,c'}(\mathbf{k})\delta_{v,v'} - \theta_{v',v}(\mathbf{k})\delta_{c,c'}\right]\left(\Omega^{(1)}_{c,v,\mathbf{k}}\right)^*\Omega^{(1)}_{c',v',\mathbf{k}}\delta(2\omega - \omega_{cv}(\mathbf{k})), \tag{2.16}$$

$$\dot{\theta}_{(2)} \equiv \frac{2\pi}{L^3}\sum_{cv\mathbf{k}}{\sum_{c'v'}}' \left[\theta_{c,c'}(\mathbf{k})\delta_{v,v'} - \theta_{v',v}(\mathbf{k})\delta_{c,c'}\right]\left(\Omega^{(2)}_{c,v,\mathbf{k}}\right)^*\Omega^{(2)}_{c',v',\mathbf{k}}\delta(2\omega - \omega_{cv}(\mathbf{k})), \tag{2.17}$$

$$\begin{aligned}\dot{\theta}_{(I)} \equiv& \frac{2\pi}{L^3}\sum_{cv\mathbf{k}}{\sum_{c'v'}}' \left[\theta_{c,c'}(\mathbf{k})\delta_{v,v'} - \theta_{v',v}(\mathbf{k})\delta_{c,c'}\right] \\ &\times \left[\left(\Omega^{(1)}_{c,v,\mathbf{k}}\right)^*\Omega^{(2)}_{c',v',\mathbf{k}} + \Omega^{(1)}_{c',v',\mathbf{k}}\left(\Omega^{(2)}_{c,v,\mathbf{k}}\right)^*\right]\delta(2\omega - \omega_{cv}(\mathbf{k})).\end{aligned} \tag{2.18}$$

Here, $\dot{\theta}_{(1)}$ is due to one-photon absorption from the 2ω beam, $\dot{\theta}_{(2)}$ is due to two-photon absorption from the ω beam, and $\dot{\theta}_{(I)}$ is the "1+2" interference term. Because of their different dependencies on the electric-field amplitudes, these three terms can in principle be separated experimentally. Each of these can be further separated into a contribution from the injected electrons and holes, e.g. $\dot{\theta}_{(1)} = \dot{\theta}_{(1;e)} + \dot{\theta}_{(1;h)}$, where the electron term contains $\theta_{c,c'}(\mathbf{k})$, and the hole term contains $\theta_{v',v}(\mathbf{k})$.

Equations (2.16), (2.17), and (2.18) encompass twelve physically distinct effects. For $\hat{\theta} = \sum_{c,\mathbf{k}}|c\mathbf{k}\rangle\langle c\mathbf{k}|$, (2.16) describes one-photon absorption

$$\dot{N}_{(1)} = \frac{e^2}{(2\hbar\omega)^2}\frac{2\pi}{L^3}\sum_{c,v,\mathbf{k}}|\mathbf{E}_{2\omega}\cdot\mathbf{v}_{c,v}(\mathbf{k})|^2\delta(2\omega - \omega_{cv}(\mathbf{k})), \tag{2.19}$$

[4]When there is small spin-splitting of bands, $(\omega_{c'v'}(\mathbf{k}) - \omega_{cv}(\mathbf{k}))$ can be nonzero but small over a large volume of $\mathbf{k}$-space; this situation is discussed in the following chapter.

(2.17) describes two-photon absorption, and (2.18) describes "1+2" population control [36]. For $\hat{\theta} = e\mathbf{v}$, (2.16) describes the circular photogalvanic effect CPGE [99], (2.17) describes two-photon current injection, and (2.18) describes "1+2" current injection [3]. For $\hat{\theta} = \mathbf{S}$, (2.16) describes one-photon spin injection [2], (2.17) describes two-photon spin injection (Chapter 4), and (2.18) describes "1+2" spin control $\dot{\boldsymbol{\mathcal{S}}}_{(I)} = \dot{\boldsymbol{\mathcal{S}}}_{(I;e)} + \dot{\boldsymbol{\mathcal{S}}}_{(I;h)}$, where

$$\dot{\boldsymbol{\mathcal{S}}}_{(I;e)} = \frac{2\pi}{L^3} \sum_{c,v,\mathbf{k}} \sum_{c'}{}' \langle c'\mathbf{k}|\mathbf{S}|c\mathbf{k}\rangle \Omega^{(1)}_{c,v,\mathbf{k}} \Omega^{(2)*}_{c',v,\mathbf{k}} \delta\left(2\omega - \omega_{cv}\left(\mathbf{k}\right)\right) + c.c. \tag{2.20a}$$

$$\dot{\boldsymbol{\mathcal{S}}}_{(I;h)} = -\frac{2\pi}{L^3} \sum_{c,v,\mathbf{k}} \sum_{v'}{}' \langle v\mathbf{k}|\mathbf{S}|v'\mathbf{k}\rangle \Omega^{(1)}_{c,v,\mathbf{k}} \Omega^{(2)*}_{c,v',\mathbf{k}} \delta\left(2\omega - \omega_{cv}\left(\mathbf{k}\right)\right) + c.c.. \tag{2.20b}$$

For $\hat{\theta} = v^i S^j$, (2.16) describes the one-photon linear PSC (Chapter 5) and the spin-polarized CPGE [116], (2.17) describes two-photon spin-current injection, and (2.18) describes "1+2" spin-current injection $\dot{K}^{ij}_{(I)} = \dot{K}^{ij}_{(I;e)} + \dot{K}^{ij}_{(I;h)}$, where

$$\dot{K}^{ij}_{(I;e)} = \frac{2\pi}{L^3} \sum_{c,v,\mathbf{k}} \sum_{c'}{}' \langle c'\mathbf{k}|v^i S^j|c\mathbf{k}\rangle \Omega^{(1)}_{c,v,\mathbf{k}} \Omega^{(2)*}_{c',v,\mathbf{k}} \delta\left(2\omega - \omega_{cv}\left(\mathbf{k}\right)\right) + c.c. \tag{2.21a}$$

$$\dot{K}^{ij}_{(I;h)} = -\frac{2\pi}{L^3} \sum_{c,v,\mathbf{k}} \sum_{v'}{}' \langle v\mathbf{k}|v^i S^j|v'\mathbf{k}\rangle \Omega^{(1)}_{c,v,\mathbf{k}} \Omega^{(2)*}_{c,v',\mathbf{k}} \delta\left(2\omega - \omega_{cv}\left(\mathbf{k}\right)\right) + c.c.. \tag{2.21b}$$

2.2 Macroscopic perspective

In this section, I study the "1+2" effects from a macroscopic perspective. To motivate the approach taken in the rest of this section, consider the right side of Eq. (2.19). It contains the electric field amplitudes, but otherwise contains only material properties and can be rewritten

$$\dot{N}_{(1)} = E^{*i}_{2\omega} E^{j}_{2\omega} \left[\frac{e^2}{(2\hbar\omega)^2} \frac{2\pi}{L^3} \sum_{c,v,\mathbf{k}} v^{i*}_{c,v}\left(\mathbf{k}\right) v^{j}_{c,v}\left(\mathbf{k}\right) \delta\left(2\omega - \omega_{cv}\left(\mathbf{k}\right)\right) \right], \tag{2.22}$$

where the material properties have been isolated in square brackets. Here superscript lowercase letters denote Cartesian components and summation over repeated indices is implied. The separation of material properties and external fields, which is the purpose of nonlinear susceptibilities, is often useful. From a macroscopic, phenomenological perspective, one can write one-photon absorption as

$$\dot{N}_{(1)} = \xi^{ij}_{(1)} E^{*i}_{2\omega} E^{j}_{2\omega}, \tag{2.23}$$

where $\xi^{ij}_{(1)}$ is a second-rank tensor satisfying $\xi^{ji}_{(1)} = \left(\xi^{ij}_{(1)}\right)^*$ so that $\dot{N}_{(1)}$ is real.[5] Even though one can compare (2.22) and (2.23) to find a microscopic expression for $\xi^{ij}_{(1)}$, (2.23) holds more generally. Any microscopic expression for $\dot{N}_{(1)}$ will have the form (2.23), even one derived under a set of assumptions different from those in Sec. 2.1. Equation (2.23) is useful because $\xi^{ij}_{(1)}$ is constrained by the symmetry of the material. If the material undergoes a point group symmetry operation that leaves it invariant, then the result of the experiment should not change. Specifically, $\xi^{ij}_{(1)}$ must be invariant under all point group symmetry operations of the material [117].

In this section, phenomenological expressions are given for each of the "1+2" effects, tensors describing the effects are defined, and I present the symmetry properties of the tensors for cubic materials.

A tensor (or pseudotensor) $\tilde{T}$ of rank n that is invariant under a set of point group operations can be constructed from a completely arbitrary tensor (or pseudotensor) T of rank n, using the formula

$$\tilde{T}^{a_1 a_2 \ldots a_n} = \sum_g \sum_{b_1 b_2 \ldots b_n} \left(\det\left(G_g\right)\right)^P T^{b_1 b_2 \ldots b_n} G_g^{b_1 a_1} G_g^{b_2 a_2} \ldots G_g^{b_n a_n}, \tag{2.24}$$

where G_g are 3×3 matrices that transform a vector under the g-th point group operation, and P is zero for tensors and one for pseudotensors. The sum over g goes over all the elements of the point group. The invariant tensor $\tilde{T}$ can be examined to find relations amongst the tensor components imposed by symmetry constraint. Also, the number of independent tensor components can be verified using character tables for the point group [117].

In this thesis, I am primarily concerned with materials of zinc-blende symmetry, which have point group T_d in the Schoenflies notation ($\bar{4}3m$ in the international notation), and materials of diamond symmetry, which have point group O_h in the Schoenflies notation ($\frac{4}{m}\bar{3}\frac{2}{m}$ or $m3m$ in the international notation) [118].

For an isotropic material, since the sum over g in equation (2.24) is an infinite sum, a different approach is preferred. Any isotropic Cartesian tensor or pseudotensor can be written as a linear combination of products of Kronecker delta functions and Levi-Civita tensors [119]. All possible linear combinations are independent for tensors or pseudotensors of rank 2–4, or 6, but for other ranks, there are further identities that reduce this number [119].

[5] In the mks system of units (see Appendix A), this unconventional one-photon absorption tensor [3] is related to the linear susceptibility $\chi^{(1)}$ by $\xi^{ij}_{(1)} = (2/\hbar)\,\varepsilon_0 \left[\mathrm{Im}\left(\chi_s^{(1)ij}\right) - i\mathrm{Re}\left(\chi_a^{(1)ij}\right)\right]$, where $\chi_s^{(1)ij} = \left(\chi^{(1)ij} + \chi^{(1)ji}\right)/2$ and $\chi_a^{(1)ij} = \left(\chi^{(1)ij} - \chi^{(1)ji}\right)/2$.

2.2.1 Current

Current injection in the presence of the field (2.1) can be written

$$\dot{J}^i = \eta^{ijk}_{(1)} E^{j*}_{2\omega} E^k_{2\omega} + \left(\eta^{ijkl}_{(I)} E^{j*}_{\omega} E^{k*}_{\omega} E^l_{2\omega} + c.c. \right) + \eta^{ijklm}_{(2)} E^{j*}_{\omega} E^{k*}_{\omega} E^l_{\omega} E^m_{\omega}, \tag{2.25}$$

where $\mathbf{J}$ is the macroscopic current density, and $\eta^{ijk}_{(1)}$, $\eta^{ijkl}_{(I)}$, and $\eta^{ijklm}_{(2)}$ are tensors describing the material response. The third rank tensor $\eta^{ijk}_{(1)}$ describes one-photon current injection (the circular photogalvanic effect [99, 116]), the fifth rank tensor $\eta^{ijklm}_{(2)}$ describes two-photon current injection, and the fourth rank tensor $\eta^{ijkl}_{(I)}$ describes "1+2" current injection [3]. Aversa and Sipe showed that $\eta^{ijkl}_{(I)}$ is related to a doubly divergent part of the third-order nonlinear susceptibility $\chi^{(3)}$ [100]. In cubic materials with point group symmetry T_d, O_h or O, a general fourth rank tensor has four independent components, but due to the intrinsic symmetry $\eta^{ikjl}_{(I)} = \eta^{ijkl}_{(I)}$, $\eta_{(I)}$ has only three independent components; there are 21 non-zero components of $\eta_{(I)}$ in the standard cubic basis: $\eta^{aaaa}_{(I)} = \eta^{bbbb}_{(I)} = \eta^{cccc}_{(I)}$, $\eta^{baab}_{(I)} = \eta^{abba}_{(I)} = \eta^{caac}_{(I)} = \eta^{acca}_{(I)} = \eta^{cbbc}_{(I)} = \eta^{bccb}_{(I)}$, and $\eta^{a(ab)b}_{(I)} = \eta^{b(bc)c}_{(I)} = \eta^{c(ca)a}_{(I)} = \eta^{a(ac)c}_{(I)} = \eta^{c(cb)b}_{(I)} = \eta^{b(ba)a}_{(I)}$ (the components in parentheses can be exchanged), where a, b, and c denote components along the principal cubic axes [3]. This can be written

$$\eta^{ijkl}_{(I)} = i\frac{\eta_{B1}}{2}\left(\delta^{ij}\delta^{kl} + \delta^{ik}\delta^{jl} \right) + i\eta_{B2}\delta^{il}\delta^{jk} + i\eta_C \delta^{ijkl}, \tag{2.26}$$

where δ^{ij} is a Kronecker delta and the only non-isotropic part is δ^{ijkl}, which I define in the principal cubic basis as $\delta^{ijkl} = 1$ when $i = j = k = l$ and zero otherwise. The three independent components are $\eta_{B1} \equiv -2i\eta^{aabb}$, $\eta_{B2} \equiv -i\eta^{abba}$, and $\eta_C \equiv 2i\eta^{aabb} + i\eta^{abba} - i\eta^{aaaa}$. Thus, in a cubic material,

$$\dot{J}^i_{(I)} = i\eta_{B1}\left(\mathbf{E}^*_{\omega} \cdot \mathbf{E}_{2\omega} \right) E^{i*}_{\omega} + i\eta_{B2}\left(\mathbf{E}_{\omega} \cdot \mathbf{E}_{\omega} \right)^* E^i_{2\omega} + i\eta_C \delta^{ijkl} E^{j*}_{\omega} E^{k*}_{\omega} E^l_{2\omega} + c.c. \tag{2.27}$$

This generalizes the notation we used previously for a calculation in the parabolic band approximation [38], with the connection $\eta_{B1} = eDB_1/\hbar$, and $\eta_{B2} = eDB_2/\hbar$, where D, B_1 and B_2 are defined in Bhat and Sipe [38]. In that, or any other spherical approximation, $\eta_C = 0$.

2.2.2 Population

The carrier density injected by the field (2.1) can be written

$$\dot{N} = \xi^{ij}_{(1)} E^{i*}_{2\omega} E^j_{2\omega} + \left(\xi^{ijk}_{(I)} E^{*i}_{\omega} E^{*j}_{\omega} E^k_{2\omega} + c.c. \right) + \xi^{ijkl}_{(2)} E^{i*}_{\omega} E^{j*}_{\omega} E^k_{\omega} E^l_{\omega}, \tag{2.28}$$

where N is the density of electron-hole pairs (equal to the density of electrons or holes), and the tensors $\xi^{ij}_{(1)}$, $\xi^{ijk}_{(I)}$, and $\xi^{ijkl}_{(2)}$ describe the material response. Specifically, $\xi^{ij}_{(1)}$ describes one-photon absorption, $\xi^{ijkl}_{(2)}$ describes two-photon absorption, and $\xi^{ijk}_{(I)}$ describes "1+2" population

control [36]. The third-rank tensor $\xi_{(I)}^{ijk}$, which has intrinsic symmetry $\xi_{(I)}^{jik} = \xi_{(I)}^{ijk}$, can be related to the second-order nonlinear susceptibilities $\chi^{(2)}(2\omega; -\omega, -\omega)$ and $\chi^{(2)}(-\omega; 2\omega, -\omega)$ by considerations of energy transfer and macroscopic electrodynamics [36]. This point is discussed further in Sec. 6.6. In centrosymmetric materials, such as those with the diamond structure (point group O_h), $\xi_{(I)}^{ijk}$ is identically zero; hence, population control requires a noncentrosymmetric material. In a material with zinc-blende symmetry (point group T_d), $\xi_{(I)}^{ijk}$ has only one independent component; in the standard cubic basis $\xi_{(I)}^{abc} = \xi_{(I)}^{cab} = \xi_{(I)}^{bca} = \xi_{(I)}^{acb} = \xi_{(I)}^{bac} = \xi_{(I)}^{cba}$ are the only non-zero components, where a, b, and c denote components along the principal cubic axes.

2.2.3 Spin current

Spin-current density is quantified by a second-rank pseudotensor K^{ij}. Note that whereas I take $K^{ij} = \langle v^i S^j \rangle$, some authors choose the first index to represent spin and the second index to represent velocity [64]. The symmetry results of this section are valid for any definition of K^{ij} that is a second-rank pseudotensor.

The spin current injected by the field (2.1) can be written

$$\dot{K}^{ij} = \mu_{(1)}^{ijkl} E_{2\omega}^{k*} E_{2\omega}^{l} + \left(\mu_{(I)}^{ijklm} E_{\omega}^{*k} E_{\omega}^{*l} E_{2\omega}^{m} + c.c.\right) + \mu_{(2)}^{ijklmn} E_{\omega}^{k*} E_{\omega}^{l*} E_{\omega}^{m} E_{\omega}^{n}, \tag{2.29}$$

where the pseudotensors $\mu_{(1)}^{ijkl}$, $\mu_{(I)}^{ijklm}$, and $\mu_{(2)}^{ijklmn}$ describe the material response. Specifically, $\mu_{(1)}^{ijkl}$ describes one-photon spin-current injection (see Chapter 5), $\mu_{(2)}^{ijklmn}$ describes two-photon spin-current injection, and $\mu_{(I)}^{ijklm}$ describes "1+2" spin-current injection. The fifth-rank pseudotensor $\mu_{(I)}^{ijklm}$ has intrinsic symmetry on exchange of k and l indices; specifically, $\mu_{(I)}^{ijlkm} = \mu_{(I)}^{ijklm}$. In an isotropic material, $\mu_{(I)}^{ijklm}$ has three independent components, while in a cubic material (with T_d, O, or O_h symmetry) $\mu_{(I)}^{ijklm}$ has six independent components. This is contrary to our previous claim that it has four independent components [38]. The four parameters A_i, $i = 1$–4, that we used previously to describe spin-current injection in an isotropic model [38] can be reduced to three independent components with identities such as $\varepsilon^{ijm}\delta^{kl} - \varepsilon^{ijk}\delta^{lm} + \varepsilon^{jkm}\delta^{il} - \varepsilon^{ikm}\delta^{jl} = 0$ [119]. For a cubic material, $\mu_{(I)}^{ijklm}$ has 54 non-zero elements in the principal cubic basis, and can be written

$$\begin{aligned}\mu_{(I)}^{ijklm} =& \frac{\mu_{N1}}{2}\left(\varepsilon^{jml}\delta^{ik} + \varepsilon^{jmk}\delta^{il}\right) + \frac{\mu_{N2}}{2}\left(\varepsilon^{iml}\delta^{jk} + \varepsilon^{imk}\delta^{jl}\right) + \mu_{N3}\varepsilon^{ijm}\delta^{kl} \\ &+ \mu_{C1}\delta^{ikln}\varepsilon^{njm} + \mu_{C2}\delta^{jkln}\varepsilon^{nim} + \mu_{C3}\frac{1}{2}\left(\delta^{ijkn}\varepsilon^{nml} + \delta^{ijln}\varepsilon^{nmk}\right),\end{aligned} \tag{2.30}$$

where the non-isotropic tensor δ^{ijkl} has nonzero components $\delta^{aaaa} = \delta^{bbbb} = \delta^{cccc} = 1$, where a, b, and c denote components along the principal cubic axes. The six independent components are $\mu_{N1} \equiv 2\mu_{(I)}^{acaba}$, $\mu_{N2} \equiv 2\mu_{(I)}^{caaba}$, $\mu_{N3} \equiv \mu_{(I)}^{abccc}$, $\mu_{C1} \equiv \mu_{(I)}^{abaac} - \mu_{N1} - \mu_{N3}$, $\mu_{C2} \equiv \mu_{(I)}^{baaac} - \mu_{N2} + \mu_{N3}$,

and $\mu_{C3} \equiv 2\mu_{(I)}^{aaacb} - \mu_{N1} - \mu_{N2}$. Thus in a cubic material,

$$\begin{aligned}\dot{K}_{(I)}^{ij} =& \mu_{N1} E_\omega^{*i} \left(\mathbf{E}_{2\omega} \times \mathbf{E}_\omega^*\right)^j + \mu_{N2} \left(\mathbf{E}_{2\omega} \times \mathbf{E}_\omega^*\right)^i E_\omega^{*j} + \mu_{N3} \varepsilon^{ijk} E_{2\omega}^k \left(\mathbf{E}_\omega^* \cdot \mathbf{E}_\omega^*\right) \\ &+ \left(\mu_{C1} \delta^{ikln} \varepsilon^{njm} + \mu_{C2} \delta^{jkln} \varepsilon^{nim}\right) E_\omega^{*k} E_\omega^{*l} E_{2\omega}^m + \mu_{C3} \delta^{ijkl} E_\omega^{*k} \left(\mathbf{E}_{2\omega} \times \mathbf{E}_\omega^*\right)^l + c.c.\end{aligned} \tag{2.31}$$

Note that the injection of $\langle \mathbf{v} \cdot \mathbf{S} \rangle$ is zero in a cubic material, i.e., $\dot{K}^{ij}$ is traceless. In an isotropic model, such as the one we used previously [38], $\mu_{C1} = \mu_{C2} = \mu_{C3} = 0$. The connection to our previous notation is $\mu_{N1} = D\left(A_1 - A_4\right)$, $\mu_{N2} = D\left(A_2 + A_4\right)$, and $\mu_{N3} = D\left(A_3 + A_4\right)$ [38].

2.2.4 Spin population

The spin density injected by the field (2.1) can be written

$$\dot{\mathcal{S}}^i = \zeta_{(1)}^{ijk} E_{2\omega}^{j*} E_{2\omega}^k + \left(\zeta_{(I)}^{ijkl} E_\omega^{*j} E_\omega^{*k} E_{2\omega}^l + c.c.\right) + \zeta_{(2)}^{ijklm} E_\omega^{j*} E_\omega^{k*} E_\omega^l E_\omega^m, \tag{2.32}$$

where $\boldsymbol{\mathcal{S}}$ is the macroscopic spin density ($\boldsymbol{\mathcal{S}} = \langle \mathbf{S} \rangle$), and the pseudotensors $\zeta_{(1)}^{ijk}$, $\zeta_{(I)}^{ijkl}$, and $\zeta_{(2)}^{ijklm}$ describe the material response. Specifically, $\zeta_{(1)}^{ijk}$ describes one-photon spin injection [2], $\zeta_{(2)}^{ijklm}$ describes two-photon spin injection (see Chapter 4), and $\zeta_{(I)}^{ijkl}$ describes "1+2" spin control. The fourth rank pseudotensor $\zeta_{(I)}^{ijkl}$ has intrinsic symmetry on the indices $j \leftrightarrow k$. Such a pseudotensor is zero in the presence of inversion symmetry; hence, "1+2" spin control requires materials of lower symmetry. For zinc-blende symmetry (point group T_d), a general fourth-rank pseudotensor has three independent parameters and 18 non-zero elements in the standard cubic basis; forcing the $j \leftrightarrow k$ symmetry leaves two independent parameters

$$i\zeta_{IA} \equiv \zeta_{(I)}^{abba} = \zeta_{(I)}^{caac} = \zeta_{(I)}^{bccb} = -\zeta_{(I)}^{acca} = -\zeta_{(I)}^{cbbc} = -\zeta_{(I)}^{baab}, \tag{2.33a}$$

$$\begin{aligned}i\zeta_{IB} \equiv& \zeta_{(I)}^{aabb} = \zeta_{(I)}^{ccaa} = \zeta_{(I)}^{bbcc} = -\zeta_{(I)}^{aacc} = -\zeta_{(I)}^{ccbb} = -\zeta_{(I)}^{bbaa} \\ =& \zeta_{(I)}^{abab} = \zeta_{(I)}^{caca} = \zeta_{(I)}^{bcbc} = -\zeta_{(I)}^{acac} = -\zeta_{(I)}^{cbcb} = -\zeta_{(I)}^{baba}.\end{aligned} \tag{2.33b}$$

In the independent-particle approximation, $\zeta_{(I)}^{ijkl}$ is purely imaginary, which can be proven using the time-reversal properties of the Bloch states. Thus, ζ_{IA} and ζ_{IB} are real.

2.3 Parabolic band approximations

Microscopic expressions for the independent tensor components governing "1+2" effects can be found by comparing the microscopic expressions in Sec. 2.1 with the definitions in Sec. 2.2. To evaluate them requires the one-particle energies and matrix elements of velocity, spin, and the product of velocity and spin. This section reviews the $\mathbf{k} \cdot \mathbf{p}$ Hamiltonian and uses a solution perturbative in the Bloch wave vector $\mathbf{k}$ to derive analytical expressions for the independent

tensor components. The eight-band Kane model is used for "1+2" current- and spin-current injection. In Appendix C, a fourteen-band model is used for "1+2" population and spin control.

From the macroscopic perspective of Sec. 2.2, "1+2" current- and spin-current injection differ from "1+2" population and spin control in the sense that the former can be nonzero even in isotropic materials, whereas the latter strictly vanish in any material with a center of inversion.

One can see that difference from a microscopic perspective as well. Consider an expansion in $\mathbf{k}$ about the Γ point of $\mathbf{v}_{n,m}(\mathbf{k})$, which is the matrix element governing optical transitions [(2.3) and (2.4)]. If the lowest-order term in the expansion is independent of $\mathbf{k}$, the associated one-photon transition is called "allowed"; otherwise, if the lowest-order term is proportional to $\mathbf{k}$, the associated one-photon transition is called "forbidden". Two-photon transitions have two velocity matrix elements, and thus have a hyphenated label depending on the lowest-order terms in the expansions for each matrix element. For example, if both matrix elements are independent of $\mathbf{k}$, the two-photon transition is called "allowed-allowed". In the eight-band Kane model, which is isotropic, one-photon transitions are allowed, and two-photon transitions are allowed-forbidden (one matrix element is allowed, and the other is forbidden). As a result, the product $\Omega^{(1)}_{c,v,\mathbf{k}}\Omega^{(2)*}_{c,v,\mathbf{k}}$ is linear in $\mathbf{k}$ to lowest order. But the sum over $\mathbf{k}$ in the microscopic expression will only survive if the summand is even in $\mathbf{k}$. Thus population and spin control vanish in the isotropic Kane model, whereas current- and spin-current injection survive due to the additional velocity matrix element, which is linear in $\mathbf{k}$ to lowest order, in their expressions.

The preceding argument is complicated by the degeneracy at the Γ point, since the expansion about the Γ point of $\mathbf{v}_{n,m}(\mathbf{k})$—given below in (2.39) and (2.40)—is best considered as a set of expansions in k for each direction $\hat{\mathbf{k}}$ [120]. But nonetheless, population and spin control vanish in the isotropic Kane model, which I have verified by explicit calculation.

Population and spin control, to lowest order, are due to the interference of allowed one-photon transitions and allowed-allowed two-photon transitions. This point was made heuristically by Fraser and van Driel for population control [37]. Allowed-allowed two-photon transitions are present in a fourteen-band model that includes upper conduction bands. The fourteen-band model is discussed in detail in Chapter 3, and the perturbative in $\mathbf{k}$ calculation of population and spin control is deferred to Appendix C.

2.3.1 Hamiltonian

The one-electron field free Hamiltonian is $H = H_0 + H_{SO}$, where $H_0 = p^2/(2m) + V$, the potential $V(\mathbf{r})$ has the symmetry of the crystal, and the spin-orbit interaction H_{SO} is

$$H_{SO} = \frac{\hbar}{4m^2c^2}\boldsymbol{\sigma}\cdot(\boldsymbol{\nabla}V\times\mathbf{p}),$$

where $\boldsymbol{\sigma}$ is the dimensionless spin operator, $\boldsymbol{\sigma} = 2\mathbf{S}/\hbar$. Note that relativistic corrections proportional to $|\boldsymbol{\sigma} \times \boldsymbol{\nabla} V|^2$ have been neglected [117]. The eigenstates of H are Bloch states $|n\mathbf{k}\rangle$ with energy $\hbar\omega_n(\mathbf{k})$. The associated spinor wave function $\phi_{n\mathbf{k}}(\mathbf{r}) \equiv \langle \mathbf{r}|n\mathbf{k}\rangle$ can be written $\phi_{n\mathbf{k}}(\mathbf{r}) = u_{n\mathbf{k}}(\mathbf{r}) \exp(i\mathbf{k}\cdot\mathbf{r})$, where the spinor functions $u_{n\mathbf{k}}(\mathbf{r})$ have the periodicity of the crystal lattice. I use the notation $|\overline{n\mathbf{k}}\rangle$ to denote the kets for the u-functions; i.e. $u_{n\mathbf{k}}(\mathbf{r}) = \langle \mathbf{r}|\overline{n\mathbf{k}}\rangle$. Note that $|\overline{n\mathbf{k}}\rangle = \exp(-i\mathbf{k}\cdot\mathbf{r})|n\mathbf{k}\rangle$. The Hamiltonian for the u-function kets is [117, 118]

$$H_{\mathbf{k}} = e^{-i\mathbf{k}\cdot\mathbf{r}} H e^{i\mathbf{k}\cdot\mathbf{r}} = H + \frac{\hbar^2 k^2}{2m} + \hbar\mathbf{k}\cdot\mathbf{v},$$

where the velocity operator $\mathbf{v} \equiv (i/\hbar)[H, \mathbf{r}]$ is

$$\mathbf{v} = \frac{1}{m}\mathbf{p} + \frac{\hbar}{4m^2c^2}(\boldsymbol{\sigma} \times \boldsymbol{\nabla} V). \tag{2.34}$$

The second term in $\mathbf{v}$, the anomalous velocity, which leads to $\mathbf{k}$-dependent spin-orbit coupling in $H_{\mathbf{k}}$, can be neglected for the processes I consider as shown in Appendix B; in the rest of this thesis, I assume that it vanishes. The Hamiltonian $H_{\mathbf{k}}$ is known as the $\mathbf{k}\cdot\mathbf{p}$ Hamiltonian.

The states $|n, \mathbf{k} = \mathbf{0}\rangle$ are a complete set of eigenstates for the Hamiltonian H on the space of cell-periodic functions. Thus cell-periodic eigenstates of $H_{\mathbf{k}}$ can be expanded in the infinite set of states $|n, \mathbf{k} = \mathbf{0}\rangle$.

2.3.2 Isotropic Kane Model

The eight-band Kane model diagonalizes the Hamiltonian $H_{\mathbf{k}}$ in a basis of eight states $|n, \mathbf{k} = \mathbf{0}\rangle$ corresponding to the eight bands closest in energy to the fundamental band gap at the Γ point [121]. The truncation to eight bands of the eigenstate expansion yields a model with isotropic, doubly-degenerate energy bands. That is, warping and spin-splitting of the bands are absent from this model. In fact, the eight band Hamiltonian is identical for both centrosymmetric and noncentrosymmetric semiconductors, and thus it is inadequate for the description of "1+2" population and spin control. Nonetheless, it is a good starting point for a microscopic model of "1+2" current and spin-current injection.

In a semiconductor of zinc-blende symmetry, the states $\{|n, \mathbf{k} = \mathbf{0}\rangle, n = 1..8\}$ can be expanded in the states $\{|S\rangle, |X\rangle, |Y\rangle, |Z\rangle\} \otimes \{|\uparrow\rangle, |\downarrow\rangle\}$, where $|S\rangle$ transforms like Γ_1, $\{|X\rangle, |Y\rangle, |Z\rangle\}$ transform like Γ_4, and $\{|\uparrow\rangle, |\downarrow\rangle\}$ are spin-1/2 states and eigenstates of S^z [118, 121].[6] Here, Γ_1 and Γ_4 are irreducible representations of the T_d point group in the Koster notation [118]. The only nonzero matrix elements of $\mathbf{p}$ amongst these states are [121]

$$P_0 \equiv -i(\hbar/m)\langle S|p_x|X\rangle = -i(\hbar/m)\langle S|p_y|Y\rangle = -i(\hbar/m)\langle S|p_z|Z\rangle. \tag{2.35}$$

[6] In a semiconductor of higher symmetry, basis states with higher symmetry are used, but they result in the same eight-band $H_{\mathbf{k}}$.

The matrix elements of $H_{\mathbf{k}}$ in a basis of these states can be written in terms of only three parameters: the fundamental band gap E_g, the split-off gap Δ_0, and the Kane energy $E_P = 2mP_0^2/\hbar^2$ [121]. Kane showed that $H_{\mathbf{k}}$ diagonalizes with ease in a basis that depends on the direction $\hat{\mathbf{k}}$; in Kane's basis, the matrix for $H_{\mathbf{k}}$ depends only on k (the magnitude of $\mathbf{k}$), and the heavy hole states decouple from the others [121]. Since the eigenstates are doubly degenerate, I express them in a notation $\left|\overline{n,s,\mathbf{k}}\right\rangle$, where n is one of $\{c, hh, lh, so\}$ and s is a spin index α or β. The eigenstates of the eight band $H_{\mathbf{k}}$ are

$$\left|\overline{j,\beta,\mathbf{k}}\right\rangle = a_j(k)\left|iS'\downarrow'\right\rangle + \frac{1}{\sqrt{2}}b_j(k)\left|\left(X'-iY'\right)\uparrow'\right\rangle + c_j(k)\left|Z'\downarrow'\right\rangle, \tag{2.36a}$$

$$\left|\overline{j,\alpha,\mathbf{k}}\right\rangle = a_j(k)\left|iS'\uparrow'\right\rangle - \frac{1}{\sqrt{2}}b_j(k)\left|\left(X'+iY'\right)\downarrow'\right\rangle + c_j(k)\left|Z'\uparrow'\right\rangle, \tag{2.36b}$$

$$\left|\overline{hh,\alpha,\mathbf{k}}\right\rangle = \frac{1}{\sqrt{2}}\left|\left(X'+iY'\right)\uparrow'\right\rangle, \tag{2.36c}$$

$$\left|\overline{hh,\beta,\mathbf{k}}\right\rangle = \frac{1}{\sqrt{2}}\left|\left(X'-iY'\right)\downarrow'\right\rangle, \tag{2.36d}$$

where the coefficients $a_j(k)$, $b_j(k)$, and $c_j(k)$ are given by Kane [121], and j runs over the bands c, lh, and so. The prime on the Γ-point basis states in (2.36) indicates the result of a $\hat{\mathbf{k}}$-dependent rotation [121]. Expanding the coefficients $a_j(k)$, $b_j(k)$, and $c_j(k)$ about $k = 0$, one finds that they only contain even or odd powers of k. The lowest order terms in that expansion are:

$$a_c(k) = 1; \qquad b_c(k) = \frac{\sqrt{2}}{3}\frac{P_0\Delta_0}{E_g(\Delta_0+E_g)}k; \qquad c_c(k) = \frac{P_0}{E_g}\frac{E_g+\frac{2}{3}\Delta_0}{E_g+\Delta_0}k; \tag{2.37a}$$

$$a_{lh}(k) = \sqrt{\frac{2}{3}}\frac{P_0}{E_g}k; \qquad b_{lh}(k) = -\frac{1}{\sqrt{3}}; \qquad c_{lh}(k) = -\sqrt{\frac{2}{3}}; \tag{2.37b}$$

$$a_{so}(k) = -\frac{1}{\sqrt{3}}\frac{P_0}{\Delta_0+E_g}k; \qquad b_{so}(k) = -\sqrt{\frac{2}{3}}; \qquad c_{so}(k) = \frac{1}{\sqrt{3}}. \tag{2.37c}$$

Expanded about $\mathbf{k} = 0$ to order k^2 the four pairs of doubly-degenerate bands are parabolic, characterized by effective masses m_n. The effective masses can be expressed in terms of E_g, Δ_0, and E_P:

$$\begin{aligned} \frac{m}{m_c} &= 1 + \frac{1}{3}E_P\left(\frac{2}{E_g}+\frac{1}{E_g+\Delta_0}\right); & \frac{m}{m_{hh}} &= 1; \\ \frac{m}{m_{lh}} &= -\frac{2E_P}{3E_g}+1; & \frac{m}{m_{so}} &= -\frac{1}{3}\frac{E_P}{E_g+\Delta_0}+1. \end{aligned} \tag{2.38}$$

Since the heavy hole bands do not couple with any of the other bands, their dispersion is the same as a free electron (i.e. they have positive curvature). In typical semiconductors, however, the heavy hole band has negative curvature. To remedy this problem, it is standard to treat the effective masses as additional independent parameters, which effectively accounts for some of

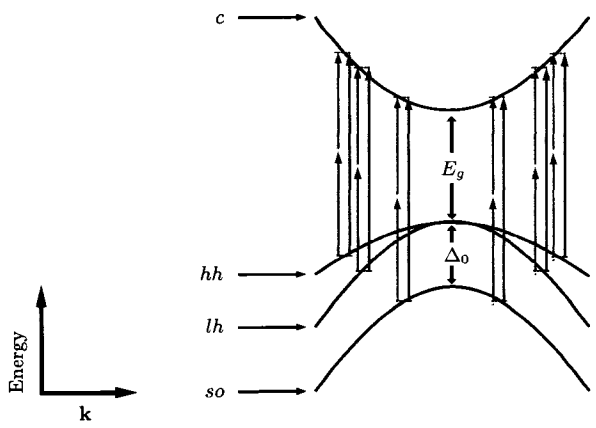

Figure 2.1: Eight band Kane model of a direct band gap semiconductor consisting of four pairs—conduction (c), heavy hole (hh), light hole (lh), and split-off (so)—of doubly-degenerate bands. The fundamental gap E_g and split-off gap Δ_0 are shown, and one- and two-photon transitions are indicated.

the interaction with remote bands. For typical semiconductors, m_{lh}, m_{hh}, and m_{so} are negative, whereas m_c is positive, as depicted in Fig. 2.1. To recover the solution of the original isotropic Kane model, one can use (2.38) to substitute the effective masses in subsequent expressions.

For the microscopic calculation of "1+2" effects in the PBA, I expand the velocity matrix elements about $\mathbf{k} = 0$ and keep the lowest order terms. In terms of the matrix elements of the u-function kets, the matrix elements of the Bloch states are

$$v_{n,s;m,s'}(\mathbf{k}) \equiv \langle n, s, \mathbf{k}| \mathbf{v} |m, s', \mathbf{k}\rangle = \langle \overline{n, s, \mathbf{k}}| \mathbf{v} |\overline{m, s', \mathbf{k}}\rangle + \frac{\hbar \mathbf{k}}{m}\delta_{nm}\delta_{ss'},$$

They can be evaluated using (2.35), (2.36), (2.37), and the rotation from the unprimed to primed states. In terms of the orthogonal triple of unit vectors $\hat{\mathbf{k}}$, $\hat{\mathbf{l}}$ and $\hat{\mathbf{m}}$,

$$\begin{aligned}
\hat{\mathbf{k}} &= \hat{\mathbf{x}} \sin\theta \cos\phi + \hat{\mathbf{y}} \sin\theta \sin\phi + \hat{\mathbf{z}} \cos\theta, \\
\hat{\mathbf{l}} &= \hat{\mathbf{x}} \cos\theta \cos\phi + \hat{\mathbf{y}} \cos\theta \sin\phi - \hat{\mathbf{z}} \sin\theta, \\
\hat{\mathbf{m}} &= -\hat{\mathbf{x}} \sin\phi + \hat{\mathbf{y}} \cos\phi,
\end{aligned}$$

these matrix elements are:

$$\mathbf{v}_{c,s;hh,s'} = \frac{1}{2}\sqrt{\frac{E_P}{m}}\left[\hat{\mathbf{l}}\sigma^0 + i\hat{\mathbf{m}}\sigma^z\right]_{s,s'}, \tag{2.39a}$$

$$\mathbf{v}_{c,s;lh,s'} = -\frac{1}{2}\sqrt{\frac{E_P}{3m}}\left[2\hat{\mathbf{k}}\sigma^0 + i\hat{\mathbf{l}}\sigma^y - i\hat{\mathbf{m}}\sigma^x\right]_{s,s'}, \tag{2.39b}$$

$$\mathbf{v}_{c,s;so,s'} = \sqrt{\frac{E_P}{6m}}\left[\hat{\mathbf{k}}\sigma^0 - i\hat{\mathbf{l}}\sigma^y + i\hat{\mathbf{m}}\sigma^x\right]_{s,s'}, \tag{2.39c}$$

$$\mathbf{v}_{hh,s;lh,s'} = \frac{1}{2}\sqrt{\frac{1}{3}}\frac{E_P}{E_g}\frac{\hbar k}{m}\left[\hat{\mathbf{l}}\sigma^0 - i\hat{\mathbf{m}}\sigma^z\right]_{s,s'}, \tag{2.39d}$$

$$\mathbf{v}_{hh,s;so,s'} = -\frac{1}{2\sqrt{6}}\frac{E_P}{(\Delta_0 + E_g)}\frac{\hbar k}{m}\left[\hat{\mathbf{l}}\sigma^0 - i\hat{\mathbf{m}}\sigma^z\right]_{s,s'}, \tag{2.39e}$$

$$\mathbf{v}_{lh,s;so,s'} = \frac{1}{3\sqrt{2}}\frac{E_P}{E_g}\frac{\hbar k}{m}\left[\frac{\Delta_0 + 2E_g}{\Delta_0 + E_g}\hat{\mathbf{k}}\sigma^0 - i\frac{1}{2}\frac{2\Delta_0 + 3E_g}{\Delta_0 + E_g}\left(\hat{\mathbf{l}}\sigma^y - \hat{\mathbf{m}}\sigma^x\right)\right]_{s,s'}. \tag{2.39f}$$

Here, σ^0 is the 2×2 identity matrix and σ^i are the Pauli spin matrices. Of course, for parabolic bands, the intraband matrix elements are

$$\mathbf{v}_{n,s;n,s'} = \delta_{s,s'}\frac{\hbar\mathbf{k}}{m_n}, \tag{2.40}$$

where m_n is the effective mass of band n.

The microscopic calculation of "1+2" spin-current injection requires matrix elements of the product of velocity and spin, $v^i S^j$. In terms of the matrix elements of the u-function kets, the matrix elements of the Bloch states are

$$\langle n,s,\mathbf{k}|\, v^i S^j \,|m,s',\mathbf{k}\rangle = \langle\overline{n,s,\mathbf{k}}|\, v^i S^j \,|\overline{m,s',\mathbf{k}}\rangle + \frac{\hbar k^i}{m}\langle\overline{n,s,\mathbf{k}}|\, S^j \,|\overline{m,s',\mathbf{k}}\rangle.$$

They can be evaluated using (2.35), the well-known action of the spin operator on $\{|\uparrow\rangle, |\downarrow\rangle\}$, (2.36), (2.37), and the rotation from the unprimed to primed states. For the conduction band, to lowest order in k,

$$\langle c,s,\mathbf{k}|\, v^i S^j \,|c,s',\mathbf{k}\rangle = \frac{\hbar k}{m_c}\frac{\hbar}{2}\left[\hat{k}^i\sigma^j(\hat{\mathbf{k}}) + Z_c\left(\sigma^i(\hat{\mathbf{k}})\hat{k}^j - \delta^{ij}\sigma^z\right)\right], \tag{2.41}$$

where

$$\sigma^i(\hat{\mathbf{k}}) \equiv \hat{l}^i\sigma^x + \hat{m}^i\sigma^y + \hat{k}^i\sigma^z,$$

and

$$Z_c \equiv \frac{1}{3}\frac{E_P\Delta_0}{E_g(\Delta_0 + E_g)}\frac{m_c}{m},$$

is a measure of the extent to which the spin and velocity of an electron in the conduction band are entangled; setting Z_c to zero gives the expressions that would have resulted if the approximation $\langle cs\mathbf{k}|\, v^i S^j \,|cs'\mathbf{k}\rangle \simeq \langle c\mathbf{k}|\, v^i \,|c\mathbf{k}\rangle\langle cs\mathbf{k}|\, S^j \,|cs'\mathbf{k}\rangle$ had been made. In GaAs, $Z_c = 0.0612$. For the

hole bands,

$$\langle hh, s, \mathbf{k}| v^i S^j |hh, s', \mathbf{k}\rangle = \frac{\hbar k}{m_{hh}} \frac{\hbar}{2} \hat{k}^i \sigma^j(\hat{\mathbf{k}}), \tag{2.42a}$$

$$\begin{aligned}\langle lh, s, \mathbf{k}| v^i S^j |lh, s', \mathbf{k}\rangle = &\frac{\hbar k}{m_{lh}} \frac{\hbar}{2} \hat{k}^i \left(\frac{2}{3}\sigma^j(\hat{\mathbf{k}}) - \frac{1}{3}\hat{k}^j \sigma^z\right) \\ &+ \frac{\hbar k}{m} \frac{\hbar}{2} \frac{1}{3} \frac{E_P}{E_g} \left[\frac{2}{3}\hat{k}^i \sigma^j(\hat{\mathbf{k}}) - \sigma^i(\hat{\mathbf{k}})\hat{k}^j + \left(\delta^{ij} - 2\hat{k}^i\hat{k}^j\right)\sigma^z\right],\end{aligned} \tag{2.42b}$$

$$\langle so, s, \mathbf{k}| v^i S^j |so, s', \mathbf{k}\rangle = \frac{1}{3}\frac{\hbar k}{m}\frac{\hbar}{2}\left[\hat{k}^i\sigma^j(\hat{\mathbf{k}}) - 2\hat{k}^i\hat{k}^j\sigma^z + \frac{E_P}{\Delta_0 + E_g}\left(\sigma^i(\hat{\mathbf{k}})\hat{k}^j - \hat{k}^i\sigma^j(\hat{\mathbf{k}}) - \delta^{ij}\sigma^z\right)\right]. \tag{2.42c}$$

Notice that (2.38) was used to make clearer the connection with the velocity matrix elements in (2.41), (2.42a), and the first term of (2.42b).

2.3.3 Current

Due to the energy denominator in the two-photon amplitude, intermediate states are generally less important the further in energy they are from the conduction and valence band of interest. I distinguish two types of terms: two-band terms, in which the intermediate band is the same as either the initial or final band, and three-band terms, in which it is different. This calculation includes all of the two-band terms, and only the three-band terms in which the intermediate band comes from the set $\{lh, hh, c\}$. I sketch the derivation for the two-band terms, but for three-band terms, I only present the results.

From the transition amplitudes (2.3) and (2.4), the microscopic expression (2.18), and the definition of the current-injection tensor (2.25),

$$\begin{aligned}\eta_{(I)}^{ijkl} = &i\frac{\pi e^4}{\hbar^3\omega^3}\frac{1}{L^3}\sum_{cv\mathbf{k}}\sum_{c'v'}{}' \left(v^i_{c,c'}(\mathbf{k})\,\delta_{v,v'} - v^i_{v',v}(\mathbf{k})\,\delta_{c,c'}\right) \\ &\times v^l_{c',v'}(\mathbf{k}) \sum_n \frac{\left\{v^{j*}_{c,n}(\mathbf{k}), v^{k*}_{n,v}(\mathbf{k})\right\}}{\omega_{nv}(\mathbf{k}) - \omega}\delta\left(2\omega - \omega_{cv}(\mathbf{k})\right),\end{aligned} \tag{2.43}$$

where $\left\{v^{j*}_{c,n}, v^{k*}_{n,v}\right\} \equiv \left(v^{j*}_{c,n}v^{k*}_{n,v} + v^{k*}_{c,n}v^{j*}_{n,v}\right)/2$ ensures the intrinsic symmetry $\eta^{ikjl}_{(I)} = \eta^{ijkl}_{(I)}$. Note that the microscopic expression (2.43) differs by a factor of two from the one given by Atanasov *et al.*, which accounts for doubly-degenerate bands with a factor of two rather than in the sum over states [3]. Switching to the double band index notation, but suppressing the spin index on energies, which are independent of the spin index,

$$\eta^{ijkl}_{(I)} = i\frac{\pi e^4}{\hbar^3\omega^3}\frac{1}{L^3}\sum_{cv\mathbf{k}}\sum_{s,p}\Delta^i_{cv}(\mathbf{k})\,v^l_{cs,vp}(\mathbf{k})\sum_{n,s'}\frac{\left\{v^{j*}_{cs,ns'}(\mathbf{k}), v^{k*}_{ns',vp}(\mathbf{k})\right\}}{\omega_{nv}(\mathbf{k}) - \omega}\delta\left(2\omega - \omega_{cv}(\mathbf{k})\right), \tag{2.44}$$

where $\mathbf{\Delta}_{cv}(\mathbf{k}) \equiv \mathbf{v}_{cs,cs}(\mathbf{k}) - \mathbf{v}_{vp,vp}(\mathbf{k})$. Then, converting the sum over $\mathbf{k}$ to an integral and using (2.40),

$$\begin{aligned}\eta_{(I)}^{ijkl} =& i\frac{\pi e^4}{\hbar^3\omega^3}\sum_{cv}\int dk\frac{k^2}{8\pi^3}\frac{m_{cv}}{\hbar k_{cv}}\delta\left(k-k_{cv}\right)\\ &\times\int d\Omega\frac{\hbar k^i}{m_{cv}}\left[\sum_{s,p}v^l_{cs,vp}(\mathbf{k})\sum_{n,s'}\frac{\left\{v^{j*}_{cs,ns'}(\mathbf{k}),v^{k*}_{ns',vp}(\mathbf{k})\right\}}{\omega_{nv}(\mathbf{k})-\omega}\right],\end{aligned} \tag{2.45}$$

where

$$k_{cv}\equiv\begin{cases}\frac{1}{\hbar}\sqrt{2m_{cv}\left(2\hbar\omega-E_g\right)} & \text{for } v=lh \text{ or } v=hh,\\ \frac{1}{\hbar}\sqrt{2m_{cv}\left(2\hbar\omega-E_g-\Delta_0\right)} & \text{for } v=so.\end{cases} \tag{2.46}$$

Two-band terms

For two-band terms, $n=c$ or $n=v$. Thus the term in square brackets in (2.45) is

$$\begin{aligned}&\sum_{s,p}v^l_{cs,vp}(\mathbf{k})\frac{1}{2}\left[\frac{1}{\omega}\left(\frac{\hbar k^j}{m_c}\right)v^{k*}_{cs,vp}(\mathbf{k})-\frac{1}{\omega}v^{j*}_{cs,vp}(\mathbf{k})\left(\frac{\hbar k^k}{m_v}\right)\right]+\left(j\leftrightarrow k\right)\\ =&\frac{1}{2\omega}\frac{\hbar k^j}{m_{cv}}\sum_{s,p}v^k_{vp,cs}(\mathbf{k})v^l_{cs,vp}(\mathbf{k})+\left(j\leftrightarrow k\right),\end{aligned}$$

and thus,

$$\eta_{(I)}^{ijkl}=i\frac{e^4}{\hbar^3\omega^4}\sum_{cv}\frac{1}{8\pi^2}\frac{\hbar k^3_{cv}}{m_{cv}}\frac{1}{2}\int d\Omega\hat{k}^i\hat{k}^j\sum_{s,p}v^k_{vp,cs}\left(\hat{\mathbf{k}}\right)v^l_{cs,vp}\left(\hat{\mathbf{k}}\right)+\left(j\leftrightarrow k\right).$$

The sums over spin yield

$$\begin{aligned}\sum_{s,s'}v^k_{hh,s';c,s}v^l_{c,s;hh,s'}&=\frac{E_P}{2m}\left(\delta^{k,l}-\hat{k}^k\hat{k}^l\right),\\ \sum_{s,s'}v^k_{lh,s';c,s}v^l_{c,s;lh,s'}&=\frac{E_P}{2m}\left(\hat{k}^k\hat{k}^l+\frac{1}{3}\delta^{k,l}\right),\\ \sum_{s,s'}v^k_{so,s';c,s}v^l_{c,s;so,s'}&=\frac{E_P}{3m}\delta^{k,l}.\end{aligned}$$

The remaining angular integrals are

$$\begin{aligned}\int d\Omega\hat{k}^i\hat{k}^j&=\frac{4\pi}{3}\delta^{i,j},\\ \int d\Omega\hat{k}^i\hat{k}^j\hat{k}^k\hat{k}^l&=\frac{4\pi}{15}\left(\delta^{i,j}\delta^{k,l}+\delta^{i,k}\delta^{j,l}+\delta^{i,l}\delta^{j,k}\right).\end{aligned}$$

The result is of the form (2.26) with $\eta_C=0$, and

$$\eta_{B1}=\frac{e}{\hbar}D\left[\left(6\sqrt{\frac{m_{c,hh}}{m}}+\frac{22}{3}\sqrt{\frac{m_{c,lh}}{m}}\right)+\left(\frac{2\hbar\omega-E_g-\Delta_0}{2\hbar\omega-E_g}\right)^{\frac{3}{2}}\frac{20}{3}\sqrt{\frac{m_{c,so}}{m}}\right], \tag{2.47a}$$

$$\eta_{B2}=\frac{e}{\hbar}D\left(-2\sqrt{\frac{m_{c,hh}}{m}}+2\sqrt{\frac{m_{c,lh}}{m}}\right), \tag{2.47b}$$

where

$$D \equiv \frac{\sqrt{2}}{60\pi}\frac{e^3 E_P}{\sqrt{m}}\frac{(2\hbar\omega - E_g)^{3/2}}{\hbar^4\omega^4}, \tag{2.48}$$

and the last term in η_{B1} should be excluded if $2\hbar\omega < E_g + \Delta_0$. The finding that $\eta_C = 0$ is a consequence of using an isotropic (spherical) band model.

Three-band terms

I refer to the three-band terms using a notation *v-n-c* (valence-intermediate-conduction). The three band terms can be evaluated from (2.45) using (2.39). Since they are more tedious to evaluate, I only present the results. I have only worked out the three-band terms *hh-lh-c* and *lh-hh-c*. They add $\eta_{B1(3BTs)}$ to η_{B1} and add $\eta_{B2(3BTs)}$ to η_{B2}, where

$$\eta_{B1(3BTs)} = 2\frac{e}{\hbar}D\frac{E_P}{E_g}\left[\left(\frac{m_{c,hh}}{m}\right)^{3/2}\left(1 + x\frac{m_{c,hh}}{m_{hh,lh}}\right)^{-1} - \frac{2}{3}\left(\frac{m_{c,lh}}{m}\right)^{3/2}\left(1 - x\frac{m_{c,lh}}{m_{hh,lh}}\right)^{-1}\right], \tag{2.49a}$$

$$\eta_{B2(3BTs)} = \frac{2}{3}\frac{e}{\hbar}D\frac{E_P}{E_g}\left[-\left(\frac{m_{c,hh}}{m}\right)^{3/2}\left(1 + x\frac{m_{c,hh}}{m_{hh,lh}}\right)^{-1} + 4\left(\frac{m_{c,lh}}{m}\right)^{3/2}\left(1 - x\frac{m_{c,lh}}{m_{hh,lh}}\right)^{-1}\right], \tag{2.49b}$$

and $x \equiv (2\hbar\omega - E_g)/(\hbar\omega)$. I have not worked out the three-band terms *hh-so-c*, *lh-so-c*, *so-hh-c*, or *so-lh-c*. They are discussed in Chapter 3 in the context of the numerical fourteen-band calculation.

Discussion

Previous calculations of $\eta_{(I)}$ in the PBA used simpler band models than the one I used here. Using a two-band model (one conduction and one valence band), Atanasov *et al.* obtained $\eta_{B1} \propto (2\hbar\omega - E_g)^{3/2}$ and $\eta_{B2} = 0$ [3]. Using a three-band model, but only accounting for two-band terms, Sheik-Bahae obtained results that differ from (2.47a) and (2.47b) by material independent factors [79].[7] The three-band model lacks the matrix elements $\mathbf{v}_{c\uparrow,lh\downarrow}$ and $\mathbf{v}_{c\downarrow,lh\uparrow}$, and thus two-band terms for η_{B1} derived from it should differ from (2.47a).

[7]To make the comparison, note that Sheik-Bahae used the approximations $m_{c,lh}/m \approx E_g/(2E_P)$ and $m_{c,hh}/m \approx E_g/E_P$ [cf. (2.38)].

2.3.4 Spin Current

The spin-current injection pseudotensor, defined in (2.29) can be written as a sum of electron and hole terms so that $\mu_{(I)}^{ijklm} = \mu_{(I;e)}^{ijklm} + \mu_{(I;h)}^{ijklm}$). From (2.21) and (2.29)

$$\mu_{(I;e)}^{ijklm} = i\frac{\pi e^3}{\hbar^3\omega^3}\frac{1}{L^3}\sum_{c,v,\mathbf{k}}{\sum_{c'}}' \left\langle c'\mathbf{k}\right| \hat{v}^i\hat{S}^j \left|c\mathbf{k}\right\rangle v_{c,v}^m(\mathbf{k}) \sum_n \frac{\left\{v_{c',n}^{k*}(\mathbf{k}), v_{n,v}^{l*}(\mathbf{k})\right\}}{\omega_{nv}(\mathbf{k}) - \omega}\delta\left(2\omega - \omega_{cv}(\mathbf{k})\right), \tag{2.50a}$$

$$\mu_{(I;h)}^{ijklm} = -i\frac{\pi e^3}{\hbar^3\omega^3}\frac{1}{L^3}\sum_{c,v,\mathbf{k}}{\sum_{v'}}' \left\langle v\mathbf{k}\right| \hat{v}^i\hat{S}^j \left|v'\mathbf{k}\right\rangle v_{c,v}^m(\mathbf{k}) \sum_n \frac{\left\{v_{c,n}^{k*}(\mathbf{k}), v_{n,v'}^{l*}(\mathbf{k})\right\}}{\omega_{nv}(\mathbf{k}) - \omega}\delta\left(2\omega - \omega_{cv}(\mathbf{k})\right), \tag{2.50b}$$

where $\left\{v_{c,n}^{k*}, v_{n,v}^{l*}\right\} \equiv \left(v_{c,n}^{k*}v_{n,v}^{l*} + v_{c,n}^{l*}v_{n,v}^{k*}\right)/2$ ensures the intrinsic symmetry $\mu_{(I)}^{ijlkm} = \mu_{(I)}^{ijklm}$. Switching to the double band index notation, but suppressing the spin index on energies, which are independent of the spin index,

$$\begin{aligned}\mu_{(I;e)}^{ijklm} = i\frac{\pi e^3}{\hbar^3\omega^3}\frac{1}{L^3}\sum_{c,v,\mathbf{k}}\sum_{s,p}\sum_{s'} &\left\langle c,s',\mathbf{k}\right| \hat{v}^i\hat{S}^j \left|c,s,\mathbf{k}\right\rangle \\ &\times v_{cs,vp}^m(\mathbf{k}) \sum_n \sum_{s''} \frac{\left\{v_{cs',ns''}^{k*}(\mathbf{k}), v_{ns'',vp}^{l*}(\mathbf{k})\right\}}{\omega_{nv}(\mathbf{k}) - \omega}\delta\left(2\omega - \omega_{cv}(\mathbf{k})\right),\end{aligned} \tag{2.51a}$$

$$\begin{aligned}\mu_{(I;h)}^{ijklm} = -i\frac{\pi e^3}{\hbar^3\omega^3}\frac{1}{L^3}\sum_{c,v,\mathbf{k}}\sum_{s,p}\sum_{p'} &\left\langle v,p,\mathbf{k}\right| \hat{v}^i\hat{S}^j \left|v,p',\mathbf{k}\right\rangle \\ &\times v_{cs,vp}^m(\mathbf{k}) \sum_n \sum_{s''} \frac{\left\{v_{cs,ns''}^{k*}(\mathbf{k}), v_{ns'',vp'}^{l*}(\mathbf{k})\right\}}{\omega_{nv}(\mathbf{k}) - \omega}\delta\left(2\omega - \omega_{cv}(\mathbf{k})\right).\end{aligned} \tag{2.51b}$$

The sums over spin states and integral over $\mathbf{k}$ can be done using steps similar to those used from (2.44) to (2.47), but they are more tedious to work out because the matrix elements of $\hat{v}^i\hat{S}^j$ are not diagonal in spin index. I only give results for transitions from the *hh* and *lh* bands; also, *so* intermediate states are not included. The neglected terms are discussed in Chapter 3 in the context of the numerical fourteen-band calculation. The spin-current injection for both electrons and holes has the form (2.30) with $\mu_{C1} = \mu_{C2} = \mu_{C3} = 0$.

For the electron spin current,

$$\mu_{N1;e} = D\frac{m}{m_c}\left(\frac{m_{c,hh}}{m}\right)^{3/2}(1+Z_c) - D\frac{m}{m_c}\left(\frac{m_{c,hh}}{m}\right)^{5/2}\frac{E_P}{3E_g}\frac{1-Z_c}{1+xm_{c,hh}/m_{hh,lh}} + D\frac{m}{m_c}\left(\frac{m_{c,lh}}{m}\right)^{3/2}\left(\frac{7}{3}-Z_c\right) - D\frac{m}{m_c}\left(\frac{m_{c,lh}}{m}\right)^{5/2}\frac{E_P}{3E_g}\frac{1}{1-xm_{c,lh}/m_{hh,lh}}, \tag{2.52a}$$

$$\mu_{N2;e} = D\frac{m}{m_c}\left(\frac{m_{c,hh}}{m}\right)^{3/2}(1+Z_c) - 3D\frac{m}{m_c}\left(\frac{m_{c,hh}}{m}\right)^{5/2}\frac{E_P}{3E_g}\frac{1-Z_c}{1+xm_{c,hh}/m_{hh,lh}} - D\frac{m}{m_c}\left(\frac{m_{c,lh}}{m}\right)^{3/2}\left(1-\frac{7}{3}Z_c\right) - Z_cD\frac{m}{m_c}\left(\frac{m_{c,lh}}{m}\right)^{5/2}\frac{E_P}{3E_g}\frac{1}{1-xm_{c,lh}/m_{hh,lh}}, \tag{2.52b}$$

$$\mu_{N3;e} = -2D\frac{m}{m_c}\left(\frac{m_{c,hh}}{m}\right)^{5/2}\frac{E_P}{3E_g}\frac{1-Z_c}{1+xm_{c,hh}/m_{hh,lh}} + 2(1-Z_c)D\frac{m}{m_c}\left(\frac{m_{c,lh}}{m}\right)^{5/2}\frac{E_P}{3E_g}\frac{1}{1-xm_{c,lh}/m_{hh,lh}}, \tag{2.52c}$$

where $x \equiv (2\hbar\omega - E_g)/(\hbar\omega)$, $m_{n,m}^{-1} = m_n^{-1} - m_m^{-1}$, and D is given in (2.48). In (2.52a) and (2.52b) ($\mu_{N1;e}$ and $\mu_{N2;e}$), the first term is from the *hh-c* transition, the second term is from the *hh-lh-c* transition, the third term is from the *lh-c* transition, and the fourth term is from the *lh-hh-c* transition. In (2.52c) for $\mu_{N3;e}$, the first term is from the *hh-lh-c* transition, and the second term is from the *lh-hh-c* transition. Note that two-band terms make no contribution to $\mu_{N3;e}$.

For the hole spin current, I have only worked out the two-band terms *hh-c* and *lh-c*, which yield $\mu_{N3;h} = 0$ and

$$\mu_{N1;h} = -D\left(\frac{m_{c,hh}}{m}\right)^{3/2}\frac{m}{m_{hh}} - \frac{17}{9}D\left(\frac{3E_P-3E_g}{2E_P-3E_g}\right)\left(\frac{m_{c,lh}}{m}\right)^{3/2}\frac{m}{m_{lh}} \tag{2.53a}$$

$$\mu_{N2;h} = -D\left(\frac{m_{c,hh}}{m}\right)^{3/2}\frac{m}{m_{hh}} - \frac{1}{3}D\left(\frac{7E_P+3E_g}{2E_P-3E_g}\right)\left(\frac{m_{c,lh}}{m}\right)^{3/2}\frac{m}{m_{lh}} \tag{2.53b}$$

For typical semiconductors, $\mu_{N1;e}$, $\mu_{N2;e}$, $\mu_{N1;h}$, and $\mu_{N2;h}$ are negative (keep in mind that e^3, m_{hh}, and m_{lh} are negative). While the holes are injected with spin opposite that of the electrons [2], their velocity is also opposite, and thus the hole and electron spin currents have the same sign.

In Bhat and Sipe, we published these results using a different notation [38].

2.4 Spin current configurations

We now examine the spin, current, and spin currents injected by optical fields with specific polarization configurations that are possible for co-propagating beams. Since the model is isotropic, we lose no generality by choosing $\hat{\mathbf{z}}$ for the propagation direction.

Fields having opposite circular polarizations inject neither current nor spin current. Co-linearly polarized fields inject a significant current [4], but only a small spin-current, proportional to μ_{N3}.

Case 1: Co-circularly polarized fields: $\mathbf{E}_{\omega/2\omega} = E_{\omega/2\omega} e^{i\phi_{\omega/2\omega}} (\hat{\mathbf{x}} \pm i\hat{\mathbf{y}}) / \sqrt{2}$. The electron spin injected by one-photon absorption from the 2ω beam is $\dot{\boldsymbol{\mathcal{S}}}_{(1;e)} = \mp (\hbar/4) \dot{N}_{(1)} \hat{\mathbf{z}}$ within the Kane model, where $\dot{N}_{(1)}$ is the one-photon carrier injection rate [2]. The electron spin injected by two-photon absorption from the ω beam, also calculated within the Kane model, is

$$\dot{\boldsymbol{\mathcal{S}}}_{(2;e)} = \mp \frac{\hbar}{2} \frac{\sqrt{m_{c,hh}} + (7/3)\sqrt{m_{c,lh}}}{3\sqrt{m_{c,hh}} + (11/3)\sqrt{m_{c,lh}}} \dot{N}_{(2)} \hat{\mathbf{z}}, \tag{2.54}$$

where only the two-band terms are included, and $\dot{N}_{(2)}$ is the two-photon carrier injection rate. There is no interference term in either the spin or carrier injection when the material (or model) possesses inversion symmetry and thus the spin injection is simply $\dot{\boldsymbol{\mathcal{S}}}_e = \dot{\boldsymbol{\mathcal{S}}}_{(1;e)} + \dot{\boldsymbol{\mathcal{S}}}_{(2;e)}$. The electrical current injection is $\dot{\mathbf{J}}_{(I)} = \sqrt{2}\hat{\mathbf{m}}\eta_{B1} E_\omega^2 E_{2\omega}$, where the direction $\hat{\mathbf{m}} \equiv \hat{\mathbf{x}} \sin(2\phi_\omega - \phi_{2\omega}) \pm \hat{\mathbf{y}} \cos(2\phi_\omega - \phi_{2\omega})$. Its magnitude is comparable to the current from co-linearly polarized fields; in fact, it is a factor of $\sqrt{2}$ smaller, since $\eta_{B1} \gg \eta_{B2}$. The spin-current injection is

$$\dot{K}^{ij}_{(I)} = \mp\sqrt{2} E_\omega^2 E_{2\omega} \left(\mu_{N1} \hat{m}^i \hat{z}^j + \mu_{N2} \hat{z}^i \hat{m}^j \right). \tag{2.55}$$

Recalling that the first index of $K^{ij}_{(I)}$ is associated with the carrier velocity, we see that the first term in $\dot{K}^{ij}_{(I)}$ shows that the electrical current is partially spin-polarized. The extent of the spin-polarization of the current f can be defined by $\dot{K}^{iz} / \left(\dot{J}^i / e \right) = \mp f\hbar/2$. In this case, $f = 2e\mu_{N1}/(\hbar\eta_{B1})$. Using parameter values appropriate to GaAs [122], $f = 0.57$ when $2\hbar\omega - E_g = 100$ meV. This value includes both electron and hole contributions to both spin-current and current, although three-band hole contributions to the spin-current are not included. The spin-polarization of the electron current distribution, evaluated using electron terms only, is $f = 0.53$. The second term in $\dot{K}^{ij}_{(I)}$ represents spins pointing along $\hat{\mathbf{m}}$ that move along $\hat{\mathbf{z}}$. Since there is no net electrical current in the $\hat{\mathbf{z}}$ direction, this is a pure spin current. It arises because the electrons have a distribution of velocities such that those with positive $\hat{\mathbf{z}}$ components have opposite average spin to those with negative $\hat{\mathbf{z}}$ components. For the electron distribution in GaAs, $\mu_{N2;e}/\mu_{N1;e} = -0.049$ at 100 meV excess photon energy. When both electron and holes are included, $\mu_{N2;e}/\mu_{N1;e} = 0.13$. The situation is schematically indicated in Fig. 2.2(a). The first term in (2.55) was experimentally studied by Stevens *et al.* [71].

Case 2: Orthogonal linearly polarized fields: $\mathbf{E}_\omega = E_\omega e^{i\phi_\omega} \hat{\mathbf{x}}$ and $\mathbf{E}_{2\omega} = E_{2\omega} e^{i\phi_{2\omega}} \hat{\mathbf{y}}$. In this case, since the fields are linearly polarized, there is no spin injection, $\dot{\boldsymbol{\mathcal{S}}}_e = \dot{\boldsymbol{\mathcal{S}}}_h = 0$, which can be verified by symmetry arguments. The electrical current depends sinusoidally on the relative phase of the two fields, $\dot{\mathbf{J}}_{(I)} = 2\eta_{B2} E_\omega^2 E_{2\omega} \sin(2\phi_\omega - \phi_{2\omega}) \hat{\mathbf{y}}$. According to the Kane model,

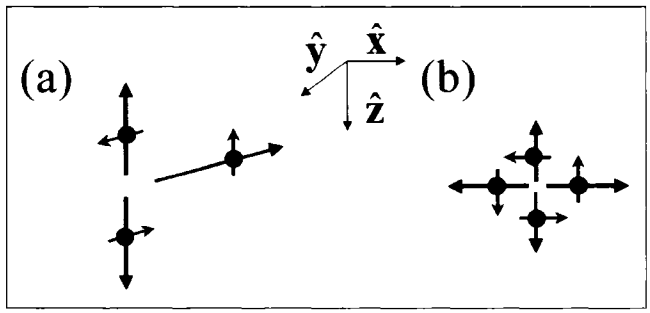

Figure 2.2: Schematic illustrations of the net electron motion combining the information of $\dot{K}^{ij}$ and $\dot{J}^{i}$ for (a) case 1 with both fields right circularly polarized, and (b) case 2, orthogonal linearly polarized fields. The directions are specified in the text.

its magnitude is much smaller than the current from co-circularly polarized fields, since the contributions from the heavy hole and light hole transitions largely cancel in η_{B2} rather than adding in η_{B1}.[8] In the notation of Atanasov *et al.* [3], the current in this case is proportional to η^{yxxy} while the current in case 1 is proportional to $\sqrt{2}\mathrm{Im}\eta^{xxyy}$, which is an order of magnitude greater than η^{yxxy} in their *ab initio* calculations. The spin current for orthogonal linearly polarized fields is

$$\dot{K}^{ij}_{(I)} = -2E_{\omega}^{2}E_{2\omega}\cos\left(2\phi_{\omega}-\phi_{2\omega}\right)\left[\left(\mu_{N1}+\mu_{N3}\right)\hat{x}^{i}\hat{z}^{j}+\left(\mu_{N2}-\mu_{N3}\right)\hat{z}^{i}\hat{x}^{j}\right]. \tag{2.56}$$

Again there are two terms, the first arising from carrier motion along $\mathbf{E}_{\omega}$ with spins aligned along the beam propagation direction, and the second arising from carrier motion along the beam propagation direction with spins aligned along $\mathbf{E}_{\omega}$. Both of these are pure spin currents, since there is no electrical current in either direction. At 100 meV excess photon energy in GaAs, $\sqrt{2}(\mu_{N1;e}+\mu_{N3;e})/\mu_{N1;e} = \sqrt{2}(\mu_{N1}+\mu_{N3})/\mu_{N1} = 1.3$. That is, when the optical phase difference is zero, the first term is 1.3 times larger than the first term of the case 1 spin-current injection. The second term of (2.56) is smaller than the first. For the electron distribution, $(\mu_{N2;e}-\mu_{N3;e})/(\mu_{N1;e}+\mu_{N3;e}) = 0.075$, while for electrons and holes, $(\mu_{N2}-\mu_{N3})/(\mu_{N1}+\mu_{N3}) = 0.23$. The electrical current injected along the $\mathbf{E}_{2\omega}$ polarization is unpolarized for all optical phases. The situation is schematically indicated in Fig. 2.2(b).

[8] It is not zero, however, as reported for the parabolic band approximation in [3].

Chapter 3

Two-colour Quantum Interference: Fourteen-band Model Calculations

3.1 Introduction

In the preceding chapter, the "1+2" effects—current injection, spin-current injection, population control, and spin control—are studied from the point of view of crystal symmetry, and with solutions of an eight-band $\mathbf{k}\cdot\mathbf{p}$ Hamiltonian that are expanded perturbatively in the Bloch wave vector $\mathbf{k}$. The eight-band model has spherical symmetry, even to higher orders in k, and thus fails to describe properties that depend on a lack of inversion symmetry such as spin-splitting, "1+2" population control, and "1+2" spin control.

One can extend the eight-band model either by incorporating remote band effects into the eight-band Hamiltonian [121], or by enlarging the basis. It is most natural to enlarge the basis to fourteen to encompass the group of six higher conduction bands that are the next closest in energy to the fundamental band gap in typical semiconductors. Fourteen-band models (also called five-level models) can accurately account for lack of inversion symmetry [123–134]. In this chapter, injection spectra for "1+2" processes are calculated using a 14×14 $\mathbf{k}\cdot\mathbf{p}$ Hamiltonian including remote band effects for five bulk semiconductors of zinc-blende symmetry: InSb, GaSb, InP, GaAs, and ZnSe. In contrast to the preceding chapter, the model is solved numerically and does not involve a perturbation in $\mathbf{k}$. Appendix C gives expressions for population and spin control based on perturbative expansions in $\mathbf{k}$ of the fourteen-band model. For each "1+2" process, I compare the fourteen-band model results with the analytical results perturbative in $\mathbf{k}$ presented in the preceding chapter and Appendix C.

Since the model used here accounts for spin-splitting, microscopic expressions for spin-current injection and spin control accounting for spin split bands are presented.

3.2 Model

As in the preceding chapter, I calculate the injection of each "1+2" process using microscopic expressions derived using velocity gauge ($\mathbf{A}\cdot\mathbf{v}$) coupling in the long-wavelength approximation, treating the field perturbatively in the Fermi's golden rule (FGR) limit, and using the independent-particle approximation [3, 36]. But for spin-current injection and spin control, one must use generalized expressions that account for the spin-splitting of the bands. All of these expressions require the unperturbed (i.e. field-free) one-particle energies and matrix elements of velocity and spin.

3.2.1 Hamiltonian

Recall from Sec. 2.3.1 that the $\mathbf{k}\cdot\mathbf{p}$ Hamiltonian can be expanded in a set of Γ-point states. The fourteen-band model truncates this expansion to a set of fourteen states [124]. The fourteen bands (counting one for each spin), which are shown in Fig. 3.1, comprise six valence bands (two each for split-off, heavy and light holes) and eight conduction bands (the two s-like ones at the band edge, and the six next lowest ones which are p-like). This "bare" fourteen-band model is further improved by treating remote bands using Löwdin perturbation theory [135], which adds $\mathbf{k}$-dependent terms to the truncated 14×14 Hamiltonian so that its solutions better approximate those of the full Hamiltonian [130]. The fourteen-band model Hamiltonian, which includes important remote band effects to order k^2, and which I denote H_{14}, is given explicitly by Pfeffer and Zawadski [130].[1] We now briefly review its derivation.

In a semiconductor of zinc-blende symmetry, the states $\{|n,\mathbf{k}=\mathbf{0}\rangle\,|n=1..14\}$ are conveniently expanded in the eigenstates of H_0, $\{|S\rangle,|X\rangle,|Y\rangle,|Z\rangle,|x\rangle,|y\rangle,|z\rangle\}\otimes\{|\uparrow\rangle,|\downarrow\rangle\}$, where, under the point group T_d, $|S\rangle$ transforms like Γ_1, $\{|X\rangle,|Y\rangle,|Z\rangle\}$ and $\{|x\rangle,|y\rangle,|z\rangle\}$ transform like Γ_4 [118]. The $\{|\uparrow\rangle,|\downarrow\rangle\}$ are the usual spin 1/2 states:

$$\langle\uparrow|\,\boldsymbol{\sigma}\,|\uparrow\rangle = -\langle\downarrow|\,\boldsymbol{\sigma}\,|\downarrow\rangle = \hat{\mathbf{z}} \tag{3.1a}$$

$$\langle\uparrow|\,\boldsymbol{\sigma}\,|\downarrow\rangle = (\langle\downarrow|\,\boldsymbol{\sigma}\,|\uparrow\rangle)^* = \hat{\mathbf{x}} - i\hat{\mathbf{y}}. \tag{3.1b}$$

The non-zero matrix elements of $(\boldsymbol{\nabla}V\times\mathbf{p})$ are

$$\langle X|\,(\boldsymbol{\nabla}V\times\mathbf{p})^y\,|Z\rangle \equiv i\frac{4m^2c^2}{3\hbar}\Delta_0,$$

$$\langle x|\,(\boldsymbol{\nabla}V\times\mathbf{p})^y\,|z\rangle \equiv i\frac{4m^2c^2}{3\hbar}\Delta_0',$$

$$\langle X|\,(\boldsymbol{\nabla}V\times\mathbf{p})^y\,|z\rangle \equiv i\frac{4m^2c^2}{3\hbar}\Delta^-,$$

[1] Eq. (5) of Pfeffer and Zawadski has one typographical error: element $(4,14)$ should be $-\sqrt{1/3}P_0k_z$ [130].

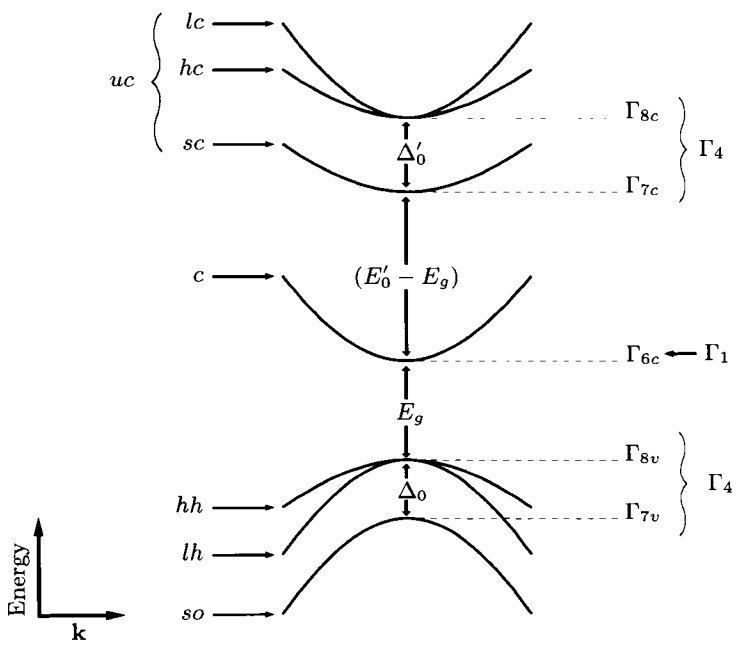

Figure 3.1: A schematic diagram of the fourteen-band model, indicating band abbreviations (left), energies (center), and symmetry of the Γ-point states (right). Γ_6, Γ_7, and Γ_8 indicate irreducible representations of the T_d double group, whereas Γ_1 and Γ_4 indicate irreducible representations of the T_d point group. Note that spin-splitting of the bands cannot be seen on this scale.

cyclic permutations of these [e.g. $\langle x|\,(\boldsymbol{\nabla}V\times\mathbf{p})^y\,|z\rangle = \langle z|\,(\boldsymbol{\nabla}V\times\mathbf{p})^x\,|y\rangle = \langle y|\,(\boldsymbol{\nabla}V\times\mathbf{p})^z\,|x\rangle$], and those generated by Hermitian conjugation of these. The above equations define the spin-orbit energies Δ_0 and Δ_0', and the interband spin-orbit coupling Δ^- [136, 137]. The fourteen basis states $\{|n\mathbf{k}=\mathbf{0}\rangle\,|n=1..14\}$ for H_{14} are

$$|\Gamma_{7v},\pm1/2\rangle = \pm\frac{1}{\sqrt{3}}\,|Z\rangle\,|\alpha_\pm\rangle + \frac{1}{\sqrt{3}}\,|X\pm iY\rangle\,|\alpha_\mp\rangle \tag{3.2a}$$

$$|\Gamma_{8v},\pm1/2\rangle = \mp\sqrt{\frac{2}{3}}\,|Z\rangle\,|\alpha_\pm\rangle + \frac{1}{\sqrt{6}}\,|X\pm iY\rangle\,|\alpha_\mp\rangle \tag{3.2b}$$

$$|\Gamma_{8v},\pm3/2\rangle = \pm\frac{1}{\sqrt{2}}\,|X\pm iY\rangle\,|\alpha_\pm\rangle \tag{3.2c}$$

$$|\Gamma_{6c},\pm1/2\rangle = i\,|S\rangle\,|\alpha_\pm\rangle \tag{3.2d}$$

$$|\Gamma_{7c},\pm1/2\rangle = \pm\frac{1}{\sqrt{3}}\,|z\rangle\,|\alpha_\pm\rangle + \frac{1}{\sqrt{3}}\,|x\pm iy\rangle\,|\alpha_\mp\rangle \tag{3.2e}$$

$$|\Gamma_{8c},\pm1/2\rangle = \mp\sqrt{\frac{2}{3}}\,|z\rangle\,|\alpha_\pm\rangle + \frac{1}{\sqrt{6}}\,|x\pm iy\rangle\,|\alpha_\mp\rangle \tag{3.2f}$$

$$|\Gamma_{8c},\pm3/2\rangle = \pm\frac{1}{\sqrt{2}}\,|x\pm iy\rangle\,|\alpha_\pm\rangle\,, \tag{3.2g}$$

where $|\alpha_+\rangle = |\uparrow\rangle$ and $|\alpha_-\rangle = |\downarrow\rangle$. The states are labeled with their transformation property under the double group for T_d, and with a pseudo-angular momentum notation. The meaning of this notation is not important for this chapter; it is discussed further in Chapter 4. In the basis (3.2), $H_{\mathbf{k}=\mathbf{0}}$ is diagonal except for terms proportional to Δ^-. The connection between the eigenvalues of $H_{\mathbf{k}=\mathbf{0}}$ for the Γ-point eigenstates and the eigenvalues of H_0 is given by Pfeffer and Zawadski [124]. The nonzero matrix elements of momentum, which appear in $H_{\mathbf{k}}$, are

$$\langle S|\,p^x\,|X\rangle = \langle S|\,p^y\,|Y\rangle = \langle S|\,p^z\,|Z\rangle \equiv imP_0/\hbar \tag{3.3a}$$

$$\langle S|\,p^x\,|x\rangle = \langle S|\,p^y\,|y\rangle = \langle S|\,p^z\,|z\rangle \equiv imP_0'/\hbar \tag{3.3b}$$

$$\langle X|\,p^y\,|z\rangle = \langle Y|\,p^z\,|x\rangle = \langle Z|\,p^x\,|y\rangle = \langle Z|\,p^y\,|x\rangle = \langle Y|\,p^x\,|z\rangle = \langle X|\,p^z\,|y\rangle \equiv imQ/\hbar. \tag{3.3c}$$

This defines the parameters P_0, P_0', and Q. They are sometimes expressed as energies E_P, $E_{P'}$, and E_Q with the connections $E_P = 2mP_0^2/\hbar^2$, etc. The first, E_P, is known as the Kane energy.

The "bare" fourteen-band model has eight empirical parameters E_g, Δ_0, E_0', Δ_0', Δ^-, P_0, Q, and P_0'. Its quantitative accuracy is improved by adding remote band effects to order k^2 [130]. Only the most important remote band effects are included [130]. They are governed by the parameters γ_1, γ_2, γ_3, F, and C_k. The parameters γ_1, γ_2, and γ_3 are modified Luttinger parameters that account for remote band effects on the valence bands; they are analogues of the usual Luttinger parameters γ_{1L}, γ_{2L}, and γ_{3L} modified to remove the couplings with Γ_{6c}, Γ_{7c}, and Γ_{8c} bands, which are already accounted for in the "bare" fourteen-band model [130].

Specifically [130],

$$\gamma_1 = \gamma_{1L} - \frac{E_P}{3E_g} - \frac{E_Q}{3E_0'} - \frac{E_Q}{3E_0' + \Delta_0'},$$
$$\gamma_2 = \gamma_{2L} - \frac{E_P}{6E_g} + \frac{E_Q}{6E_0'},$$
$$\gamma_3 = \gamma_{3L} - \frac{E_P}{6E_g} - \frac{E_Q}{6E_0'}.$$

The parameter F accounts for remote band effects on the conduction band (Γ_{6c}), essentially fixing its effective mass to the experimentally observed value. Finally, the parameter C_k is the small **k**-linear term in the valence bands due to interactions with remote bands [137]. The remote band effects can be removed by setting $\gamma_1 = -1$ and $\gamma_2 = \gamma_3 = F = C_k = 0$. The model includes neither remote band effects on the *uc* bands, nor remote band effects on the Γ_{6c}-Γ_{8v} and Γ_{6c}-Γ_{7v} momentum matrix elements, though such terms exist in principle [132].

In summary, H_{14} is a fourteen-band approximation to $H_{\mathbf{k}}$ that incorporates some remote band effects. It has thirteen parameters. Numerical solutions to H_{14} give $|\overline{n\mathbf{k}}\rangle$. The complete Hamiltonian, which I denote H_{14}, can be found in Eq. (5) of Pfeffer and Zawadzki [130]. Note that their notation is slightly different from mine. With their notation on the left, and mine on the right: $E_0 = -E_g$, $E_1 = E_0' - E_g$, $\Delta_1 = \Delta_0'$, $\overline{\Delta} = \Delta^-$, $P_1 = P_0'$. Also, my Δ_0 differs from theirs by a minus sign. Other authors have also used different notations [132]. The fourteen bands are shown schematically in Fig. 3.1 along with the symmetry notation of the Γ-point states, and the notation used to label the bands.

3.2.2 Material parameters

Numerical values for the thirteen parameters of the model are listed in Table 3.1 for InSb, GaSb, InP, GaAs, and ZnSe. They are taken from the literature, where they were chosen to fit low-temperature experimental data. Of the two parameter sets discussed by Pfeffer and Zawadzki for GaAs, I use the one corresponding to $\alpha = 0.085$ that they find gives better results [130]. For InP, GaSb, and InSb, I use parameters from Cardona, Christensen and Fasal [137]. For cubic ZnSe, I use the parameters given by Mayer and Rossler [127], I use a calculated value of C_k [137], and I use $\Delta^- = -0.238\,\text{eV}$ to give a k^3 conduction band spin-splitting that matches the *ab initio* calculation of Cardona, Christensen and Fasal [137]. Winkler used these same parameters for ZnSe, but took $\Delta^- = 0$ [132]. There is more uncertainty in the parameters for ZnSe than in those for the other materials [127], but I include it as an example of a semiconductor with a larger band gap.

The parabolic-band approximation calculations use parameters from Table 3.1, and average effective masses derived from the parameters in Table 3.1.

Table 3.1: Material parameters.

	GaAs	InP	GaSb	InSb	ZnSe
E_g (eV)	1.519	1.424	0.813	0.235	2.820
Δ_0 (eV)	0.341	0.108	0.75	0.803	0.403
E_0' (eV)	4.488	4.6	3.3	3.39	7.330
Δ_0' (eV)	0.171	0.50	0.33	0.39	0.090
Δ^- (eV)	−0.061	0.22	−0.28	−0.244	−0.238
P_0 (eVÅ)	10.30	8.65	9.50	9.51	10.628
Q (eVÅ)	7.70	7.24	8.12	8.22	9.845
P_0' (eVÅ)	3.00	4.30	3.33	3.17	9.165
γ_{1L}	7.797	5.05	13.2	40.1	4.30
γ_{2L}	2.458	1.6	4.4	18.1	1.14
γ_{3L}	3.299	1.73	5.7	19.2	1.84
F	−1.055	0	0	0	0
C_k (meVÅ)	−3.4	−14	0.43	−9.2	−14

3.2.3 Matrix elements

The relations between matrix elements of the Bloch states and matrrix elements of the u-function kets (defined in Sec. 2.3.1) are

$$\mathbf{v}_{nm}(\mathbf{k}) \equiv \langle n\mathbf{k}|\,\mathbf{v}\,|m\mathbf{k}\rangle = \langle\overline{n\mathbf{k}}|\,\mathbf{v}\,|\overline{m\mathbf{k}}\rangle + \frac{\hbar\mathbf{k}}{m}\delta_{nm}, \tag{3.4}$$

$$\langle n\mathbf{k}|\,\mathbf{S}\,|m\mathbf{k}\rangle = \langle\overline{n\mathbf{k}}|\,\mathbf{S}\,|\overline{m\mathbf{k}}\rangle \tag{3.5}$$

$$\langle n\mathbf{k}|\,v^iS^j\,|m\mathbf{k}\rangle = \langle\overline{n\mathbf{k}}|\,v^iS^j\,|\overline{m\mathbf{k}}\rangle + \frac{\hbar k^i}{m}\langle\overline{n\mathbf{k}}|\,S^j\,|\overline{m\mathbf{k}}\rangle\,. \tag{3.6}$$

The matrix elements of the velocity operator, $\mathbf{v}$, neglecting the anomalous velocity as discussed in Appendix B, can be calculated using (2.34), (3.3), and the right side of (3.4). The matrix elements of the spin operator $\mathbf{S}$, where $\mathbf{S} = (\hbar/2)\,\boldsymbol{\sigma}$, can be found from Eq. (3.1). The matrix elements of v^iS^j can be similarly found in the basis of eigenstates of H_0. Each of these can then be rotated to the basis (3.2) in which the states $|\overline{m\mathbf{k}}\rangle$ are expanded.

It is well known that in a crystal, $\mathbf{v}_{nn}(\mathbf{k}) = \nabla_{\mathbf{k}}\omega_n(\mathbf{k})$. More generally,

$$\mathbf{v}_{nm}(\mathbf{k}) = \nabla_{\mathbf{k}}\langle n\mathbf{k}|\,H\,|m\mathbf{k}\rangle = \langle\overline{n\mathbf{k}}|\,\nabla_{\mathbf{k}}H_{\mathbf{k}}\,|\overline{m\mathbf{k}}\rangle\,. \tag{3.7}$$

These identities can be proven from the definitions $H_{\mathbf{k}} = e^{-i\mathbf{k}\cdot\mathbf{r}}He^{i\mathbf{k}\cdot\mathbf{r}}$ and $\mathbf{v} = (i/\hbar)\,[H,\mathbf{r}]$ (see Sec. 2.3.1), even for a non-local Hamiltonian. But when remote band effects are included in a finite band model, they no longer hold. That is, $\mathbf{v}_{nm}(\mathbf{k})$ calculated using (3.4) and

eigenstates of H_{14} is not equal to $\langle \overline{n\mathbf{k}} | \nabla_{\mathbf{k}} H_{14} | \overline{m\mathbf{k}} \rangle$. I explicitly restore these identities by using $\langle \overline{n\mathbf{k}} | \nabla_{\mathbf{k}} H_{14} | \overline{m\mathbf{k}} \rangle$ to calculate $\mathbf{v}_{nm}(\mathbf{k})$. This approach can be described as including remote band effects in the velocity operator. It was used for an eight band calculation of linear absorption by Enders *et al.* [138]. This step is not critically important for the effects calculated here, since remote band effects are generally small.

3.2.4 k-space integration

The optical calculations in the rest of this chapter have the form Θ (this is unrelated to the notation $\hat{\Theta}$ in Chapter 2), where

$$\Theta = \sum_{c,v} \int d^3k f_{cv}(H_{\mathbf{k}}) \delta(\hbar\omega_{cv}(\mathbf{k}) - 2\hbar\omega), \tag{3.8}$$

where f_{cv} depends on matrix elements and energies of eigenstates of $H_{\mathbf{k}}$, and where $\omega_{nm}(\mathbf{k}) \equiv \omega_n(\mathbf{k}) - \omega_m(\mathbf{k})$. The form Θ follows from (2.18), and also holds when spin-splitting is taken into account below. The integral in (3.8) is understood to be restricted to the first Brillioun Zone, but I do not actively enforce the restriction, since the photon energies considered here cause transitions well within the first Brillioun Zone. Writing $\mathbf{k} = (k_{cv}, \theta_{\mathbf{k}}, \phi_{\mathbf{k}})$ in spherical coordinates, where k_{cv} is the solution to

$$\hbar\omega_{cv}(k_{cv}, \theta_{\mathbf{k}}, \phi_{\mathbf{k}}) - 2\hbar\omega = 0, \tag{3.9}$$

we have

$$\Theta = \sum_{c,v} \int_0^{\pi} \int_0^{2\pi} \frac{k_{cv}^2 \sin\theta_{\mathbf{k}} f_{cv}(H_{\mathbf{k}})}{\left|\hbar(\mathbf{v}_{cc}(\mathbf{k}) - \mathbf{v}_{vv}(\mathbf{k})) \cdot \hat{\mathbf{k}}\right|} d\phi_{\mathbf{k}} d\theta_{\mathbf{k}}, \tag{3.10}$$

where I have used $\nabla\omega_n(\mathbf{k}) = \mathbf{v}_{nn}(\mathbf{k})$. For all of the optical calculations in this chapter, (3.10) is equal to

$$\Theta = 8 \sum_{c,v} \int_0^{\pi/2} \int_0^{\pi/2} \frac{k_{cv}^2 \sin\theta_{\mathbf{k}} f_{cv}(H_{\mathbf{k}})}{\left|\hbar(\mathbf{v}_{cc}(\mathbf{k}) - \mathbf{v}_{vv}(\mathbf{k})) \cdot \hat{\mathbf{k}}\right|} d\phi_{\mathbf{k}} d\theta_{\mathbf{k}} \tag{3.11}$$

due to the cubic symmetry of the crystal. I solve (3.9) numerically using Ridders' method, and evaluate each integral in (3.11) numerically using Simpson's Rule converged to a desired relative accuracy [139]. It is numerically convenient to do the sum over any degenerate bands before the integral over $\theta_{\mathbf{k}}$ and $\phi_{\mathbf{k}}$.

3.2.5 Approximations

The calculations of "1+2" effects in the following sections of this chapter are primarily labeled by the Hamiltonian used to approximate $H_{\mathbf{k}}$. The complete fourteen-band model is denoted H_{14}. The bare fourteen-band model, denoted $H_{14\text{-Bare}}$, is H_{14} without remote band effects.

The 8×8 subset of the fourteen band Hamiltonian within the basis $\{\Gamma_{6c}, \Gamma_{8v}, \Gamma_{7v}\}$ is denoted H_8. The spherical eight-band model, denoted $H_{8\text{Sph}}$, is derived from H_8 by setting $C_k = 0$ and replacing γ_2 and γ_3 by $\tilde{\gamma} \equiv (2\gamma_2 + 3\gamma_3)/5$;[140] it is a spherical approximation to the Kane model including remote band effects [121]. The aforementioned calculations are non-perturbative in $\mathbf{k}$; that is, in each case, the Hamiltonian is solved numerically at each $\mathbf{k}$. The perturbative calculations of Appendix C are denoted PBA (parabolic-band approximation).

The microscopic expression for each of the "1+2" effects contains a sum over intermediate bands, which originates from the two-photon amplitude. Unless otherwise noted, calculations include all possible intermediate bands (eg., H_{14} includes fourteen intermediate bands, and $H_{8\text{Sph}}$ includes eight intermediate bands). Calculations that restrict this sum are secondarily labeled to reflect the restriction. The label "H_{14}, no *uc*" uses H_{14}, but does not include *uc* bands as intermediate states. The label "H_{14}, no *uc*/*so*" uses H_{14}, but includes neither *uc* nor *so* bands as intermediate states. The label "H_{14}, 2BT" uses H_{14}, but only includes two-band terms (terms for which the intermediate band is the same as the initial or final band). Similar labels are used for $H_{8\text{Sph}}$, for example, "$H_{8\text{Sph}}$-PBA, no so" uses the perturbative solution to $H_{8\text{Sph}}$ and does not include *so* intermediate states.

3.3 Current

To calculate $\eta_{(I)}$, I use the microscopic expression Eq. (2.43) in Sec. 2.3.3. It is similar to the expression given by Atanasov *et al.* [3], but modified to explicitly include the sum over spin states [33, 114]. An alternate microscopic expression has been derived in the length gauge [100], but it has not yet been used in a calculation. In the independent-particle approximation that I employ here, $\eta_{(I)}$ is purely imaginary [3] and hence η_{B1}, η_{B2}, and η_C are real, although they can be complex if excitonic effects are included (see Chapter 6).

The spectra of η_{B1}, η_{B2}, and η_C, calculated for GaAs, are shown in Fig. 3.2(a) along with the contributions to each tensor component from each possible initial valence band. For a given photon energy, electrons photoexcited from the *hh* band have higher energies and velocities than electrons photoexcited from the *lh* band; hence the dominant component η_{B1} is larger for *hh*-*c* transitions than *lh*-*c* transitions. The smallness of η_{B2} is due to contributions from the *hh*-*c* transitions having opposite sign to the *lh*-*c* transitions, as shown with the parabolic band model in Sec. 2.3.3.

Figure 3.2(b) separates each tensor component into an electron contribution and a hole contribution (denoted η_e and η_h by Atanasov *et al.* [3]). Electrons make a larger contribution to η_{B1} than holes, due to the lower effective mass (and hence higher velocity) of an electron than of a hole (much lower, in the case of a heavy hole) with the same crystal momentum.

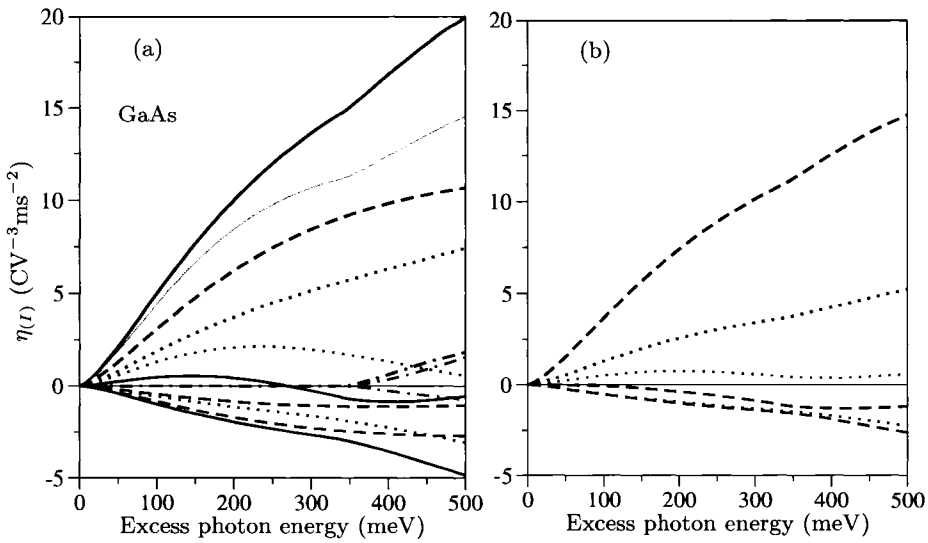

Figure 3.2: (colour): Spectra of η_{B1} (black lines), η_{B2} (red lines), and η_C (blue lines) for GaAs. Panel (a) shows the contributions from each initial valence band; dashed, dotted, and dashed-dotted lines include only transitions from the *hh*, *lh*, and *so* bands respectively, while the solid lines include all three transitions. The thin solid, light brown line in (a) is the total Re $\left(\eta_{(I)}^{aaaa}\right)$. Panel (b) separates the total into electron (dashed) and hole (dotted) contributions.

Holes dominate η_{B2} at lower photon energies, while electrons dominate η_{B2} at higher energies. Both electrons and holes contribute equally to the anisotropic component η_C.

To help in understanding the importance of the various intermediate states, in Fig. 3.3 we compare the calculated current injection tensor elements with various degrees of approximation described in Sec. 3.2.5.

The component η_{B1} (and hence $\eta_{(I)}^{aaaa}$, since η_{B1} is larger than $\eta_{B2} + \eta_C$) is dominated by two-band terms. Three-band terms cause the increase, by as much as 34%, of η_{B1} [the difference between the dashed and solid black lines in Fig. 3.3(a)]. Although not shown in Fig. 3.3, most of the increase is due to three-band terms with the *so* band as an intermediate state. Terms with the *uc* bands as intermediate states only cause a small increase to η_{B1} (the difference between the dotted and solid black lines). The warping of the bands is clearly not important for η_{B1}, since the calculation with $H_{8\text{Sph}}$ closely approximates the calculation "H_{14}, no *uc*", which includes the same intermediate states. Surprisingly, the "$H_{8\text{Sph}}$-PBA, 2BT" result from Sec. 2.3.3 closely approximates the complete, non-perturbative fourteen-band calculation, even at excess photon energies for which band nonparabolicity is significant. This is due to a fortuitous compensation between the neglect of nonparabolicity and the neglect of three-band terms. The compensation is not as complete for all materials.

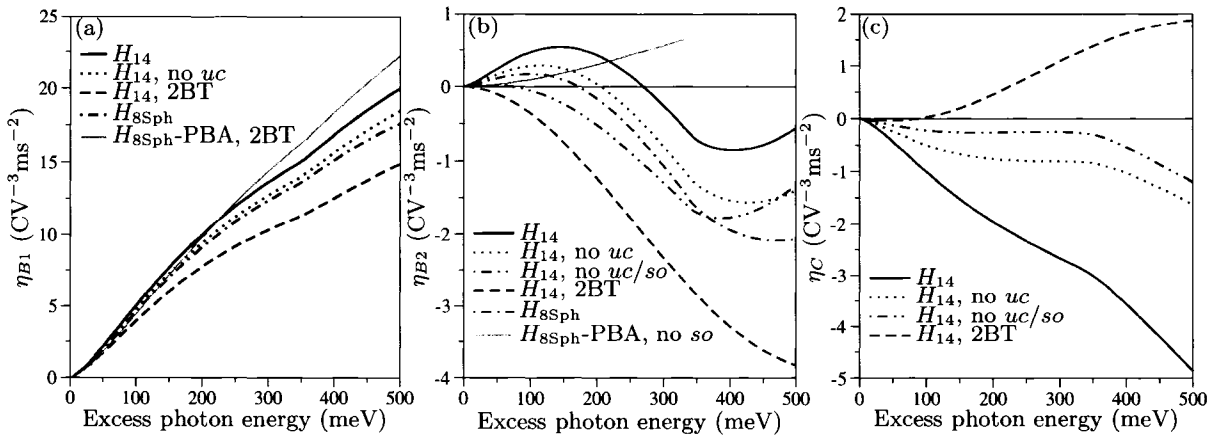

Figure 3.3: (colour): Approximations for GaAs current injection tensor components (a) η_{B1}, (b) η_{B2}, and (c) η_C. The approximations are described in Sec. 3.2.5.

The component η_{B2}, which determines the current due to orthogonal linearly polarized fields, is less forgiving to approximations than the component η_{B1}. We have already seen in Fig. 3.2 that η_{B2} is small due to a near cancellation of *hh* and *lh* initial states. Reasonable accuracy on η_{B2} thus requires higher accuracy on the contribution from each initial state. In particular, three-band terms must not be neglected. By comparing the dashed-dotted and solid lines in Fig. 3.3(b), it can be seen that, whereas the sum of the two-band terms is negative, the sum of the three-band terms is positive and of the same magnitude. It is useful to divide the three-band terms into three groups: those with intermediate state from the *hh* or *lh* bands, those with intermediate state from the *so* band, and those with intermediate state from one of the *uc* bands. I find that each group contributes roughly the same positive amount to η_{B2} for excess photon energies less than Δ_0. The groups are added successively to the 2BTs in the dashed, dotted, and solid lines in Fig. 3.3(b). Three-band terms with *so* intermediate states are less important at the higher excess photon energies in Fig. 3.3(b). The warping of the bands makes a small, but non-negligible contribution to η_{B2}, as seen in the difference between the dashed-double-dotted and dotted lines of Fig. 3.3(b). The solid brown line in Fig. 3.3(b) is the "H_{8Sph}-PBA, no *so*" result from Sec. 2.3.3. At low excess photon energies, it greatly underestimates η_{B2} due to the neglect of *so* and *uc* intermediate states, while at excess photon energies greater than 100 meV, this is partly compensated for by the neglect of nonparabolicity. It appears from the difference between "H_{8Sph}-PBA, no *so*" and "H_{14}, no *uc*/*so*" in Fig. 3.3(b) that nonparabolicity becomes important at energies above 70 meV.

The term η_C is purely due to cubic anisotropy by definition; in any model that is spherically symmetric it is identically zero. There is no cubic anisotropy in the "bare" (i.e. without remote

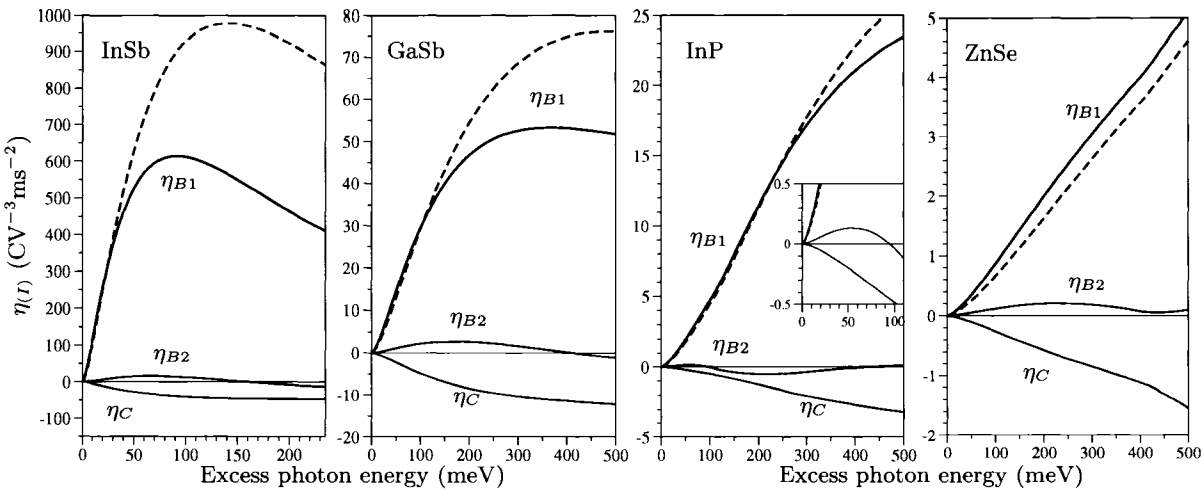

Figure 3.4: (colour): η_{B1} (black), η_{B2} (red), and η_C (blue) for (a) InSb, (b) GaSb, (c) InP, and (d) ZnSe. The solid lines are calculated with the complete fourteen-band model. The dashed line for η_{B1} is "$H_{8\mathrm{Sph}}$-PBA, 2BT". The inset of panel (c) shows the area near the origin in more detail.

band effects) eight-band model on the set $\{\Gamma_{6c}, \Gamma_{8v}, \Gamma_{7v}\}$. Cubic anisotropy in the fourteen-band model is due to the momentum matrix elements governed by the parameters E_Q and $E_{P'}$, the interband spin-orbit coupling Δ^-, and remote bands through $(\gamma_2 - \gamma_3)$ and C_k. From Fig. 3.3(c), it can be seen that three-band terms are important for η_C. In fact, with only 2BTs included, η_C is positive for GaAs, whereas it is negative with all terms included. From Fig. 3.3(c) it can also be seen that the *so* band and *uc* bands are important as intermediate states for η_C.

My calculation of $\eta_{(I)}$ is of the same order of magnitude as the *ab initio* calculation of Atanasov *et al.* [3], but its spectral dependence is different. In particular, η_{B1} agrees more closely with the PBA calculation, as seen in Fig. 3.3(a). Atanasov *et al.* had attributed the difference between their *ab initio* and PBA calculations to the assumption of **k**-independent velocity matrix elements in the PBA [3]. However, my calculation accounts for the **k**-dependence of velocity matrix elements and agrees closely (for η_{B1} and $\mathrm{Re}\eta^{aaaa}$) to the PBA. The earlier *ab initio* calculation [3] was, in fact, inaccurate at low photon energies due to various computational issues; an improved *ab initio* calculation agrees with the spectral dependence at low photon energy given here [141].

Figure 3.4 shows the spectra of η_{B1}, η_{B2}, and η_C calculated with H_{14} for InSb, GaSb, InP, and ZnSe. The dashed black line in Fig. 3.4 is the PBA result (2.47a). The PBA appears to be a reasonable approximation to η_{B1} for excess energies less than about $0.2E_g$. In each

material, $\eta_{B2} \ll \eta_{B1}$ and in each material except for ZnSe, the sign of η_{B2} changes as a function of frequency. The component η_C, which arises due to cubic anisotropy, is negative for each material.

The cubic anisotropy of current injection due to colinearly polarized fields can be significant enough that it should be measurable. For fields colinearly polarized along $\hat{\mathbf{e}}$, specified by polar angles θ and ϕ relative to the cubic axes,

$$\dot{\mathbf{J}}_{(I)} \cdot \hat{\mathbf{e}} = 2\mathrm{Im}\left(E_\omega^2 E_{2\omega}^*\right)\left(\eta_{B1} + \eta_{B2} + \eta_C - \frac{\eta_C}{2} f(\theta,\phi)\right), \tag{3.12}$$

where $f(\theta,\phi) = \sin^2(2\theta) + \sin^4(\theta)\sin^2(2\phi)$. In general, $\dot{\mathbf{J}}_{(I)}$ also has a component perpendicular to $\hat{\mathbf{e}}$ that is proportional to η_C, but it vanishes for $\hat{\mathbf{e}}$ parallel to $\langle 001\rangle$, $\langle 110\rangle$, $\langle 111\rangle$. The field polarization that maximizes the current injection depends on the relative sign of η_C and $\mathrm{Re}\eta^{aaaa} = \eta_{B1} + \eta_{B2} + \eta_C$. When they have the opposite sign, current injection is a minimum for $\hat{\mathbf{e}} \parallel \langle 001\rangle$ ($f = 0$) and a maximum for $\hat{\mathbf{e}} \parallel \langle 111\rangle$ ($f = 4/3$); for light normally incident on a $\{001\}$ surface, the largest current injection occurs when $\hat{\mathbf{e}} \parallel \langle 110\rangle$ ($f = 1$). When they have the same sign, current-injection is a maximum for $\hat{\mathbf{e}} \parallel \langle 001\rangle$ and a minimum for $\hat{\mathbf{e}} \parallel \langle 111\rangle$. From the GaAs results shown in Fig. 3.2(a), the current injection for the three cases $\hat{\mathbf{e}} \parallel \langle 001\rangle$, $\hat{\mathbf{e}} \parallel \langle 110\rangle$, and $\hat{\mathbf{e}} \parallel \langle 111\rangle$ are in the ratio 1 to 1.14 to 1.20 at the band edge, 1 to 1.15 to 1.20 at 200 meV excess photon energy, and 1 to 1.22 to 1.29 at 500 meV excess photon energy. In contrast, the *ab initio* calculation of Atanasov *et al.* yields larger ratios, for example 1 to 1.32 to 1.43 at 300 meV excess photon energy [3]. This disagreement is consistent with the inaccuracy of the *ab initio* calculation discussed above. Initial experiments with GaAs used $\hat{\mathbf{e}} \parallel [001]$ [4, 71], whereas Roos *et al.* exploited the larger signal for $\hat{\mathbf{e}} \parallel [110]$ [72]. For each of the materials shown in Fig. 3.4, the minimum current injection is for $\hat{\mathbf{e}} \parallel \langle 001\rangle$. It is worth noting that two-photon absorption is also a minimum with $\hat{\mathbf{e}} \parallel \langle 001\rangle$ for many semiconductors [142–144]. It seems that both "1+2" current injection and two-photon absorption with linearly polarized fields are larger for $\hat{\mathbf{e}}$ directed along the bonds.

The cubic anisotropy of "1+2" current injection is pronounced for cross-linearly polarized fields and opposite-circularly polarized fields. For example, for cross-linearly polarized fields normally incident on (001) with $\hat{\mathbf{e}}_\omega = \hat{\mathbf{a}}\cos\phi + \hat{\mathbf{b}}\sin\phi$ and $\hat{\mathbf{e}}_{2\omega} = -\hat{\mathbf{a}}\sin\phi + \hat{\mathbf{b}}\cos\phi$,

$$\dot{\mathbf{J}}_{(I)} = \mathrm{Im}\left(E_\omega^2 E_{2\omega}^*\right)\left[\left(2\eta_{B2} + \eta_C \sin^2(2\phi)\right)\hat{\mathbf{e}}_{2\omega} - \frac{\eta_C}{2}\sin(4\phi)\,\hat{\mathbf{e}}_\omega\right]. \tag{3.13}$$

For fields with opposite circular polarizations, the current injection is proportional to η_C and is hence purely anisotropic.

The component η_C causes a type of current injection that has not previously been noted. In all "1+2" experiments considered thus far with light normally incident on a surface, the direction of current injection lies in the plane of the surface. However, with co-linearly polarized light

fields normally incident on a (111) surface, the current can have a component into (or out of) the surface. The current in this case is

$$\dot{\mathbf{J}}_{(I)} = 2\mathrm{Im}\left(E_{\omega}^{2}E_{2\omega}^{*}\right)\left[\left(\eta_{B1}+\eta_{B2}+\frac{1}{2}\eta_{C}\right)\hat{\mathbf{e}}+\left(\sqrt{2}/6\right)\eta_{C}\cos\left(3\theta\right)\hat{\mathbf{z}}\right], \tag{3.14}$$

where $\hat{\mathbf{z}}$ is the [111] direction, and θ is the angle between $\hat{\mathbf{e}}$ and the $[2\bar{1}\bar{1}]$ direction. Thus, η_C is responsible for this "surfacing" current.

3.4 Spin current

As in Sec. 2.1 and Sec. 2.3.4, the spin-current injection can be divided into a contribution from electrons $\dot{K}^{ij}_{(I;e)}$, and a contribution from holes $\dot{K}^{ij}_{(I;h)}$; that is, $\dot{K}^{ij}_{(I)} = \dot{K}^{ij}_{(I;e)} + \dot{K}^{ij}_{(I;h)}$ (similarly, $\mu^{ijklm}_{(I)} = \mu^{ijklm}_{(I;e)} + \mu^{ijklm}_{(I;h)}$). Expressions in the PBA for both the electron and hole spin current are given in the preceding chapter, but here I focus on the electron spin current.

In the preceding chapter, a microscopic expression for the spin-current injection is derived in the FGR limit of perturbation theory and applied to a model in which all bands are doubly degenerate [see (2.21a)]. However, it is unsuitable for a calculation with H_{14}, which accounts for the small splitting of the spin degeneracy that occurs in materials of zinc-blende symmetry [137, 145, 146]. If the spin-split bands were well separated, then the microscopic expression for $\dot{K}^{ij}_{(I;e)}$ would be

$$\dot{K}^{ij}_{(I;e)} = \frac{2\pi}{L^3}\sum_{c,v,\mathbf{k}}\langle c\mathbf{k}|\, v^i S^j\, |c\mathbf{k}\rangle\left[\left(\Omega^{(2)}_{c,v,\mathbf{k}}\right)^{*}\Omega^{(1)}_{c,v,\mathbf{k}}+c.c.\right]\delta\left(2\omega-\omega_{cv}\left(\mathbf{k}\right)\right),$$

where L^3 is a normalization volume, the one-photon amplitude $\Omega^{(1)}_{c,v,\mathbf{k}}$ is given in (2.3), and the two-photon amplitude $\Omega^{(2)}_{c,v,\mathbf{k}}$ is given in (2.4).

However, for the photon energies and materials studied here, the spin-splitting is small; it is comparable to the broadening that one would calculate from the scattering time of the states, and also to the laser bandwidth for typical ultrafast experiments. Thus, the spin-split bands should be treated as quasidegenerate in FGR, with the result

$$\dot{K}^{ij}_{(I;e)} = \frac{2\pi}{L^3}\sum_{c,c'}{}'\sum_{v,\mathbf{k}}\langle c\mathbf{k}|v^i S^j|c'\mathbf{k}\rangle\left(\Omega^{(2)}_{c,v,\mathbf{k}}\right)^{*}\Omega^{(1)}_{c',v,\mathbf{k}}\frac{1}{2}\left[\delta\left(2\omega-\omega_{cv}\left(\mathbf{k}\right)\right)+\delta\left(2\omega-\omega_{c'v}\left(\mathbf{k}\right)\right)\right]+c.c.,$$

where the prime on the summation indicates a restriction to pairs (c, c') for which either $c' = c$, or c and c' are a quasidegenerate pair. This same issue arises in the fourteen-band calculations of "1+2" spin control (Sec. 3.6), two-photon spin injection (Chapter 4), and one-photon spin-current injection (Chapter 5). In Chapter 5, the optical excitation of the coherence between spin-split bands is justified using the semiconductor optical Bloch equation approach. That

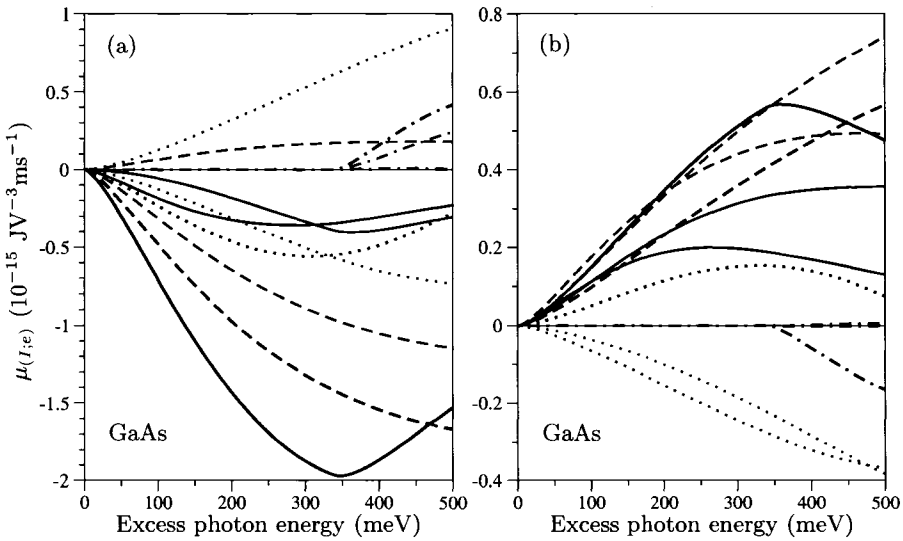

Figure 3.5: (colour): Calculated spectra of GaAs spin-current injection components and their contributions from each initial valence band; dashed, dotted, and dashed-dotted lines include only transitions from the *hh*, *lh*, and *so* bands respectively, while the solid lines include all three transitions. Panel (a) shows μ_{N1} (black lines), μ_{N2} (red lines), and μ_{N3} (blue lines). Panel (b) shows μ_{C1} (black lines), μ_{C2} (red lines), and μ_{C3} (blue lines).

approach yields the same result as the simpler approach taken here. Note that this issue does not arise for "1+2" current injection or "1+2" population control, since $\langle c\mathbf{k}|\mathbf{v}|c'\mathbf{k}\rangle$ and $\langle c\mathbf{k}|c'\mathbf{k}\rangle$ vanish between spin-split bands.

Using the time-reversal properties of the Bloch functions, I find that $\mu_{(I;e)}$ is real, and can be written as

$$\mu_{(I;e)}^{ijklm} = i\left(\frac{e}{\hbar\omega}\right)^3 \frac{\pi}{2L^3} \sum_{c,c'}{}' \sum_{v,\mathbf{k}} \sum_{n} \delta\left(2\omega - \omega_{cv}\left(\mathbf{k}\right)\right) \mathrm{Re}\left\{ \frac{\langle c\mathbf{k}|\, v^i S^j \,|c'\mathbf{k}\rangle}{\omega_{nv\mathbf{k}} - \omega} \left[M_{c,c',v}^{klm} - \left(M_{c',c,v}^{klm}\right)^* \right] \right\}, \tag{3.15}$$

where

$$M_{c,c',v}^{klm} \equiv \frac{1}{2} v_{c'v}^{m}(\mathbf{k}) \left[v_{cn}^{k*}(\mathbf{k}) v_{nv}^{l*}(\mathbf{k}) + v_{cn}^{l*}(\mathbf{k}) v_{nv}^{k*}(\mathbf{k}) \right]. \tag{3.16}$$

That $\mu_{(I;e)}$ in (3.15) is purely real is a consequence of the independent-particle approximation (see Chapter 6).

The spectra of the independent components of $\mu_{(I;e)}$, calculated for GaAs, are shown in Fig. 3.5 and Fig. 3.6. Figure 3.5 includes contributions from each possible initial valence band. Figure 3.6 shows the spin-current injection calculated with various degrees of approximation described in Sec. 3.2.5. The only other calculation of "1+2" spin-current injection for bulk GaAs is the calculation in Sec. 2.3.4, which uses a spherical, parabolic band approximation to

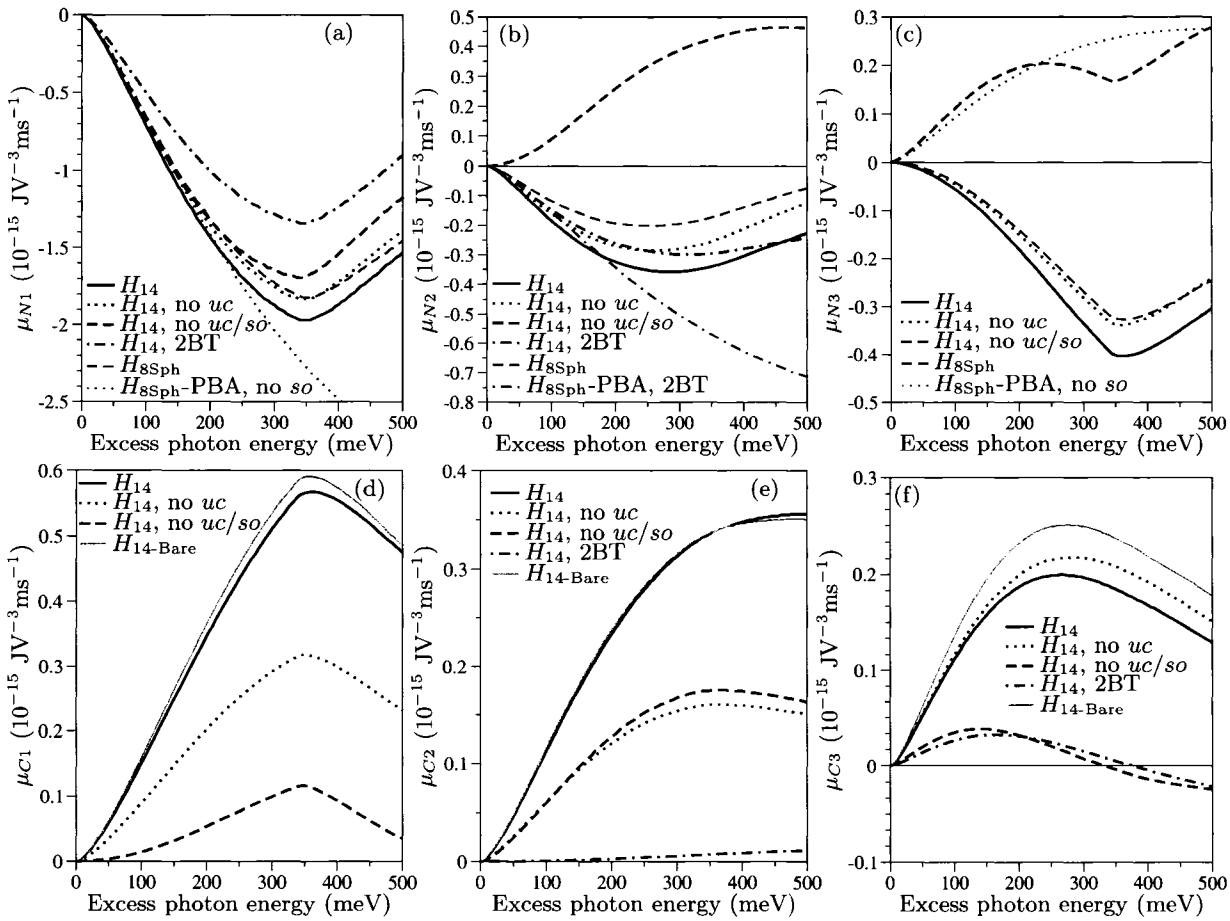

Figure 3.6: (colour): Approximations for GaAs spin current components (a) μ_{N1}, (b) μ_{N2}, (c) μ_{N3}, (d) μ_{C1}, (e) μ_{C2}, (f) μ_{C3}. The approximations are described in Sec. 3.2.5.

the eight-band model; it is shown in Fig. 3.6 for μ_{N1}, μ_{N2}, and μ_{N3}.

The term μ_{N1} has the largest magnitude of the six independent parameters of $\mu_{(I;e)}$. Since it is negative for *hh* and *lh* transitions but positive for *so* transitions, it peaks in magnitude at $2\hbar\omega$ just above $E_g + \Delta_0$ (the energy at which *so* transitions become allowed). Two band terms make the largest contribution to μ_{N1}, followed by three-band terms with *hh* or *lh* intermediate states. The *so* and *uc* intermediate states make a very small contribution to μ_{N1} for excess energies less than 200 meV. The warping of the bands is not important for μ_{N1}, since the calculation with $H_{8\mathrm{Sph}}$ closely approximates the "H_{14}, no *uc*" calculation, which includes the same intermediate states. The "$H_{8\mathrm{Sph}}$-PBA, no *so*" calculation, which is derived in Sec. 2.3.4, is a good approximation to μ_{N1} at excess energies below 250 meV; nonparabolicity becomes important at higher energies. The *hh* contribution has a larger magnitude than the *lh* contribution in part because three-band terms increase the magnitude of the *hh* contribution, but decrease

that of the *lh* contribution, as expected from the PBA expression (2.52a).

The term μ_{N2} is negative for *hh* transitions, positive for *lh* transitions, and negligible for *so* transitions. The calculation "H_{14}, 2BT" is a good approximation to the calculation H_{14}. However, the three-band terms are not small; rather, they nearly cancel. In particular the transition *hh-lh-c* makes a large positive contribution to μ_{N2}, while the transition *hh-so-c* makes a large negative contribution. Since the PBA result in Sec. 2.3.4 includes the former but not the latter, it is a poor approximation to μ_{N2}. But by including only 2BTs, it is a fair approximation for excess energies less than 200 meV. This agreement is fortuitous, since the calculation $H_{8\text{Sph}}$ underestimates the magnitude of μ_{N2}, and the PBA leads to an overestimation of the magnitude of μ_{N2}.

The term μ_{N3} is negligible when only 2BTs are included, in agreement with the PBA result in Sec. 2.3.4. The *hh-lh-c* transitions are positive, while the *lh-hh-c* transitions are negative; the former is larger, and thus μ_{N3} is positive when *so* intermediate states are neglected. Both *lh-so-c* and *hh-so-c* are negative and substantial enough to make the total μ_{N3} negative. Consequently, the PBA result in Sec. 2.3.4, which neglects *so* intermediate states, is a poor approximation to μ_{N3}. Upper conduction bands make a fairly small contribution to μ_{N3}, and warping does not seem to be important for μ_{N3} since the calculation with $H_{8\text{Sph}}$ is a good approximation.

As expected, the terms μ_{C1}, μ_{C2}, and μ_{C3} are zero when calculated with $H_{8\text{Sph}}$.

The term μ_{C1} is negligible when only 2BTs are included. Transitions with intermediate states in the set $\{hh, lh, so\}$ comprise roughly two-thirds of μ_{C1}. The anisotropy of these transitions is not simply due to the warping of the *hh* and *lh* bands, which I have determined by a calculation (not shown) using H_8 without the remote band contribution to the velocity. Rather, it comes from wave function mixing of the Γ_{8c} and Γ_{7c} states into the valence and *c* band states. The cubic anisotropy of two-photon absorption has been attributed to such wave function mixing [128, 142]. The other third of the full μ_{C1} is due to transitions with the *uc* intermediate state, which would be forbidden close to the Γ point if the material were isotropic. I also note that each three-band term makes a positive contribution to μ_{C1}.

The term μ_{C2} is nearly negligible when only 2BTs are included. Transitions from the *hh* and *lh* bands have opposite sign, and those from the *so* band are negligible. About half of μ_{C2} is due to the transitions *hh-lh-c* and *lh-hh-c*, and the other half is due to transitions with the *uc* intermediate states. Transitions with *so* intermediate states are negligible. As with μ_{C1}, the anisotropy of the *hh-lh-c* and *lh-hh-c* transitions is due to the wave function mixing of the Γ_{8c} and Γ_{7c} states into the *hh*, *lh*, and *c* band states.

The term μ_{C3} is positive for *hh* transitions, negative for *lh* transitions, and negligible for *so* transitions. The transitions *hh-so-c* and *lh-so-c* account for most of the value of μ_{C3}, but 2BTs are not negligible. Transitions with *uc* intermediate states reduce the value of μ_{C3} by as much

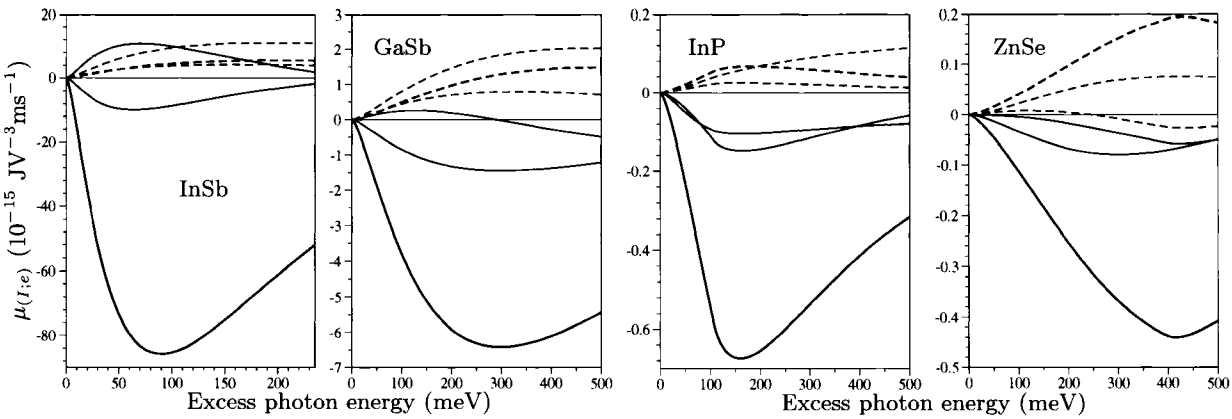

Figure 3.7: Spectra of spin current components for InSb, GaSb, InP, and ZnSe: μ_{N1} (solid black line), μ_{N2} (solid red line), μ_{N3} (solid blue line), μ_{C1} (dashed black line), μ_{C2} (dashed red line), and μ_{C3} (dashed blue line).

as 10%. Most of μ_{C3}, especially at energies less than 200 meV, is due to the warping of the hh and lh bands. Consistent with this, I find that remote band effects are somewhat important for μ_{C3}; when remote band effects are removed, the calculation of μ_{C3} is about 25% larger than the full calculation. Note that μ_{C3} is far more sensitive to remote band effects than any other optical property calculated in this thesis.

In Fig. 3.7 I plot the spectra of the independent components of the spin current density pseudotensor for InSb, GaSb, InP, and ZnSe. The spin current tensor is largest for InSb in agreement with the PBA expressions in Appendix C. I also note that μ_{N3} is positive for InSb and GaSb at low excess photon energy, whereas it is negative for InP, GaAs, and ZnSe.

3.4.1 Configurations

Co-circularly polarized fields generate a spin-polarized current, which can be characterized by its degree of spin polarization f (see Sec. 2.4), where $f \equiv (2e/\hbar)\, \dot{K}_e^{ij} \hat{q}^i \hat{n}^j / |\dot{\mathbf{J}}_e|$, where $\hat{\mathbf{n}}$ is a unit vector normal to the polarization plane of the fields, and $\hat{\mathbf{q}}$ is a unit vector in the direction of $\mathbf{J}_e$. Essentially, $f = \langle vS \rangle / \langle v \rangle$. Since this measure aims to characterize the photoexcited distribution of electrons, I neglect holes from both $\dot{K}$ and $\dot{J}$.[2] For fields normally incident on a (001) surface (i.e. $\mathbf{e}_\omega = \mathbf{e}_{2\omega} = (\hat{\mathbf{x}} \pm i\hat{\mathbf{y}})/\sqrt{2}$), the spin current is

$$\dot{K}^{ij}_{(I)} = \mp\sqrt{2} E_{2\omega} E_\omega^2 \left[\left(\mu_{N1} + \frac{\mu_{C1}}{2} \right) \hat{m}^i_\pm \hat{z}^j + \left(\mu_{N2} + \frac{\mu_{C2}}{2} \right) \hat{z}^i \hat{m}^j_\pm \right],$$

[2]The calculation of f in Bhat and Sipe included electrons in $\dot{K}$ but both electrons and holes in $\dot{J}$ [38].

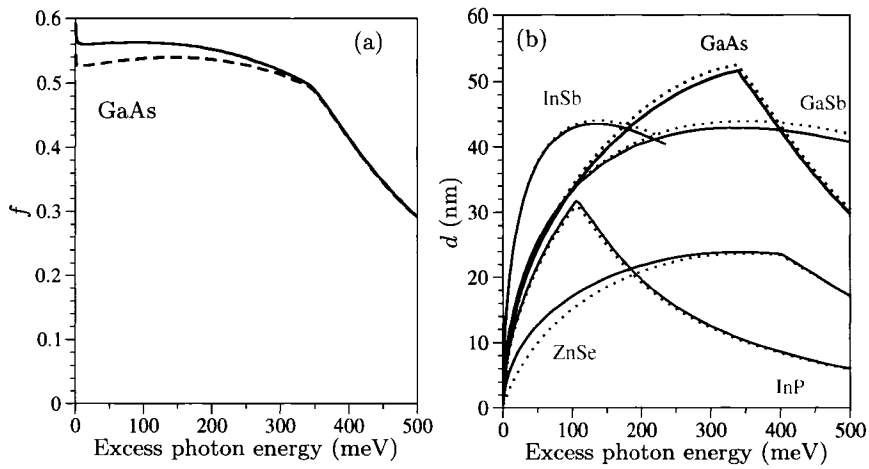

Figure 3.8: (a) Degree of polarization of spin-polarized current due to co-circularly polarized fields. (b) Displacement of spins in pure spin current due to cross-linearly polarized fields.

where

$$\hat{\mathbf{m}}_{\pm} = \sin(2\phi_\omega - \phi_{2\omega})\,\hat{\mathbf{x}} \pm \cos(2\phi_\omega - \phi_{2\omega})\,\hat{\mathbf{y}},$$

the current is $\dot{\mathbf{J}}_{(I)} = \sqrt{2}E_{2\omega}E_\omega^2\,(\eta_{B1} + \eta_C/2)\,\hat{\mathbf{m}}_{\pm}$, and the degree of spin polarization is

$$f = \frac{2e}{\hbar}\frac{\mu_{N1} + \mu_{C1}/2}{\eta_{B1} + \eta_C/2}. \tag{3.17}$$

For fields normally incident on a (111) surface, $\dot{\mathbf{J}}_{(I)} = \sqrt{2}E_{2\omega}E_\omega^2\,(\eta_{B1} + \eta_C/3)\,\hat{\mathbf{m}}_{\pm}$, and

$$f = \frac{2e}{\hbar}\frac{\mu_{N1} + \mu_{C1}/3 + \mu_{C3}/3}{\eta_{B1} + \eta_C/3}. \tag{3.18}$$

The degree of spin polarization is plotted for GaAs in Fig. 3.8(a). The cubic anisotropy is small, but clearly seen, especially at low excess photon energies. The other materials have very similar degrees of spin polarization.

A pure spin current, without an electrical current, can be generated with cross-linearly polarized fields, as shown in Sec. 2.4. To generalize (2.56) to include cubic anisotropy, I consider fields polarized in the (001) plane, with the ω field polarized at an angle θ to the $\hat{\mathbf{x}}$ axis (i.e. [100]) and the 2ω field polarized at an angle θ to the $\hat{\mathbf{y}}$ axis ($\mathbf{e}_\omega = \hat{\mathbf{x}}\cos\theta + \hat{\mathbf{y}}\sin\theta$ and $\mathbf{e}_{2\omega} = -\hat{\mathbf{x}}\sin\theta + \hat{\mathbf{y}}\cos\theta$). The spin current is

$$\dot{K}_{(I)}^{ij} = -\frac{1}{2}E_{2\omega}E_\omega^2\cos(2\phi_\omega - \phi_{2\omega})\left[(4\mu_{N1} + 4\mu_{N3} + 3\mu_{C1} + \mu_{C1}\cos(4\theta))\,e_\omega^i\hat{z}^j\right.$$
$$\left. -\mu_{C1}\sin(4\theta)\,e_{2\omega}^i\hat{z}^j - \mu_{C2}\sin(4\theta)\,\hat{z}^i e_{2\omega}^j + (4\mu_{N2} - 4\mu_{N3} + 3\mu_{C2} + \mu_{C2}\cos(4\theta))\,\hat{z}^i e_\omega^j\right]$$

This pure spin current is typically measured by the resulting displacement of up and down spins [41, 42]. The finite displacement results from transport and scattering of the electrons.

Using the Boltzmann transport equation in the relaxation time approximation with space-charge effects justifiably neglected [42], one finds $d^i(\hat{\mathbf{z}}) = (4\tau/\hbar)\,\dot{K}^{ij}\hat{z}^j / \left(\dot{N}_{(1)} + \dot{N}_{(2)}\right)$. Here, $\mathbf{d}(\hat{\mathbf{z}})$ is the displacement of spins measured with respect to the quantization direction $\hat{\mathbf{z}}$, τ is the momentum relaxation time, and $\dot{N}_{(i)}$ is the i-photon carrier injection rate. I assume the field intensities have been chosen to balance one- and two-photon absorption, a condition that is θ-dependent due to the cubic anisotropy of two-photon absorption. Thus,

$$\mathbf{d}(\hat{\mathbf{z}}) \cdot \mathbf{e}_\omega = \frac{\tau}{\hbar} \frac{(4\mu_{N1} + 4\mu_{N3} + 3\mu_{C1} + \mu_{C1}\cos(4\theta))}{\sqrt{\xi_{(1)}^{xx}\xi_{(2)}^{xxxx}\left(1 - (\sigma/2)\sin^2(2\theta)\right)}} \tag{3.19}$$

and

$$\mathbf{d}(\hat{\mathbf{z}}) \cdot \mathbf{e}_{2\omega} = \frac{\tau}{\hbar} \frac{\mu_{C1}\sin(4\theta)}{\sqrt{\xi_{(1)}^{xx}\xi_{(2)}^{xxxx}\left(1 - (\sigma/2)\sin^2(2\theta)\right)}}, \tag{3.20}$$

where σ is the two-photon absorption cubic-anisotropy factor given explicitly in the next section [128, 142]. At $\theta = 0$ and $\theta = \pi/4$, $\mathbf{d}$ is parallel to $\mathbf{e}_\omega$. The spin separation distance is plotted in Fig. 3.8(b), where I have assumed a momentum relaxation time of 100 fs for each material.

This calculation of the spin separation distance is a significant improvement over my initial calculations [41, 42], which used the eight-band PBA and neglected three-band terms from the two-photon amplitude ("$H_{8\mathrm{Sph}}$-PBA, 2BT"). Stevens *et al.* measured a spin separation distance of 20 nm in a GaAs multiple quantum well at an excess photon energy of 200 meV, and estimated a momentum relaxation time of $\tau = 45$ fs [41]. For $\tau = 45$ fs, I calculate a spin separation distance of 20.0 nm for bulk GaAs at 200 meV. Hübner *et al.* measured a spin separation distance of 24 nm (the photoluminescence spot separation is half this distance) in cubic ZnSe at an excess photon energy of 280 meV, and estimated a momentum relaxation time of $\tau = 100$ fs [42]. The calculation in Fig. 3.8(b) gives $d = 23.6$ nm for ZnSe at 280 meV. In both cases, I now find very good agreement with the experiment, whereas the previous model resulted in larger spin separation distances. Of course, this agreement is contingent on the accuracy of the momentum relaxation time estimates.

Note that both the degree of spin polarization for co-circularly polarized fields and the spin-separation distance, plotted in Fig. 3.8, have a kink at excess photon energy Δ_0 and decrease at higher excess photon energies. A similar kink and decrease, due to the onset of transitions from the *so* band, occurs for both one-photon spin injection [2] and two-photon spin injection (see Chapter 4).

3.5 Population control

I calculate $\xi_{(I)}$ with the microscopic expression (C.1) in Appendix B, which is also given by Fraser *et al.* [36]. It is derived in the independent-particle approximation, and is restricted to

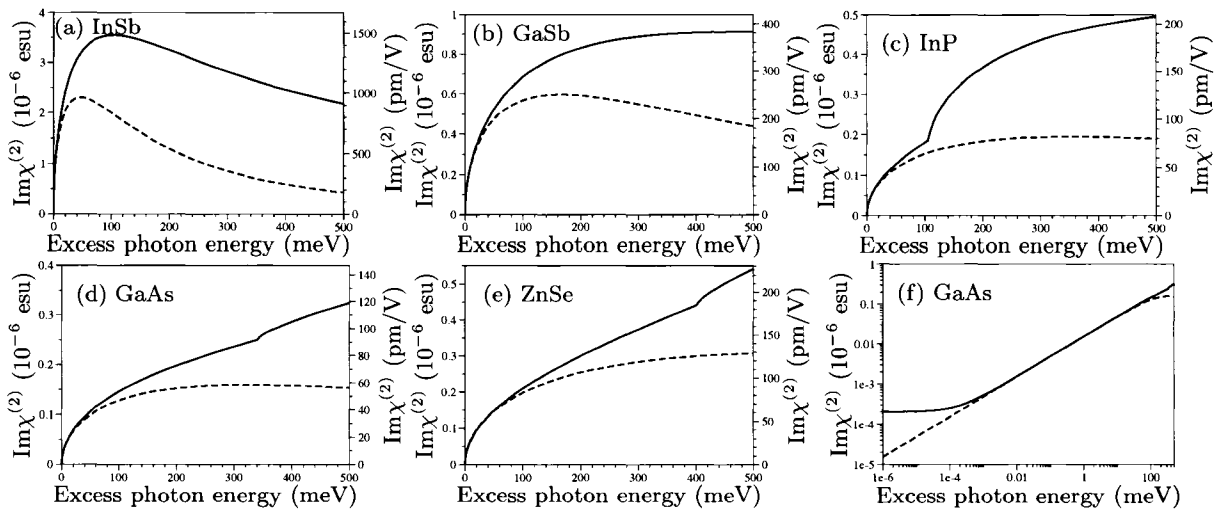

Figure 3.9: Im$\chi^{(2)}$ calculated with H_{14} (solid line) and H_{14}-PBA (dashed line) for (a) InSb, (b) GaSb, (c) InP, (d) GaAs, and (e) ZnSe. Panel (f) shows the GaAs calculations on a log-log plot.

$\hbar\omega < E_g < 2\hbar\omega$ [36]. Under those conditions, $\xi_{(I)}$ is real and is proportional to the imaginary part of the susceptibility for second harmonic generation (SHG) [36, 101]; specifically, (in mks)

$$\xi_{(I)}^{abc} = (2\varepsilon_0/\hbar)\,\mathrm{Im}\chi^{(2)cba}(-2\omega;\omega,\omega)\,. \tag{3.21}$$

This connection to SHG is important because the imaginary part of $\chi^{(2)}(-2\omega;\omega,\omega)$ has sometimes been presented *en route* to a calculation of $|\chi^{(2)}|$ [147–153]. As well, analytic expressions have been derived for the dispersion of SHG by using simple band models, with approximations appropriate for $2\hbar\omega$ near the band gap [147, 154–158]. However, these earlier works did not connect Im$\chi^{(2)}(-2\omega;\omega,\omega)$ with population control, and in fact typically stated that it was not independently observable.

Fig. 3.9 shows the calculation of Im$\chi^{(2)cba}(-2\omega;\omega,\omega)$ for InSb, GaSb, InP, GaAs and ZnSe. Also shown for comparison is the PBA expression (C.3), derived in Appendix C. Each spectrum can be divided into roughly three regions. At very low excess photon energies, visible in the log-log plot Fig. 3.9(f), the spectrum is roughly independent of ω. This flat part of the spectrum disappears if C_k is set to zero; hence, it is due to the **k**-linear term in the c band spin-splitting. Next higher in photon energy, up to about 100 meV in GaSb, InP, GaAs, and ZnSe (up to about 15 meV in InSb), is a region where the agreement with the analytic expression (C.3) is best. In this region, the ratio X_2/X_1, defined in Appendix C, is 0.37 for InSb, 0.30 for GaSb, −0.25 for InP, 0.08 for GaAs, and 0.07 for ZnSe. At higher photon energies, the dispersion of Im$\chi^{(2)cba}(-2\omega;\omega,\omega)$ deviates from the PBA expression due to band nonparabolicity and

warping, **k**-dependence of matrix elements, and transitions from the split-off band, which are not included in (C.3).

If I remove the two-band transitions *hh*-{*hh*, *c*}-*c*, *lh*-{*lh*, *c*}-*c*, and *so*-{*so*, *c*}-*c*, then the calculation of $\mathrm{Im}\chi^{(2)}$ (or $\xi_{(I)}$) is unchanged. This is expected for materials of zinc-blende symmetry [155, 159]. So-called "virtual hole terms" were argued to make only a small contribution to $\chi^{(2)}(0)$ by Aspnes [159], and they have been neglected in some previous calculations of $\chi^{(2)}$ dispersion [148, 150]. By removing the virtual hole terms *lh*-{*so*, *hh*}-*c* and *hh*-{*so*, *lh*}-*c*, leaving only {*so*, *lh*, *hh*}-*uc*-*c* transitions, $\xi_{(I)}$ is reduced by only 6–10% over the range from the band edge to 500 meV above the gap for GaAs. It is thus clear that inclusion of the *uc* bands is necessary for a calculation of population control. For some purposes it is also sufficient, since if remote band effects are removed from the model, leaving the "bare" fourteen-band model [124, 128], $\xi_{(I)}$ is decreased by only 7–10% from its full value for GaAs.

For most materials, the results in Fig. 3.9 are in reasonable agreement with previous calculations of $\mathrm{Im}\chi^{(2)}$ [147, 150, 152, 153], although most previous calculations had poor spectral resolution in this energy range. However, for ZnSe, the situation is more complicated. The calculation of Huang and Chin is about an order of magnitude smaller than mine [150], and that of Ghahramani *et al.* is about 5 times smaller than mine [149]. Note also that Huang and Chin calculated $\chi^{(2)}(0)$ for ZnSe to be an order of magnitude smaller than experimental results [150]. Wagner *et al.* have measured the dispersion of $|\chi^{(2)}|$, which is an upper bound on $\mathrm{Im}\chi^{(2)}$; for ZnSe it is about a factor of two smaller than my calculation of $\mathrm{Im}\chi^{(2)}$ [160]. Note that Wagner *et al.* give a different set of band parameters than I have used here [160].

The magnitude of $\xi^{abc}_{(I)}$ determines the magnitude of population control, but in an experiment one is more interested in the depth of the phase-dependent modulation of the carrier absorption, i.e. the control ratio R [36]. It is

$$R = \frac{\dot{N}_{(I)}}{\dot{N}_{(1)} + \dot{N}_{(2)}} = \frac{\xi^{ijk}_{(I)} E^{i*}_{2\omega} E^{j}_{\omega} E^{k}_{\omega} + c.c.}{\xi^{ij}_{(1)} E^{i*}_{2\omega} E^{j}_{2\omega} + \xi^{ijkl}_{(2)} E^{i*}_{\omega} E^{j*}_{\omega} E^{k}_{\omega} E^{l}_{\omega}},$$

and it can also be viewed as $R = \left(\dot{N} - [\dot{N}]_{\mathrm{avg}}\right)/[\dot{N}]_{\mathrm{avg}}$, where $[\dot{N}]_{\mathrm{avg}}$ is the carrier injection averaged over the phase modulation. This ratio is largest for field amplitudes that equalize $\dot{N}_{(1)}$ and $\dot{N}_{(2)}$ [37]; in what follows, I assume this condition has been met. The ratio then depends only on $\xi^{ijk}_{(I)}$, $\xi^{ij}_{(1)}$, $\xi^{ijkl}_{(2)}$, and the polarizations of the two fields. For light normally incident on a (111) surface, linearly-polarized fields yield $R = \sqrt{2}\xi^{abc}_{(I)}/\sqrt{3\xi^{aa}_{(1)}\xi^{aaaa}_{(2)}(1-\sigma/2)}$, while opposite circularly-polarized fields yield

$$R = 2\xi_{(I)}/\sqrt{3\xi_{(1)}\xi^{aaaa}_{(2)}(1-\sigma/6-\delta)}, \tag{3.22}$$

where

$$\sigma \equiv \frac{\xi_{(2)}^{aaaa} - \xi_{(2)}^{aabb} - 2\xi_{(2)}^{abab}}{\xi_{(2)}^{aaaa}} \quad \text{and} \quad \delta \equiv \frac{\xi_{(2)}^{aaaa} + \xi_{(2)}^{aabb} - 2\xi_{(2)}^{abab}}{2\xi_{(2)}^{aaaa}} \tag{3.23}$$

are two-photon absorption anisotropy and circular dichroism parameters [128, 142]. Stevens *et al.* found that for light normally incident on a (111) surface of GaAs, opposite circularly polarized fields yield the largest ratio [66, 75]. For light normally incident on a (110) surface, fields linearly polarized along $[1\bar{1}1]$ yield

$$R = 2\xi_{(I)}/\sqrt{3\xi_{(1)}\xi_{(2)}^{aaaa}(1 - 2\sigma/3)}. \tag{3.24}$$

The polarization configuration that yields a global maximum for the control ratio depends on the material and photon energy; I have found that (3.22) is the maximum except for very close to the band edge, where (3.24) is the maximum.

To calculate the population control ratio, it is desirable to use values of $\xi_{(I)}$, $\xi_{(1)}$, and $\xi_{(2)}$ calculated within the same set of approximations. I use microscopic expressions for $\xi_{(1)}$ and $\xi_{(2)}$ in the independent-particle approximation [3] [they can also be derived from (2.16) and (2.17)], and calculate them within the fourteen-band model. Note that my calculation of two-photon absorption ($\xi_{(2)}$) is similar to that of Hutchings and Wherrett [128], but that I include remote band effects.

Fig. 3.10 shows the calculated spectra of the population control ratio (3.22) for various semiconductors. For each material, the ratio is close to unity at the band edge, then drops steeply, but flattens out to some non-zero ratio as photon energy is increased. In general, the smaller the band gap (or conduction band effective mass) of the material, the narrower the range over which the ratio drops, and the lower the ratio at higher excess photon energy. Worth noting is the particularly large ratio for ZnSe. Also plotted in Fig. 3.10 is the ratio appropriate for linearly-polarized fields normally incident on a (111) surface of GaAs, which was the configuration in the experiment of Fraser *et al.* [36]. For all materials, the ratio (3.24) reaches exactly unity at the band edge, in agreement with the PBA calculation (C.9) in Appendix C. .

The only previous theoretical calculation of the population-control ratio, which was for GaAs, missed finding the large ratio near the band edge because it was based on *ab initio* calculations of $\xi_{(1)}$, $\xi_{(2)}$ and $\xi_{(I)}$ that had poor spectral resolution near the band edge [36]. Over the rest of the spectrum shown in Fig. 3.10, it is about a factor of two smaller than my calculation. This is consistent with the previous calculation being based on a calculation of the two-photon absorption coefficient $\xi_{(2)}$ that is too large by comparison with other calculations [128, 144].

The population-control ratio has been measured only in GaAs [36, 37, 66, 67, 75]. The measured ratios on (111)-GaAs, at excess photon energies of 180 meV [36, 37] and 312 meV

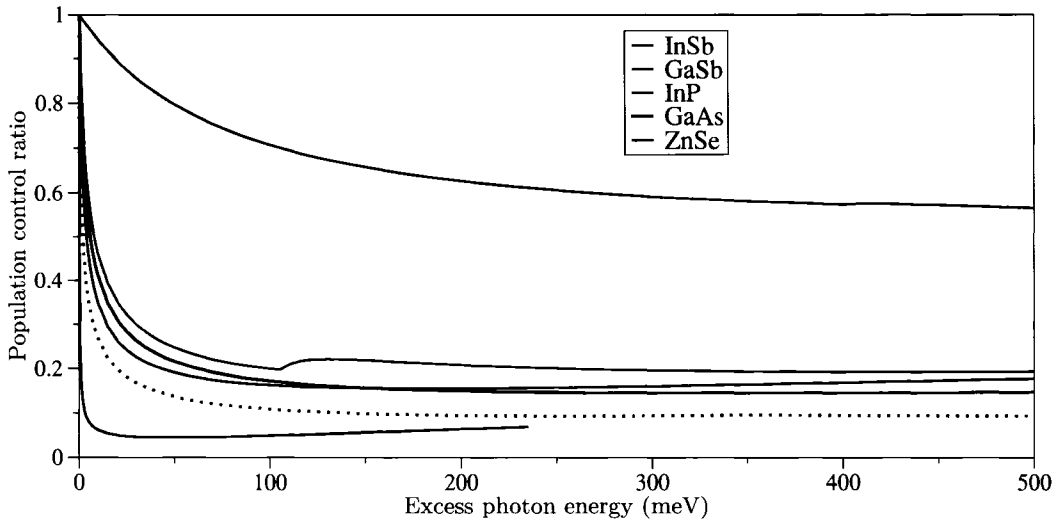

Figure 3.10: (Colour) Calculated population control ratios appropriate for opposite circularly polarized fields normally incident on a (111) surface of InSb, GaSb, InP, GaAs, and ZnSe. The blue, dotted line is the ratio for linearly polarized fields normally incident on a (111) surface of GaAs.

[66, 75] were 4 to 5 times smaller than my calculation. Some of the difference can be attributed to phase mismatch and large sample thickness [36, 37, 66, 75]. An experiment on a (110)-grown multiple quantum well was complicated by an additional cascaded second harmonic effect [67].

3.6 Spin control

The spin injection can be divided into a contribution from electrons $\dot{\mathcal{S}}_{(I;e)}$, and a contribution from holes $\dot{\mathcal{S}}_{(I;h)}$; that is, $\dot{\mathcal{S}}_{(I)} = \dot{\mathcal{S}}_{(I;e)} + \dot{\mathcal{S}}_{(I;h)}$ [similarly, $\zeta_{(I)} = \zeta_{(I;e)} + \zeta_{(I;h)}$, where $\zeta_{(I)}$ is defined in (2.32)].

I treat the spin-split bands as quasidegenerate when taking the FGR limit of perturbation theory, as discussed for the spin current in Sec. 3.4, deriving the microscopic expression

$$\dot{\mathcal{S}}_{(I;e)} = \frac{2\pi}{L^3} \sum_{c,c'}{}' \sum_{v,\mathbf{k}} \langle c\mathbf{k}| \mathbf{S} |c'\mathbf{k}\rangle \left(\Omega^{(2)}_{c,v,\mathbf{k}}\right)^* \Omega^{(1)}_{c',v,\mathbf{k}} \frac{1}{2} \left[\delta\left(2\omega - \omega_{cv}\left(\mathbf{k}\right)\right) + \delta\left(2\omega - \omega_{c'v}\left(\mathbf{k}\right)\right)\right] + c.c.,$$

where the prime on the summation indicates a restriction to pairs (c, c') for which either $c' = c$, or c and c' are a quasidegenerate pair. Using the time-reversal properties of the Bloch functions,

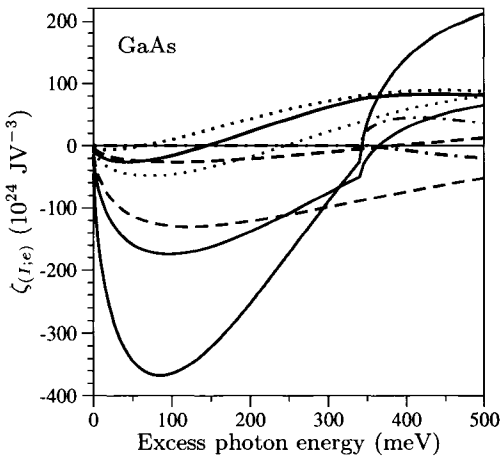

Figure 3.11: (colour) Spin control pseudotensor components ζ_{IA} (black lines), ζ_{IB} (red lines), and $(\zeta_{IA} + 2\zeta_{IB})$ (blue line) with breakdown of initial states. Dotted lines include transitions from the *lh* band, dashed lines include transitions from the *hh* band, dashed-dotted lines include transitions from the *so* band, and solid lines include all transitions.

I find that $\zeta_{(I;e)}$ is purely imaginary and can be written

$$\zeta^{ijkl}_{(I;e)} = i\left(\frac{e}{\hbar\omega}\right)^3 \frac{\pi}{2L^3} \sum_{c,c'}{}' \sum_{v,\mathbf{k}} \sum_{n} \delta\left(2\omega - \omega_{cv}\left(\mathbf{k}\right)\right) \mathrm{Re}\left\{\frac{\langle c\mathbf{k}|\, S^i \,|c'\mathbf{k}\rangle}{\omega_{nv\mathbf{k}} - \omega}\left[M^{jkl}_{c,c',v} + \left(M^{jkl}_{c',c,v}\right)^*\right]\right\}, \tag{3.25}$$

where $M^{jkl}_{c,c',v}$ is given in Eq. (3.16).

The spectra of ζ_{IA} and ζ_{IB} for GaAs are shown in Figs. 3.11 and 3.12. Figure 3.11 includes the contributions from each possible initial valence band. Figure 3.12 shows the spin control calculated with various degrees of approximation described in Sec. 3.2.5.

The term ζ_{IA} decreases from zero at the band edge to a maximum negative value at 40 meV, mostly due to transitions from the *hh* band, and is positive at higher excess photon energies, mostly due to transitions from the *lh* band. The low energy behavior is in agreement with the PBA result (C.12a), in which the ratio of *hh* : *lh* transitions is $(m_{c,hh}/m_{c,lh})^{3/2}$. Transitions with *so* and *uc* intermediate states dominate the decrease in ζ_{IA} at low excess photon energies, as seen in Fig. 3.12(a); they are the only non-zero transitions in the PBA result (C.12a). The contribution from *uc* intermediate states is negative and approximately constant over most of the spectrum, whereas the contribution from *so* intermediate states goes from negative to positive as transitions from the *so* band become allowed ($2\hbar\omega > E_g + \Delta_0$). The contribution from 2BTs, which is zero in the PBA, is positive over the whole spectrum. The breakdown of the PBA is due to the increase in magnitude of the 2BTs. In fact, the sum of the PBA and the 2BTs is a good approximation to the full calculation. I also note that a calculation with H_8

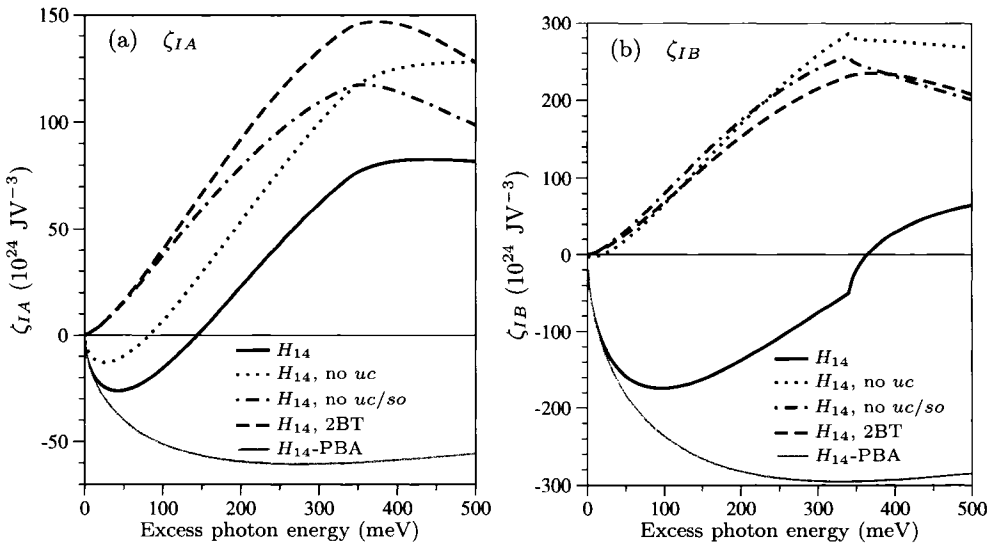

Figure 3.12: Spin control pseudotensor for GaAs. The approximations are described in Sec. 3.2.5.

yields a near negligible result for ζ_{IA}; thus, the contribution from intermediate states within the set $\{so, lh, hh, c\}$ (including 2BTs) is due to the mixing of the Γ_{7c} and Γ_{8c} wavefunctions with these states.

The term ζ_{IB} is larger in magnitude than the term ζ_{IA} over most of the calculated spectrum. It falls to a maximum negative value at 95 meV, sharply increases when transitions from the *so* band become allowed, and is positive at higher excess photon energy. At lower photon energies, transitions from the *hh* band and transitions from the *lh* band both make negative contributions to ζ_{IB}; in the PBA result (C.12b) the ratio of $hh : lh$ transitions is $(m_{c,hh}/m_{c,lh})^{3/2}$. Fig. 3.12(b) reveals that ζ_{IB} is essentially due to contributions from *uc* intermediate states, and 2BTs. Over the whole spectrum, the former are negative while the latter are positive. The smallness of the contribution from *so* intermediate states is also seen in the PBA result (C.12b), since $Z_+ \gg Z'_-$ in that expression. I also note that a calculation with H_8 yields a near negligible result for ζ_{IB}; thus, the contribution from intermediate states within the set $\{so, lh, hh, c\}$ (including 2BTs) is due to the mixing of the Γ_{7c} and Γ_{8c} wave functions with these states.

I have also calculated the spin control pseudotensor for the semiconductors InSb, GaSb, InP, and ZnSe. The results are shown in Fig. 3.13 along with the allowed-allowed parabolic band approximations (C.12a) and (C.12b).

The magnitude of spin control is determined by $\zeta_{(I)}$, but in an experiment one is more interested in the depth of the phase dependent modulation of the spin polarization signal. One possible definition for the signal is the ratio of spin injection measured with both ω and 2ω fields

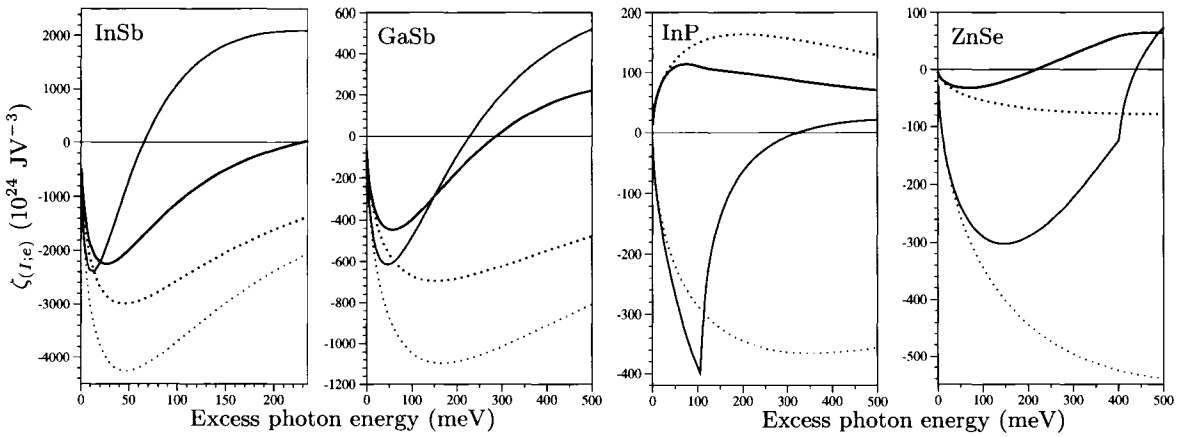

Figure 3.13: (colour) Spin control calculated for InSb, GaSb, InP, and ZnSe. Black lines are ζ_{IA} and red lines are ζ_{IB}. Solid lines are the full calculation using H_{14}. Dotted lines are the parabolic band approximation calculated with (C.12a) and (C.12b).

to the sum of the spin injections measured with circularly polarized fields of each frequency [66]. The amplitude of its modulation is

$$\frac{\left|\dot{\mathcal{S}}^z_{(I)}\right|}{\dot{\mathcal{S}}^z_{(1)}(\sigma^+) + \dot{\mathcal{S}}^z_{(2)}(\sigma^+)}, \tag{3.26}$$

where the argument (σ^+) indicates injection with a σ^+ polarized field. This ratio, which is largest for field amplitudes that equalize $\dot{\mathcal{S}}^z_{(1)}(\sigma^+)$ and $\dot{\mathcal{S}}^z_{(2)}(\sigma^+)$, was measured by Stevens *et al.* with excess photon energies of 150 meV and 280 meV [66, 67].

The ratio (3.26) has an undesirable feature: it can exceed unity. Close to the band edge in many semiconductors (at 2 meV in GaAs), there is a photon energy for which $\dot{\mathcal{S}}^z_{(2)}(\sigma^+) = 0$ (see Chapter 4). At that photon energy, it is impossible to choose field amplitudes to balance one- and two-photon spin injection with circular polarized fields $[\dot{\mathcal{S}}^z_{(1)}(\sigma^+) = \dot{\mathcal{S}}^z_{(2)}(\sigma^+)]$, and thus the maximum ratio has a singularity. Even if the condition $\dot{\mathcal{S}}_{(1)}(\sigma^+) = \dot{\mathcal{S}}_{(2)}(\sigma^+)$ is relaxed, the ratio (3.26) can exceed unity. This is because $\dot{\mathcal{S}}^z_{(1)}(\sigma^+)$ and $\dot{\mathcal{S}}^z_{(2)}(\sigma^+)$ have opposite sign close to the band gap (see Chapter 4), and thus it is possible, by appropriate choice of field amplitudes, to make the denominator of the ratio arbitrarily small.

An alternate ratio to characterize the spin control, which has an upper bound of unity, is

$$R_S = \frac{2}{\hbar}\frac{\left|\dot{\mathcal{S}}^z_{(I)}\right|}{\dot{N}_{(1)} + \dot{N}_{(2)}}. \tag{3.27}$$

It is the amplitude of phase-dependent oscillation of the degree of spin polarization, and it is most useful when there is little or no population control. I assume the fields are chosen to

balance one- and two-photon absorption. For most photon energies and materials this is nearly the same as balancing one- and two-photon spin injection.

For normal incidence on a (111) sample, opposite circularly polarized fields yield

$$R_S = \frac{2}{\hbar} \frac{|\zeta_{IA} + 2\zeta_{IB}|}{\sqrt{3\xi^{aa}_{(1)}\xi^{aaaa}_{(2)}\left(1 - \sigma/6 - \delta\right)}}.$$

For normal incidence on a (110) sample, opposite circularly polarized fields

$$R_S = \frac{2}{\hbar} \frac{3\,|\zeta_{IA} + 2\zeta_{IB}|}{4\sqrt{2\xi^{aa}_{(1)}\xi^{aaaa}_{(2)}\left(1 - \delta - \sigma/8\right)}},$$

and orthogonal linearly polarized fields (xy-polarized) yield

$$R_S\left(\alpha\right) = \frac{2}{\hbar} \frac{\left|\left(\zeta_{IA} + 2\zeta_{IB}\right)\left(r + 3\sin^2\alpha\right)\cos\alpha\right|}{2\sqrt{\xi^{aa}_{(1)}\xi^{aaaa}_{(2)}\left(1 - \frac{1}{2}\sigma\left(\sin^2\alpha\right)\left(1 + 3\cos^2\alpha\right)\right)}},$$

where $r \equiv -2\zeta_{IA}/(\zeta_{IA} + 2\zeta_{IB})$ [66], and α is the angle between the polarization of the ω field ($\mathbf{E}_\omega$) and the [001] axis, which lies in the (110) plane. The angle that maximizes R_S depends on photon energy through r and σ. I determine it numerically.

The ratio R_S for GaAs is plotted in Fig. 3.14(a). For (111)-incidence, opposite circularly polarized fields yield the highest ratio over the studied range of photon energies. For (110)-incidence, opposite circularly polarized fields yield the highest ratio, except for between 190 meV and 415 meV when xy-polarized fields the highest ratio. For xy-polarized fields, the angle that yields the largest ratio decreases from 0.99 rad to 0.53 rad from the band edge to 320 meV, and is zero for higher excess energies.

The ratio R_S for the five semiconductors InSb, GaSb, InP, GaAs, and ZnSe are plotted in Fig. 3.14(b). At low photon energy, opposite circularly polarized fields normally incident on (111) yield the largest ratio for InSb, GaSb, GaAs, and ZnSe, whereas orthogonal linearly polarized fields normally incident on (110) yield the largest ratio for InP.

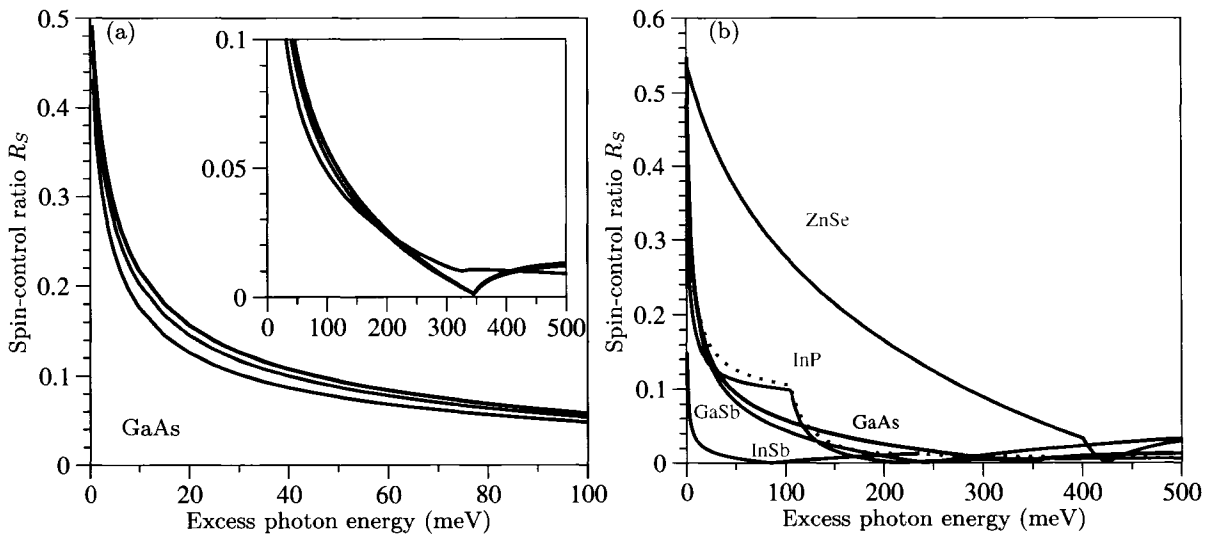

Figure 3.14: (colour) Spin-control ratio normalized by carrier population [Eq. (3.27)]. In (a), for GaAs, black lines are (111)-incident, opposite circularly polarized fields; green lines are (110)-incident, opposite circularly polarized fields; and red lines are (110)-incident, orthogonal linearly polarized fields. In (b), for InSb, GaSb, InP, GaAs, and ZnSe, solid lines are (111)-incident, opposite circularly polarized fields. The dotted line in (b) is (110)-incident, orthogonal linearly polarized fields for InP.

Chapter 4

Two-photon Spin Injection

4.1 Introduction

In this chapter, a comparison is made between the degree of spin polarization of electrons excited by one- and two-photon absorption of circularly polarized light in bulk zinc-blende semiconductors. The macroscopic symmetry and microscopic theory for two-photon spin injection are reviewed, and the latter is generalized to account for spin-splitting of the bands. The degree of spin polarization of one- and two-photon spin injection are calculated for GaAs, InP, GaSb, InSb, and ZnSe using the fourteen-band model described in the preceding chapter. By including the higher conduction bands in the calculation, cubic anisotropy and the role of allowed-allowed transitions can be investigated. The allowed-allowed transitions do not conserve angular momentum and can cause a high degree of spin polarization close to the band edge; a value of 78% is calculated in GaSb, but by varying the material parameters it could be as high as 100%. The selection rules for spin injection from allowed-allowed transitions are presented, and interband spin-orbit coupling is found to play an important role.

It is well known that linear absorption of circularly polarized light in a semiconductor produces spin-polarized electrons in the conduction band [2]. This occurs as a result of the entanglement of electron spin and motion caused by the spin-orbit coupling in the material; in the absence of spin-orbit coupling, there would be no net spin polarization of the excited carriers. For many common semiconductors, the highest valence states are in the degenerate heavy- and light-hole bands at the Γ point. Consequently, the highest degree of spin polarization that can be achieved is 50%. Such a situation occurs when the photon energy exceeds the band gap, but is not large enough to excite carriers out of the split-off band. This can be understood from selection rules that result from the symmetry of the states at the Γ point [2].

One way to increase the spin polarization of the injected electrons is to use materials where the degeneracy between heavy and light hole bands is removed by strain and/or quantum

confinement, so that one can excite carriers only from one band. From the symmetry of the states, one then expects 100% spin polarization. And indeed both theory [2] and experiments [161, 162] have shown a significant enhancement of the degree of spin polarization. The spin polarization could also be increased by using compounds with crystal structures having no valence band degeneracy [163–165].

Spin injection can also arise from two-photon absorption. For certain applications this might have advantages over one-photon spin injection due to a much longer absorption depth, which allows spin excitation throughout the volume of a bulk sample. Two-photon spin injection has been investigated in lead chalcogenides (PbTe, PbSe, and PbS), which are cubic, and have direct fundamental band gaps at the L points [18]. High degrees of spin polarization in these materials have been predicted [18], but not observed [166–169]. The focus in this chapter is on semiconductors that have a direct fundamental band gap at the Γ point, such as GaAs. Based on arguments involving the conservation of angular momentum, it was recently suggested that 100% spin polarization could be achieved in unstrained bulk GaAs from two-photon absorption [19]. However, earlier theoretical results, including Eq. (2.54), predict a two-photon spin polarization of no more than 64% for this class of cubic semiconductors [18, 170, 171]. And time- and polarization-resolved experiments in (001)-oriented GaAs reveal an initial degree of spin polarization of 49% for both one- and two-photon spin injection at wavelengths of 775 and 1550 nm [20]. Equality of one- and two-photon spin injection was also observed by Stevens *et al.* in an experiment with (111)-oriented GaAs [66].

In this chapter, I present microscopic calculations of two-photon spin injection that go beyond the spherical approximation made by earlier calculations. I show how the simple argument based on conservation of angular momentum breaks down, and examine the transitions that give rise to the partial spin polarization. The calculated one- and two-photon degrees of spin polarization are not equal for all materials, and I find that, in fact, two-photon spin injection can be fully polarized, but only from transitions that do *not* conserve angular momentum.

Optical transitions near the Γ point can be summarized with sketches such as those in Fig. 4.1 (c.f. Fig. 3.1). The symmetry of the states at the Γ point of a crystal with zinc-blende symmetry is as follows. The conduction band (Γ_{6c}) is s-like with two degenerate spin states, while the valence bands are p-like. The p-like orbitals are coupled to the electron spin to form four states (the heavy and light hole bands, Γ_{8v}) that are total angular momentum ($j = 3/2$)-like, and two states at lower energy (the split-off band, Γ_{7v}) that are ($j = 1/2$)-like [118]. Note that these states are commonly referred to as if they were eigenstates of total angular momentum, even though they are not [118]. The levels corresponding to the split-off band are not shown in Fig. 4.1. The selection rules for the transitions between the Γ_{7v}, Γ_{8v}, and

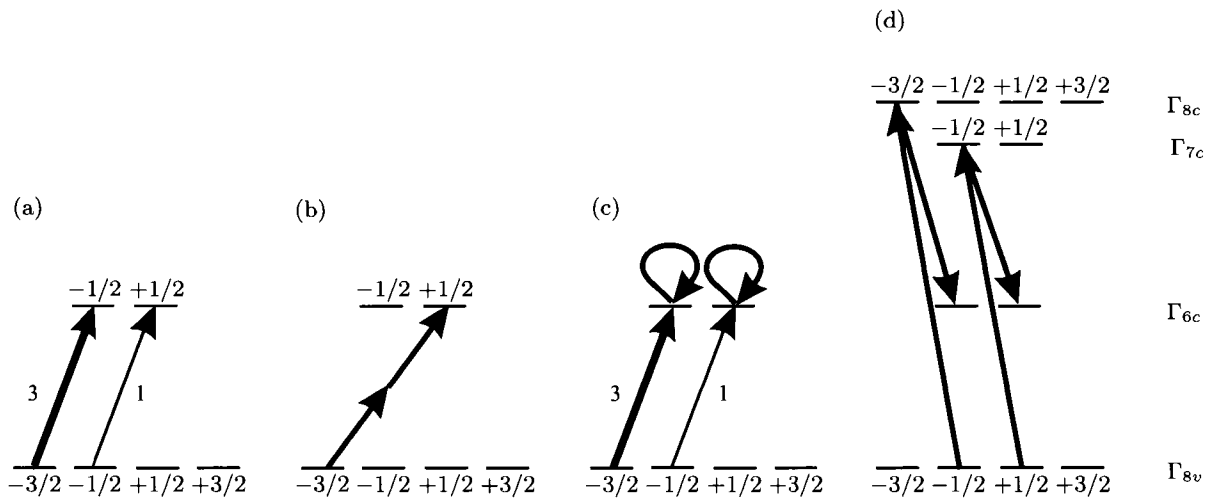

Figure 4.1: Optical transitions in a bulk zinc-blende semiconductor for circularly polarized light σ^+ allowed by the selection rules: (a) for one-photon absorption, (b) for two-photon absorption as suggested by Matsuyama *et al.* [19], (c) two-photon allowed-forbidden transitions with a conduction band as an example of an intermediate state, and (d) two-photon allowed-allowed transitions for vanishing interband spin-orbit coupling and light incident along a $\langle 001 \rangle$ direction. The quantum number m_j for the projection of total angular momentum on the light propagation direction of all states involved is indicated in the figures. The thickness of arrows and adjacent number in (a) and (c) express the relative transition probabilities.

Γ_{6c} states are the same as for the states of a spherically symmetric system [2].[1] Thus they can be understood using angular momentum arguments. By applying the familiar selection rule that one-photon absorption of circularly polarized light with positive helicity (σ^+) must change the projection of total angular momentum by $+1$, one sees that only the two transitions shown in Fig. 4.1(a) are allowed. An examination of Clebsch-Gordan coefficients reveals that the transition from the $m_j = -3/2$ state of the valence band to the $m_j = -1/2$ state of the conduction band is three times as probable as the transition from the $m_j = -1/2$ state of the valence band to the $m_j = +1/2$ of the conduction band. Thus, near the band edge, one expects a value of 50% for the net degree of electron spin polarization

$$P \equiv \frac{N_\downarrow - N_\uparrow}{N_\downarrow + N_\uparrow}, \tag{4.1}$$

where $N_\downarrow$ ($N_\uparrow$) is the concentration of electrons with spin down (up).

The idea of angular momentum conservation was applied to two-photon absorption by

[1] Recall from Chapter 2 that the eight-band Kane model is isotropic.

Matsuyama *et al.* [19]. They argue that because the total angular momentum of the two right circularly polarized photons is +2, only the transition from $m_j = -3/2$ to $m_j = +1/2$ is allowed [see also Fig. 4.1(b)]. Therefore, they suggest that even in a bulk semiconductor with degenerate valence bands the resulting electron spin polarization should be 100%, and indeed with an opposite sign with respect to one-photon spin injection.

On the other hand, the degree of spin polarization due to two-photon spin injection has been calculated several times [18, 170, 171], including in Sec. 2.4, using the eight-band Kane model [121]. Ivchenko calculated the degree of spin polarization in the limit of large spin-orbit splitting [18, 170]. Arifzhanov and Ivchenko improved the calculation by allowing the split-off band to act as an intermediate state; they gave the degree of spin polarization at the band edge as a function of E_g/Δ_0, where E_g is the band gap energy and Δ_0 is the spin-orbit splitting [171]. For GaAs, one infers a 51% degree of spin polarization from their results. Note that, in contrast to one-photon spin injection, the degree of spin polarization of two-photon spin injection near the band edge depends not only on the symmetry of the states, but also on various material parameters. In (2.54), with only two-band transitions included, I give a very simple expression for the two-photon degree of spin polarization in terms of the conduction and valence band effective masses, from which one infers for GaAs a spin polarization of 48%.

In most III-V semiconductors, the next higher conduction bands are p-like (Γ_{7c} and Γ_{8c}) [118]. The role that these higher bands play in two-photon spin injection has not previously been investigated. It is known that $\mathbf{k} \cdot \mathbf{p}$ mixing with these bands is responsible for cubic anisotropy of two-photon absorption [128, 142]. The higher conduction bands can also act as intermediate states in the two-photon amplitude. Such transitions are qualitatively different than transitions within the set of bands nearest to the fundamental band gap [172–175].

In Sec. 4.2 we review the symmetry of two-photon spin injection and I present my calculation, which includes the higher conduction bands. In contrast to previous calculations of two-photon spin injection [18, 170, 171] [including (2.54)], this calculation is not perturbative in $\mathbf{k}$. In Sec. 4.3 I discuss the transitions responsible for the degree of spin polarization in two-photon absorption [Figs. 4.1 (c) and (d)]. In Appendix C.3, I derive expressions for the degree of two-photon spin injection due to so-called "allowed-allowed" transitions.

4.2 Calculation of two-photon spin injection

For an electric field of the form $\mathbf{E}(t) = \mathbf{E}_\omega \exp(-i\omega t) + c.c.$ (I sometimes write $\mathbf{E}_\omega = E_\omega \hat{\mathbf{e}}_\omega$), the two-photon spin injection rate can be written phenomenologically as $\dot{\mathcal{S}}^i = \zeta_{(2)}^{ijklm} E_\omega^j E_\omega^k E_\omega^{l*} E_\omega^{m*}$, where $\zeta_{(2)}^{ijklm}$ is a fifth rank pseudotensor symmetric on exchange of indices j and k, and on exchange of indices l and m; superscript lowercase letters denote Cartesian components and

repeated indices are to be summed over [33]. For the point groups T_d and O_h, appropriate to most cubic semiconductors, a general fifth rank pseudotensor has ten independent components. Forcing the $j \leftrightarrow k$ and $l \leftrightarrow m$ symmetries, and the condition for reality of $\dot{\mathcal{S}}$, $\zeta_{(2)}^{ilmjk} = (\zeta_{(2)}^{ijklm})^*$, leaves three independent real components.

I define $\zeta_{2A} \equiv -i\zeta^{abccc}$ and $\zeta_{2B} \equiv \mathrm{Im}\zeta^{aabac}$, where the indices a, b, and c denote components along the standard cubic axes [100], [010], and [001]. Then the three independent real components are $\mathrm{Re}\zeta_{2A}$, $\mathrm{Im}\zeta_{2A}$, and ζ_{2B}. In the standard cubic basis, the non-zero components of $\zeta_{(2)}^{ijklm}$ are

$$\begin{aligned}
&\zeta_{(2)}^{abbbc} = \zeta_{(2)}^{abccc} = \zeta_{(2)}^{bacaa} = \zeta_{(2)}^{bccac} = \zeta_{(2)}^{caaab} = \zeta_{(2)}^{cabbb} = i\zeta_{2A} \\
&\zeta_{(2)}^{abcbb} = \zeta_{(2)}^{accbc} = \zeta_{(2)}^{baaac} = \zeta_{(2)}^{baccc} = \zeta_{(2)}^{cabaa} = \zeta_{(2)}^{cbbab} = -i\zeta_{2A}^* \\
&\zeta_{(2)}^{aabac} = \zeta_{(2)}^{bbcab} = \zeta_{(2)}^{cacbc} = -\zeta_{(2)}^{aacab} = -\zeta_{(2)}^{babbc} = -\zeta_{(2)}^{cbcac} = i\zeta_{2B},
\end{aligned}$$

as well as those generated by exchanging $j \leftrightarrow k$ and/or $l \leftrightarrow m$, for a total of 48 components.

The point group symmetry allows spin injection for linearly polarized light, associated with $\mathrm{Im}\zeta_{2A}$. However, from a microscopic expression for $\zeta_{(2)}^{ijklm}$ in the independent-particle approximation [see Eq. (4.4), (4.5), or (4.6) below], one can show that $\zeta_{(2)}^{ijklm}$ must be purely imaginary due to the time-reversal properties of the Bloch states. One might expect deviations from the independent-particle approximation within an exciton binding energy of the band edge (see Chapter 6) [174, 176]. In what follows, I assume the independent-particle approximation is valid, which leaves the two-photon spin injection specified in terms of two real parameters ζ_{2A} and ζ_{2B}.

The component of the spin-injection rate along one of the cubic axes can be written compactly (with no summation convention) as [18]

$$\dot{\mathcal{S}}^i = 2i\left(\mathbf{E}_\omega \times \mathbf{E}_\omega^*\right)^i \left(\zeta_{2A}\left|\mathbf{E}_\omega\right|^2 + \left(2\zeta_{2B} - \zeta_{2A}\right)\left|E_\omega^i\right|^2\right). \tag{4.2}$$

If the material were isotropic, the spin injection rate could be described by only one real parameter; $\zeta_{2A} = 2\zeta_{2B}$ and the second term in Eq. (4.2) would be zero.

The cubic anisotropy means that the two-photon spin injection from circularly polarized light depends on the angle of incidence of the light relative to the cubic axes. For circularly polarized light incident along $\hat{\mathbf{n}}$ specified by polar angles θ and ϕ relative to the cubic axes,

$$\dot{\boldsymbol{\mathcal{S}}} \cdot \hat{\mathbf{n}} = \mp 2\zeta_{2A}|E_\omega|^4 \left(1 + \frac{2\zeta_{2B} - \zeta_{2A}}{4\zeta_{2A}} f\left(\theta, \phi\right)\right), \tag{4.3}$$

where $f\left(\theta, \phi\right) = \sin^2\left(2\theta\right) + \sin^4\left(\theta\right)\sin^2\left(2\phi\right)$. The upper (lower) sign is for right (left) circular polarization. The analogous equation for two-photon absorption is given by Hutchings and Wherrett [128]. Equation (4.3) has extrema for light incident along $\langle 001 \rangle$ and $\langle 111 \rangle$ directions.

Due to the cubic anisotropy, the net injected spin is not always parallel to $\hat{\mathbf{n}}$, although it is when $\hat{\mathbf{n}}$ is along $\langle 001 \rangle$ or $\langle 111 \rangle$. In particular, for light along a $\langle 001 \rangle$ direction, $|\dot{\boldsymbol{\mathcal{S}}}| = 2\zeta_{2A}|E_\omega|^4$, while for light incident along a $\langle 111 \rangle$ direction, $|\dot{\boldsymbol{\mathcal{S}}}| = (4/3)\left(\zeta_{2A} + \zeta_{2B}\right)|E_\omega|^4$.

4.2.1 Microscopic calculation

Microscopic expressions for the two-photon spin injection rate, derived using the assumptions discussed in Sec. 1.1 and the independent-particle approximation, have been given before [18, 33, 171]. However, all previous calculations, and the result (2.54) in Chapter 2, used semiconductor models in which all bands are doubly degenerate. In such a case, one finds that

$$\dot{\boldsymbol{\mathcal{S}}} = \frac{2\pi}{L^3} \sum_{c,c',v,\mathbf{k}}{}' \langle c\mathbf{k}| \mathbf{S} |c'\mathbf{k}\rangle \, \Omega^{(2)*}_{c,v,\mathbf{k}} \Omega^{(2)}_{c',v,\mathbf{k}} \delta\left[2\omega - \omega_{cv}(\mathbf{k})\right], \tag{4.4}$$

where $|n\mathbf{k}\rangle$ is a Bloch state with energy $\hbar\omega_n(\mathbf{k})$, L^3 is a normalization volume, $\mathbf{S}$ is the spin operator, $\omega_{nm}(\mathbf{k}) \equiv \omega_n(\mathbf{k}) - \omega_m(\mathbf{k})$, the prime on the summation indicates a restriction to pairs (c, c') for which $\omega_{cc'} = 0$, and $\Omega^{(2)}_{c,v,\mathbf{k}}$ is the two-photon amplitude given in (2.4). However, the spin degeneracy is removed in real crystals of zinc-blende symmetry [145, 146], albeit with a small energy splitting. Thus, (4.4) is unsuitable for a calculation with the fourteen-band model, which accounts for this spin-splitting [130].

If the spin-split bands were well separated, a straightforward FGR derivation would yield

$$\dot{\boldsymbol{\mathcal{S}}} = \frac{2\pi}{L^3} \sum_{c,v,\mathbf{k}} \langle c\mathbf{k}| \mathbf{S} |c\mathbf{k}\rangle \left|\Omega^{(2)}_{c,v,\mathbf{k}}\right|^2 \delta\left[2\omega - \omega_{cv}(\mathbf{k})\right], \tag{4.5}$$

which is a simpler result than (4.4). However, in GaAs the splitting is at most a few meV for conduction states within 500 meV of the band edge [137]. Since this is comparable to the broadening that one would calculate from the scattering time of the states (and also to the laser bandwidth for experiments with pulses shorter than 100 fs), spin-split pairs of bands should be treated as quasidegenerate in FGR. Thus in place of Eq. (4.4) or (4.5) I use,

$$\dot{\boldsymbol{\mathcal{S}}} = \frac{2\pi}{L^3} \sum_{c,c',v,\mathbf{k}}{}' \langle c\mathbf{k}| \mathbf{S} |c'\mathbf{k}\rangle \, \Omega^{(2)*}_{c,v,\mathbf{k}} \Omega^{(2)}_{c',v,\mathbf{k}} \frac{1}{2} \left\{\delta\left[2\omega - \omega_{cv}(\mathbf{k})\right] + \delta\left[2\omega - \omega_{c'v}(\mathbf{k})\right]\right\}, \tag{4.6}$$

where the prime on the summation indicates a restriction to pairs (c, c') for which either $c' = c$, or c and c' are a quasidegenerate pair. The coherence between quasidegenerate bands is optically excited and grows with their populations, as is the case with simpler band models that neglect spin splitting, including the isotropic Kane model from Chapter 2 [18, 33, 170, 171]. This same issue arises in the fourteen-band calculations of "1+2" spin-current injection and "1+2" spin control (Chapter 3), and one-photon spin-current injection (Chapter 5). In Chapter 5, it is

justified using the semiconductor optical Bloch equation approach. That approach yields the same result as the approach taken here, which is simpler.

Using the time-reversal properties of the Bloch functions, the expression for $\zeta_{(2)}^{ijklm}$ that follows from (4.6) can be simplified to give

$$\zeta_{(2)}^{ijklm} = i\left(\frac{e}{\hbar\omega}\right)^4 \frac{2\pi}{L^3} \sum_{c,c',v,\mathbf{k}}{}' \sum_{n,n'} \delta\left[2\omega - \omega_{cv}\left(\mathbf{k}\right)\right] \mathrm{Im}\left[\frac{\langle c\mathbf{k}| S^i |c'\mathbf{k}\rangle \left(V^{jklm} - V^{lmjk}\right)/2}{\left(\omega_{nv}\left(\mathbf{k}\right) - \omega\right)\left(\omega_{n'v}\left(\mathbf{k}\right) - \omega\right)}\right], \quad (4.7)$$

where

$$V^{jklm} \equiv \left\{\mathbf{v}_{c',n'}\left(\mathbf{k}\right), \mathbf{v}_{n',v}\left(\mathbf{k}\right)\right\}^{jk} \left\{\mathbf{v}_{c,n}^{*}\left(\mathbf{k}\right), \mathbf{v}_{n,v}^{*}\left(\mathbf{k}\right)\right\}^{lm},$$

and $\{\mathbf{v}_1, \mathbf{v}_2\}^{ij} \equiv (v_1^i v_2^j + v_1^j v_2^i)/2$.

The photoinjection rate for the density of electron-hole pairs is, from (2.17),

$$\dot{N}_{(2)} = \frac{2\pi}{L^3} \sum_{c,v,\mathbf{k}} \left|\Omega_{c,v,\mathbf{k}}^{(2)}\right|^2 \delta\left[2\omega - \omega_{cv}\left(\mathbf{k}\right)\right]. \quad (4.8)$$

From Eqs. (4.6) and (4.8), the degree of spin polarization, P, can be calculated, since

$$P = -\frac{2}{\hbar}\frac{\dot{\boldsymbol{\mathcal{S}}} \cdot \hat{\mathbf{n}}}{\dot{N}_{(2)}}. \quad (4.9)$$

The sign of P is chosen so that a positive P corresponds to an excess of electrons with spin down, i.e. spin opposite the photon angular momentum.

To evaluate the degree of spin polarization, I use a $\mathbf{k} \cdot \mathbf{p}$ model that diagonalizes the one-electron Hamiltonian (including spin-orbit coupling) within a basis set of fourteen Γ-point states, and includes important remote band effects [130]. The fourteen states (counting one for each spin) comprise six valence band states (the split-off, heavy, and light hole bands), and eight conduction band states (the two lowest, which are s-like, and the six next-lowest, which are p-like).

The model is the same as that used in the preceding chapter, except that here the remote band velocity is not included, even though remote band terms are included. The effect of the remote band velocity contributions to one-photon absorption was discussed by Enders *et al.* [138]. In this calculation, removing the remote band terms from the Hamiltonian changes P for GaAs by at most 2%. Thus I feel justified in the neglect of the remote band contributions to the velocity operator.

This two-photon spin injection calculation is similar to the two-photon absorption calculation of Hutchings and Wherrett [128]. I can reproduce their results by removing remote band effects, which they did not include.

Table 4.1: Calculated band-edge two-photon P.

	InSb (%)	GaSb (%)	InP (%)	GaAs (%)	ZnSe (%)
[001]	−49.3	−58.9	58.7	−20.5	−14.5
[111]	−73.3	−78.4	−16.6	−60.0	−57.1

4.2.2 Calculation results

The calculated degrees of electron spin polarization, P, are shown for GaAs, InP, GaSb, InSb, and cubic ZnSe in Fig. 4.2 as a function of excess photon energy, $2\hbar\omega - E_g$, where E_g is the fundamental band gap. I also show, for comparison, the degree of electron spin polarization due to one-photon absorption, which is discussed in Chapter 5. For each semiconductor, the one-photon degree of spin polarization is 50% at the band edge as expected from the Γ-point selection rules.

In GaAs, so long as the excess photon energy is less than the split-off energy (341 meV) and greater than about 50 meV, there is a near equality of one- and two-photon P's. This agrees recent experimental results [20, 66].

Close to the band edge however, there is a feature of the two-photon P that has not previously been identified; it is seen more clearly in the insets of Fig. 4.2. The values of the two-photon P at the band edge for each material are listed in Table 4.1. This feature is further discussed in Sec. 4.3, but I note here that it does not appear in a spherical approximation. To show this, I have calculated the two-photon P with the 8×8 Kane model that includes only the valence bands and the Γ_{6c} conduction bands, has $C_k = 0$, and has γ_2 and γ_3 replaced by $\tilde{\gamma} \equiv (2\gamma_2 + 3\gamma_3)/5$ to give spherical bands [140] ("$H_{8\mathrm{Sph}}$" in the notation of Sec. 3.2.5); the result, which is independent of crystal orientation, is shown in the dashed-dotted lines in Fig. 4.2.

Both one- and two-photon P's decrease as the excess photon energy is increased. This is due to band mixing away from the Γ point, which changes the selection rules. At excess photon energies above the split-off energy, the one-photon P decreases due to transitions from the split-off valence band [2]. The two-photon P also decreases due to these transitions, but less so.

The possibility of cubic anisotropy in two-photon spin injection was first pointed out by Ivchenko [18], although it has not been calculated until now. Cubic anisotropy in two-photon absorption, on the other hand, has been calculated by Hutchings and Wherrett [128]. They found that near the band edge two-photon absorption of circularly polarized light in GaAs should be about 10% greater for light incident along [111] compared to along [001] [128]. The results of my calculation for GaAs indicate that two-photon spin injection varies with crystal

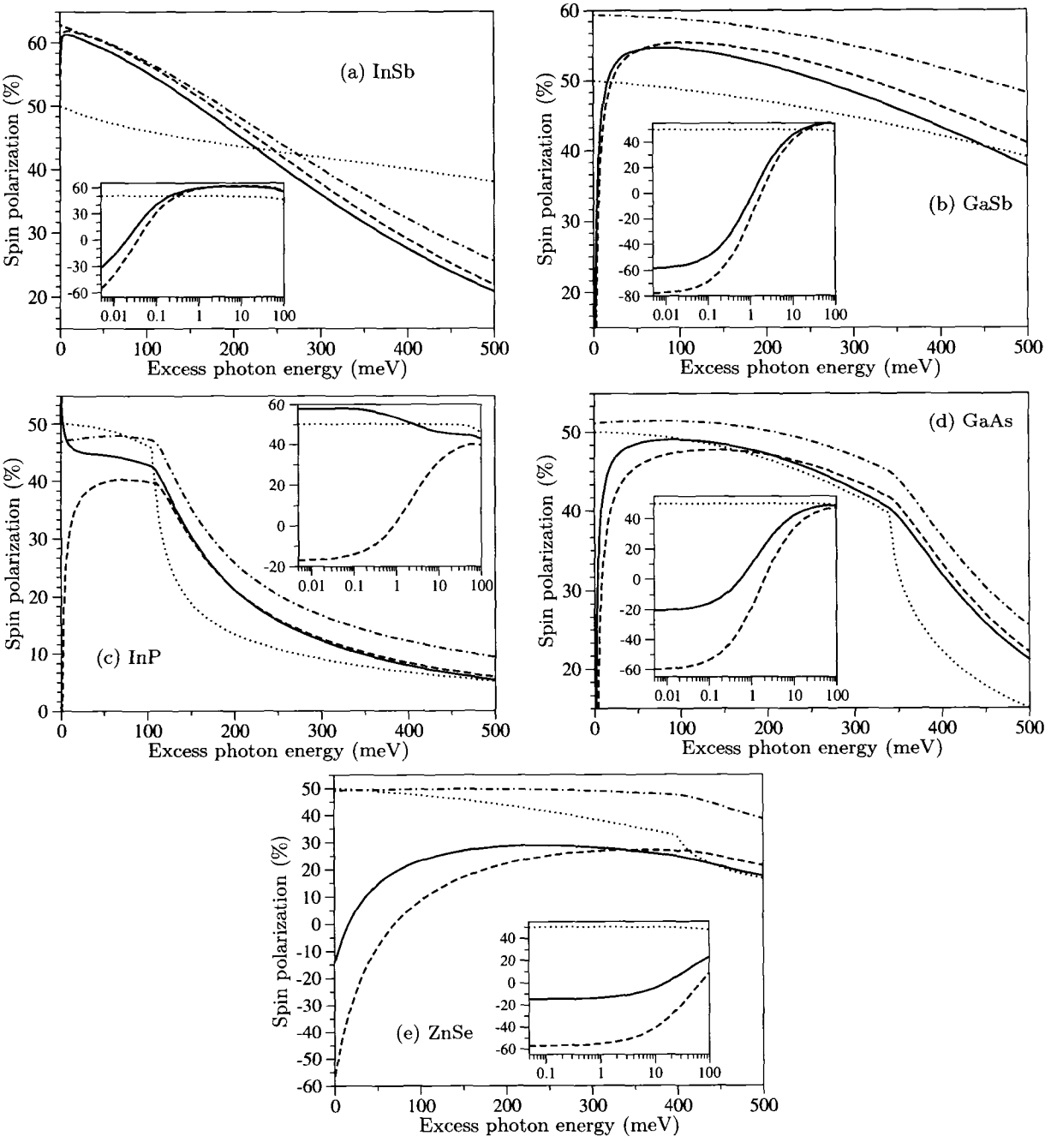

Figure 4.2: Calculated degrees of electron spin polarization P in (a) InSb, (b) GaSb, (c) InP, (d) GaAs, and (e) cubic ZnSe. The solid (dashed) lines are for two-photon excitation with light incident along a $\langle 001 \rangle$ ($\langle 111 \rangle$) direction and the dotted lines are for one-photon excitation. The dashed-dotted lines are for two-photon excitation calculated with an eight band (Γ_{7v}, Γ_{8v}, and Γ_{6c}) spherical model. The insets show P close to the band edge. The sign of P is given by Eq. (4.9).

orientation by a similar amount. Hence the degree of spin polarization shown in Fig. 4.2(d), which is the ratio of the two, varies with crystal orientation by only a few percent for most photon energies in the range I investigated. This is not the case, however, for excess photon energies very close to the band gap, as can be seen in the inset of Fig. 4.2(d). The cubic anisotropy is more substantial for ZnSe and InP.

4.3 Discussion

The prediction of a 100% degree of two-photon spin injection mentioned in Sec. 4.1 uses arguments familiar from spherically symmetric systems. At first it might seem incorrect to even apply these in cubic systems. For the crystal Hamiltonian is not rotationally invariant and thus does not conserve angular momentum: The lattice is viewed as fixed and able to provide any amount of torque. However, the deviation from spherical symmetry is small in many cases, and hence angular momentum arguments should have approximate validity. Stated more technically, since T_d is a subgroup of O_h, which is a subgroup of the full rotation group, the Hamiltonian can be written as the sum of spherical, cubic and tetrahedral parts with the latter two treated as perturbations [132, 140, 177–179]. The eight band Kane model (even including remote band effects but with $\gamma_{2L} = \gamma_{3L}$ and $C_k = 0$) is spherically symmetric, but can nonetheless accurately describe many properties of electrons in semiconductors. It has been used, in particular, for earlier calculations of one- and two-photon spin injection [2, 18, 170, 171], and for "1+2" current and spin-current injection (see Chapter 2). In a spherical model however, the transitions depicted in Fig. 4.1(b) do not occur. By examining the possible intermediate states [i.e. band n in Eq. (2.4)], we can see which transitions do occur, and understand the transfer of angular momentum.

4.3.1 Allowed-forbidden transitions

When the intermediate state is in the same band as either the initial or final state (a so-called "two-band transition"), one of the photons causes an intraband transition. These two-band transitions dominate two-photon absorption in GaAs [172] and indeed in most semiconductors [173–175]. They are "allowed-forbidden" transitions because the intraband transition, proportional to the velocity of electrons in the band, is zero at the Γ point. Consequently, it is not possible to derive the two-photon degree of spin polarization using the states at the Γ point as can be done for one-photon excitation [Fig. 4.1(a)], "1+2" population control (C.1), "1+2" spin control (C.2), or allowed-allowed two-photon transitions [Fig. 4.1(d)]. Instead, one must go away from the Γ point and sum over all $\mathbf{k}$ directions. With this caveat in mind, I nonetheless give a schematic illustration of a two-band transition in Fig. 4.1(c). One should bear in mind

that, away from the Γ point, one cannot in general associate states in the heavy hole band with $J_z = \pm 3/2$ and states in the light hole band with $J_z = \pm 1/2$, since this is only true for $\mathbf{k} \parallel \mathbf{z}$. It is essentially due to this complication that the sum over directions of $\mathbf{k}$ gives a two-photon P that depends on the details of the bands.

The slower decrease of the two-photon P compared to the one-photon P at excess photon energies greater than the split-off energy can be understood from a consideration of two-band transitions. The one-photon P decreases in this regime due to the selection rules involving transitions from the split-off band [2]. The same selection rules apply to the interband part of the two-band transition, but the intraband part of transitions from the split-off band is much weaker than the transitions from the heavy and light hole bands, since the latter excite to states higher in the conduction band that have higher velocity.

There are also allowed-forbidden transitions of the three-band variety (*hh–lh–c*, *hh–so–c*, *lh–hh–c*, and *lh–so–c*); in these cases, the inter-valence band matrix elements can connect states of opposite spin. Their effect on the two-photon spin polarization approximately cancels out in GaAs, as one can see by comparing a calculation that neglects them (2.54) with one that includes them [171].

Within a spherical model, allowed-forbidden transitions must conserve angular momentum; two-photon absorption with circularly polarized light must transfer two units of angular momentum to each electron-hole pair that is created. In order to understand how this leads to an incomplete electron spin polarization, one should form eigenstates of angular momentum, even away from the Γ point. Such states can be formed in a spherical model with envelope functions over an expansion of Bloch states [180]. Any treatment of electron angular momentum must then take into account both the cell-periodic part and the envelope-function part of the electron wave function. It is the latter that is neglected in the argument of Matsuyama [19].

Yet even without that analysis it is clear that, in a simple two-band spherical model consisting of a single spin degenerate valence band and a single spin degenerate conduction band, the two units of angular momentum are divided equally between the two parts of the electron wave function. This can be inferred from the fact that the envelope function for the relative motion of the electron and hole has one unit of orbital angular momentum (i.e. it is a p wave) [176]. A two-band spherical model can be mocked-up from an eight-band spherical model by setting the heavy and light hole band masses equal [174, 177]. Doing so with (2.54) one sees that in that case the two-photon P is 50% [since $(1 + 7/3)/(3 + 11/3) = 1/2$] at the band edge. More generally, the maximum two-photon P in a spherical model is 64% [171]. This can be seen from (2.54) by varying the effective masses to maximize P; the maximum is 7/11 when $m_{c,lh} \gg m_{c,hh}$. In Arifzhanov and Ivchenko, the maximum 7/11 occurs for $\Delta_0 \gg E_g$.

4.3.2 Allowed-allowed transitions

Allowed-allowed transitions are those for which both matrix elements in the two-photon amplitude (2.4) are non-zero at the Γ point. Allowed-allowed transitions have a different frequency dependence than allowed-forbidden transitions. Near $2\hbar\omega \gtrsim E_g$ the former varies as $(2\hbar\omega - E_g)^{1/2}$ while the latter varies as $(2\hbar\omega - E_g)^{3/2}$. Hence, allowed-allowed transitions can dominate allowed-forbidden transitions in a frequency range close to the band edge. For GaAs, however this range is only 10 meV [128, 172]. As seen in the fourteen-band calculation shown in the inset of Fig. 4.2(d), the two-photon degree of spin polarization in this range can be very different from the rest of the spectrum. These transitions are necessarily due to lower symmetry parts of the Hamiltonian; in a system with true spherical symmetry one could not have a two-photon transition from a p state to an s state, since two-photon transitions cannot connect states of opposite parity.

The selection rules for allowed-allowed transitions are worked out in Appendix C.3. Consider first the simple approximation of vanishing interband spin-orbit coupling Δ^- (denoted $\bar{\Delta}$ by Pfeffer and Zawadzki [130]). Then the basis states given in (3.2) are the energy eigenstates at the Γ point. For σ^+ polarized light incident along [001], the only allowed-allowed transitions are depicted in Fig. 4.1(d); these can be derived from Table III of Lee and Fan [174]. The product of the two matrix elements in the two-photon amplitude is the same for both transitions. Thus, if the spin-orbit splitting of the upper conduction bands Δ_0' can be neglected compared to the other energy differences, then P is zero [see Eq. (C.19) with $\Delta^- = 0$]. For σ^+ polarized light incident along [111], the non-zero transitions are i) $|\Gamma_{8v}', +1/2\rangle$ to $|\Gamma_{8c}', -3/2\rangle$ to $|\Gamma_{6c}', -1/2\rangle$; ii) $|\Gamma_{8v}', +3/2\rangle$ to ($|\Gamma_{8c}', -1/2\rangle$ and $|\Gamma_{7c}', -1/2\rangle$) to $|\Gamma_{6c}', +1/2\rangle$; and iii) $|\Gamma_{8v}', -3/2\rangle$ to ($|\Gamma_{8c}', -1/2\rangle$ and $|\Gamma_{7c}', -1/2\rangle$) to $|\Gamma_{6c}', +1/2\rangle$. Here the prime indicates that the states are rotated so that the quantization axis is [111] rather than [001]. If the spin-orbit splitting of the upper conduction bands Δ_0' can be neglected compared to the other energy differences, then the third of these is zero and the probability for the second is three times that of the first, resulting in $P = -0.5$ [see Eq. (C.20)].

However, close to the band edge, where allowed-allowed transitions dominate, the full fourteen-band calculation [see Table 4.1 or the insets of Figs. 4.2(a)–(e)] does not agree with these simple arguments. There is significant difference between materials; for GaAs $P = -0.21$ and $P = -0.60$ for light incident along [001] and [111] respectively. The disagreement is due to the importance of the spin-orbit mixing between the valence and upper conduction conduction bands, characterized by a nonvanishing Δ^-.

The interband spin-orbit coupling Δ^- would be zero if the material had inversion symmetry [136, 137, 181]. In contrast to most of the other parameters in the fourteen-band model, the

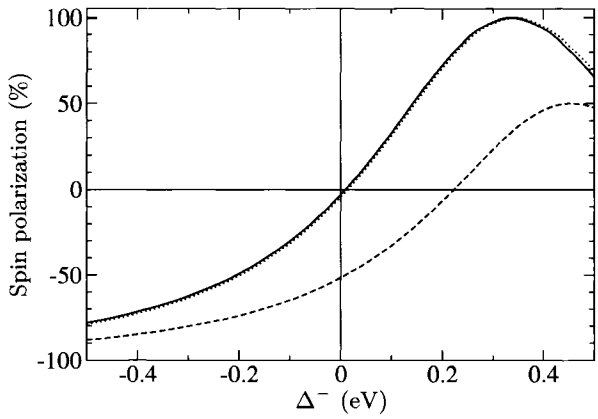

Figure 4.3: Sensitivity of the GaAs band-edge two-photon P to Δ^-. The solid (dashed) line is for two-photon excitation with circularly polarized light incident along a $\langle 001 \rangle$ ($\langle 111 \rangle$) direction as calculated with the fourteen-band model. The dotted line is Eq. (C.19).

value of Δ^- has not been determined by directly fitting it to one or more experimental results. Rather, it has been calculated by various methods: the empirical pseudopotential method (-61 meV for GaAs) [124, 130, 182], the tight binding method (-85 meV for GaAs) [137], the *ab initio* linear-muffin-tin-orbitals method (-110 meV for GaAs) [137], and by an indirect fitting with a 30×30 $\mathbf{k} \cdot \mathbf{p}$ Hamiltonian (-70 meV for GaAs) [137, 181].

In light of the variation in calculated values of the interband spin-orbit coupling Δ^-, I have investigated the dependence of the band edge two-photon degree of spin polarization on Δ^-. The result, shown in Fig. 4.3, is rather dramatic. First, it shows that for small Δ^-, P due to [001] incident light is proportional to Δ^-, whereas P due to [111] incident light is less sensitive to Δ^-. Second, it indicates that a 100% degree of spin polarization could indeed be possible due to two-photon absorption. But this possibility is *not* due to the transfer of angular momentum from the light to the electrons. Since it results from allowed-allowed transitions that are only non-zero due to the lack of inversion symmetry and could only occur for certain crystal orientations, I suggest that some of the angular momentum comes from the crystal lattice itself.

The selection rules for allowed-allowed transitions including interband spin-orbit coupling are given for [001] incident light in Eqs. (C.13–C.18) and an expression for the resulting spin polarization is given in Eq. (C.19). It is worth noting that P is independent of the valence-upper conduction momentum matrix parameter Q.

This allows us to see how the small spin-orbit mixing between valence and upper conduction bands can have an important effect on the band edge spin-polarization. Allowed-allowed transitions between the unmixed states [Fig. 4.1(d)] are proportional to the small matrix element P_0', which would be zero if there were inversion symmetry. And since the intermediate state is

in an upper conduction band, the energy denominator of the two-photon transition amplitude is large, which further reduces the amplitude for these transitions. The interband spin-orbit mixing, proportional to Δ^-/E_0', is small, but it introduces allowed-allowed transitions with a valence band as an intermediate state. Then, instead of being proportional to P_0', the transition is proportional to P_0, and the energy denominator is smaller. This allows the condition $CP_0' = DP_0\Delta^-$ to be met with fairly modest interband spin-orbit mixing.

4.4 Conclusion

I have presented the first calculation of two-photon spin injection that goes beyond a spherical model. The cubic anisotropy of the two-photon P is small for most of the semiconductors I investigated at photon energies where allowed-forbidden transitions dominate, although it is somewhat larger in ZnSe and InP than in the others. Allowed-allowed transitions, which do not appear in a spherical model, and hence do not conserve angular momentum, are found to strongly modify the two-photon P close to the band edge, and cause a large cubic anisotropy. I have identified the selection rules responsible for these transitions, and found that interband spin-orbit coupling plays an important role.

Measuring the two-photon P due to allowed-allowed transitions would be challenging in most semiconductors, since they only dominate in a narrow energy range, and the absorption rate is small close to the band edge. However, such a measurement could serve as a means of determining the parameter Δ^-, which contributes to the electron g factor [137] and the spin splitting of bands [127, 130].

I emphasize that the calculations presented here are all in the independent-particle approximation, and in particular neglect the Coulomb interaction between the optically excited electron and hole. Hence, two-photon injection of spin-polarized bound excitons is outside the scope of this chapter. Excitonic effects on "1+2" excitation are discussed in Chapter 6. Close to the band edge, excitonic effects are known to enhance two-photon absorption [174, 176, 183–185]. Two-photon spin injection will be similarly enhanced, and thus the two-photon P will be less sensitive to excitonic effects since it is a ratio of the two (see Eq. 4.9). Certainly, for excess photon energies greater than an exciton binding energy, I do not expect excitonic effects to greatly modify the results presented here. However, within an exciton binding energy of the band edge, the enhancements of allowed-allowed and allowed-forbidden transitions may differ [184, 185], envelope-hole coupling may modify the selection rules leading to two-photon spin injection [186], and the electron spin lifetime will be shorter due to the Bir-Aronov-Pikus mechanism of spin relaxation [187]. Thus, a complete theory of two-photon spin injection close to the band edge should include excitonic effects. Nonetheless, the two-photon P due to allowed-allowed

transitions predicted here in the independent-particle approximation should be observable in materials for which the dominance of allowed-allowed transitions extends beyond an exciton binding energy of the band edge.

Chapter 5

Pure Spin Current from One-Photon Absorption of Linearly Polarized Light in Noncentrosymmetric Semiconductors

5.1 Introduction

Chapters 2 and 3 show that "1+2" excitation can inject either a spin-polarized electrical current (SPEC) or a pure spin current(PSC), the latter distinguished by the absence of an accompanying charge current. That prediction led to the first observations of PSCs [41, 42]. There have been many recent proposals for PSC schemes involving spin-pumping or spin Hall effects [43, 44, 48–55, 60, 62], some of which have been experimentally observed [45–47].

In this chapter, I show theoretically that a ballistic PSC can be generated in noncentrosymmetric semiconductors, merely by one-photon absorption. This feature of one-photon absorption of linearly polarized light does not seem to have been appreciated previously: It occurs even in unstrained bulk GaAs, it can be generated by a single, weak continuous wave (CW) laser beam, and it arises from the symmetry of the crystal itself. I calculate the linear PSC using the 14×14 $\mathbf{k} \cdot \mathbf{p}$ model used in preceding chapters. I also use an extension of the model to show that the linear PSC can be increased with the application of strain.

In the notation of Sec. 2.2.3, the linear PSC comes from $\mu_{(1)}^{ijkl}$. Whereas $\eta_{(1)}^{ijk}$, the tensor for one-photon current injection (see Sec. 2.2.1), is zero in bulk GaAs, $\mu_{(1)}^{ijkl}$ can be nonzero, resulting in a PSC. The linear PSC does not rely on carrier scattering, but to connect with experiments, I include an estimate of the spin-separation distance using a simple model of

momentum relaxation.

As in preceding chapters, I consider a semiconductor with filled valence bands and empty conduction bands, ignore interactions amongst the electrons, and treat the coupling between light and the electrons perturbatively in the long-wavelength limit using $\mathbf{A} \cdot \mathbf{v}$ coupling. But whereas preceding chapters used microscopic expressions based on the Fermi's golden rule (FGR) limit of the wave function evolution, I here use microscopic expressions based on the evolution of the density matrix, i.e. the semiconductor optical Bloch equations (SOBEs) [104, 106, 188]. And whereas preceding chapters studied the effects of monochromatic or bichromatic fields, this chapter studies the effect of a pulsed field. The SOBE approach more naturally accommodates a phenomenological dephasing rate, and hence better justifies the optical excitation of the coherences between spin-split bands, which are added by hand in the FGR approach. The use of a pulsed field results in an integral over time for the spin current, rather than a spin-current injection rate. I have elsewhere derived the results presented here with the FGR approach and a monochromatic field [189].

In Sec. 5.2, I indicate that, within these approximations, one-photon absorption of linearly polarized light excites a distribution of electrons in $\mathbf{k}$-space that is even in $\mathbf{k}$, no matter what the symmetry of the material; no net electrical current results.[1] Further, electrons excited into the conduction band at opposite $\mathbf{k}$ points will have opposite spin polarization, resulting in no net spin injection. In noncentrosymmetric crystals however, the spin polarization injected at a given $\mathbf{k}$ need not vanish.[2] Thus, in such a case, there will be a PSC, since the velocities of electrons at opposite $\mathbf{k}$ points are opposite. Then in Sec. 5.3, I give a microscopic expression for $\mu_{(1)}$, and calculate the linear PSC with the fourteen-band model including strain.

5.2 Proof of linear pure spin current

The electric field inside the semiconductor is $\mathbf{E}(t) = \mathbf{E}_\omega(t) \exp(-i\omega t) + c.c.$, where $\mathbf{E}_\omega(t)$ is a slowly varying envelope function, and $\hbar\omega > E_g$. Note that this is a change from other chapters in this thesis, in which $E_g > \hbar\omega$.

The SOBEs are dynamical equations for the single-particle density matrix elements $\rho_{nm}(t)$. Versions of the SOBEs have been derived in the independent-particle approximation using both the velocity gauge [104] and the length gauge [101, 106]. Both give the same result for the problem at hand. The SOBEs are solved perturbatively by an iterative method whereby $(n+1)$-th order terms of the density matrix are driven by terms involving products of the

[1] Linear photogalvanic effects, due to asymmetric scattering or a shift in charge density upon excitation can occur [99], but not within these approximations.

[2] This was exploited by Alvarado *et al.*, who detected a spin polarization in electrons photoemitted from (110) GaAs [190].

electric field and n-th order terms of the density matrix (see, e.g. Aversa and Sipe [106]). The zeroth-order density matrix, the initial condition, is the ground state. The only nonzero first-order density matrices are the interband coherences ρ_{vc}. In second-order, there are also electron populations ρ_{cc}, hole populations ρ_{vv}, inter-conduction band coherences $\rho_{cc'}$, and inter-valence band coherences $\rho_{vv'}$.

To second-order, for conduction bands c and c' (which can be the same),

$$\rho_{cc'} = \frac{\pi e^2}{\hbar^2} \sum_v \int_{-\infty}^{t} dt' \frac{\mathbf{E}_\omega (t') \cdot \mathbf{v}_{cv}}{\omega_{cv}} \frac{\mathbf{E}^*_\omega (t') \cdot \mathbf{v}_{vc'}}{\omega_{c'v}} e^{(-i\omega_{cc'} - \gamma_{cc'})(t-t')} (D_{cv} + D^*_{c'v}), \tag{5.1}$$

where $\omega_{nm}(\mathbf{k}) \equiv \omega_n(\mathbf{k}) - \omega_m(\mathbf{k})$, $\hbar\omega_n(\mathbf{k})$ is the energy of the Bloch state $|n\mathbf{k}\rangle$, the velocity matrix element $\mathbf{v}_{cv}(\mathbf{k}) \equiv \langle c\mathbf{k}| \mathbf{v} |v\mathbf{k}\rangle$, $\gamma_{nm}(\mathbf{k})$ is the dephasing rate of the coherence ρ_{nm}, and $D_{nm} \equiv \delta(\omega - \omega_{nm}) - (i/\pi)\mathcal{P}(\omega - \omega_{nm})^{-1}$, where $\mathcal{P}$ indicates the principal part. In deriving (5.1) it has been assumed that interband dephasing is fast compared with the time of the pusle. The dephasing rates account for some of the many-body interactions in an approximate way [104, 188].

The photoexcited electron density is $N_{(1)} = \sum_{c,\mathbf{k}} \rho_{cc,\mathbf{k}}(t)$. Defining $N_{cv}(\mathbf{k})$ as the electron density excited from band v to band c at $\mathbf{k}$ (i.e. $N_{(1)} = \sum_{\mathbf{k},c,v} N_{cv}(\mathbf{k})$), one finds from Eq. (5.1) that $(d/dt + \gamma_{cc}) N_{cv}(\mathbf{k}) = \dot{N}^{(\mathrm{inj})}_{cv}(\mathbf{k})$, where

$$\dot{N}^{(\mathrm{inj})}_{cv}(\mathbf{k}) \equiv \frac{2\pi e^2}{\hbar^2\omega^2} \frac{1}{L^3} |\mathbf{E}_\omega \cdot \mathbf{v}_{cv}(\mathbf{k})|^2 \delta(\omega_{cv}(\mathbf{k}) - \omega),$$

and L^3 is a normalization volume [c.f. (2.16)] [103]. Time-reversal symmetry of the Bloch states yields Kramers degeneracy, $\omega_n(-\mathbf{k}) = \omega_{\bar{n}}(\mathbf{k})$, where a bar above a band index denotes the band with the opposite spin. As well, the velocity matrix elements satisfy $\mathbf{v}_{cv}(-\mathbf{k}) = -[\mathbf{v}_{\bar{c}\bar{v}}(\mathbf{k})]^*$.[3] Using these two properties, it follows that when the light is linearly polarized, $\dot{N}^{(\mathrm{inj})}_{cv}(-\mathbf{k}) = \dot{N}^{(\mathrm{inj})}_{\bar{c}\bar{v}}(\mathbf{k})$. Consequently, the photocurrent injection rate, given by

$$e \sum_{\mathbf{k},c,v} [\mathbf{v}_{cc}(\mathbf{k}) - \mathbf{v}_{vv}(\mathbf{k})] \dot{N}^{(\mathrm{inj})}_{cv}(\mathbf{k}),$$

is zero for linearly polarized light; hence, any spin current must be a PSC.

The photoexcited electron spin density is $\boldsymbol{\mathcal{S}} = \sum_{c,c',\mathbf{k}} \langle c'\mathbf{k}| \mathbf{S} |c\mathbf{k}\rangle \rho_{cc',\mathbf{k}}(t)$, where $\mathbf{S}$ is the spin operator. Note that for excitation near the band edge $\hbar\omega_{cc'}$ is either less than a few meV (if c and c' are equal, or are the spin-split lowest conduction bands) or greater than a few eV (if c or c' is a higher conduction band) [137, 145]. At times t longer than the pulse width t_L, the integral over t' in Eq. (5.1) will be negligible unless $\omega_{cc'} < 1/t_L$. For long pulses, a similar argument can be made but with $\gamma_{cc'}$ replacing $1/t_L$; however, in this chapter, I focus on typical ultrafast experiments [41, 42], for which one can neglect spin relaxation and carrier

[3] The phases of states and partitioning of degenerate subspaces can always be chosen so that this is true [117].

recombination occurring on longer timescales. Thus the integral over t' allows one to neglect coherences other than those between spin-split pairs of bands. I expand the retained coherences in powers of $\omega_{cc'}/\omega$ and keep only the lowest order term. This neglects the precession of the spins due to the spin-splitting of the bands, which is justified since the precession period is long compared to the momentum scattering time [2]. Writing $\boldsymbol{\mathcal{S}} = \sum_{\mathbf{k}} \boldsymbol{\mathcal{S}}(\mathbf{k})$, where $\boldsymbol{\mathcal{S}}(\mathbf{k})$ is the electron spin density at $\mathbf{k}$ one finds $\mathcal{S}^i(\mathbf{k}) = \sum_{j,l} \zeta^{ijl}_{(1)}(\mathbf{k}) \int_{-\infty}^{t} E^{j*}_{\omega}(t') E^{l}_{\omega}(t')\, dt'$, where superscript indices denote Cartesian components,

$$\zeta^{ijl}_{(1)}(\mathbf{k}) \equiv \frac{\pi e^2}{\hbar^2\omega^2}\frac{1}{L^3}\sum_{v,c,c'}{}' \langle c'\mathbf{k}|\, S^i\, |c\mathbf{k}\rangle\, v^j_{vc'}(\mathbf{k})\, v^l_{cv}(\mathbf{k}) \left[\delta\left(\omega_{cv}(\mathbf{k})-\omega\right)+\delta\left(\omega_{c'v}(\mathbf{k})-\omega\right)\right], \quad (5.2)$$

and the prime on the summation indicates a restriction to pairs (c, c') for which either $c' = c$, or c and c' are a quasidegenerate pair. Thus the coherence between bands c and $\bar{c}$ is optically excited and grows with the population, as in simpler band models that neglect spin splitting [2]. If one were to neglect the coherence between spin-split bands, the net degree of spin polarization, $|\boldsymbol{\mathcal{S}}|/\left(N_{(1)}\hbar/2\right)$, would only be 10% in GaAs compared to the accepted 50% with Eq. (5.2).

From the time-reversal properties of the Bloch states, the spin matrix elements satisfy the property $\langle n, -\mathbf{k}|\, \mathbf{S}\, |m, -\mathbf{k}\rangle = -\langle \bar{n}, \mathbf{k}|\, \mathbf{S}\, |\bar{m}, \mathbf{k}\rangle^*$.[4] Using this property, Kramers degeneracy, and the time-reversal property of the velocity matrix elements, one finds $\boldsymbol{\mathcal{S}}(-\mathbf{k}) = -\boldsymbol{\mathcal{S}}(\mathbf{k})$ for linear polarized excitation. Thus there is no net spin injection from linearly polarized light, and if $\boldsymbol{\mathcal{S}}(\mathbf{k})$ is nonzero for some $\mathbf{k}$, there is a PSC.

5.3 Microscopic calculation

One might naively quantify a PSC by $(I_{\uparrow} - I_{\downarrow})$, where $I_{\uparrow(\downarrow)}$ is the current due to up (down) electrons. A more general measure that naturally accounts for a distribution of carrier velocities and spins is to use a spin current density pseudotensor $K^{ij} \equiv \langle \hat{v}^i \hat{S}^j \rangle$ as I have done in Chapters 2 and 3. When there is no accompanying charge current, the spin current is a PSC.

Phenomenologically, the injection of a spin current due to one-photon absorption can be written in terms of a material response pseudotensor $\mu_{(1)}$, as $K^{ij} = \sum_{l,m} \mu^{ijlm}_{(1)} \int E^{l*}_{\omega}(t') E^{m}_{\omega}(t')\, dt'$. This generalizes the definition of $\mu_{(1)}$ in Sec. 2.2.3 to excitation by a pulse. The spin current pseudotensor $\mu_{(1)}$ satisfies the intrinsic symmetry $\mu^{ijlm}_{(1)} = \left(\mu^{ijml}_{(1)}\right)^*$. It is further constrained by the symmetry of the material, since it must be invariant under the point group transformations of the crystal. It vanishes for materials with inversion symmetry, but can be nonzero for the symmetries appropriate to zinc-blende and wurtzite crystals. The symmetry analysis of $\mu^{ijlm}_{(1)}$ and the other one-photon effect tensors is discussed in Appendix D.

[4] The phases of states and partitioning of degenerate subspaces can always be chosen so that this is true [117].

The microscopic expression for $\mu_{(1)}^{ijlm}$ is derived from Eq. (5.1), with the same approximations made for Eq. (5.2). Using time reversal properties of the Bloch functions, one can then show that $\mu_{(1)}^{ijlm}$ is real, and can be written as

$$\mu_{(1)}^{ijlm} = \frac{\pi e^2}{\hbar^2 \omega^2} \frac{1}{L^3} \sum_{\mathbf{k},v} {\sum_{c,c'}}' \delta\left(\omega_{cv}\left(\mathbf{k}\right) - \omega\right) \mathrm{Re}\left[\left\langle c'\mathbf{k}\right| v^i S^j \left|c\mathbf{k}\right\rangle v_{vc'}^l\left(\mathbf{k}\right) v_{cv}^m\left(\mathbf{k}\right) + \left(l \leftrightarrow m\right)\right]. \quad (5.3)$$

In an ultrafast experiment, a PSC can be measured by the resulting displacement of up and down spins. To estimate the spin separation, I use the optically injected electron distribution as a source term in the Boltzmann transport equation. By neglecting space-charge effects, which are negligible for a PSC, the Boltzmann equation can be solved in the relaxation time approximation [42]. This approach neglects scattering during optical excitation, but for ultrafast experiments the error should not be too large. If one measures the spin with respect to the quantization direction $\hat{\mathbf{a}}$, the up and down spin populations are separated by an average displacement $\mathbf{d}\left(\hat{\mathbf{a}}\right)$. I find $d^i\left(\hat{\mathbf{a}}\right) = \sum_j \left(4\tau/\hbar\right) K^{ij} \hat{a}^j / N$, where τ is the momentum relaxation time.

To calculate the PSC for bulk GaAs, I use the fourteen-band model described in detail in Chapter 3, although the remote band contributions to the velocity are not included in this calculation. It is a $\mathbf{k}\cdot\mathbf{p}$ model that diagonalizes the one-electron Hamiltonian (including spin-orbit coupling) within a basis set of fourteen Γ point states and includes important remote band effects [130]. The model contains thirteen parameters chosen to fit low-temperature experimental data [130].

Strain is included by the deformation potential method of Pikus and Bir, which amounts to adding $\mathbf{k}$-independent terms to H_{14} that are proportional to the strain [120, 191]. The deformation potentials amongst valence and lowest conduction band states are well established [192]. Between the valence and p-like conduction band states, there are two deformation potentials for the strain considered in this chapter, a_{cv} and b_{cv} [193–195]. I use $b_{cv} = -2.3\,\mathrm{eV}$, which is an average of tight-binding calculations [193, 194], and consistent with experiment [196]. The parameter a_{cv} couples to the hydrostatic component of strain [194]; neither it nor the deformation potentials amongst p-like upper-conduction band states affect my results. I also neglect the small effect of strain on spin-orbit coupling [194].

For GaAs, I present results for light linearly polarized along [001]. In the standard cubic basis, $K^{xx} = -K^{yy} \equiv \kappa$ are the only two nonzero components of the spin current. Alternately, using a basis where $\hat{\mathbf{x}} \parallel [001]$, $\hat{\mathbf{z}} \parallel [110]$ and $\hat{\mathbf{y}} \parallel [1\bar{1}0]$, the only two nonzero components of the spin current are $K^{zy} = K^{yz} = \kappa$. That is, there is a net PSC of electrons with spin component along $[1\bar{1}0]$ and velocity component along [110], and an equal PSC with spin component along [110] and velocity component along $[1\bar{1}0]$. Under strain in the [001] direction, the point group

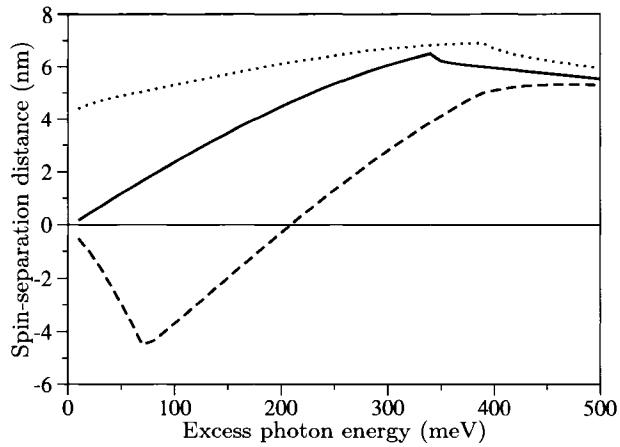

Figure 5.1: Calculated spin separation in GaAs under no strain (thick line), under 1% tensile strain (dotted line), and under 1% compressive strain (dashed line). Transitions from the split-off band begin to contribute at $\approx 350\,\text{meV}$.

symmetry of the crystal is reduced from T_d to D_{2d}, but $K^{zy} = K^{yz}$ remain the only nonzero components of the spin current. I have considered 1% biaxial strain; under tensile (compressive) strain, the lattice dilates (contracts) by 1% in the [100] and [010] directions and contracts (dilates) by 0.93% in the [001] direction, with the latter determined from the elastic constants C_{11} and C_{12} [192].

The calculated spin separation distances, $|\mathbf{d}|$, for these PSCs are plotted in Fig. 5.1 as a function of photon energy above the band gap, where I have assumed a momentum relaxation time of 100 fs; note that the band gap for each case is different. A density functional theory calculation for wurtzite CdSe found a spin separation distance of similar magnitude [82]. For comparison, experiments on PSCs generated with harmonically related fields in GaAs/AlGaAs quantum wells [41] and ZnSe [42] measured spin separations of 20 nm and 24 nm respectively.

To illustrate the spin-momentum correlation implied by the calculation of $\mathbf{d}$, I plot in Fig. 5.2 calculated angular distributions of the injected carrier density $N(\hat{\mathbf{k}}) \equiv \sum_{|\mathbf{k}|} N(\mathbf{k})$ and degree of spin polarization $\mathbf{s}(\hat{\mathbf{k}}) \equiv \left[\sum_{|\mathbf{k}|} \boldsymbol{\mathcal{S}}(\mathbf{k})\right] / N(\hat{\mathbf{k}})$ for the excited conduction band electrons in GaAs.

In unstrained GaAs, $s_{\max}$, the maximum over $\mathbf{k}$ of $|\mathbf{s}(\hat{\mathbf{k}})| / (\hbar/2)$, rises from zero at the band edge to a maximum of 12% at the photon energy when transitions from the split-off valence band become allowed. Under strain, $s_{\max}$ is largest near the band edge. In Fig. 5.2(b), $s_{\max}$ is 15% while in Fig. 5.2(c) it is 44%.

It is clear that strain can increase the PSC, especially at lower energies where strain-induced splitting of the heavy and light hole bands increases the spin polarization of the photogenerated electrons. Under tensile (compressive) strain the light hole band moves to higher (lower) energy

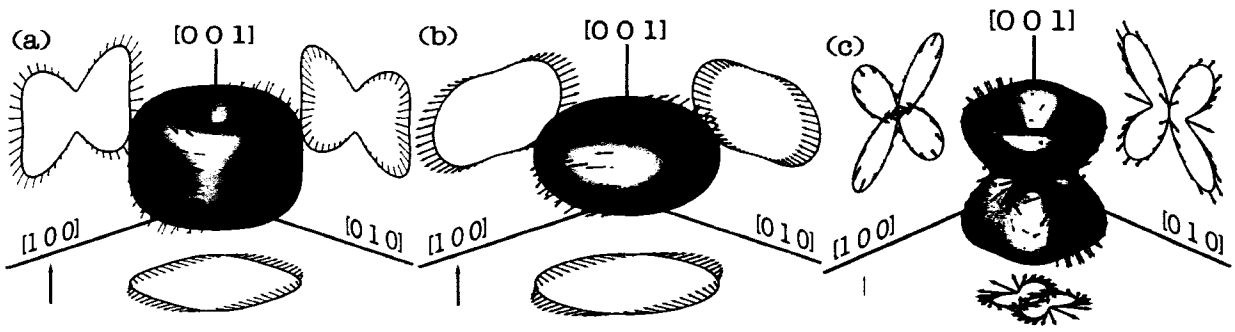

Figure 5.2: (colour) (a) Calculated $\hat{\mathbf{k}}$-space distributions of photoexcited electrons in unstrained GaAs with excess photon energy 300 meV. The surface represents the injected carrier density, $N(\hat{\mathbf{k}})$; the radius of the surface in any direction $\hat{\mathbf{k}}$ is proportional to $N(\hat{\mathbf{k}})$. The vectors affixed to the surface give the degree of spin polarization, $\mathbf{s}(\hat{\mathbf{k}})$, of electrons excited with crystal momentum in the direction $\hat{\mathbf{k}}$. The cross sections through the centers of the distributions, along with the projection of spins on the cross sections, have been displaced to aid visualization. (b) and (c) are as in (a), but at 20 meV excess photon energy and for 1% tensile and compressive strains respectively. The reference spin in the lower left corner of each panel is $0.25\hbar/2$.

than the heavy hole band. The calculated splitting between heavy- and light-hole bands at the Γ point is 84 meV for tensile strain and 69 meV for compressive strain.

Note that in Eq. (5.3) I have assumed that $\mathbf{v}$ and $\mathbf{S}$ commute. This is no longer true when the anomalous velocity term, $\hbar(\boldsymbol{\sigma} \times \boldsymbol{\nabla} V) / (4m^2c^2)$, is included in $\mathbf{v}$. The linear PSC I have described here does not require that term, in contrast to other effects [55, 64]. In fact, I have neglected the anomalous velocity (see Appendix B).

While the calculations of ballistic PSCs that I have presented here are appropriate for bulk semiconductors, larger PSCs might be possible in heterostructures, which can be prepared with large structural asymmetry. As well, I note that since only linear absorption is involved, this effect could be studied even with CW beams, and in nanostructures, where short spin transport distances could still have significant consequences.

In a material with low enough symmetry, one-photon absorption of circularly polarized light can generate a ballistic current without an applied voltage [99]; this so-called circular photogalvanic effect (CPGE) is a SPEC [116, 197]. It is tempting to understand the linear PSC as a superposition of opposite SPECs due to two fields with opposite helicity. However, the CPGE cannot occur in crystals with zinc-blende symmetry, although it can in wurtzite CdSe [198] and strained GaAs [199]. It is worth noting that in addition to describing the linear PSC, the spin-current response pseudotensor in Eq. (5.3) can also describe the SPEC due to the CPGE.

Finally, I point out that a PSC can be generated even with unpolarized light. Averaging over polarization directions in a plane, one obtains $K^{ij} = \int E_\omega^2 dt' \sum_{l,m} \left(\delta^{lm} - \hat{n}^l \hat{n}^m\right) \mu_{(1)}^{ijlm}/2$, where $\hat{n}$ is the propagation direction of the light. This PSC is smaller than that due to linearly polarized light. In materials with T_d symmetry, the PSC due to unpolarized light incident along a cubic axis is smaller by a factor of two than the PSC due to light polarized along a cubic axis.

Chapter 6

Two-colour Quantum Interference: Excitonic Effects

6.1 Introduction

Chapters 2 and 3 establish that quantum interference between one- and two-photon transition amplitudes allows for the control of carrier population, carrier spin polarization, photocurrent injection, and spin-current injection. The experimenter can control these processes by adjusting the phases of the optical fields.

But the controllable optical phases are not the only source of phase between the transition amplitudes. In general, there is also a material-dependent intrinsic phase [200]. Phenomenologically, the intrinsic phase appears as a phase shift in the dependence of the process on a relative phase parameter of the optical fields. Additionally, selectivity between two processes is possible when their intrinsic phases differ [201]; for example, "1+3" experiments on diatomic molecules have controlled the branching ratio of ionization and dissociation channels [202]. The intrinsic phase can be strongly frequency-dependent near resonances [202], and the hope that it might serve as a new spectroscopic observable [203, 204] has led to efforts to understand its physical origin.

Whereas a resonance is necessary for a phase shift to a "1+3" process [203], it is not necessary for a phase shift to a "1+2" process. For example, an intrinsic phase in the "1+2" photoionization of atoms is predicted from the simple model of a δ-function potential [205, 206].

Nevertheless, microscopic theories for the interband "1 + 2" processes in bulk semiconductors, including those in Chapters 2 and 3, have predicted trivial intrinsic phases [3, 36]. The photocurrent, for example, was predicted to be proportional to the sine of the relative phase parameter for all final energies [3]. Each of these theories uses the independent-particle approximation, in which the Coulomb attraction between the injected electron and hole is neglected.

That approximation is expected to be good for final energies well above the band gap, since in this case the electron and hole travel quickly away from each other. However, close to the band gap, one generally expects to see deviations from the independent-particle approximation. In the one-photon absorption spectrum, for instance, it is well known that the electron-hole attraction is responsible for exciton lines below the band gap, and for an enhancement of the absorption above the gap known as *Sommerfeld* or *Coulomb enhancement* [104].

The effect of the electron-hole attraction on one-photon absorption has been studied with various degrees of sophistication. On the one hand, modern *ab initio* calculations that include Coulomb effects have recently given very good quantitative agreement with experimental spectra [207–211], although at the cost of significant computational overhead. On the other hand, simple models of Wannier excitons can describe Coulomb effects near the band edge of many direct-gap semiconductors. These excitonic effects have long been understood qualitatively on the basis of a simple two-band model in the effective mass approximation [212], which is even quantitatively accurate for typical semiconductors [210]. Excitonic effects on one-photon current injection (the circular photogalvanic effect) were studied by Shelest and Éntin [98, 213].

Excitonic effects on nonlinear optical properties of bulk semiconductors have also been studied in the effective mass, Wannier exciton approximation [107, 174, 176, 183–186, 214–220], and only recently with *ab initio* methods [109]. The two-photon absorption spectrum shows a different set of exciton lines and a Coulomb enhancement that is weaker than its one-photon counterpart.

One- and two-photon absorption spectra have been measured sufficiently often that excitonic effects on them are well established. In contrast, semiconductor "1+2" interference experiments have been done typically at only a single energy and typically many exciton binding energies above the band gap. Moreover, these initial experiments lacked an absolute calibration of the relative optical phase, and thus were insensitive to the intrinsic phase. With such a calibration, which is technically possible [221], one could verify the predictions I present here. A nontrivial intrinsic phase would have implications for the use of "1 + 2" current injection as an absolute measurement of the carrier-envelope phase of an ultrashort optical pulse [72, 77, 78].

In this chapter, I extend the theory of "1+2" coherent control of bulk semiconductor interband transitions beyond the independent-particle approximation to include the electron-hole interaction. The focus is on photon energies that excite carriers above the band edge, but close enough to it so that transition amplitudes based on low-order expansions in $\mathbf{k}$ are applicable. Consistent with the rest of this thesis, I use a perturbative treatment in the fields. In this limit of low photoinjected carrier density, the only interparticle interaction of importance is that between a single electron and hole. I show that, due to the electron-hole attraction, a nontrivial phase shift does in fact occur in the control of current and spin current, but not in

the control of carrier population or spin polarization. The intrinsic phase can be understood in terms of partial-wave phase shifts due to the Coulomb potential between electron and hole. In addition, I find an enhancement of each process, and relate it to the Coulomb enhancements of one- and two-photon absorption.

In the next section, I establish notation necessary to describe the "1+2" processes in terms of one- and two-photon transition amplitudes. In Sec. 6.3, I present the microscopic model. The transition amplitudes are worked out in Sec. 6.4. The final expressions for the "1+2" effects are given in Sec. 6.5, and numerical results for GaAs are presented. In Sec. 6.6, further understanding of the enhancement and intrinsic phase is discussed, and I examine the ratios often used as figures of merit for "1+2" effects. Intermediate-state Coulomb enhancement is examined in Appendix E.

6.2 Preliminaries

In Sec. 2.1, I derived a microscopic expression for the optical injection of a quantity $\langle\hat{\theta}\rangle$, which could stand for current density, population density, spin-current density, or spin density. When the carrier-carrier Coulomb interaction is included, a similar microscopic expression can be derived, but instead of Bloch states, the expression contains eigenstates of a Hamiltonian that includes the carrier-carrier Coulomb interaction. These final states in the Fermi's golden rule (FGR) calculation will be specified in detail in the next section. For the present discussion, I write them as $|n\rangle$, having velocity $\mathbf{v}_{nn}$, probability amplitude $c_n(t)$, and energy $\hbar\omega_n$ above the ground state. With this generality, the label n can represent the set of quantum numbers for either an interacting or independent electron-hole pair.

The derivation follows Sec. 2.1, with the result that

$$\begin{aligned}\frac{d}{dt}\langle\hat{\Theta}\rangle &= \frac{1}{L^3}\sum_{n,n'}\langle n|\hat{\Theta}|n'\rangle\frac{d}{dt}c_{n'}(t)c_n^*(t)\\ &= \frac{2\pi}{L^3}\sum_{n,n'}{}'\langle n|\hat{\Theta}|n'\rangle\left[\Omega_{n'}^{(1)}+\Omega_{n'}^{(2)}\right]\left[\left(\Omega_n^{(1)}\right)^*+\left(\Omega_n^{(2)}\right)^*\right]\delta\left(2\omega-\omega_n\right)\\ &= \frac{2\pi}{L^3}\sum_{n,n'}{}'\langle n|\hat{\Theta}|n'\rangle\left\{\left(\Omega_n^{(1)}\right)^*\Omega_{n'}^{(1)}+\left(\Omega_n^{(2)}\right)^*\Omega_{n'}^{(2)}+\left(\Omega_n^{(1)}\Omega_n^{(2)*}+c.c.\right)\right\}\delta\left(2\omega-\omega_n\right),\end{aligned} \tag{6.1}$$

where the prime on the summation indicates a restriction to terms satisfying $\omega_n=\omega_{n'}$, L^3 is a normalization volume, and $\Omega_n^{(i)}$ is the amplitude for an i-photon transition. The $\Omega_n^{(i)}$ take the

form

$$\Omega_n^{(1)} = \mathbf{E}_{2\omega} \cdot \mathbf{D}_n^{(1)} \tag{6.2}$$

$$\Omega_n^{(2)} = \mathbf{E}_{\omega}\mathbf{E}_{\omega} : \mathrm{D}_n^{(2)}, \tag{6.3}$$

where the vector $\mathbf{D}_n^{(1)}$ and second-rank tensor $\mathrm{D}_n^{(2)}$ depend only on properties of the material. The transition amplitudes are given in detail in Sec. 6.4.

Recall from Sec. 2.2.1 that the rate of photocurrent injection into an unbiased bulk semiconductor by a two-colour light field $\mathbf{E}(t) = \mathbf{E}_{\omega}\exp(-i\omega t) + \mathbf{E}_{2\omega}\exp(-i2\omega t) + c.c.$ can be written

$$\frac{dJ_{(I)}^i}{dt} = \eta_{(I)}^{ijkl} E_{\omega}^{*j} E_{\omega}^{*k} E_{2\omega}^{l} + c.c., \tag{6.4}$$

where superscripts denote Cartesian components and repeated indices are to be summed over [3]. The fourth-rank current-injection tensor, $\eta_{(I)}^{ijkl}$, is purely imaginary in the independent-particle approximation [3], but can be complex in general. I define the intrinsic phase δ^{ijkl} of the component $\eta_{(I)}^{ijkl}$ as

$$\delta^{ijkl} = \arctan\left[\frac{\mathrm{Re}\left(\eta_{(I)}^{ijkl}\right)}{\mathrm{Im}\left(\eta_{(I)}^{ijkl}\right)}\right], \tag{6.5}$$

so that it is zero or π in the independent-particle approximation. When the electron-hole interaction is included in the set of approximations used here, all the components of $\eta_{(I)}$ have the same phase. That is,

$$\eta_{(I)}^{ijkl} = ie^{i\delta}\left|\eta_{(I)}^{ijkl}\right|. \tag{6.6}$$

The intrinsic phase δ appears as a phase shift in the dependence of the current injection on the phase of the optical fields. For co-linearly polarized fields [$\mathbf{E}_{\omega} = E_{\omega}\exp(i\phi_{\omega})\hat{\mathbf{x}}$ and $\mathbf{E}_{2\omega} = E_{2\omega}\exp(i\phi_{2\omega})\hat{\mathbf{x}}$], for example, the current injection is

$$\frac{d\mathbf{J}_{(I)}}{dt} = 2E_{\omega}^2 E_{2\omega}\left|\eta_{(I)}^{xxxx}\right|\sin\left(2\phi_{\omega} - \phi_{2\omega} - \delta\right)\hat{\mathbf{x}}.$$

Consistent with the rest of this thesis, this discussion is predicated on a conceptual separation of the injection and relaxation processes. I focus on the former, but note that Coulomb effects other than the excitonic effects considered here play a role in scattering, especially at high densities of excited carriers. Such Coulomb effects, which are outside the scope of this thesis, have been recently studied in lower dimensional systems [56, 58, 59]. A comparison of (6.1) with (6.4) yields

$$\eta_{(I)}^{ijkl} = \frac{2\pi e}{L^3}\sum_n v_{nn}^i \left(D_n^{(2)*}\right)^{jk}\left(D_n^{(1)}\right)^l \delta\left(2\omega - \omega_n\right). \tag{6.7}$$

Recall from Sec. 2.2.2 that the carrier injection rate can be written in terms of one- and two-photon absorption tensors $\xi_{(1)}^{ij}$ and $\xi_{(2)}^{ijkl}$, and a "1+2" population control tensor $\xi_{(I)}^{ijk}$. Using

6.1, 6.2, and 6.3,

$$\xi_{(1)}^{ij} = \frac{2\pi}{L^3} \sum_n \left(D_n^{(1)*} \right)^i \left(D_n^{(1)} \right)^j \delta \left(2\omega - \omega_n \right), \tag{6.8}$$

$$\xi_{(2)}^{ijkl} = \frac{2\pi}{L^3} \sum_n \left(D_n^{(2)*} \right)^{ij} \left(D_n^{(2)} \right)^{kl} \delta \left(2\omega - \omega_n \right), \tag{6.9}$$

and

$$\xi_{(I)}^{ijk} = \frac{2\pi}{L^3} \sum_n \left(D_n^{(2)*} \right)^{ij} \left(D_n^{(1)} \right)^k \delta \left(2\omega - \omega_n \right). \tag{6.10}$$

They are purely real in the independent-particle approximation.

Recall from Sec. 2.2.3 that "1+2" spin-current injection can be written in terms of a pseudotensor $\zeta_{(I)}^{ijkl}$, and recall from Sec. 2.2.4 that "1+2" spin-current injection can be written in terms of a pseudotensors $\mu_{(I)}^{ijklm}$. In the independent-particle approximation, $\zeta_{(I)}^{ijkl}$ is purely imaginary [66], while $\mu_{(I)}^{ijklm}$ is purely real [33]. They are complex in general; hence, one can define their intrinsic phases with equations such as (6.5).

The phases of the material response tensors $\eta_{(I)}$, $\xi_{(I)}$, $\mu_{(I)}$, and $\zeta_{(I)}$ are related to the phases of the one- and two-photon matrix elements, $\mathbf{D}_n^{(1)}$ and $\mathsf{D}_n^{(2)}$. The one- and two-photon matrix elements also appear, respectively, in the one- and two-photon absorption coefficients, as can be seen from (6.8) and (6.9). There have been many theoretical investigations of one- and two-photon absorption near the direct gap of bulk semiconductors that include excitonic effects [222, 223]. However, since one- and two-photon absorptions are insensitive to the phases of the transition amplitudes, those calculations took no care to get the phases of the transition amplitudes correct. In the next two sections I derive expressions for the transition amplitudes with the correct phases, including excitonic effects.

6.3 Model

The first part of this section reviews the two-band effective-mass model of Wannier excitons; the two bands are nondegenerate conduction and valence bands that are parabolic and isotropic with a direct gap E_{cv}^g at $\mathbf{k} = \mathbf{0}$ (the Γ point) [103, 224]. This model has been used to study excitonic effects on one-photon absorption [212], two-photon absorption [176], and other nonlinear optical processes [214–220]. I subsequently describe a generalization that accounts for degeneracy and multiple bands. It has been used for two-photon absorption [174], and has been implicit whenever two-band results have been applied to actual semiconductors.

The total Hamiltonian of the system can be written in the form $H = H_B + H_C + H_{\text{int}}(t)$. Here, $H_0 = H_B + H_C$ is the field-free Hamiltonian made up of the single-particle part H_B and the part due to the Coulomb interaction between carriers H_C, and $H_{\text{int}}(t)$ is the interaction Hamiltonian in the velocity gauge. Compared to preceding chapters, only H_C is new.

The initial state is the "vacuum" $|0\rangle$; it corresponds to completely filled valence bands and empty conduction bands. If the Coulomb interaction were neglected in a two-band model consisting of valence (v) and conduction (c) bands, the final states would be of the form $a^\dagger_{c\mathbf{k}} a_{v\mathbf{k}} |0\rangle$, where the operator $a^\dagger_{n\mathbf{k}}$ creates an electron in an eigenstate of H_B, a Bloch state $|n, \mathbf{k}\rangle$ with band index n and wave vector $\mathbf{k}$ (see Sec. 2.1). The photon momentum has been neglected, consistent with the long-wavelength approximation. The Coulomb interaction couples states at different $\mathbf{k}$; thus, accounting for H_C, the final states are of the form

$$|cv\boldsymbol{\kappa}\rangle \equiv \sum_{\mathbf{k}} A^{\boldsymbol{\kappa}}_{cv}(\mathbf{k})\, a^\dagger_{c\mathbf{k}} a_{v\mathbf{k}} |0\rangle\,, \tag{6.11}$$

where $\boldsymbol{\kappa}$ labels the state; its physical meaning is given below. In the effective mass Wannier exciton approximation, the Fourier transform

$$\psi^{\boldsymbol{\kappa}}_{cv}(\mathbf{r}) = \sum_{\mathbf{k}} A^{\boldsymbol{\kappa}}_{cv}(\mathbf{k})\, e^{i\mathbf{k}\cdot\mathbf{r}}, \tag{6.12}$$

which is the wave function for the relative coordinate between electron and hole, is a hydrogenic wave function satisfying

$$-\frac{\hbar^2}{2m_{cv}}\nabla^2\psi^{\boldsymbol{\kappa}}_{cv}(\mathbf{r}) - V_C(r)\psi^{\boldsymbol{\kappa}}_{cv}(\mathbf{r}) = \left[E_{cv}(\boldsymbol{\kappa}) - E^g_{cv}\right]\psi^{\boldsymbol{\kappa}}_{cv}(\mathbf{r}), \tag{6.13}$$

where $m_{cv}^{-1} = m_c^{-1} + m_v^{-1}$ is the reduced mass in terms of the (positive) conduction- and valence-band effective masses, and $V_C(r)$ is the Coulomb potential, $V_C(r) = e^2/(\epsilon r)$, screened by the static dielectric constant ϵ [104, 178, 212]. The state has energy

$$E_{cv}(\boldsymbol{\kappa}) = \frac{\hbar^2\kappa^2}{2m_{cv}} + E^g_{cv}.$$

I choose the states to be normalized over the volume L^3 by $\langle m, \mathbf{k}|n, \mathbf{k}'\rangle = \delta_{n,m}\delta_{\mathbf{k},\mathbf{k}'}$ and $\langle cv\boldsymbol{\kappa}|cv\boldsymbol{\kappa}'\rangle = \delta_{\boldsymbol{\kappa},\boldsymbol{\kappa}'}$; as a result $\psi^{\boldsymbol{\kappa}}_{cv}(\mathbf{r})$ is unitless, having the normalization $\int d^3r\, [\psi^{\boldsymbol{\kappa}}_{cv}(\mathbf{r})]^*\, \psi^{\boldsymbol{\kappa}'}_{cv}(\mathbf{r}) = L^3\delta_{\boldsymbol{\kappa},\boldsymbol{\kappa}'}$.

The focus of this chapter is on the unbound solutions to (6.13); bound-exciton states lack relative velocity between the electron and hole, and hence do not contribute to the ballistic current injection or spin-current injection. For a FGR calculation of the current injection or spin-current injection, the unbound state must behave asymptotically like an outgoing plane wave in the relative coordinate between electron and hole; $\boldsymbol{\kappa}$ is the wave vector of the outgoing plane wave. Specifically, one must use "ionization states" rather than scattering states [225], as was done for atomic "1+2" ionization [205]. They are related by $[\psi^{\boldsymbol{\kappa}}_{cv}(\mathbf{r})]_{\text{ion}} = \{[\psi^{-\boldsymbol{\kappa}}_{cv}(\mathbf{r})]_{\text{scatt}}\}^*$ [226]. Calculations of one- or two-photon absorption are insensitive to an error in this choice of boundary condition, but the present calculation is not, since it is sensitive to the relative phase of the transition amplitudes.

The ionization state wave functions that solve (6.13) can be expressed as a sum over partial waves,

$$\psi_{cv}^{\boldsymbol{\kappa}}(\mathbf{r}) = e^{\frac{\pi}{2a_{cv}\kappa}} \sum_{l=0}^{\infty} \frac{\Gamma\left(l+1+\frac{i}{a_{cv}\kappa}\right)}{(2l)!} (2i\kappa r)^l e^{-i\kappa r} P_l\left(\frac{\mathbf{r}\cdot\boldsymbol{\kappa}}{r\kappa}\right) {}_1F_1\left(l+1+\frac{i}{a_{cv}\kappa}; 2l+2; 2i\kappa r\right), \tag{6.14}$$

where $a_{cv} \equiv \epsilon\hbar^2/\left(m_{cv}e^2\right)$ is the exciton Bohr radius, and κ and r mean $|\boldsymbol{\kappa}|$ and $|\mathbf{r}|$.[1] The P_l are Legendre polynomials, ${}_1F_1$ is a confluent hypergeometric function, and Γ is the Gamma function.

Such a two-band model of Wannier excitons is useful for the description of many optical properties. However, near the band gap at the Γ point of a typical zinc-blende semiconductor there are, counting spin, eight bands (Fig. 2.1): two each of conduction (c), heavy hole (hh), light hole (lh) and split-off hole (so). Other bands, especially the next-higher conduction bands (Fig. 3.1), can also be important for some processes, especially for population and spin control.

The existence of multiple bands and band degeneracy modifies the exciton Hamiltonian, i.e., the operator acting on $\psi_{cv}^{\boldsymbol{\kappa}}(\mathbf{r})$ in the left side of (6.13). In the effective-mass approximation, using a basis of Γ-point states, the kinetic part of the Wannier exciton Hamiltonian has a matrix structure [228, 229]. Even though this approximation neglects band warping, nonparabolicity, and inversion asymmetry, the Hamiltonian lacks analytic eigenstates [229]. This is essentially due to the degeneracy of the hh and lh bands at the Γ point. As a result of the difference between m_{hh} and m_{lh} there is "envelope-hole coupling," [230] which is a spin-orbit-like coupling between the orbital angular momentum of the exciton envelope function and the total angular momentum of the valence band Γ-point Bloch functions [140]. Baldereschi and Lipari split the effective-mass Hamiltonian into a sum of terms based on symmetry, and showed that in a spherical approximation the envelope-hole coupling could be treated as a perturbation to the diagonal part, which has analytic, hydrogenic eigenstates [177, 178]. In order to extract the main physics, while preserving the simplicity of the two-band model, I neglect envelope-hole coupling entirely. In this approximation, (6.13) remains valid for each conduction-valence band pair, however one must use "average" effective masses for degenerate bands. Specifically, the effective mass of the valence bands hh, lh, and so is m/γ_{1L}, where m is the free-electron mass, and γ_{1L} is one of the Luttinger parameters [178]. The upper conduction bands have a different average effective mass. Note that $\psi_{cv}^{\boldsymbol{\kappa}}(\mathbf{r})$ is independent of c and v within the set of bands $\{c, hh, lh, so\}$. The effect of envelope-hole coupling has been studied for bound-exciton states [177, 178, 186], but not for optical processes involving unbound excitons in the continuum.

Even within this model, the presence of multiple bands provides two types of terms in

[1] This follows from the relation between ionization and scattering states, and the scattering states given in, e.g., Schiff [227].

the sum over intermediate states in the two-photon amplitude: two-band terms, in which the intermediate and final states are in the same exciton series [i.e., two states of the form (6.11) with the same c and v], and three-band terms, in which the intermediate and final states are in different series. Three-band terms are important for some processes but not for others. For current control, three-band terms are important for cross-linearly polarized fields (see Sec. 3.3), and for spin-current control, they are important for the spin current due to colinearly polarized fields (see Sec. 2.4). Three-band terms are essential for population and spin control (see Sec. 3.4 and Sec. 3.6).

The velocity matrix elements involving the state $|cv\boldsymbol{\kappa}\rangle$ are

$$\langle cv\boldsymbol{\kappa}|\,\mathbf{v}\,|0\rangle = \sum_{\mathbf{k}} \left[A^{\boldsymbol{\kappa}}_{cv}\left(\mathbf{k}\right)\right]^{*} \mathbf{v}_{cv}\left(\mathbf{k}\right), \tag{6.15}$$

$$\langle cv\boldsymbol{\kappa}|\,\mathbf{v}\,|c'v'\boldsymbol{\kappa}'\rangle = \sum_{\mathbf{k}} \left[A^{\boldsymbol{\kappa}}_{cv}\left(\mathbf{k}\right)\right]^{*} A^{\boldsymbol{\kappa}'}_{c'v'}\left(\mathbf{k}\right)\left[\mathbf{v}_{cc'}\left(\mathbf{k}\right)\delta_{v,v'} - \mathbf{v}_{v'v}\left(\mathbf{k}\right)\delta_{c,c'}\right], \tag{6.16}$$

where $\mathbf{v}_{nm}\left(\mathbf{k}\right) \equiv \langle n,\mathbf{k}|\,\mathbf{v}\,|m,\mathbf{k}\rangle$ is the velocity matrix element between Bloch states.

6.4 Transition amplitudes

The transition amplitudes in the independent-particle approximation are presented in (2.3) and (2.3). Here, I rename them $\Omega^{(1\text{-free})}_{cv\boldsymbol{\kappa}}$ and $\Omega^{(2\text{-free})}_{cv\boldsymbol{\kappa}}$, and use $\boldsymbol{\kappa}$ instead of $\mathbf{k}$ in preparation for a comparison with the transition amplitudes with excitonic effects included. Thus,

$$\Omega^{(1\text{-free})}_{cv\boldsymbol{\kappa}} = i\frac{e}{2\hbar\omega}\mathbf{E}_{2\omega}\cdot\mathbf{v}_{cv}\left(\boldsymbol{\kappa}\right), \tag{6.17}$$

and $\Omega^{(2\text{-free})}_{cv\boldsymbol{\kappa}} = \sum_{c',v'}\Omega^{(2\text{-free})}_{cc'vv'\boldsymbol{\kappa}}$, where

$$\Omega^{(2\text{-free})}_{cc'vv'\boldsymbol{\kappa}} \equiv \left(\frac{e}{\hbar\omega}\right)^{2} \frac{\left\{\mathbf{E}_{\omega}\cdot\left[\mathbf{v}_{cc'}\left(\boldsymbol{\kappa}\right)\delta_{v,v'} - \delta_{c,c'}\mathbf{v}_{v'v}\left(\boldsymbol{\kappa}\right)\right]\right\}\left(\mathbf{E}_{\omega}\cdot\mathbf{v}_{c'v'}\left(\boldsymbol{\kappa}\right)\right)}{E_{c'v'}\left(\boldsymbol{\kappa}\right)/\hbar - \omega}. \tag{6.18}$$

With excitonic effects included, using the perturbation $H_{\text{int}}\left(t\right)$ to second order gives the transition amplitudes

$$\Omega^{(1)}_{cv\boldsymbol{\kappa}} = \frac{ie}{2\hbar\omega}\mathbf{E}_{2\omega}\cdot\langle cv\boldsymbol{\kappa}|\,\mathbf{v}\,|0\rangle, \tag{6.19}$$

and

$$\Omega^{(2)}_{cv\boldsymbol{\kappa}} = \left(\frac{e}{\hbar\omega}\right)^{2} \sum_{c'v'\boldsymbol{\kappa}'} \frac{\left(\mathbf{E}_{\omega}\cdot\langle cv\boldsymbol{\kappa}|\,\mathbf{v}\,|c'v'\boldsymbol{\kappa}'\rangle\right)\left(\mathbf{E}_{\omega}\cdot\langle c'v'\boldsymbol{\kappa}'|\,\mathbf{v}\,|0\rangle\right)}{E_{c'v'}\left(\boldsymbol{\kappa}'\right)/\hbar - \omega}, \tag{6.20}$$

where the sum over intermediate states is over both bound and free excitons. The two-photon transition amplitude is more difficult to deal with due to the sum over intermediate states; however, in the set of approximations described in Sec. 6.3, it has been done exactly [174, 176, 184].

In order to proceed analytically, it is common to use (6.15) and (6.16), and then make an expansion in $\mathbf{k}$ of the velocity matrix elements $\mathbf{v}_{nm}(\mathbf{k})$ about the Γ point [104, 174, 176, 183, 184, 212]. However, due to the degeneracy at the Γ point, the coefficients of such an expansion can depend on the direction of $\mathbf{k}$ [120]. To proceed, I note that Wannier excitons have large spatial extent and hence only a small region of wave vectors is important for them, i.e., $A_{cv}^{\boldsymbol{\kappa}}(\mathbf{k})$ is peaked in the region of $\mathbf{k}$ near $\boldsymbol{\kappa}$ [224]. This is especially true for final states with energies above the band gap. Thus, I expand $\mathbf{v}_{nm}(\mathbf{k})$ about the Γ point, approached in the direction $\hat{\boldsymbol{\kappa}}$,

$$v_{nm}^{i}(\mathbf{k}) = v_{nm}^{i}(\hat{\boldsymbol{\kappa}}) + \mathbf{k}\cdot\boldsymbol{\nabla}_{\mathbf{k}} v_{nm}^{i}(\hat{\boldsymbol{\kappa}}) + \ldots, \tag{6.21}$$

where $v_{nm}^{i}(\hat{\boldsymbol{\kappa}}) \equiv \lim_{\lambda\to 0}\langle n,\Gamma|\,\mathbf{v}\,|m,\lambda\boldsymbol{\kappa}\rangle$ and $\boldsymbol{\nabla}_{\mathbf{k}} v_{nm}^{i}(\hat{\boldsymbol{\kappa}}) \equiv \lim_{\lambda\to 0}\boldsymbol{\nabla}_{\boldsymbol{\kappa}}\langle n,\Gamma|\,\mathbf{v}\,|m,\lambda\boldsymbol{\kappa}\rangle$.

Optical transitions due to the first term in (6.21) are called "allowed", while those due to the second term are called "forbidden". In this thesis, I do not consider materials for which the allowed valence to conduction band transition vanishes. Keeping only the allowed term in (6.15),[212]

$$\langle cv\boldsymbol{\kappa}|\,\mathbf{v}\,|0\rangle = \mathbf{v}_{cv}(\hat{\boldsymbol{\kappa}})\;\left[\psi_{cv}^{\boldsymbol{\kappa}}(\mathbf{r}=\mathbf{0})\right]^{*}. \tag{6.22}$$

For the intravalence and intraconduction band transitions, the first two terms of (6.21) in (6.16) give [184]

$$\begin{aligned}\langle cv\boldsymbol{\kappa}|\,\mathbf{v}\,|c'v'\boldsymbol{\kappa}'\rangle = {}& \left[\delta_{v,v'}\mathbf{v}_{cc'}(\hat{\boldsymbol{\kappa}}) - \delta_{c,c'}\mathbf{v}_{v'v}(\hat{\boldsymbol{\kappa}})\right]\int\frac{d^3r}{L^3}\left[\psi_{cv}^{\boldsymbol{\kappa}}(\mathbf{r})\right]^{*}\psi_{c'v'}^{\boldsymbol{\kappa}'}(\mathbf{r})\\ &-\left[\delta_{v,v'}\boldsymbol{\nabla}_{\mathbf{k}} v_{cc'}^{i}(\hat{\boldsymbol{\kappa}}) - \delta_{c,c'}\boldsymbol{\nabla}_{\mathbf{k}} v_{v'v}^{i}(\hat{\boldsymbol{\kappa}})\right] i\int\frac{d^3r}{L^3}\left[\psi_{cv}^{\boldsymbol{\kappa}}(\mathbf{r})\right]^{*}\boldsymbol{\nabla}\psi_{c'v'}^{\boldsymbol{\kappa}'}(\mathbf{r}).\end{aligned} \tag{6.23}$$

In particular [184, 231],

$$\langle cv\boldsymbol{\kappa}|\,\mathbf{v}\,|cv\boldsymbol{\kappa}\rangle = \sum_{\mathbf{k}}\left[A_{cv}^{\kappa}(\mathbf{k})\right]^{*}A_{cv}^{\kappa}(\mathbf{k})\,\frac{\hbar}{m_{cv}}\mathbf{k} = -i\frac{\hbar}{m_{cv}}\int\frac{d^3r}{L^3}\left[\psi_{cv}^{\kappa}(\mathbf{r})\right]^{*}\nabla_{\mathbf{r}}\psi_{cv}^{\kappa}(\mathbf{r}) = \hbar\boldsymbol{\kappa}/m_{cv}. \tag{6.24}$$

For Ge and for simple models of zinc-blende semiconductors that neglect lack of inversion symmetry, the first term in (6.23) always vanishes. This means that there are only allowed-forbidden two-photon transitions (the interband transition is allowed, while the intraband transition is forbidden). When the first term is nonvanishing, there are allowed-allowed two-photon transitions.[2]

I write $\Omega_{cv\boldsymbol{\kappa}}^{(2)} = \Omega_{cv\boldsymbol{\kappa}}^{(2:\text{a-f})} + \Omega_{cv\boldsymbol{\kappa}}^{(2:\text{a-a})}$, and discuss the allowed-forbidden and allowed-allowed transitions separately.

[2]In principle, for noncentrosymmetric materials, there is also a small contribution to the allowed-forbidden two-photon transition from the first term in (6.23) and the term in $\langle cv\boldsymbol{\kappa}|\,\mathbf{v}\,|0\rangle$ that comes from the second term in (6.21); I neglect it in what follows, but note that when compared to the dominant allowed-forbidden contribution that is considered here, it has a different Coulomb enhancement but the same intrinsic phase (see Eq. 2.32 of Rustagi *et al.* [184]).

Using (6.14), (6.22), and (6.19), the one-photon transition amplitude is [212]

$$\Omega_{cv\boldsymbol{\kappa}}^{(1)} = \Omega_{cv\boldsymbol{\kappa}}^{(1\text{-free})} \exp\left(\frac{\pi}{2a_{cv}\kappa}\right) \Gamma\left(1 - \frac{i}{a_{cv}\kappa}\right), \tag{6.25}$$

where only the allowed term is kept in $\Omega_{cv\boldsymbol{\kappa}}^{(1\text{-free})}$.[3] The transition is to an s wave. The one-photon absorption coefficient is proportional to the norm of $\Omega_{cv\boldsymbol{\kappa}}^{(1)}$ [see Chapter 2] [212].

For allowed-forbidden two-photon transitions, substituting (6.22) and the second term of (6.23) into (6.20),

$$\Omega_{cv\boldsymbol{\kappa}}^{(2\text{:a-f})} = \frac{e^2}{\omega^2\hbar} \sum_{c'v'} \left[\mathbf{E}_\omega \cdot \mathbf{v}_{c'v'}\left(\hat{\boldsymbol{\kappa}}\right)\right] E_\omega^i \left[\delta_{v,v'} \boldsymbol{\nabla}_{\mathbf{k}} v_{cc'}^i\left(\hat{\boldsymbol{\kappa}}\right) - \delta_{c,c'} \boldsymbol{\nabla}_{\mathbf{k}} v_{v'v}^i\left(\hat{\boldsymbol{\kappa}}\right)\right] \cdot \mathbf{M}_{cc'vv'}\left(\boldsymbol{\kappa}\right), \tag{6.26}$$

where

$$\mathbf{M}_{cc'vv'}\left(\boldsymbol{\kappa}\right) \equiv -i \int d^3r \left[\psi_{cv}^{\boldsymbol{\kappa}}\left(\mathbf{r}\right)\right]^* \boldsymbol{\nabla} G_{c'v'}\left(\mathbf{r}, \mathbf{0}; \hbar\omega - E_{c'v'}^g\right), \tag{6.27}$$

and the Coulomb Green function,

$$G_{cv}\left(\mathbf{r}, \mathbf{r}'; \Omega\right) = \frac{1}{L^3} \sum_{\boldsymbol{\kappa}} \frac{\psi_{cv}^{\boldsymbol{\kappa}}(\mathbf{r}) \left[\psi_{cv}^{\boldsymbol{\kappa}}(\mathbf{r}')\right]^*}{E_{cv}\left(\kappa\right) - E_{cv}^g - \Omega},$$

is known analytically [176]. In particular,

$$G_{cv}(\mathbf{r}, \mathbf{0}; \hbar\omega - E_{cv}^g) = \frac{m_{cv}}{2\pi r\hbar^2} \Gamma\left(1 - \gamma_{cv}\right) W_{\gamma_{cv},\frac{1}{2}}\left(\frac{2r}{a_{cv}\gamma_{cv}}\right), \tag{6.28}$$

where I define

$$\gamma_{cv} \equiv \sqrt{\frac{B_{cv}}{E_{cv}^g - \hbar\omega}},$$

$B_{cv} = \hbar^2/\left(2m_{cv}a_{cv}^2\right)$ is the exciton binding energy, and $W_{\gamma,1/2}\left(z\right)$ is a Whittaker function with the integral representation

$$W_{\gamma,1/2}\left(z\right) = \frac{ze^{-\frac{z}{2}}}{\Gamma\left(1-\gamma\right)} \int_0^\infty dt \left(\frac{1+t}{t}\right)^\gamma e^{-zt}. \tag{6.29}$$

Since the Green function depends only on the magnitude of $\mathbf{r}$, only the p wave of the final state survives the integral in Eq. (6.27) over the angles of $\mathbf{r}$, $\int d\Omega P_1\left(\hat{\mathbf{r}} \cdot \hat{\boldsymbol{\kappa}}\right) \hat{\mathbf{r}} = 4\pi\hat{\boldsymbol{\kappa}}/3$. The integral over r can be done using [176]

$$\int_0^\infty r^{\sigma-1} e^{-pr} {}_1F_1\left(\alpha; \sigma; \lambda r\right) dr = \Gamma\left(\sigma\right) \frac{p^{\alpha-\sigma}}{\left(p-\lambda\right)^\alpha}. \tag{6.30}$$

The final result is

$$\Omega_{cv\boldsymbol{\kappa}}^{(2\text{:a-f})} = \exp\left(\frac{\pi}{2a_{cv}\kappa}\right) \Gamma\left(2 - \frac{i}{a_{cv}\kappa}\right) \sum_{c'v'} N_{cc'vv'}^{(\text{a-f})}\left(\kappa\right) \Omega_{cc'vv'\boldsymbol{\kappa}}^{(2\text{-free})}, \tag{6.31}$$

[3] Note that a_{cv} in this chapter is the exciton Bohr radius defined after (6.14). It is unrelated to the deformation potential a_{cv} in Chapter 5.

where only the allowed-forbidden term is kept in $\Omega^{(\text{2-free})}_{cc'vv'\boldsymbol{\kappa}}$, and

$$N^{(\text{a-f})}_{cc'vv'}(\kappa) \equiv \left(1+a^2_{c'v'}\kappa^2\gamma^2_{c'v'}\right)2\int_0^1 \frac{S\left(\frac{1+S}{1-S}\right)^{\gamma_{c'v'}}\exp\left[-\frac{2}{a_{cv}\kappa}\arctan\left(a_{c'v'}\kappa\gamma_{c'v'}S\right)\right]}{\left(1+a^2_{c'v'}\kappa^2\gamma^2_{c'v'}S^2\right)^2}dS. \quad (6.32)$$

For allowed-allowed two-photon transitions, substituting (6.22) and the first term of (6.23) into (6.20),

$$\Omega^{(\text{2:a-a})}_{cv\boldsymbol{\kappa}} = \left(\frac{e}{\hbar\omega}\right)^2\sum_{c'v'}\mathbf{E}_\omega\cdot\left[\delta_{vv'}v^i_{cc'}(\hat{\boldsymbol{\kappa}})-\delta_{c,c'}v^i_{v'v}(\hat{\boldsymbol{\kappa}})\right]\mathbf{E}_\omega\cdot\mathbf{v}_{c'v'}(\hat{\boldsymbol{\kappa}})$$
$$\times\hbar\int d^3r\left[\psi^{\boldsymbol{\kappa}}_{cv}(\mathbf{r})\right]^*G_{c'v'}\left(\mathbf{r},\mathbf{0};\hbar\omega-E^g_{c'v'}\right).$$

Since $G_{c'v'}$ depends only on the magnitude of $\mathbf{r}$ [Eq. (6.28)], only the s part of the final state will survive the integration over angles of $\mathbf{r}$. Again I use (6.29) for the Whittaker function. The integral over the magnitude of $\mathbf{r}$ can be done using an identity obtained by taking a derivative with respect to p of both sides of (6.30). Finally,

$$\Omega^{(\text{2:a-a})}_{cv\boldsymbol{\kappa}} = \exp\left(\frac{\pi}{2a_{cv}\kappa}\right)\Gamma\left(1-\frac{i}{a_{cv}\kappa}\right)\sum_{c'v'}\Omega^{(\text{2-free})}_{cc'vv'\boldsymbol{\kappa}}N^{(\text{a-a})}_{cc'vv'}(\kappa), \quad (6.33)$$

where only the allowed-allowed term is kept in $\Omega^{(\text{2-free})}_{cc'vv'\boldsymbol{\kappa}}$, and

$$N^{(\text{a-a})}_{cc'vv'}(\kappa) \equiv \left[1+\left(a_{c'v'}\kappa\gamma_{c'v'}\right)^2\right]2$$
$$\times\int_0^1 S\left(1-S\frac{a_{c'v'}\gamma_{c'v'}}{a_{cv}}\right)\left(\frac{1+S}{1-S}\right)^{\gamma_{c'v'}}\frac{\exp\left[-\frac{2}{a_{cv}\kappa}\arctan\left(a_{c'v'}\kappa\gamma_{c'v'}S\right)\right]}{\left[1+\left(a_{c'v'}\kappa\gamma_{c'v'}S\right)^2\right]^2}dS. \quad (6.34)$$

This agrees with Eq. 2.28 of Rustagi [184], but note that $N^{(\text{a-a})}_{cc'vv'}(\kappa) = \left[1+\left(a_{c'v'}\kappa\gamma_{c'v'}\right)^2\right]I_{s,k}(\kappa)$, where $I_{s,k}(\kappa)$ is given, with a typographical error, in Eq. 2.25 of that paper.

The factors $N^{(\text{a-f})}_{cc'vv'}$ and $N^{(\text{a-a})}_{cc'vv'}$, which appear in (6.32) and (6.34) are the enhancements due to the Coulomb interaction in the intermediate states; they are discussed further in Appendix E.

6.5 Results

The one- and two-photon transition amplitudes were presented in the preceding section on the basis of an expansion in $\mathbf{k}$ of the Bloch-state velocity matrix elements. The allowed one-photon transition amplitude $\Omega^{(1)}$ is in (6.25), the allowed-forbidden two-photon transition amplitude is in (6.31), and the allowed-allowed two-photon transition amplitude is in (6.33). From them, $\mathbf{D}^{(1)}_{cv\boldsymbol{\kappa}}$ and $\mathsf{D}^{(2)}_{cv\boldsymbol{\kappa}}$ can be extracted by comparison with the definitions in (6.2) and (6.3).

6.5.1 Current injection

The "1+2" current injection is dominated by interference of allowed one-photon transitions and allowed-forbidden two-photon transitions, as shown in Sec. 3.3. Substitution of these into (6.7), and application of the identities $\Gamma(x+1) = x\Gamma(x)$ and

$$\Gamma(1-ix)\Gamma(1+ix) = \frac{\pi x}{\sinh(\pi x)}, \tag{6.35}$$

yields the final result for the current-injection tensor

$$\eta_{(I)}^{ijkl} = \sum_{c,v}\left(1+\frac{i}{a_{cv}\kappa_{cv}}\right)\Xi(a_{cv}\kappa_{cv})\sum_{c',v'}N_{cc'vv'}^{(\text{a-f})}(\kappa_{cv})\,\eta_{cc'vv'}^{ijkl}, \tag{6.36}$$

where

$$\kappa_{cv} \equiv \frac{1}{a_{cv}}\sqrt{\frac{2\hbar\omega - E_{cv}^{g}}{B_{cv}}}, \tag{6.37}$$

$$\Xi(x) \equiv \frac{(\pi/x)\exp(\pi/x)}{\sinh(\pi/x)} = \frac{2\pi}{x}\left[1-\exp(-2\pi/x)\right]^{-1}, \tag{6.38}$$

and

$$\eta_{cc'vv'}^{ijkl} \equiv \frac{2\pi e}{L^3}\sum_{\boldsymbol{\kappa}}\Delta_{cv}^{i}(\boldsymbol{\kappa})\left(D_{cc'vv'\boldsymbol{\kappa}}^{(\text{2-free})*}\right)^{jk}\left(D_{cv\boldsymbol{\kappa}}^{(\text{1-free})}\right)^{l}\delta\left[2\omega - E_{cv}(\kappa)/\hbar\right], \tag{6.39}$$

with $\boldsymbol{\Delta}_{cv}(\boldsymbol{\kappa}) \equiv (\mathbf{v}_{cc}(\boldsymbol{\kappa}) - \mathbf{v}_{vv}(\boldsymbol{\kappa})) = \hbar\boldsymbol{\kappa}/m_{cv}$ and

$$\left(D_{cc'vv'\boldsymbol{\kappa}}^{(\text{2-free})}\right)^{jk} = \left(\frac{e}{\hbar\omega}\right)^2\frac{\left\{\left(\mathbf{v}_{cc'}(\boldsymbol{\kappa})\,\delta_{v,v'} - \delta_{c,c'}\mathbf{v}_{v'v}(\boldsymbol{\kappa})\right),\mathbf{v}_{c'v'}(\boldsymbol{\kappa})\right\}^{jk}}{E_{c'v'}(\kappa)/\hbar - \omega}, \tag{6.40}$$

where $\{\mathbf{v}_1,\mathbf{v}_2\}^{ij} \equiv (v_1^i v_2^j + v_1^j v_2^i)/2$ and

$$\left(D_{cv\boldsymbol{\kappa}}^{(\text{1-free})}\right)^{l} = i\frac{e}{2\hbar\omega}v_{cv}^{l}(\boldsymbol{\kappa}). \tag{6.41}$$

Note that only the allowed part of (6.41) and the allowed-forbidden part of (6.40) should be retained for a consistent solution. I have written (6.36) to separate the parts due to the electron-hole interaction. In the independent-particle approximation, the current-injection tensor $\eta_{(I\text{-free})}^{ijkl}$ is [3]

$$\eta_{(I\text{-free})}^{ijkl} = \sum_{c,c',v,v'}\eta_{cc'vv'}^{ijkl}; \tag{6.42}$$

it is evaluated for parabolic bands in Sec. 2.3.3.

For GaAs, I present in Fig. 6.1 the magnitude of $\eta_{(I)}^{xxxx}$, based on $\eta_{cc'vv'}^{xxxx}$ calculated by two methods. The first method uses the isotropic, parabolic Kane model and includes only two-band terms (see Sec. 2.3.3). Since the Coulomb corrections to $\eta_{(I)}$ in (6.36) do not depend on the spin index, the sum over spin indices from (6.36) can be included in $\eta_{cc'vv'}^{ijkl}$; it is then straightforward to extract $\eta_{cc'vv'}^{xxxx}$ from Sec. 2.3.3. I use effective-mass ratios for conduction,

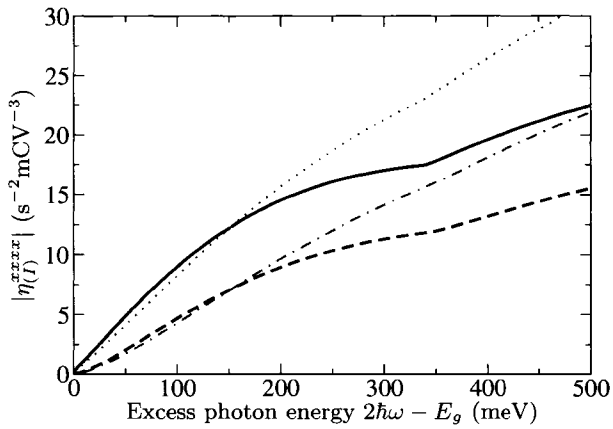

Figure 6.1: Magnitude of the diagonal element of the current-injection tensor for GaAs with [Eq. (6.36)] and without [Eq. (6.42)] excitonic effects. The grey dotted and dashed-dotted lines are based on a parabolic-band calculation of $\eta^{xxxx}_{cc'vv'}$ that only includes two-band terms; the dotted line includes excitonic effects, while the dashed-dotted line does not. The black solid and dashed lines are based on $\eta^{xxxx}_{cc'vv'}$ calculated with a nonperturbative solution of the 8×8 $\mathbf{k} \cdot \mathbf{p}$ Hamiltonian; the solid line includes excitonic effects, while the dashed line does not.

heavy-hole, light-hole, and split-off bands of 0.067, 0.51, 0.082, and 0.154, respectively, $E_P = 27.86\,\text{eV}$, the fundamental band gap E_g is 1.519 eV, and valence-band spin-orbit splitting is 0.341 eV [124, 232]. These parameters are consistent with those listed in Table 3.1. The second method solves the 8×8 $\mathbf{k} \cdot \mathbf{p}$ Hamiltonian, including remote-band effects, but in a spherical approximation with warping and spin-splitting neglected by replacing γ_2 and γ_3 with $\tilde{\gamma} \equiv (2\gamma_2 + 3\gamma_3)/5$ [140] ("$H_{8\text{Sph}}$" in the notation of Sec. 3.2.5); the calculation is nonperturbative in $\mathbf{k}$ (hence it includes band nonparabolicity), and it includes both two- and three-band terms in the two-photon amplitude. The solid and dotted lines in Fig. 6.1 are calculated with (6.36), and hence include excitonic effects; the Coulomb enhancement part of the calculation uses $B_{cv} = 4.2\,\text{meV}$ [233] and the band parameters listed above. Note that the solid black line in Fig. 6.1 is inconsistent in the sense that the Coulomb enhancement is based on an expansion in $\mathbf{k}$, whereas the free-particle result that it enhances is nonperturbative in $\mathbf{k}$; nevertheless, such an approach has given good agreement with experiments for one- and two-photon absorption [234, 235].

The Coulomb enhancement of $\eta^{xxxx}_{(I)}$ can be clearly seen in Fig. 6.1. There is a kink in each curve at excess photon energy 341 meV corresponding to the onset of transitions from the *so* band. At higher energies, the Coulomb enhancement of *so* transitions is larger than the Coulomb enhancements of *hh* and *lh* transitions, since the former transitions are to conduction-

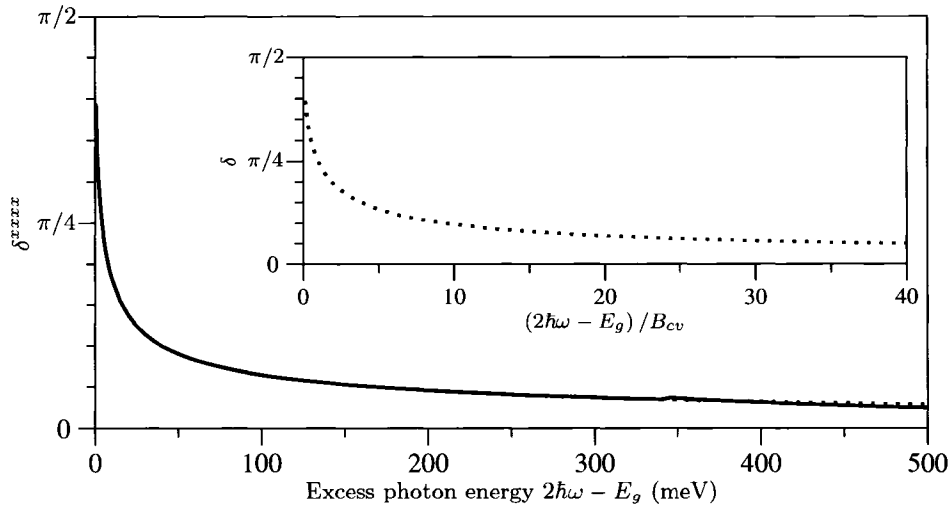

Figure 6.2: Phase shift of the current (intrinsic phase of $\eta_{(I)}^{xxxx}$) in GaAs due to excitonic effects. The solid line is calculated with Eqs. (6.5) and (6.36), and the dotted line is calculated with Eq. (6.43). The inset is Eq. (6.43) plotted in scaled units.

band states with lower energy. Hence, the kink in $\eta_{(I)}$ is enhanced by excitonic effects.

I extract the intrinsic phase of $\eta_{(I)}^{xxxx}$ using (6.5). The solid line in Fig. 6.2 is the intrinsic phase of $\eta_{(I)}^{xxxx}$ calculated for GaAs with the nonperturbative 8×8 $\mathbf{k} \cdot \mathbf{p}$ Hamiltonian; the result for the parabolic-band model is nearly identical. Since I have used a spherical exciton model, the intrinsic phase is the same for all components of $\eta_{(I)}^{ijkl}$. The intrinsic phase has its maximum value of $\pi/2$ at the band edge, and goes to zero as the light frequency increases. The decrease is smooth except for a small kink at the onset of transitions from the *so* band. In fact, for excess photon energies less than the split-off energy, the intrinsic phase has the simple analytic form

$$\delta(\omega) = \arctan\left(\sqrt{\frac{B_{cv}}{2\hbar\omega - E_g}}\right). \tag{6.43}$$

Equation (6.43) is plotted as the dotted line in Fig. 6.2; compared to the solid line, it is identical below the onset of *so* transitions, and it makes a good approximation above the the onset of *so* transitions. Since (6.43) only depends on the excess photon energy scaled by the exciton binding energy, I plot it as a function of this scaled energy in the inset of Fig. 6.2; it is useful for finding the intrinsic phase of materials other than GaAs.

In $\eta_{(I)}^{ijkl}$ [Eq. (6.36)], the two- and three-band terms have different intermediate-state Coulomb enhancement $N_{cc'vv'}^{(\text{a-f})}$. For many materials, however, $N_{cc'vv'}^{(\text{a-f})}$ is approximately equal for all the terms $\eta_{cc'vv'}^{ijkl}$ that contribute significantly to the total $\eta_{(I\text{-free})}^{ijkl}$, as shown in Appendix E for GaAs. Thus, at photon energies for which transitions from the heavy- and light-hole bands dominate

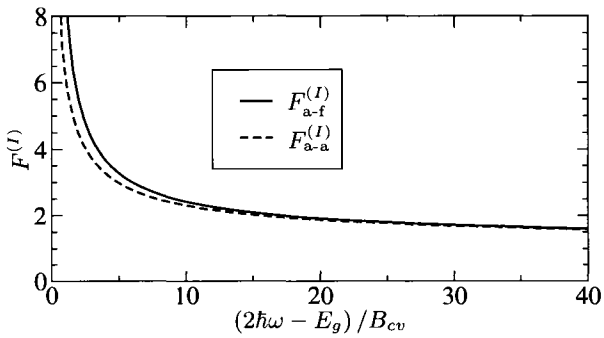

Figure 6.3: Approximate Coulomb-enhancement factors. The solid line, applicable to current and spin-current control, is $F^{(I)}_{\text{a-f}}$ [Eq. (6.45)] with $N^{(\text{a-f})}_{ccvv} = 1$, and the dotted line, applicable to carrier population and spin control, is $F^{(I)}_{\text{a-a}}$ [Eq. (6.50)] with $N^{(\text{a-a})}_{ccvv} = 1$.

$\eta_{(I)}$, the Coulomb enhancement becomes approximately independent of the sum over bands and one can make the simplification

$$\eta^{ijkl}_{(I)} \approx F^{(I)}_{\text{a-f}} \exp(i\delta)\, \eta^{ijkl}_{(I\text{-free})}, \tag{6.44}$$

where the intrinsic phase is given by (6.43), and

$$F^{(I)}_{\text{a-f}}(\omega) \equiv \Xi(a_{cv}\kappa_{cv}) \sqrt{1 + (a_{cv}\kappa_{cv})^{-2}}\, N^{(\text{a-f})}_{ccvv}(\kappa_{cv}), \tag{6.45}$$

The Coulomb-enhancement factor $F^{(I)}_{\text{a-f}}(\omega)$ is plotted in Fig. 6.3 with the approximation that $N^{(\text{a-f})}_{ccvv} = 1$ (see Appendix E).

6.5.2 Carrier population control

The "1+2" carrier population control is dominated by interference of allowed one-photon transitions and allowed-allowed two-photon transitions (see Chapter 3) [37, 75]. Substitution of these into (6.10), and application of the Gamma function identity (6.35) yields

$$\xi^{ijk}_{(I)} = \sum_{c,v} \Xi(a_{cv}\kappa_{cv}) \sum_{c'v'} N^{(\text{a-a})}_{cc'vv'}(\kappa_{cv})\, \xi^{ijk}_{cc'vv'}, \tag{6.46}$$

where

$$\xi^{ijk}_{cc'vv'} = \frac{2\pi e}{L^3} \sum_{\boldsymbol{\kappa}} \left(D^{(\text{2-free})*}_{cc'vv'\boldsymbol{\kappa}}\right)^{jk} \left(D^{(\text{1-free})}_{cv\boldsymbol{\kappa}}\right)^{l} \delta\left[2\omega - E_{cv}(\kappa)/\hbar\right], \tag{6.47}$$

and $\mathrm{D}^{(\text{2-free})}_{cc'vv'\boldsymbol{\kappa}}$ and $\mathbf{D}^{(\text{1-free})}_{cv\boldsymbol{\kappa}}$ are given by (6.40) and (6.41). Note that only the allowed part of (6.41) and the allowed-allowed part of (6.40) should be retained for a consistent solution. In the independent-particle approximation,

$$\xi^{ijk}_{(I\text{-free})} = \sum_{c'v'} \xi^{ijk}_{cc'vv'}. \tag{6.48}$$

Thus, population control has a Coulomb enhancement due to excitonic effects, but no phase shift.

Note that (6.46) gives the population-control tensor at final energies above the band edge. There can also be population control of bound excitons when both one- and two-photon transitions are to the same excitonic state. This can occur, for example, at s excitons due to allowed-allowed two-photon transitions [185] interfering with allowed one-photon transitions.

If $N^{(\text{a-a})}_{cc'vv'}(\kappa_{cv})$ is approximately the same for all the terms that significantly contribute to $\xi_{(I)}$, then, at photon energies for which transitions from the heavy and light hole bands dominate $\xi_{(I)}$, the Coulomb enhancement becomes approximately independent of the sum over bands, and one can make the simplification,

$$\xi^{ijk}_{(I)} \approx F^{(I)}_{\text{a-a}} \xi^{ijk}_{(I\text{-free})}, \tag{6.49}$$

where

$$F^{(I)}_{\text{a-a}}(\omega) \equiv \Xi(a_{cv}\kappa_{cv}) N^{(\text{a-a})}_{ccvv}(\kappa_{cv}). \tag{6.50}$$

The Coulomb enhancement factor $F^{(I)}_{\text{a-a}}(\omega)$ is plotted in Fig. 6.3 with the approximation that $N^{(\text{a-a})}_{ccvv} = 1$ (see Appendix E).

6.5.3 Spin-current injection and spin control

The "1+2" spin-current injection is dominated by interference of allowed one-photon transitions and allowed-forbidden two-photon transitions, whereas "1+2" spin control is dominated by interference of allowed one-photon transitions and allowed-allowed two-photon transitions (see Chapter 3). Under the approximations that led to (6.44) and (6.49), the spin-current injection pseudotensor is

$$\mu^{ijklm}_{(I)} = F^{(I)}_{\text{a-f}} \exp(i\delta) \mu^{ijklm}_{(I\text{-free})}, \tag{6.51}$$

where $F^{(I)}_{\text{a-f}}$ is given by (6.45), δ is given by (6.43), and $\mu_{(I\text{-free})}$ is the spin-current injection pseudotensor in the independent-particle approximation. Under similar approximations, the spin-control pseudotensor is

$$\zeta^{ijkl}_{(I)} = F^{(I)}_{\text{a-a}} \zeta^{ijkl}_{(I\text{-free})}, \tag{6.52}$$

where $F^{(I)}_{\text{a-a}}$ is given by (6.50), and $\zeta_{(I\text{-free})}$ is the spin-control pseudotensor in the independent-particle approximation. Spin control, like carrier population control, has a Coulomb enhancement but no phase shift. There can also be spin control of bound excitons, but it has not been included in (6.52).

6.6 Discussion

We now examine the relationship between the Coulomb enhancements of the "1+2" processes and of one- and two-photon absorption; the latter are denoted by $F^{(1)}$ and $F^{(2)}$ so that for $i \in \{1,2\}$, $\dot{n}^{(i)} = \dot{n}^{(i)}_{\text{free}} F^{(i)}$. The relationship is particularly simple at photon energies for which transitions from the heavy- and light-hole bands are dominant and intermediate-state Coulomb enhancement is the same for each significant term in the sum over intermediate states. The Coulomb enhancements for the "1+2" processes are then given by (6.45) and (6.50). For one-photon absorption, $F^{(1)} = \Xi(a_{cv}\kappa_{cv})$ [212]. In noncentrosymmetric semiconductors, two-photon absorption is dominated by allowed-allowed transitions just above the band gap, and by allowed-forbidden transitions at higher final energies; the crossover point in GaAs is a few meV above the band gap [172]. At photon energies for which allowed-allowed transitions dominate two-photon absorption, from (6.33),

$$F^{(2)} = \Xi(a_{cv}\kappa_{cv}) \left[N^{(\text{a-a})}_{ccvv}(\kappa_{cv})\right]^2, \tag{6.53}$$

and thus

$$F^{(I)}_{\text{a-a}} = \sqrt{F^{(1)}F^{(2)}} \text{ and } F^{(I)}_{\text{a-f}} = C\sqrt{F^{(1)}F^{(2)}}, \tag{6.54}$$

where $C \equiv \left[N^{(\text{a-f})}_{ccvv}(\kappa_{cv}) / N^{(\text{a-a})}_{ccvv}(\kappa_{cv})\right] \sqrt{1 + (a_{cv}\kappa_{cv})^{-2}}$, while at photon energies for which allowed-forbidden transitions dominate two-photon absorption, from (6.31),

$$F^{(2)} = \Xi(a_{cv}\kappa_{cv}) \left(1 + (a_{cv}\kappa_{cv})^{-2}\right) \left(N^{(\text{a-f})}_{ccvv}(\kappa_{cv})\right)^2, \tag{6.55}$$

and thus

$$F^{(I)}_{\text{a-a}} = (1/C)\sqrt{F^{(1)}F^{(2)}} \text{ and } F^{(I)}_{\text{a-f}} = \sqrt{F^{(1)}F^{(2)}}. \tag{6.56}$$

Note that, based on Appendix E, $C \approx \sqrt{1 + B_{cv}/(2\hbar\omega - E_g)}$, which is the ratio of the two curves in Fig. 6.3. In centrosymmetric semiconductors, there are no allowed-allowed transitions, and only (6.56) applies.

The "1+2" processes are often described by ratios. For example, a useful quantity to describe the current is the swarm velocity [68, 236], defined as the average velocity per injected electron-hole pair

$$\mathbf{v}_{\text{swarm}} \equiv \frac{(d\mathbf{J}/dt)}{e\,(dn/dt)}.$$

The swarm velocity is a maximum when the relative intensities of the two colours are chosen such that $\dot{N}_{2\omega} = \dot{N}_{\omega}$; returning to (6.1), if one associates the one- and two-photon amplitudes with the arms of an effective interferometer, this condition corresponds to balancing that interferometer. For fields colinearly polarized along $\hat{\mathbf{x}}$, the maximum swarm speed is

$$v_{\text{swarm}} = \frac{1}{e} \frac{\left|\eta^{xxxx}_{(I)}\right|}{\sqrt{\xi^{xx}_{(1)}\xi^{xxxx}_{(2)}}}. \tag{6.57}$$

A useful quantity to describe pure spin currents is the maximum spin-separation distance [42]; it is proportional to $\mu_{(I)}/\sqrt{\xi_{(1)}\xi_{(2)}}$. As a consequence of (6.56), the maximum swarm speed, and the maximum spin-separation distance, are *unaffected* by excitonic effects when allowed-forbidden transitions dominate two-photon absorption.[4] However, close to the band edge, where allowed-allowed transitions dominate two-photon absorption, excitonic effects increase these ratios by a factor C over their value in the independent-particle approximation. In contrast, as a consequence of (6.56), excitonic effects do not affect the maximum control ratio for population and spin control ($\xi_{(I)}/\sqrt{\xi_{(1)}\xi_{(2)}}$ and $\zeta_{(I)}/\sqrt{\xi_{(1)}\xi_{(2)}}$ respectively [36, 66, 75]) close to the band edge and decrease them by a factor C at higher photon energies for which allowed-forbidden transitions dominate two-photon absorption.

In the terminology of Seideman [203], the excitonic phase shift of the "1+2" current and spin current is a direct phase shift. This phase shift is due to the complex nature of the final state as it appears in the transition amplitudes. Thus it can be understood in terms of the partial-wave phase shifts of the final state caused by the Coulomb potential between electron and hole. The Coulomb interaction is rather unique due to its long-range nature, so we first suppose that the potential between the electron and hole falls off more rapidly than $1/r$. In that simpler problem, the final-state wave function is written as

$$\psi_{\boldsymbol{\kappa}}(\mathbf{r}) = \sum_{l=0}^{\infty} i^l e^{-i\delta_l(\kappa)} (2l+1) \frac{u_{\kappa,l}(r)}{r} P_l\left(\frac{\mathbf{r}\cdot\boldsymbol{\kappa}}{r\kappa}\right),$$

where the $u_{\kappa,l}(r)$ are real [226]. If the potential between the particles is ignored, then the partial-wave phase shifts, $\delta_l(\kappa)$ are zero. The allowed one-photon pathway reaches an s wave, while the allowed-forbidden two-photon pathway reaches a p wave. Substituting this form for the wave function into the one- and two-photon transition amplitudes yields $\Omega_{\boldsymbol{\kappa}}^{(1)} = \Omega_{\boldsymbol{\kappa}}^{(1\text{-free})} e^{i\delta_0(\kappa)} f_0(\kappa)$ for the one-photon rate, where $f_0(\kappa)$ is real and depends on $u_{\kappa,0}(r)$, and $\Omega_{\boldsymbol{\kappa}}^{(2:\text{a-f})} = \Omega_{\boldsymbol{\kappa}}^{(2\text{-free})} e^{i\delta_1(\kappa)} f_1(\kappa)$ for the two-photon rate, where $f_1(\kappa)$ is real and depends on $u_{\kappa,0}(r)$ and $u_{\kappa,1}(r)$. Here $\Omega_{\boldsymbol{\kappa}}^{(i\text{-free})}$ is the i-photon transition amplitude when the potential between the particles is ignored. It is then straightforward to see from (6.7) that the relative shift of the partial waves is responsible for the phase shift of the current and spin current. That is,

$$\delta = \delta_0 - \delta_1. \tag{6.58}$$

The use of ionization states as opposed to scattering states was important to get the correct sign of the intrinsic phase. With scattering states, one would find $\delta = \delta_1 - \delta_0$. In contrast, the allowed-allowed two-photon pathway reaches an s wave and thus there is no phase shift for population control or spin control.

[4] At higher excitation densities, the Coulomb interaction can modify the maximum spin-separation distance through the momentum relaxation time.

Due to the long-range nature of the Coulomb potential, the partial-wave phase shifts have a logarithmic r dependent part, but it is the same for all partial waves and thus does not appear in the relative phase. The part of the Coulomb partial-wave phase shift $\delta_l(\kappa)$ that does not depend on r is $\arg\{\Gamma[l+1+i/(a_{cv}\kappa)]\}$ [226, 231]; when inserted into (6.58), this reproduces (6.43).

The expression (6.58) for the intrinsic phase in terms of the scattering phases is particularly simple, since each pathway connects to only a single parity. This contrasts with "1+2" ionization from an atomic s state, for which the one-photon transition is to a p wave and the two-photon transition is to both s and d waves; the intrinsic phase is thus a weighting of the p-s and p-d partial-wave shifts [205]. Materials for which the first term in (6.21) is forbidden (Cu_2O is an example) have these same selection rules [176, 184, 212]; hence, they will have an intrinsic phase with a similar weighting.

The absence of a phase shift in population control can be connected to a symmetry of the second-order nonlinear optical susceptibility. From considerations of energy transfer and macroscopic electrodynamics, $\xi_{(I)}$ is related to the nonlinear susceptibility $\chi^{(2)}$ by

$$\xi_{(I)}^{ijk} = (i\epsilon_0/\hbar)\left[\chi^{(2)kij}(2\omega;-\omega,-\omega) - \chi^{(2)jki}(-\omega;2\omega,-\omega)\right]. \tag{6.59}$$

In the independent-particle approximation [101],

$$\chi^{(2)ijk}(2\omega;-\omega,-\omega) = \left[\chi^{(2)jik}(-\omega;2\omega,-\omega)\right]^*, \tag{6.60}$$

which is a generalization of overall permutation symmetry to resonant absorption. As a result of (6.60), Fraser *et al.* showed that $\xi_{(I)}$ is proportional to $\mathrm{Im}\chi^{(2)}$, and is thus purely real [36]. The finding that $\xi_{(I)}$ remains real when excitonic effects are included suggests that (6.60) holds more generally. In fact, it can be shown that (6.60) holds for any Hamiltonian symmetric under time-reversal so long as $\hbar\omega$ is not resonant.

6.7 Summary and Outlook

This chapter extended the theory of interband "1+2" processes in bulk semiconductors to include the electron-hole interaction. Following previous theories [3, 33, 36], including those in Chapters 2 and 3, I have used a framework based on (i) a separation of the initial carrier photoinjection and the subsequent carrier scattering, and (ii) a perturbative expansion in the optical-field amplitudes, with injection rates obtained in a FGR limit for the bichromatic field. The injection rates for carrier population control, spin control, current injection, and spin-current injection, have been described phenomenologically by tensors $\xi_{(I)}$, $\zeta_{(I)}$, $\eta_{(I)}$, and $\mu_{(I)}$, respectively (see Sec. 2.2). Like previous theories, I have used the long-wavelength limit, and

neglected nonlocal corrections to the interaction Hamiltonian. But whereas previous theories of "1+2" photoinjection used the independent-particle approximation, I have included excitonic effects. I have shown that excitonic effects cause (i) an enhancement of each "1+2" process, and (ii) a phase shift for current injection and spin-current injection. The main results, the modifications of the aforementioned tensors relative to the independent-particle approximation are given in (6.44), (6.49), (6.51), and (6.52). These particularly simple results are valid at photon energies for which transitions from the heavy- and light-hole bands are dominant; more general results are given for $\eta_{(I)}$ and $\xi_{(I)}$ in (6.36) and (6.46).

The results are based on the effective-mass model of Wannier excitons; degenerate bands are included, but I use a spherical approximation to the exciton Hamiltonian, and I neglect envelope-hole coupling. This is a good approximation for many typical semiconductors, including GaAs, since the electron-hole envelope function extends over many unit cells due to the screening of the Coulomb interaction by the static dielectric constant [140, 177, 178, 186, 230]. As a consequence of making the spherical approximation, the phase shifts and Coulomb enhancements I find in this paper are independent of crystal orientation.

Also, the results are limited to low excess photon energy since (i) the Wannier exciton Hamiltonian assumes parabolic Bloch bands, and (ii) I have truncated the expansion in $\mathbf{k}$ of the Bloch-state velocity matrix elements, which is the basis of the transition amplitude expansion. By comparing the black dashed line and grey dashed-dotted line in Fig. 6.1, one sees that higher order terms in $\mathbf{k}$ (for both bands and velocities) are important in GaAs for excess photon energies greater than about 200 meV. This can be considered the limit of validity of my calculation. However, combining the Coulomb enhancement calculated assuming parabolic bands with the nonperturbative independent-particle approximation result (as was done for the solid black line in Fig. 6.1) likely gives a good approximation for a few hundred more meV; this was the case for one- and two-photon absorption [234, 235].

Chapter 7

Conclusion

Spin is a fundamental property of the electron. Understanding the control and transport of electron spins in semiconductors is important from a fundamental point of view, but also for the development of new technologies. In solid state systems, electron spin can be controlled by light only indirectly, through the relativistic effect of spin-orbit coupling. Interband transitions in bulk semiconductors are the most fundamental optical transitions in semiconductor physics. In this thesis, I have shown (Chapter 5) that one-photon absorption of linearly polarized light—the simplest interband optical transition—can generate a spin current in bulk GaAs, one of the most well-studied semiconductors. This fact had not been previously known, despite the fact that such transitions have been studied for many years. I have also expanded the potential toolkit for optical manipulation of spin and spin currents by making the first study of the spin of carrier distributions excited by "1+2" excitation (Chapters 2, 3, and 6). The "1+2" excitation is a low-order nonlinear process with a two-colour optical field, which has been studied in recent years in many physical systems including atoms, molecules, semiconductors, and semiconductor heterostructures. It is the simplest optical excitation that can display control over a physical process with the phases of the optical fields. As such it is inherently interesting, but it is also important as a means for measuring the carrier-envelope phase of an ultrashort optical pulse. For applications such as this, the detailed microscopic investigations of "1+2" excitation I have presented in this thesis are essential.

Optical excitation of carriers has several advantages over other methods of manipulating carriers in semiconductors: a wide range of carrier densities can be studied by varying the field intensities, carrier transport can be studied in undoped samples (and ballistic transport can be studied in unbiased samples), and a wide range of nonequilibrium carrier distributions can be generated by optical fields. This thesis has shown, in particular, that optical fields can excite carrier distributions that have a pure spin current. This led to the first observation of a pure spin current in a semiconductor. Pure spin currents are of fundamental interest, and many

methods for generating them have been proposed and studied in recent years.

In studying the spin properties of photoexcited carrier distributions, I have also studied the carrier population, and the net current. A knowledge of all four properties—number of carriers, net spin, net current, and net spin current—gives one sufficient information about the carrier distribution to calculate, for instance, how a subsequent probe pulse will interact with the material, or how the carriers will radiate as these quantities change rapidly due to ultrafast excitation. The main contributions of this thesis are the proposals that one-photon absorption can inject PSCs, "1+2" excitation can inject ballistic spin currents (both SPECs and PSCs), and "1+2" excitation can inject an electron spin polarization that depends on the phase of the fields. But I also presented thorough studies of each of these effects, "1+2" current injection and population control, and two-photon spin injection. Many of the effects predicted in this thesis have now been observed experimentally.

As discussed in Sec. 1.1, the theoretical framework for calculating these effects is similar to the framework of the nonlinear optical susceptibilities. That section discusses many of the assumptions and limitations of the calculations in this thesis.

In Chapters 2, 3, and 6, I presented studies of "1+2" excitation with three different electronic structure calculations. In Sec. 2.2, I analyzed the symmetry of each "1+2" effect, especially for materials with cubic symmetry. Since the results of Sec. 2.2 rely only on the symmetry of the crystal, they apply to all three chapters, and quite generally. In the rest of Chapter 2, I used the isotropic eight-band Kane model in the parabolic band approximation (PBA) to evaluate the current, and spin-current injections. The main results are (2.47), (2.49), (2.52), and (2.53). Parabolic band approximations of "1+2" spin control and population control are calculated using fourteen-bands in Appendix C. The main results are (C.3) and (C.12). Together, Chapter 2 and Appendix C establish that, close to the band edge, "1+2" current injection and spin-current injection result from the interference of allowed one-photon transitions and allowed-forbidden two-photon transitions, while "1+2" population control and spin control result from the interference of allowed one-photon transitions and allowed-allowed two-photon transitions. This conclusion is validated by agreement with the results of Chapter 3 at low excess photon energy.

Using an electrode detection technique, Stevens *et al.* observed the current due to "1+2" excitation with co-circularly polarized fields, found agreement with the predictions in Chapter 2, and hence inferred that the current was spin-polarized (Case 1 in Sec. 2.4) [71]. The "1+2" transverse PSC with orthogonally polarized fields (Case 2 in Sec. 2.4) has been observed using spatially-resolved pump-probe techniques [41], spatially-resolved photoluminescence techniques [42], and optical grating techniques [74].

In Chapter 3, I evaluated the "1+2" effects with a nonperturbative numerical solution

to the fourteen-band $\mathbf{k} \cdot \mathbf{p}$ Hamiltonian. With this calculation, which is more accurate than the calculation in Chapter 2, I examined the relative importance of each possible initial and intermediate state to get a better microscopic understanding of each "1+2" effect. This explains the limitations of the PBA results of Chapter 2 and Appendix C. I applied the calculation to five semiconductors to present a sense of how the "1+2" effects can vary from material to material. The main results of this chapter are Figures 3.2–3.14.

More recent experiments measure the "1+2" longitudinal PSCs, and are thus sensitive to μ_{N2} and μ_{N3}, which each changed sign between the calculations of Chapter 2 and 3; preliminary results confirm the signs of μ_{N2} and μ_{N3} calculated with the more accurate fourteen-band model in Chapter 3 [83]. Recently, "1+2" spin control has been observed using pump-probe techniques on (111)- and (110)-GaAs [66, 67]. The experiment on (110)-GaAs was complicated by a cascaded second-harmonic generation process and propagation effects, which are interesting in their own right, but make a direct comparison with the results in Chapter 3 difficult; the calculation in Chapter 3 was used as an input into a propagation calculation that produced results in general agreement with the experiment [67]. Both experiments used large excess photon energies (150 meV and 280 meV). The experiment on (111)-GaAs, which was not complicated by propagation effects, used a 280 meV excess photon energy and observed a maximum spin-control ratio of 2% [66].

Small control ratios were also measured in population control experiments at similar excess photon energies [36, 37, 66, 67]. The calculations in Chapter 3 predict that much larger population control ratios and spin control ratios are possible under excitation closer to the band edge. Based on the PBA results in Appendix C, one can understand that large control ratios can be expected when allowed-allowed two-photon transitions dominate allowed-forbidden two-photon transitions. Such a situation occurs close to the band edge within an energy range that is larger for materials with larger conduction band effective mass such as ZnSe. Experimental confirmation of this prediction of large control ratios could generate interest in using population control and spin control in some technological application, perhaps for optical switching.

In Chapter 6, I extended the theory of the "1+2" effects to include the electron-hole interaction, which is neglected in rest of the thesis, and earlier theories of "1+2" excitation. The main contribution of Chapter 6 is the identification of the intrinsic phase for "1+2" current injection and "1+2" spin-current injection, and the calculation of Coulomb enhancements of each "1+2" effect. The underlying single-particle band structure of Chapter 6 is the PBA of Chapter 2 and Appendix C, although with the added approximation of equal heavy- and light-hole effective masses. This approximation allowed for analytic solutions of the excitonic Hamiltonian, which in turn allowed for physical insight into the problem. For example, I related the intrinsic phase to the partial wave phase shifts of the Coulomb potential between the electron and hole, and I

related the Coulomb enhancement of the "1+2" effects to the Coulomb enhancements of one- and two-photon absorption. The main results of Chapter 6 are summarized in Sec. 6.7.

It is interesting to ask if there are other sources of intrinsic phases to the current (or spin current) besides the one that I have identified here, as these might produce spectral features in the intrinsic phase. One possibility is the coupling between bound *so-c* excitons and the unbound *hh-c* or *lh-c* excitons, since it is known that the intrinsic phase can show spectral features near a resonance [204]. Another possibility is the envelope-hole coupling between the continua of unbound *hh-c* and *lh-c* excitons that was neglected in my treatment.

Thus far, semiconductor "1+2" experiments have lacked the calibration of the optical phases necessary to measure the intrinsic phases predicted in Chapter 6, and have lacked the spectral resolution to confirm the Coulomb enhancements predicted in Chapter 6. The intrinsic phase will be challenging to observe experimentally since it is most significant in a narrow range of photon energies above the band edge. But it may have consequences for the use of "1+2" current injection as a measure of the carrier-envelope phase of an ultrashort optical pulse [77, 78].

The intrinsic phase and Coulomb enhancement might be greater in reduced dimensional systems, which have greater exciton binding energies. The carrier-carrier Coulomb interaction was included in the theory for "$1+2$" control of electrons in biased asymmetric quantum wells, although the intrinsic phase was not identified [31]. Marti *et al.* recently included excitonic effects in a theory for "1+2" non-resonant excitation in a quantum wire, but did not find any nontrivial intrinsic phase [59]. Duc *et al.* recently included the carrier-carrier Coulomb interaction in a theory for "1+2" current injection and spin-current injection in unbiased quantum wells [58]. They did not initially study the phase dependence of the effects, but they have confirmed that their calculation yields a nontrivial intrinsic phase [237]. Since carbon nanotubes have strong excitonic effects [238], they would be interesting materials in which to study the intrinsic phase. The "1+2" current injection has been studied in carbon nanotubes and graphene sheets, but only in the independent-particle approximation [239].

Since "1+2" population control and second harmonic generation are related, the methods used in this thesis to calculate "1+2" population control can be extended to a calculation of second harmonic generation. Such a task would require a Kramers-Kronig transformation on $\mathrm{Im}\chi^{(2)}$ to get $\mathrm{Re}\chi^{(2)}$, and hence would require the former to be specified over a larger range of frequency than I have studied here. Hutchings and Arnold have calculated second harmonic generation with the fourteen-band model, although they did not include remote band effects [131]. Others have used PBA expressions for contributions from several critical points to obtain $\mathrm{Im}\chi^{(2)}$ over a wide spectral range [147, 158]. Those PBA results are still used to model experiments [160], and could be improved by the inclusion of terms proportional to interband spin-orbit coupling parameterized by Δ^{-}, which I include in Appendix C. In InSb, such terms

contribute as much as 37% to $\mathrm{Im}\chi^{(2)}$. Excitonic effects on second harmonic generation have recently been studied with *ab initio* methods [109], but it would be valuable to also study them with a simpler band model.

In Chapter 4, I applied the fourteen-band model of Chapter 3 to two-photon spin injection, which had previously only been studied with isotropic models. I compared one- and two-photon spin injection, and showed that allowed-allowed transitions, which are absent from isotropic calculations and are not restricted by angular momentum conservation, permit very high degrees of spin polarization. The main results of Chapter 4 are Fig. 4.2 and the allowed-allowed band edge results C.19 and C.20 in Appendix C. The two-photon degree of spin polarization has not yet been measured close to the band edge, but at higher excess photon energies, recent experiments agree with the calculation in Chapter 4 [20].

The theoretical considerations of angular momentum that I raised in Chapter 4 would be interesting to pursue further. I showed that in a spherical model part of the photon angular momentum is transferred to the carrier spins, and hypothesized that the rest of it is transferred to the orbital motion of the carriers. It would be challenging to calculate the transferred orbital angular momentum directly, since the position operator is ill-defined for an infinite, periodic crystal [105]. It would then be interesting to apply that calculation to a non-spherical model in which total angular momentum need not be conserved.

In Chapter 5, I showed that a pure spin current can be optically injected from one-photon absorption alone. I calculated this effect with the fourteen-band model of Chapter 3, and also with additional terms in the Hamiltonian that account for applied strain. I showed that the one-photon PSC is smaller than the "1+2" PSC, even when increased by strain. In this chapter, I used a theoretical approach based on the density matrix rather than the wave function. The density matrix approach is not essential, but it more clearly demonstrates the approximations inherent in the calculation. The one-photon PSC has been observed experimentally [83]. PSCs due to one-photon absorption have now been studied in quantum well systems [240], and would be interesting to study in other systems of lower symmetry, which could yield even larger PSCs.

Although I proposed the one-photon PSC, and calculated it with the fourteen-band model, I did not derive an expression for it in the PBA as I did for the other optical effects in the thesis. The spin-separation distance in unstrained GaAs appears to be proportional to excess photon energy close to the band edge, which suggests that a perturbative approach should bear fruit. It would be interesting to see which parameters of the model are responsible for the PSC, and hence find materials that have larger PSCs. Since the effect relies on noncentrosymmetry, it should be possible to attribute it to wave function mixing between upper conduction bands and valence bands and/or spin-splitting of the bands. Both of these are due to the momentum matrix element P' and the interband spin-orbit coupling Δ^-.

The formalism to describe the one-photon PSC can also describe the SPEC due to the circular photogalvanic effect (CPGE) [116]. In fact, the pseudotensor $\mu_{(1)}^{ijkl}$ describes both processes: the former for a linearly polarized field, and the latter for a circularly polarized field. Other researchers have attributed the one-photon SPEC to spin-splitting of the bands [116, 197], whereas my preliminary investigations in unstrained GaAs attribute the one-photon PSC to wave function mixing between upper conduction bands and valence bands. Even though these two points are not necessarily at odds—since the CPGE vanishes in materials with zinc-blende symmetry—it would be good to better understand the microscopic origin of both effects.

Throughout this thesis I have argued that the coherence between spin-split bands will grow like the band populations in typical experiments. Consequently, I treated spin-split bands as quasidegenerate in FGR for the derivation of microscopic expressions of each optical process. For excitation with long pulses, this requires the spin-splitting to be smaller than the energy associated with the dephasing between spin-split bands. It would be interesting to study experimental situations—perhaps at higher excess photon energies, or in heterostructures with larger spin splitting—where the quasidegenerate assumption breaks down.

Nonlinear optical properties are a more stringent test of electronic structure calculations than linear optical properties. By making extensive comparisons between the PBA and the fourteen-band model, I have shown the limitations of the former for the calculation of these nonlinear properties. It is interesting to note the importance of interband spin-orbit coupling (Δ^-) on effects for which allowed-allowed transitions are important—"1+2" spin-control, "1+2" population control, and band edge two-photon spin injection. Linear optical properties are much less sensitive to the parameter Δ^-.

In a sense, this thesis completes the phenomenology of interband "1+2" excitation in semiconductors by adding spin and spin current to the list of properties that can be controlled. It presents the first optical method for generating a pure spin current, and also shows that pure spin currents were inadvertently generated even in the simplest early experiments on one-photon absorption in semiconductors. The detailed study of these effects, using an accurate band model and incorporating excitonic effects, is necessary as they begin to be used to study spin relaxation and transport [74], and to measure the carrier-envelope phase of an ultrashort pulse [77, 78].

Appendix A

Notes on systems of electromagnetic units

There are two commonly used systems of electromagnetic units: the Gaussian system, and the International System of Units (SI). Their differences, which Jackson discusses in a detailed appendix [241], stem from adopting different proportionality constants for Coulomb's law (the force F between two point charges q_1 and q_2 separated by a distance r). In the Gaussian system

$$F = \frac{q_1 q_2}{r^2},$$

whereas in SI

$$F = \frac{q_1 q_2}{4\pi\varepsilon_0 r^2}.$$

The Gaussian system, typically used with cgs units (centimeters, grams, and seconds), is favoured by theorists, because it makes most electromagnetic formulas simpler; in particular, the four fields appearing in Maxwell's equations all have the same units. The SI-mks system, which uses the SI choice for Coulomb's law and SI units (meters, kilograms, and seconds), is favoured by experimentalists. Table 3 of the appendix in Jackson is useful for converting formulas between the two systems of electromagnetic units [241]. For example, when converting a Gaussian formula to SI, the electric field $\mathbf{E}$ should be replaced by $\mathbf{E}\sqrt{4\pi\varepsilon_0}$, the electric charge e should be replaced by $e/\sqrt{4\pi\varepsilon_0}$, and the current density $\mathbf{J}$ should be replaced by $\mathbf{J}/\sqrt{4\pi\varepsilon_0}$. Appendix A of Boyd discusses the two systems of units in the context of nonlinear optics [84].

In this thesis, I have used both systems of units. On the one hand, I have used the Gaussian system for theoretical derivations. For example, the interaction Hamiltonians in Sec. 1.1 are written in the Gaussian system of units. On the other hand, I have used the SI-mks system to plot results. For example, all of the figures use SI-mks units, with the exception of Fig. 3.9, which uses both systems.

Note that many of the formulas in this thesis are the same in both systems of units. For example, the transition amplitudes (2.3) and (2.4) contain the product $e\mathbf{E}$, which is the same in formulas for both systems of units, since it is a force.

Moreover, I state that the formulas in Sec. 2.2 defining new tensors and pseudotensors—$\eta_{(i)}$, $\xi_{(i)}$, $\mu_{(i)}$, and $\zeta_{(i)}$, where i stands for 1, 2 or I—are the same in both systems of units. As a consequence, all microscopic expressions for the tensors and pseudotensors are the same in both systems of units.

As an example, consider $\eta_{(I)}^{ijkl}$, which is defined in (2.25). Suppose that definition is in Gaussian units. Then, according to the conversion rules, to keep the definition (2.25) the same in SI, $\eta_{(I)}^{ijkl}$ should be replaced by $\eta_{(I)}^{ijkl}/(4\pi\varepsilon_0)^2$. Now suppose the microscopic expression (2.43) is in Gaussian units. Then, making the replacements for $\eta_{(I)}^{ijkl}$ and e (all other quantities are unchanged), one finds that (2.43) is the same in SI.

This feature does not hold for the conventional linear and nonlinear susceptibilities [84], and thus the relations between them and the tensors $\eta_{(i)}$ and $\xi_{(i)}$, where i stands for 1, 2 or I are different in each system of units. Where I have written such relations—in a footnote after (2.23), in (3.21), and in (6.59)—I have favoured SI.

Appendix B

Neglect of the anomalous velocity and k-dependent spin-orbit coupling

The anomalous velocity, i.e. $\mathbf{v}_A \equiv (\mathbf{v} - \mathbf{p}/m) = \hbar(\boldsymbol{\sigma} \times \boldsymbol{\nabla} V) / (4m^2c^2)$, which leads to $\mathbf{k}$-dependent spin-orbit coupling in $H_\mathbf{k}$ from the term $\hbar\mathbf{k} \cdot \mathbf{v}_A$, is often neglected from $\mathbf{k} \cdot \mathbf{p}$ models [123, 124, 130, 242, 243]. Some authors have treated matrix elements of $\boldsymbol{\nabla} V$ as additional independent parameters [145, 156, 244, 245], but I here relate them to other parameters of the model, thereby demonstrating that they can be safely neglected.

Bir and Pikus showed that the identity $[H_0, \mathbf{p}] = i\hbar\boldsymbol{\nabla} V$ leads to $\langle X| \nabla_y V |Z\rangle = 0$ [120]. An application of that identity to the remaining nonzero matrix elements yields

$$\langle S| \nabla_x V |X\rangle = \frac{1}{\hbar^2} (E_S - E_X) mP_0, \tag{B.1a}$$

$$\langle S| \nabla_x V |x\rangle = -\frac{1}{\hbar^2} (E_x - E_S) mP_0', \tag{B.1b}$$

$$\langle X| \nabla_y V |z\rangle = \langle Z| \nabla_y V |x\rangle = -\frac{1}{\hbar^2} (E_x - E_X) mQ, \tag{B.1c}$$

and similar results for cyclic permutations and Hermitian conjugates of these. The energies E_S, E_X, and E_x are the eigenvalues of $|S\rangle$, $|X\rangle$, and $|x\rangle$ with respect to the Hamiltonian H_0. Their values are fixed by the requirement that the eigenvalues of $H_{\mathbf{k}=\mathbf{0}}$ give the parameters E_g, E_0', Δ_0, and Δ_0' [124]. Neglecting the small contribution from Δ^-, $E_S - E_X = E_g + \Delta_0/3$, $E_x - E_S = E_0' - E_g + 2\Delta_0'/3$, and $E_x - E_X = E_0' + 2\Delta_0'/3 + \Delta_0/3$.

Bahder gives the matrix for $\hbar\mathbf{k} \cdot \mathbf{v}_A$ within the eight-band model and defines the parameter [244]

$$C_0 = \frac{1}{\sqrt{3}} \frac{\hbar^2}{4m^2c^2} \langle S| \nabla_x V |X\rangle .$$

Ostromek used the value $C_0 = 0.16$ eV Å to fit the eight-band model to experimental results

[245]. However, using (B.1a) and parameters from Table 3.1 for GaAs, $C_0 = 5 \times 10^{-6}$ eV Å.[1]

From the point of view of the theory of invariants [120, 132, 246, 247], **k**-dependent spin-orbit coupling amounts to using different values of P_0 for Γ_8 and Γ_7 valence bands (and similar changes for P_0' coupling and Q coupling) [132]. In terms of C_0, $P_0 \rightarrow P_7 \equiv P_0 + 2\sqrt{3}C_0$ for couplings with Γ_7 bands and $P_0 \rightarrow P_8 \equiv P_0 - \sqrt{3}C_0$ for couplings with Γ_8 bands. From (B.1a),

$$\frac{P_7 - P_8}{P_0} = \frac{3\,(E_S - E_X)}{4mc^2},$$

which is very small since $mc^2 = 5.11 \times 10^5$ eV.

The above suggests that **k**-dependent spin-orbit coupling can be neglected for bulk, cubic materials. As a check, I have repeated the calculations of two-photon spin injection in GaAs (Chapter 4), and one-photon linear PSC (Chapter 5) including such coupling only between valence and lowest conduction bands and the associated anomalous velocity. Using the consistent value of $C_0 = 5 \times 10^{-6}\,\text{eVÅ}$, the results are unchanged. Even when using the overly large coupling value of $C_0 = 0.16\,\text{eVÅ}$, the two-photon P decreases only by $\approx 2\%$ for excess energies between 0.1 and 200 meV, and the linear PSC spin-separation distance changes by less than 0.1 nm.

[1] Note that C_0 is unrelated to the **k**-linear term C_k.

Appendix C

Allowed-Allowed Transitions in the Parabolic Band Approximation

In this appendix, I derive expressions for "1+2" population control, "1+2" spin control, and two-photon spin injection in the parabolic band approximation (PBA) due to allowed Γ-point transitions in the fourteen-band model. These analytical results, which are perturbative in $\mathbf{k}$, are compared in numerical, nonperturbative results in Chapters 3 and 4.

To calculate optical effects due to allowed one-photon transitions, allowed-allowed two-photon transitions, or their interference, one needs the velocity matrix elements for the eigenstates at the Γ point. By approximating the velocity matrix elements by their value at the Γ point, the integral over $\mathbf{k}$ in the microscopic expressions for the optical effects becomes straightforward. As a further simplification, I approximate all the bands as spherical and parabolic, neglecting the small $\mathbf{k}$-linear term C_k. Since the bands are doubly degenerate at the Γ point, even for models that include spin-splitting, I can use microscopic expressions such as those in Sec. 2.1.

The Γ-point basis states are given in (3.2). However, all but the Γ_{6c} states are not eigenstates at the Γ point due to spin-orbit coupling between upper conduction and valence bands parameterized by Δ^-. The Hamiltonian at the Γ point in this basis has off-diagonal elements, but the order of the basis can be arranged so that it is block diagonal with blocks at most 2×2. For the bands $|\Gamma_{7v}, +1/2\rangle$ and $|\Gamma_{7c}, +1/2\rangle$ (or for the bands $|\Gamma_{7v}, -1/2\rangle$ and $|\Gamma_{7c}, -1/2\rangle$), the block is

$$\begin{bmatrix} -E_g - \Delta_0 & -\frac{2}{3}\Delta^- \\ -\frac{2}{3}\Delta^- & E_0' - E_g \end{bmatrix}.$$

Since $\Delta^- / (E_0' + \Delta_0) \ll 1$, the off-diagonal part can be treated as a perturbation. To first order

in the perturbation, we have eigenvectors

$$|so\uparrow/\downarrow\rangle = |\Gamma_{7v}, \pm 1/2\rangle + \frac{2\Delta^-}{3}\frac{1}{E_0' + \Delta_0}|\Gamma_{7c}, \pm 1/2\rangle$$
$$|sc\uparrow/\downarrow\rangle = |\Gamma_{7c}, \pm 1/2\rangle - \frac{2\Delta^-}{3}\frac{1}{E_0' + \Delta_0}|\Gamma_{7v}, \pm 1/2\rangle .$$

For the Γ_8 bands, the blocks are

$$\begin{bmatrix} -E_g & \frac{1}{3}\Delta^- \\ \frac{1}{3}\Delta^- & E_0' - E_g + \Delta_0' \end{bmatrix},$$

with eigenvectors to first order in $\Delta^-/(E_0' + \Delta_0')$,

$$|hh\uparrow/\downarrow\rangle = |\Gamma_{8v}, \pm 3/2\rangle - \frac{\Delta^-}{3}\frac{1}{E_0' + \Delta_0'}|\Gamma_{8c}, \pm 3/2\rangle$$
$$|lh\uparrow/\downarrow\rangle = |\Gamma_{8v}, \pm 1/2\rangle - \frac{\Delta^-}{3}\frac{1}{E_0' + \Delta_0'}|\Gamma_{8c}, \pm 1/2\rangle$$
$$|hc\uparrow/\downarrow\rangle = |\Gamma_{8c}, \pm 3/2\rangle + \frac{\Delta^-}{3}\frac{1}{E_0' + \Delta_0'}|\Gamma_{8v}, \pm 3/2\rangle$$
$$|lc\uparrow/\downarrow\rangle = |\Gamma_{8c}, \pm 1/2\rangle + \frac{\Delta^-}{3}\frac{1}{E_0' + \Delta_0'}|\Gamma_{8v}, \pm 1/2\rangle$$

Velocity matrix elements between these Γ-point eigenstates can be worked out from (3.2), and (3.3). I present here those that can contribute to transitions from initial hh and lh bands. Note that amongst Γ_{8v} states, by exact cancellation, $\mathbf{v}_{lh,s,hh,s'}(\Gamma) = 0$. Between Γ_{7v} and Γ_{8v} states,

$$\hbar\mathbf{v}_{so,s,hh,s'}(\Gamma) = \frac{Q\Delta^-}{3}\left(\frac{2}{E_0' + \Delta_0} + \frac{1}{E_0' + \Delta_0'}\right)\frac{1}{\sqrt{6}}\left[\sigma^z\hat{\mathbf{x}} - i\sigma^0\hat{\mathbf{y}} + 2\sigma^x\hat{\mathbf{z}}\right]_{s,s'}$$
$$\hbar\mathbf{v}_{so,s,lh,s'}(\Gamma) = \frac{Q\Delta^-}{3}\left(\frac{2}{E_0' + \Delta_0} + \frac{1}{E_0' + \Delta_0'}\right)\frac{1}{\sqrt{2}}\left[-\sigma^x\hat{\mathbf{x}} + \sigma^y\hat{\mathbf{y}}\right]_{s,s'}$$

Between Γ_{6c} and Γ_{8v} states,

$$\hbar\mathbf{v}_{c,s,lh,s'}(\Gamma) = P_8\frac{1}{\sqrt{6}}\left[-2\sigma^z\hat{\mathbf{z}} + \sigma^x\hat{\mathbf{x}} + \sigma^y\hat{\mathbf{y}}\right]_{s,s'}$$
$$\hbar\mathbf{v}_{c,s,hh,s'}(\Gamma) = P_8\frac{1}{\sqrt{2}}\left[\sigma^z\hat{\mathbf{x}} + i\sigma^0\hat{\mathbf{y}}\right]_{s,s'}$$

Between Γ_{6c} and Γ_{7v} states,

$$\hbar\mathbf{v}_{so,s,c,s'}(\Gamma) = P_7\frac{1}{\sqrt{3}}\left[\sigma^z\hat{\mathbf{z}} + \sigma^x\hat{\mathbf{x}} + \sigma^y\hat{\mathbf{y}}\right]_{s,s'}$$

Between Γ_{6c} and Γ_{8c} states,

$$\hbar\mathbf{v}_{c,s,lc,s'}(\Gamma) = P_8'\frac{1}{\sqrt{6}}\left[-2\sigma^z\hat{\mathbf{z}} + \sigma^x\hat{\mathbf{x}} + \sigma^y\hat{\mathbf{y}}\right]_{s,s'}$$
$$\hbar\mathbf{v}_{c,s,hc,s'}(\Gamma) = P_8'\frac{1}{\sqrt{2}}\left[\sigma^z\hat{\mathbf{x}} + i\sigma^0\hat{\mathbf{y}}\right]_{s,s'}$$

Between Γ_{6c} and Γ_{7c} states,

$$\hbar \mathbf{v}_{c,s,sc,s'}(\Gamma) = P_7' \frac{1}{\sqrt{3}} \left[\sigma^z \hat{\mathbf{z}} + \sigma^x \hat{\mathbf{x}} + \sigma^y \hat{\mathbf{y}}\right]_{s,s'}$$

Between Γ_{7c} and Γ_{8v} states (for these, I drop terms proportional to $(\Delta^-)^2$),

$$\hbar \mathbf{v}_{sc,s,lh,s'}(\Gamma) = \frac{Q}{\sqrt{2}} \left[-\sigma^x \hat{\mathbf{x}} + \sigma^y \hat{\mathbf{y}}\right]_{s,s'}$$
$$\hbar \mathbf{v}_{sc,s,hh,s'}(\Gamma) = \frac{Q}{\sqrt{6}} \left[\sigma^z \hat{\mathbf{x}} - i\sigma^0 \hat{\mathbf{y}} + 2\sigma^x \hat{\mathbf{z}}\right]_{s,s'}$$

Between Γ_{8c} and Γ_{8v} states, dropping terms proportional to $(\Delta^-)^2$,

$$\hbar \mathbf{v}_{lh,s,hc,s'}(\Gamma) = \frac{Q}{\sqrt{3}} \left[\sigma^z \hat{\mathbf{x}} - i\sigma^0 \hat{\mathbf{y}} - \sigma^x \hat{\mathbf{z}}\right]_{s,s'}$$
$$\hbar \mathbf{v}_{hh,s,lc,s'}(\Gamma) = \frac{Q}{\sqrt{3}} \left[-\sigma^z \hat{\mathbf{x}} - i\sigma^0 \hat{\mathbf{y}} + \sigma^x \hat{\mathbf{z}}\right]_{s,s'}$$

and $\hbar \mathbf{v}_{lh,s,lc,s'}(\Gamma) = \hbar \mathbf{v}_{hh,s,hc,s'}(\Gamma) = 0$. In the above equations, I have defined effective matrix element parameters

$$P_8 = P_0 - \frac{\Delta^-}{3} \frac{P_0'}{E_0' + \Delta_0'}$$
$$P_7 = P_0 + \frac{2\Delta^-}{3} \frac{P_0'}{E_0' + \Delta_0}$$
$$P_8' = P_0' + \frac{\Delta^-}{3} \frac{P_0}{E_0' + \Delta_0'}$$
$$P_7' = P_0' - \frac{2\Delta^-}{3} \frac{P_0}{E_0' + \Delta_0}.$$

C.1 "1+2" Population Control

The microscopic expression for population control is, from (2.3), (2.4), (2.18), and (2.28),

$$\xi_{(I)}^{ijk} = i \frac{e^3}{\hbar^3 \omega^3} \frac{\pi}{L^3} \sum_{cv\mathbf{k}} \sum_n \frac{\left\{v_{n,c}^i(\mathbf{k}), v_{v,n}^j(\mathbf{k})\right\}}{\omega_{nv}(\mathbf{k}) - \omega} v_{c,v}^k(\mathbf{k}) \, \delta(2\omega - \omega_{cv}(\mathbf{k})), \tag{C.1}$$

where $\left\{v_{n,c}^i(\mathbf{k}), v_{v,n}^j(\mathbf{k})\right\} \equiv (1/2)\left[v_{n,c}^i(\mathbf{k}) v_{v,n}^j(\mathbf{k}) + v_{n,c}^j(\mathbf{k}) v_{v,n}^i(\mathbf{k})\right]$ ensures the intrinsic symmetry $\xi_{(I)}^{jik} = \xi_{(I)}^{ijk}$. Switching to double index, changing the sum over $\mathbf{k}$ to an integral using $(1/L^3)\sum_{\mathbf{k}} = (1/8\pi^3)\int k^2 dk d\Omega$, and approximating velocities and the energy denominator by their values at the Γ point yields

$$\xi_{(I)}^{abc} = i \frac{e^3}{\hbar^3 \omega^3} \frac{1}{2\pi} \sum_{v,n} \frac{k_{cv} m_{cv}}{\hbar\omega_{nv}(\Gamma) - \hbar\omega} \left[\sum_{s,p} \sum_{s'} \left\{v_{ns',cs}^a(\Gamma), v_{vp,ns'}^b(\Gamma)\right\} v_{cs,vp}^c(\Gamma)\right],$$

where k_{cv} is given in (2.46). From cubic symmetry, only $\xi^{abc}_{(I)}$ needs to be evaluated. The sums over spin states can be worked out from the multiplication rules of the Pauli matrices: $\sigma^a\sigma^b = i\epsilon^{dce}\sigma^e + \delta^{cd}\sigma^0$. For hh-Γ_{8c}-c, the term in square brackets is zero. For lh-Γ_{8c}-c, the term in square brackets is $i\,(2/3)\,P'_8 Q P_8/\hbar^3$. For hh-Γ_{7c}-c, the term in square brackets is zero. For lh-Γ_{7c}-c, the term in square brackets is $i\,(2/3)\,P'_7 Q P_8/\hbar^3$. For hh-Γ_{7v}-c, the term in square brackets is zero. For lh-Γ_{7v}-c, the term in square brackets is

$$i\frac{2}{3}\frac{P_7}{\hbar}\frac{Q\Delta^-}{3\hbar}\left(\frac{2}{E'_0+\Delta_0}+\frac{1}{E'_0+\Delta'_0}\right)\frac{P_8}{\hbar}.$$

The result, which gives $\xi^{abc}_{(I)}$ in mks, is

$$\begin{aligned}\xi^{abc}_{(I)} =& \frac{-e^3}{3\pi}\frac{2}{\hbar}\sqrt{E_{P8}E_Q}\left[\left(\frac{m_{c,hh}}{m}\right)^{3/2}+\left(\frac{m_{c,lh}}{m}\right)^{3/2}\right]\frac{\sqrt{2\hbar\omega-E_g}}{(2\hbar\omega)^3}\\ &\times\left[\frac{\sqrt{E_{P8'}}}{E'_0+\Delta'_0-\hbar\omega}+\frac{\sqrt{E_{P7'}}}{E'_0-\hbar\omega}-\frac{\sqrt{E_{P7}}}{\Delta_0+\hbar\omega}\frac{\Delta^-}{3}\left(\frac{2}{E'_0+\Delta_0}+\frac{1}{E'_0+\Delta'_0}\right)\right].\end{aligned} \tag{C.2}$$

Expanding the effective matrix elements and eliminating terms of the order $(\Delta^-)^2$ yields the final result

$$\xi^{abc}_{(I)} = \frac{-e^3}{3\pi}\frac{2}{\hbar}\left[\left(\frac{m_{c,hh}}{m}\right)^{3/2}+\left(\frac{m_{c,lh}}{m}\right)^{3/2}\right]\frac{\sqrt{2\hbar\omega-E_g}}{(2\hbar\omega)^3}\sqrt{E_Q}\,(X_1+X_2+X_3), \tag{C.3}$$

where

$$X_1 = \sqrt{E_P E_{P'}}\left(\frac{1}{E'_0-\hbar\omega}+\frac{1}{E'_0+\Delta'_0-\hbar\omega}\right), \tag{C.4}$$

$$X_2 = -\frac{\Delta^-}{3}E_P\left[\frac{2\,(E'_0+\Delta_0)^{-1}}{E'_0-\hbar\omega}-\frac{(E'_0+\Delta'_0)^{-1}}{E'_0+\Delta'_0-\hbar\omega}+\frac{2\,(E'_0+\Delta_0)^{-1}+(E'_0+\Delta'_0)^{-1}}{\Delta_0+\hbar\omega}\right], \tag{C.5}$$

$$X_3 = -\frac{\Delta^-}{3}\frac{E_{P'}}{E'_0+\Delta'_0}\left(\frac{1}{E'_0-\hbar\omega}+\frac{1}{E'_0+\Delta'_0-\hbar\omega}\right). \tag{C.6}$$

Note that $\left(-e^3\right)$ is positive. For typical semiconductors, X_3 can be neglected and

$$\frac{X_2}{X_1} \approx -\frac{\Delta^-}{2\,(\Delta_0+\hbar\omega)}\sqrt{\frac{E_P}{E_{P'}}}.$$

In X_2, the most important term is the last, which comes from the interference of $\{hh, lh\}$-*so*-c two-photon transitions and $\{hh, lh\}$-c one-photon transitions.

The expression (C.3) only includes the allowed-allowed transitions from the hh and lh bands. At photon energies for which $2\hbar\omega > E_g + \Delta_0$, one should add the contribution due to the transition *so*-*uc*-*c*.

Because of (3.21), (C.3) is also an analytical expression for $\mathrm{Im}\chi^{(2)abc}(-2\omega;\omega,\omega)$. Jha and Wynne have also used **k**-independent velocity matrix elements and spherical, parabolic bands

to derive an expression for $\chi^{(2)abc}(-2\omega;\omega,\omega)$, but they did not include the interband spin-orbit coupling term Δ^- [158]. Taking the imaginary part of their Eq. 4.4 for $\hbar\omega < E_g < 2\hbar\omega$, and correcting a factor of π error, reproduces the $\mathrm{Im}\chi^{(2)abc}(-2\omega;\omega,\omega)$ one would find from (C.3) but with $X_2 = X_3 = 0$. Also, they make the approximation $\hbar\omega \approx E_g/2$ in the term X_1.

To get a PBA expression for the population control ratio requires PBA expressions for one- and two-photon absorption. I take the same approach used to derive (C.3), but for simplicity, I take $\Delta^- = 0$ in the following. In the PBA, at photon energies $2\hbar\omega < E_g + \Delta_0$, one-photon absorption is

$$\xi_{(1)}^{ij} = \frac{e^2}{3\pi}\frac{\sqrt{2m}E_P}{\hbar^2}\left(\left(\frac{m_{c,lh}}{m}\right)^{\frac{3}{2}} + \left(\frac{m_{c,hh}}{m}\right)^{\frac{3}{2}}\right)\frac{\sqrt{2\hbar\omega - E_g}}{(2\hbar\omega)^2}\delta^{ij}. \tag{C.7}$$

In a material of cubic symmetry, the two-photon absorption tensor $\xi_{(2)}^{ijkl}$ has three independent components $\xi_{(2)}^{aaaa}$, $\xi_{(2)}^{aabb}$, and $\xi_{(2)}^{abab}$, which are alternately parameterized by the set $\left\{\xi_{(2)}^{aaaa}, \sigma, \delta\right\}$ [see (3.23)]. The allowed-forbidden two-photon absorption in the isotropic Kane model, neglecting three- and four-band terms, is

$$\xi_{(2)}^{ijkl} = \bar{\xi}_{(2)}\left[\sqrt{\frac{m_{c,hh}}{m}}\left(\frac{3}{2}\delta^{ik}\delta^{jl} + \frac{3}{2}\delta^{il}\delta^{jk} - \delta^{ij}\delta^{kl}\right) + \sqrt{\frac{m_{c,lh}}{m}}\left(\frac{11}{6}\delta^{ik}\delta^{jl} + \frac{11}{6}\delta^{il}\delta^{jk} + \delta^{ij}\delta^{kl}\right)\right], \tag{C.8}$$

where

$$\bar{\xi}_{(2)} \equiv \frac{64\sqrt{2}}{15\pi}\frac{e^4 E_P}{\sqrt{m}}\frac{(2\hbar\omega - E_g)^{\frac{3}{2}}}{(2\hbar\omega)^6}.$$

Note the additional symmetry, $\xi_{(2)}^{aaaa} = 2\xi_{(2)}^{abab} + \xi_{(2)}^{aabb}$ in this isotropic model. The allowed-allowed two-photon absorption, neglecting $\Delta_0'/(E_0' - E_g + \hbar\omega)$, has $\xi_{(2)}^{aaaa} = \xi_{(2)}^{aabb} = 0$ and

$$\xi_{(2)}^{abab} = \xi_{(1)}^{aa}\frac{e^2}{\omega^2 m^2}\frac{2m}{E_P}\frac{E_{P_0'}E_Q}{(E_0' - E_g + \hbar\omega)^2},$$

which agrees with Arifzhanov and Ivchenko [171]. Thus, at photon energies for which allowed-allowed transitions dominate two-photon absorption,

$$R \approx \frac{\xi_{(I)}}{\sqrt{\xi_{(1)}\xi_{(2)}^{abba}}} = 1, \tag{C.9}$$

whereas when allowed-forbidden transitions dominate two-photon absorption,

$$R = 2\hbar\omega\sqrt{\frac{E_Q E_{P'}}{E_P(2\hbar\omega - E_g)}}\sqrt{\frac{\left(\frac{m_{c,hh}}{m}\right)^{3/2} + \left(\frac{m_{c,lh}}{m}\right)^{3/2}}{\frac{9}{10}\sqrt{\frac{m_{c,hh}}{m}} + \frac{11}{10}\sqrt{\frac{m_{c,lh}}{m}}}}\left\{\frac{1}{\Delta_0' + E_0' - E_g + \hbar\omega} + \frac{1}{E_0' - E_g + \hbar\omega}\right\} \tag{C.10}$$

C.2 "1+2" Spin Control

From (2.3), (2.4), (2.20a), and (2.32),

$$\zeta_{(I;e)}^{ijkl} \equiv i\frac{e^3}{2\hbar^3\omega^3}\frac{2\pi}{L^3}\sum_{\mathbf{k}}{\sum_{c,c'}}'\sum_{v}\langle c\mathbf{k}|\, S^i\,|c'\mathbf{k}\rangle\, v^l_{c',v}(\mathbf{k})\sum_{n}\frac{\left\{v^j_{n,c}(\mathbf{k}),v^k_{v,n}(\mathbf{k})\right\}}{\omega_{nv}(\mathbf{k})-\omega}\delta\left(2\omega-\omega_{cv}(\mathbf{k})\right)$$

Proceeding as with population control, I take the velocity matrix elements at their Γ point value, etc. and

$$\langle c,s,\Gamma|\, S^i\,|c,s',\Gamma\rangle = \frac{\hbar}{2}\left[\sigma^i\right]_{s,s'}$$

$$\zeta_{(I;e)}^{ijkl} \equiv i\frac{e^3}{4\pi\hbar^2\omega^3}\sum_{v,n}\frac{k_{cv}m_{cv}}{\hbar\omega_{nv}(\Gamma)-\hbar\omega}\left[\sum_{s,s',p,s''}\left[\sigma^i\right]_{s,s'}\left\{v^j_{n,s'',c,s}(\Gamma),v^k_{v,p,n,s''}(\Gamma)\right\}v^l_{c,s',v,p}(\Gamma)\right]. \tag{C.11}$$

There are two independent components to $\zeta_{(I)}^{ijkl}$, $\zeta_{IA} = -i\zeta_{(I)}^{zxxz}$ and $\zeta_{IB} = -i\zeta_{(I)}^{zzxx}$. For ζ_{IA}, the term in square brackets is

$$-\frac{2}{3}\frac{P'_8}{\hbar}\frac{Q}{\hbar}\frac{P_8}{\hbar}$$

for initial lh and intermediate Γ_{8c} (only intermediate hc is nonzero); is

$$\frac{2}{3}\frac{P'_7}{\hbar}\frac{Q}{\hbar}\frac{P_8}{\hbar}$$

for initial lh and intermediate Γ_{7c}; is

$$\frac{2}{3}\frac{P_7}{\hbar}\frac{P_8}{\hbar}\frac{Q\Delta^-}{\hbar 3}\left(\frac{2}{E'_0+\Delta_0}+\frac{1}{E'_0+\Delta'_0}\right)$$

for initial lh and intermediate Γ_{7v}; and is zero for initial hh and all n since $v^z_{c,s',hh,p}(\Gamma)=0$. The result is

$$\begin{aligned}\zeta_{IA} =& \frac{-e^3}{3\pi}\frac{\sqrt{2\hbar\omega-E_g}}{(2\hbar\omega)^3}\left(\left(\frac{m_{c,lh}}{m}\right)^{3/2}+\left(\frac{m_{c,hh}}{m}\right)^{3/2}\right)\sqrt{E_Q E_{P8}}\\ &\times\left[\frac{\sqrt{E_{P8'}}}{E'_0+\Delta'_0-\hbar\omega}-\frac{\sqrt{E_{P7'}}}{E'_0-\hbar\omega}+\frac{\Delta^-}{3}\left(\frac{2}{E'_0+\Delta_0}+\frac{1}{E'_0+\Delta'_0}\right)\frac{\sqrt{E_{P7}}}{\Delta_0+\hbar\omega}\right]\end{aligned}$$

For ζ_{IB}, the term in square brackets in (C.11) is

$$\frac{1}{2}\frac{Q}{\hbar}\frac{P_8}{\hbar}\frac{P'_8}{\hbar}$$

for initial hh and intermediate Γ_{8c} (only intermediate lc is nonzero); is

$$-\frac{1}{6}\frac{P'_8}{\hbar}\frac{Q}{\hbar}\frac{P_8}{\hbar}$$

for initial lh and intermediate Γ_{8c} (only intermediate hc is nonzero); is

$$\frac{1}{2}\frac{P'_7}{\hbar}\frac{Q}{\hbar}\frac{P_8}{\hbar}$$

for initial hh and intermediate Γ_{7c}; is

$$-\frac{1}{6}\frac{P_7'}{\hbar}\frac{Q}{\hbar}\frac{P_8}{\hbar}$$

for initial lh and intermediate Γ_{7c}; is

$$\frac{1}{2}\frac{P_7}{\hbar}\frac{P_8}{\hbar}\frac{Q\Delta^-}{\hbar 3}\left(\frac{2}{E_0'+\Delta_0}+\frac{1}{E_0'+\Delta_0'}\right)$$

for initial hh and intermediate Γ_{7v}; and is

$$-\frac{1}{6}\frac{P_7}{\hbar}\frac{P_8}{\hbar}\frac{Q\Delta^-}{\hbar 3}\left(\frac{2}{E_0'+\Delta_0}+\frac{1}{E_0'+\Delta_0'}\right)$$

for initial lh and intermediate Γ_{7v}. The result is

$$\begin{aligned}\zeta_{IB} =& \frac{-e^3}{6\pi}\frac{\sqrt{2\hbar\omega-E_g}}{(2\hbar\omega)^3}\left(\left(\frac{m_{c,hh}}{m}\right)^{3/2}+\left(\frac{m_{c,lh}}{m}\right)^{3/2}\right)\sqrt{E_Q E_{P8}}\\ &\times\left[\frac{-\sqrt{E_{P8'}}}{E_0'+\Delta_0'-\hbar\omega}-\frac{\sqrt{E_{P7'}}}{E_0'-\hbar\omega}+\frac{\Delta^-}{3}\left(\frac{2}{E_0'+\Delta_0}+\frac{1}{E_0'+\Delta_0'}\right)\frac{\sqrt{E_{P7}}}{\Delta_0+\hbar\omega}\right].\end{aligned}$$

Expanding the effective matrix elements and eliminating terms of the order $(\Delta^-)^2$ yields the final result

$$\zeta_{IA} = -\frac{(-e^3)}{3\pi}\left(\left(\frac{m_{c,hh}}{m}\right)^{3/2}+\left(\frac{m_{c,lh}}{m}\right)^{3/2}\right)\frac{\sqrt{2\hbar\omega-E_g}}{(2\hbar\omega)^3}\sqrt{E_Q}\left(Z_- + Z_+' + Z_-''\right), \quad \text{(C.12a)}$$

$$\zeta_{IB} = -\frac{(-e^3)}{6\pi}\left(\left(\frac{m_{c,hh}}{m}\right)^{3/2}+\left(\frac{m_{c,lh}}{m}\right)^{3/2}\right)\frac{\sqrt{2\hbar\omega-E_g}}{(2\hbar\omega)^3}\sqrt{E_Q}\left(Z_+ + Z_-' + Z_+''\right), \quad \text{(C.12b)}$$

where

$$\begin{aligned}Z_\pm &= \sqrt{E_P E_{P'}}\left(\frac{1}{E_0'-\hbar\omega}\pm\frac{1}{E_0'+\Delta_0'-\hbar\omega}\right)\\ Z_\pm' &= -\frac{\Delta^- E_P}{3}\left[\left(\frac{2}{E_0'+\Delta_0}+\frac{1}{E_0'+\Delta_0'}\right)\frac{1}{\Delta_0+\hbar\omega}\right.\\ &\qquad\left.+\frac{2}{E_0'+\Delta_0}\frac{1}{E_0'-\hbar\omega}\pm\frac{1}{E_0'+\Delta_0'}\frac{1}{E_0'+\Delta_0'-\hbar\omega}\right]\\ Z_\pm'' &= -\frac{\Delta^- E_{P'}}{3}\frac{1}{E_0'+\Delta_0'}\left(\frac{1}{E_0'-\hbar\omega}\pm\frac{1}{E_0'+\Delta_0'-\hbar\omega}\right)\end{aligned}$$

In $Z_\pm$, the first term is from intermediate sc states and the second term is from intermediate lc and hc states. In $Z_\pm'$, the first term is from intermediate so states, the second term is from intermediate sc states, and the third term is from intermediate lc and hc states. In $Z_\pm''$, the first term is from intermediate so states, and the second term is from intermediate hc and lc states. The term $Z_\pm''$ can be neglected for typical semiconductors. Note that $(\zeta_{IA}+2\zeta_{IB})$ has contributions only from intermediate so and sc states. This only includes transitions from initial hh and lh states; transitions from initial so states, which contribute when $2\hbar\omega > E_g+\Delta_0$, have been neglected.

C.3 Allowed-allowed contribution to two-photon spin injection

To calculate $\dot{\mathbf{S}}$ and $\dot{N}$ due to allowed-allowed transitions, one can approximate all the matrix elements and energies in the two-photon amplitude by their value at the Γ point, thus avoiding the integral over $\mathbf{k}$. Since the bands are doubly degenerate at the Γ point, one can use Eq. (4.4).

C.3.1 Light incident along [001]

Since I use a basis of states with spin quantized along $\hat{\mathbf{z}}$, $\langle c,\Gamma|\, S^z\,|c',\Gamma\rangle \propto \delta_{c,c'}$ and we have

$$\dot{\mathcal{S}}^z = \frac{\pi\hbar}{L^3}\sum_v \left[\left|\Omega^{(2)}_{c\uparrow,v,\Gamma}\right|^2 - \left|\Omega^{(2)}_{c\downarrow,v,\Gamma}\right|^2\right]\sum_{\mathbf{k}}\delta\left[2\omega - \omega_{cv}\left(\mathbf{k}\right)\right]$$

where $c\uparrow$ and $c\downarrow$ are shorthand for the bands with states $|\Gamma_{6c},\pm 1/2\rangle$.

For σ^+ light, with polarization $\hat{\mathbf{e}}_\omega = \left(\hat{\mathbf{x}} + i\hat{\mathbf{y}}\right)/\sqrt{2}$, and $\dot{\boldsymbol{\mathcal{S}}} \parallel \hat{\mathbf{z}}$ from Eq. (4.2) and the degree of spin polarization is

$$P = \frac{\sum_v\left[\left|\Omega^{(2)}_{c\downarrow,v,\Gamma}\right|^2 - \left|\Omega^{(2)}_{c\uparrow,v,\Gamma}\right|^2\right]}{\sum_v\left[\left|\Omega^{(2)}_{c\downarrow,v,\Gamma}\right|^2 + \left|\Omega^{(2)}_{c\uparrow,v,\Gamma}\right|^2\right]}.$$

The non-zero matrix elements of $\hat{\mathbf{e}}_\omega\cdot\hat{\mathbf{v}}$ in the eigenstate basis that can cause a two-photon transition between v and c are

$$\mathbf{e}_\omega\cdot\mathbf{v}_{hc\downarrow,lh\downarrow}\left(\Gamma\right) = -\sqrt{\frac{2}{3}}Q \tag{C.13}$$

$$\mathbf{e}_\omega\cdot\mathbf{v}_{c\downarrow,hc\downarrow}\left(\Gamma\right) = P_0' + \frac{\Delta^-}{3}\frac{1}{E_0'+\Delta_0'}P_0 \tag{C.14}$$

$$\mathbf{e}_\omega\cdot\mathbf{v}_{sc\downarrow,lh\uparrow}\left(\Gamma\right) = -Q \tag{C.15}$$

$$\mathbf{e}_\omega\cdot\mathbf{v}_{c\uparrow,sc\downarrow}\left(\Gamma\right) = \sqrt{\frac{2}{3}}\left(P_0' - \frac{2\Delta^-}{3}\frac{P_0}{E_0'+\Delta_0}\right) \tag{C.16}$$

$$\mathbf{e}_\omega\cdot\mathbf{v}_{so\downarrow,lh\uparrow}\left(\Gamma\right) = \frac{-\Delta^- Q/3}{E_0'+\Delta_0}\left(\frac{E_0'+\Delta_0}{E_0'+\Delta_0'}+2\right) \tag{C.17}$$

$$\mathbf{e}_\omega\cdot\mathbf{v}_{c\uparrow,so\downarrow}\left(\Gamma\right) = \sqrt{\frac{2}{3}}\left(P_0 + \frac{2\Delta^-}{3}\frac{P_0'}{E_0'+\Delta_0}\right), \tag{C.18}$$

where I have dropped terms second order in Δ^-. Note that $\mathbf{e}_\omega\cdot\mathbf{v}_{hh\downarrow,lh\downarrow}\left(\Gamma\right) = 0$ by an exact cancellation, as it should from symmetry considerations. Thus,

$$\Omega^{(2)}_{c\downarrow,lh\downarrow,\Gamma} = -\left(\frac{e}{\hbar\omega}\right)^2\hbar\left|E_\omega\right|^2\sqrt{\frac{2}{3}}Q\left[AP_0' + BP_0\Delta^-\right],$$

where $A \equiv \left(E_0'+\Delta_0'-E_g/2\right)^{-1}$ and $B \equiv \left(E_0'+\Delta_0'\right)^{-1}A/3$. Also,

$$\Omega^{(2)}_{c\uparrow,lh\uparrow,\Gamma} = -\left(\frac{e}{\hbar\omega}\right)^2\hbar\left|E_\omega\right|^2\sqrt{\frac{2}{3}}Q\left[CP_0' - DP_0\Delta^-\right],$$

where $C \equiv (E_0' - E_g/2)^{-1}$,

$$D \equiv \frac{1}{E_0' + \Delta_0}\left[\frac{1}{E_g/2 + \Delta_0}\frac{1}{3}\left(\frac{E_0' + \Delta_0}{E_0' + \Delta_0'} + 2\right) + \frac{2}{3}C\right],$$

and I have dropped terms proportional to $QP_0'(\Delta^-)^2$. The degree of spin polarization is then

$$P = \frac{(AP_0' + BP_0\Delta^-)^2 - (CP_0' - DP_0\Delta^-)^2}{(AP_0' + BP_0\Delta^-)^2 + (CP_0' - DP_0\Delta^-)^2}. \tag{C.19}$$

C.3.2 Light incident along [111]

For σ^+ light incident along [111], it is more tedious to obtain an expression like Eq. (C.19) since there are more non-zero matrix elements of $\hat{\mathbf{e}}_\omega \cdot \hat{\mathbf{v}}$ than for σ^+ light incident along [001]. By rotating the basis to states quantized along [111], the matrix of elements of $\hat{\mathbf{e}}_\omega \cdot \hat{\mathbf{v}}$ becomes simpler, but the Hamiltonian is no longer in 2×2 blocks. When $\Delta^- = 0$, the latter is not an issue. In that case, I find

$$\begin{aligned}
\Omega^{(2)}_{c\downarrow,lh\uparrow,\Gamma} &= \frac{2}{3}i\left(\frac{e}{\hbar\omega}\right)^2 \hbar\,|E_\omega|^2\, QP_0'A \\
\Omega^{(2)}_{c\uparrow,hh\uparrow,\Gamma} &= \frac{2}{3\sqrt{3}}i\left(\frac{e}{\hbar\omega}\right)^2 \hbar\,|E_\omega|^2\, QP_0'\,(A + 2C) \\
\Omega^{(2)}_{c\uparrow,hh\downarrow,\Gamma} &= -i\frac{\sqrt{2}}{3\sqrt{3}}\left(\frac{e}{\hbar\omega}\right)^2 \hbar\,|E_\omega|^2\, QP_0'\,(C - A)\,,
\end{aligned}$$

where A and C are as defined in the previous subsection, and $\uparrow$ and $\downarrow$ are along [111]. With the assumption that $\Delta_0' \ll E_0' - E_g/2$, $A \approx C$ and I find that

$$P\left(\Delta^- = 0\right) = -1/2. \tag{C.20}$$

Appendix D

Symmetry of one-photon effects

In this appendix, I present the symmetry constraints on the one-photon effects—absorption, spin injection, current injection, and spin-current injection—that are discussed in Chapter 5. I present results for the point group T_d, which applies to semiconductors with zinc-blende symmetry, and for the point group D_{2d}, which applies to semiconductors with zinc-blende symmetry under strain along one of the cubic axes.

The one-photon absorption tensor $\xi^{ij}_{(1)}$ is a second-rank tensor satisfying the reality condition $\xi^{ij}_{(1)} = \xi^{ji*}_{(1)}$, and real in the independent-particle approximation (IPA). The one-photon spin injection pseudotensor $\zeta^{ijk}_{(1)} = \sum_{\mathbf{k}} \zeta^{ijk}_{(1)}(\mathbf{k})$ is a third-rank pseudotensor satisfying the reality condition $\zeta^{ikj}_{(1)} = \zeta^{ijk*}_{(1)}$, and imaginary in the IPA. Thus, in the IPA, $\zeta^{ijk}_{(1)} = Z^{il}\varepsilon^{ljk}$, where Z^{ij} is an arbitrary, real tensor. The one-photon current injection tensor $\eta^{ijk}_{(1)}$ is a third-rank tensor satisfying the reality condition $\eta^{ikj}_{(1)} = \eta^{ijk*}_{(1)}$, and imaginary in the IPA. Thus, in the IPA, $\eta^{ijk}_{(1)} = \gamma^{il}\varepsilon^{ljk}$, where γ^{ij} is an arbitrary, real pseudotensor [116]. The one-photon spin-current injection tensor $\mu^{ijkl}_{(1)}$ is a fourth-rank pseudotensor satisfying the reality condition $\mu^{ijlk}_{(1)} = \mu^{ijkl*}_{(1)}$, and real in the independent-particle approximation.

Td symmetry

For T_d, $\xi^{ij}_{(1)} \propto \delta^{ij}$ [84], $\zeta^{ijk}_{(1)} \propto \varepsilon^{ijk}$ [2], and $\eta^{ijk}_{(1)} = 0$ [99]. The spin-current has two independent components and non-zero elements

$$\mu^{xxyy}_{(1)} = \mu^{zzxx}_{(1)} = \mu^{yyzz}_{(1)} = -\mu^{xxzz}_{(1)} = -\mu^{zzyy}_{(1)} = -\mu^{yyxx}_{(1)},$$

and

$$\begin{aligned}\mu^{xyxy}_{(1)} &= \mu^{zxzx}_{(1)} = \mu^{yzyz}_{(1)} = -\mu^{xzxz}_{(1)} = -\mu^{zyzy}_{(1)} = -\mu^{yxyx}_{(1)} \\ &= \mu^{xyyx}_{(1)} = \mu^{zxxz}_{(1)} = \mu^{yzzy}_{(1)} = -\mu^{xzzx}_{(1)} = -\mu^{zyyz}_{(1)} = -\mu^{yxxy}_{(1)}.\end{aligned}$$

There is no second-rank pseudotensor that is invariant under the point group T_d. Thus, $\mu_{(1)}^{ijkl}\delta^{kl}$ is zero, which can easily be verified from the non-zero components of $\mu_{(1)}^{ijkl}$.

D2d symmetry

The point group D_{2d} has a preferred axis, which I will choose to be the z-axis in what follows. One-photon absorption has two independent components and non-zero elements $\xi_{(1)}^{xx} = \xi_{(1)}^{yy}$ and $\xi_{(1)}^{zz}$. The spin injection is has two independent components and non-zero elements

$$\zeta_{(1)}^{xyz} = -\zeta_{(1)}^{xzy} = \zeta_{(1)}^{yzx} = -\zeta_{(1)}^{yxz}$$
$$\zeta_{(1)}^{zxy} = -\zeta_{(1)}^{zyx},$$

or alternately $Z^{xx} = Z^{yy}$ and Z^{zz}. The current injection has one independent component with nonzero elements

$$\eta_{(1)}^{xyz} = -\eta_{(1)}^{xzy} = -\eta_{(1)}^{yzx} = \eta_{(1)}^{yxz}$$

or alternately $\gamma^{xx} = -\gamma^{yy} = \eta_{(1)}^{xyz}$. The spin-current injection tensor has seven independent components and non-zero elements

$$\mu^{xxyy} = -\mu^{yyxx}$$
$$\mu^{zzxx} = -\mu^{zzyy}$$
$$\mu^{yyzz} = -\mu^{xxzz}$$

$$\mu^{xyxy} = \mu^{xyyx} = -\mu^{yxyx} = -\mu^{yxxy}$$
$$\mu^{zxzx} = \mu^{zxxz} = -\mu^{zyzy} = -\mu^{zyyz}$$
$$\mu^{yzyz} = \mu^{yzzy} = -\mu^{xzxz} = -\mu^{xzzx}$$

$$\mu^{xxxx} = -\mu^{yyyy}$$

The first group of six elements are all equal under T_d, the second group of twelve elements are all equal under T_d, and the last two are zero under T_d.

Appendix E

Intermediate-state Coulomb enhancement

Consider the functions $N^{(\text{a-f})}$ and $N^{(\text{a-a})}$, which appear in (6.32) and (6.34); I refer to them collectively as N. First, note that due to the energy-conserving δ-function in (6.7), κ will be equal to κ_{cv} [see Eq. (6.37)], and thus N is a function only of ω, E^g_{cv}, $E^g_{c'v'}$, m_{cv}, and $m_{c'v'}$. Second, note that N is defined so that $N \to 1$ if the electron-hole attraction is turned off, for example by letting $\epsilon \to \infty$.[1] This allows N to be identified as part of the Coulomb enhancement. In particular, N is the enhancement due to the Coulomb interaction in the intermediate states; if the Coulomb interaction is neglected for the intermediate states, $N = 1$ [185]. [Note that Lee and Fan [174] did not allow for $v' \neq v$ in N (related to J_j in their notation).]

Since the integrand is smooth for the parameter range of interest, numerical integration of N is straightforward; however, it need not be undertaken. Further simplification is possible since the parameter γ can be considered to be much less than one. Since most materials have an exciton binding energy that is much smaller than the band gap, $\hbar\omega$ is detuned from the band edge by many exciton binding energies at photon energies consistent with the approximations made here. In GaAs, for example, when $2\hbar\omega$ is within 500 meV of the gap, γ is at most 0.09. An expansion of $N^{(\text{a-f})}$ for small γ,

$$N^{(\text{a-f})} = 1 + \frac{2}{3}\gamma_{c'v'} + \left(\frac{4}{3}\ln 2 - \frac{1}{3}\right)\gamma^2_{c'v'} + \left(S_0 - \frac{2}{15}a^2_{cv}\kappa^2\right)\gamma^3_{c'v'} + O\left(\gamma^4_{c'v'}\right),$$

where $S_0 \approx 0.5633$, shows that $N^{(\text{a-f})}$ is approximately 1 and nearly constant as a function of ω. The same is true of $N^{(\text{a-a})}$, which has the expansion

$$N^{(\text{a-a})} = 1 - \frac{2}{a_{cv}}\left(a_{c'v'} - a_{cv}\right)P + O\left(\gamma^4_{c'v'}\right),$$

[1] Mahan instead defines a quantity $J_\kappa = N(\kappa)\gamma^2\left(1 + (a\gamma\kappa)^2\right)^{-1}$ [176].

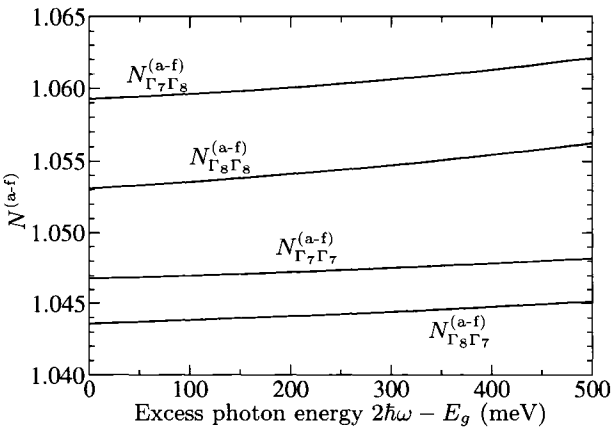

Figure E.1: The factor $N^{(a\text{-}f)}$ [intermediate-state Coulomb enhancement, see Eq. (6.31)] for GaAs. The first (second) subscript is v (v'); subscripts for $c = c' = \Gamma_6$ are not shown; Γ_8 denotes the heavy and light hole bands, and Γ_7 denotes the split-off band.

where, with $S_1 \approx 1.645$,

$$P \equiv \gamma_{c'v'} + \left(2\ln 2 - \frac{a_{c'v'}}{a_{cv}}\right)\gamma_{c'v'}^2 + \left(\frac{2a_{c'v'}^2}{3a_{cv}^2} - \frac{2a_{c'v'}}{a_{cv}} - \frac{1}{3}a_{c'v'}^2\kappa^2 + S_1\right)\gamma_{c'v'}^3.$$

In fact, when $m_{cv} = m_{c'v'}$, $N^{(a\text{-}a)} = 1$ even to fourth order in $\gamma_{c'v'}$. Fig. E.1 shows a numerical integration of $N^{(a\text{-}f)}$ using the parameters of GaAs.

Bibliography

[1] E. Braun, Proc. R. Soc. London A **371**, 104 (1980).

[2] M. I. Dyakonov and V. I. Perel, *Optical Orientation* (North-Holland, Amsterdam, 1984), vol. 8 of *Modern Problems in Condensed Matter Sciences*, Chap. 2.

[3] R. Atanasov, A. Haché, J. L. P. Hughes, H. M. van Driel, and J. E. Sipe, Phys. Rev. Lett **76**, 1703 (1996).

[4] A. Haché, Y. Kostoulas, R. Atanasov, J. L. P. Hughes, J. E. Sipe, and H. M. vanDriel, Phys. Rev. Lett **78**, 306 (1997).

[5] D. D. Awschalom and J. M. Kikkawa, Physics Today **52**, 33 (1999).

[6] S. A. Wolf, D. D. Awschalom, R. A. Buhrman, J. M. Daughton, S. von Molnár, M. L. Roukes, A. Y. Chtchelkanova, and D. M. Treger, Science **294**, 1488 (2001).

[7] D. Awschalom, D. Loss, and N. Samarth, eds., *Semiconductor spintronics and quantum computation* (Springer-Verlag, Berlin, 2002).

[8] I. Žutić, J. Fabian, and S. Das Sarma, Rev. Mod. Phys. **76**, 1 (2004).

[9] M. Oestreich, J. Hübner, D. Hagele, P. J. Klar, W. Heimbrodt, W. W. Rühle, D. E. Ashenford, and B. Lunn, Appl. Phys. Lett. **74**, 1251 (1999).

[10] R. Fiederling, M. Keim, G. Reuscher, W. Ossau, G. Schmidt, A. Waag, and L. W. Molenkamp, Nature **402**, 787 (1999).

[11] Y. Ohno, D. K. Young, B. Beschoten, F. Matsukura, H. Ohno, and D. D. Awschalom, Nature **402**, 790 (1999).

[12] P. R. Hammar, B. R. Bennett, M. J. Yang, and M. Johnson, Phys. Rev. Lett **83**, 203 (1999).

[13] S. Gardelis, C. G. Smith, C. H. W. Barnes, E. H. Linfield, and D. A. Ritchie, Phys. Rev. B **60**, 7764 (1999).

[14] D. Hagele, M. Oestreich, W. W. Rühle, N. Nestle, and K. Eberl, Appl. Phys. Lett. **73**, 1580 (1998).

[15] J. M. Kikkawa and D. D. Awschalom, Nature **397**, 139 (1999).

[16] J. Rudolph, D. Hägele, H. M. Gibbs, G. Khitrova, and M. Oestreich, Appl. Phys. Lett. **82**, 4516 (2003).

[17] J. S. Blakemore, J. Appl. Phys. **53**, R123 (1982).

[18] E. L. Ivchenko, Sov. Phys. Solid State **14**, 2942 (1973).

[19] T. Matsuyama, H. Horinaka, W. Wada, T. Kondo, M. Hangyo, T. Nakanishi, S. Okumi, and K. Togawa, Jpn. J. Appl. Phys. **40**, L555 (2001).

[20] R. D. R. Bhat, P. Nemec, Y. Kerachian, H. M. van Driel, and J. E. Sipe, Phys. Rev. B **71**, 035209 (2005).

[21] E. A. Manykin and A. M. Afanasev, Sov. Phys. JETP **25**, 828 (1967).

[22] M. Shapiro and P. Brumer, J. Chem. Soc., Faraday Trans. **93**, 1263 (1997).

[23] R. J. Gordon, L. Zhu, and T. Seideman, Acc. Chem. Res. **32**, 1007 (1999).

[24] Y. Y. Yin, C. Chen, D. S. Elliott, and A. V. Smith, Phys. Rev. Lett **69**, 2353 (1992).

[25] N. B. Baranova, I. M. Beterov, B. Y. Zel'dovich, I. I. Ryabtsev, A. N. Chudinov, and A. A. Shul'ginov, JETP Lett. **55**, 439 (1992).

[26] B. Sheehy, B. Walker, and L. F. DiMauro, Phys. Rev. Lett **74**, 4799 (1995).

[27] E. M. Baskin and M. V. Éntin, JETP Lett. **48**, 601 (1988).

[28] M. V. Éntin, Sov. Phys. Semicond. **23**, 664 (1989).

[29] K. N. Alekseev, M. V. Erementchouk, and F. V. Kusmartsev, Europhys. Lett. **47**, 595 (1999).

[30] E. Dupont, P. B. Corkum, H. C. Liu, M. Buchanan, and Z. R. Wasilewski, Phys. Rev. Lett **74**, 3596 (1995).

[31] W. Pötz, Appl. Phys. Lett. **72**, 3002 (1998).

[32] J. B. Khurgin, Appl. Phys. Lett. **73**, 13 (1998).

[33] A. Najmaie, R. D. R. Bhat, and J. E. Sipe, Phys. Rev. B **68**, 165348 (2003).

[34] D. H. Marti, M.-A. Dupertuis, and B. Deveaud, Phys. Rev. B **69**, 35335 (2004).

[35] A. Najmaie, A. L. Smirl, and J. E. Sipe, Phys. Rev. B **71**, 075306 (2005).

[36] J. M. Fraser, A. I. Shkrebtii, J. E. Sipe, and H. M. van Driel, Phys. Rev. Lett **83**, 4192 (1999).

[37] J. M. Fraser and H. M. van Driel, Phys. Rev. B **68**, 85208 (2003).

[38] R. D. R. Bhat and J. E. Sipe, Phys. Rev. Lett **85**, 5432 (2000).

[39] S. Datta and B. Das, Appl. Phys. Lett. **56**, 665 (1990).

[40] S. Das Sarma, J. Fabian, X. Hu, and I. Zutic, Solid State Commun. **119**, 207 (2001).

[41] M. J. Stevens, A. L. Smirl, R. D. R. Bhat, A. Najmaie, J. E. Sipe, and H. M. van Driel, Phys. Rev. Lett **90**, 136603 (2003).

[42] J. Hübner, W. W. Rühle, M. Klude, D. Hommel, R. D. R. Bhat, J. E. Sipe, and H. M. van Driel, Phys. Rev. Lett **90**, 216601 (2003).

[43] M. I. Dyakonov and V. I. Perel, **35A**, 459 (1971).

[44] J. E. Hirsch, Phys. Rev. Lett **83**, 1834 (1999).

[45] Y. K. Kato, R. C. Myers, A. C. Gossard, and D. D. Awschalom, Science **306**, 1910 (2004).

[46] J. Wunderlich, B. K. J. Sinova, and T. Jungwirth, Phys. Rev. Lett **94**, 047204 (2005).

[47] S. K. Watson, R. M. Potok, C. M. Marcus, and V. Umansky, Phys. Rev. Lett **91**, 258301 (2003).

[48] E. Mucciolo, C. Chamon, and C. Marcus, Phys. Rev. Lett **89**, 146802 (2002).

[49] Q.-F. Sun, H. Guo, and J. Wang, Phys. Rev. Lett **90**, 258301 (2003).

[50] W. Long, Q.-F. Sun, H. Guo, and J. Wang, Appl. Phys. Lett. **83**, 1397 (2003).

[51] T. Aono, Phys. Rev. B **67**, 155303 (2003).

[52] P. Sharma and P. W. Brouwer, Phys. Rev. Lett **91**, 166801 (2003).

[53] M. Governale, F. Taddei, and R. Fazio, Phys. Rev. B **68**, 155324 (2003).

[54] R. Benjamin and C. Benjamin, Phys. Rev. B **69**, 85318 (2004).

[55] A. Mal'shukov, C. Tang, C. Chu, and K. Chao, Phys. Rev. B **68**, 233307 (2003).

[56] I. Rumyantsev, A. Najmaie, R. D. R. Bhat, and J. E. Sipe, in *CLEO/IQEC and PhAST Technical Digest* (The Optical Society of America, Washington, DC, 2004), presentation IWA5.

[57] D. H. Marti, M.-A. Dupertuis, and B. Deveaud, Annals of Physics **316**, 234 (2004).

[58] H. T. Duc, T. Meier, and S. W. Koch, Phys. Rev. Lett **95**, 086606 (2005).

[59] D. H. Marti, M.-A. Dupertuis, and B. Deveaud, Phys. Rev. B **72**, 075357 (2005).

[60] S. Murakami, N. Nagaosa, and S.-C. Zhang, Science **301**, 1348 (2003).

[61] S. Murakami, N. Nagaosa, and S.-C. Zhang, Phys. Rev. B **69**, 235206 (2004).

[62] J. Sinova, D. Culcer, Q. Niu, N. A. Sinitsyn, T. Jungwirth, and A. H. MacDonald, Phys. Rev. Lett **92**, 126603 (2004).

[63] S. Murakami, N. Nagaosa, and S.-C. Zhang, Phys. Rev. Lett **93**, 156804 (2004).

[64] E. Rashba, Phys. Rev. B **68**, 241315 (2003).

[65] E. I. Rashba, Phys. Rev. B **70**, 161201 (2004).

[66] M. J. Stevens, R. D. R. Bhat, J. E. Sipe, H. M. van Driel, and A. L. Smirl, phys. stat. sol. (b) **238**, 568 (2003).

[67] M. J. Stevens, R. D. R. Bhat, X. Y. Pan, H. M. van Driel, J. E. Sipe, and A. L. Smirl, J. Appl. Phys. **97**, 093709 (2005).

[68] A. Haché, J. E. Sipe, and H. M. van Driel, IEEE J. Quant. Electron. **34**, 1144 (1998).

[69] D. Côté, J. M. Fraser, M. DeCamp, P. H. Bucksbaum, and H. M. van Driel, Appl. Phys. Lett. **75**, 3959 (1999).

[70] D. Côté, N. Laman, A. Springthorpe, and H. M. van Driel (2003), unpublished.

[71] M. J. Stevens, A. L. Smirl, R. D. R. Bhat, J. E. Sipe, and H. M. van Driel, J. Appl. Phys. **91**, 4382 (2002).

[72] P. A. Roos, Q. Quraishi, S. T. Cundiff, R. D. R. Bhat, and J. E. Sipe, Opt. Express **11**, 2081 (2003).

[73] M. J. Stevens, A. Najmaie, R. D. R. Bhat, J. E. Sipe, and H. M. van Driel, J. Appl. Phys. **94**, 4999 (2003).

[74] Y. Kerachian, P. Nemec, H. M. van Driel, and A. L. Smirl, J. Appl. Phys. **96**, 430 (2004).

[75] M. J. Stevens, R. D. R. Bhat, A. Najmaie, H. M. van Driel, J. E. Sipe, and A. L. Smirl, in *Optics of Semiconductors and Their Nanostructures*, edited by H. Kalt and M. Hetterich (Springer, Berlin, 2004), vol. 146 of *Springer Series in Solid-State Sciences*, p. 209.

[76] M. J. Stevens, R. D. R. Bhat, J. E. Sipe, H. M. van Driel, and A. L. Smirl, Semicond. Sci. Technol. **19**, S397 (2004).

[77] T. M. Fortier, P. A. Roos, D. J. Jones, S. T. Cundiff, R. D. R. Bhat, and J. Sipe, Phys. Rev. Lett **92**, 147403 (2004).

[78] P. A. Roos, X. Li, J. A. Pipis, S. T. Cundiff, R. D. R. Bhat, and J. E. Sipe, J. Opt. Soc. Am. B **22**, 365 (2005).

[79] M. Sheik-Bahae, Phys. Rev. B **60**, R11257 (1999).

[80] P. Král and J. E. Sipe, Phys. Rev. B **61**, 5381 (2000).

[81] R. D. R. Bhat and J. E. Sipe, Phys. Rev. B **72**, 075205 (2005).

[82] R. D. R. Bhat, F. Nastos, A. Najmaie, and J. E. Sipe, Phys. Rev. Lett **94**, 096603 (2005).

[83] A. L. Smirl, private communication.

[84] R. W. Boyd, *Nonlinear Optics* (Academic Press, 1992).

[85] M. Bieler, N. Laman, H. M. van Driel, and A. L. Smirl, Appl. Phys. Lett. **86**, 061102 (2005).

[86] T. Brabec and F. Krausz, Reviews of Modern Physics **72**, 545 (2000).

[87] E. Charron, A. Giusti-Suzor, and F. H. Mies, Phys. Rev. Lett **71**, 692 (1993).

[88] E. Charron, A. Giusti-Suzor, and F. H. Mies, Phys. Rev. A **49**, R641 (1994).

[89] J. Z. Kaminski and F. Ehlotzky, Phys. Rev. A **50**, 4404 (1994).

[90] D. W. Schumacher, F. Weihe, H. G. Muller, and P. H. Bucksbaum, Phys. Rev. Lett **73**, 1344 (1994).

[91] E. Cormier and M. Lewenstein, Eur. Phys. J. D **12**, 227 (2000).

[92] D. B. Milosevic and W. Becker, Phys. Rev. A **62**, 011403 (2000).

[93] D. B. Milosevic and W. Sandner, Optics Letters **25**, 1532 (2000).

[94] I. J. Kim, C. M. Kim, H. T. Kim, G. H. Lee, Y. S. Lee, J. Y. Park, D. J. Cho, and C. H. Nam, Phys. Rev. Lett **94**, 243901 (2005).

[95] O. D. Mücke, T. Tritschler, M.Wegener, U. Morgner, and F. X. Kärtner, Phys. Rev. Lett **89**, 127401 (2002).

[96] T. Tritschler, O. D. Mücke, M. Wegener, U. Morgner, and F. X. Kärtner, Phys. Rev. Lett **90**, 217404 (2003).

[97] A. Othonos, J. Appl. Phys. **83**, 1789 (1998).

[98] V. I. Belinicher and B. I. Sturman, Sov. Phys. Usp. **23**, 199 (1980).

[99] B. I. Sturman and V. M. Fridkin, *The Photovoltaic and Photorefractive Effects in Non-centrosymmetric Materials* (Gordon and Breach, Philadelphia, 1992).

[100] C. Aversa and J. E. Sipe, IEEE J. Quant. Electron. **32**, 1570 (1996).

[101] J. E. Sipe and A. I. Shkrebtii, Phys. Rev. B **61**, 5337 (2000).

[102] D. Côté, N. Laman, and H. M. van Driel, Appl. Phys. Lett. **80**, 905 (2002).

[103] P. Y. Yu and M. Cardona, *Fundamentals of semiconductors* (Springer-Verlag, Berlin, 1996), Chap. 6.

[104] H. Haug and S. W. Koch, *Quantum Theory of the Optical and Electronic Properties of Semiconductors* (World Scientific, Singapore, 1993).

[105] E. I. Blount, in *Solid State Physics: Advances in Research and Applications* (Academic, New York, 1962), vol. 13, pp. 305–373.

[106] C. Aversa and J. E. Sipe, Phys. Rev. B **52**, 14636 (1995).

[107] R. Girlanda, A. Quattropani, and P. Schwendimann, Phys. Rev. B **24**, 2009 (1981).

[108] S. Ismail-Beigi, E. K. Chang, and S. G. Louie, Phys. Rev. Lett **87**, 087402 (2001).

[109] E. K. Chang, E. L. Shirley, and Z. H. Levine, Phys. Rev. B **65**, 35205 (2002).

[110] D. J. Hilton and C. L. Tang, Phys. Rev. Lett **89**, 146601 (2002).

[111] Z. G. Yu, S. Krishnamurthy, M. van Schilfgaarde, and N. Newman, Phys. Rev. B **71**, 245312 (2005).

[112] R. J. Elliott, Physical Review **96**, 266 (1954).

[113] Y. Yafet, in *Solid State Physics*, edited by F. Seitz and D. Turnbull (Academic, New York, 1963), vol. 14 of *Modern Problems in Condensed Matter Physics*, p. 2.

[114] H. M. van Driel and J. E. Sipe, in *Ultrafast Phenomena in Semiconductors*, edited by K. T. Tsen (Springer-Verlag, New York, 2001), pp. 261–306.

[115] J. W. Negele, *Quantum Many-Particle Systems* (Addison-Wesley, 1988).

[116] S. D. Ganichev and W. Prettl, J. Phys. Cond. Matter **15**, R935 (2003).

[117] M. Lax, *Symmetry principles in solid state and molecular physics* (Dover edition, Mineola, N.Y., 2001).

[118] P. Y. Yu and M. Cardona, *Fundamentals of Semiconductors* (Springer, Berlin, 1996), Chap. 2.

[119] E. A. Kearsley and J. T. Fong, J. Res. Nat. Bur. Stand. B. Math. Sci. **79**, 49 (1975).

[120] G. L. Bir and G. E. Pikus, *Symmetry and Strain-Induced Effects in Semiconductors* (John Wiley & Sons, New York, 1974).

[121] E. O. Kane, J. Phys. Chem. Solids **1**, 249 (1957).

[122] G. Bastard, *Wave Mechanics Applied to Semiconductor Heterostructures* (Halsted, New York, 1988), Chap. 2.

[123] U. Rössler, Solid State Commun. **49**, 943 (1984).

[124] P. Pfeffer and W. Zawadzki, Phys. Rev. B **41**, 1561 (1990).

[125] H. Mayer and U. Rössler, Phys. Rev. B **44**, 9048 (1991).

[126] H. Mayer, U. Rössler, and M. Ruff, Phys. Rev. B **47**, 12929 (1993).

[127] H. Mayer and U. Rössler, Solid State Commun. **87**, 81 (1993).

[128] D. C. Hutchings and B. S. Wherrett, Phys. Rev. B **49**, 2418 (1994).

[129] D. C. Hutchings and B. S. Wherrett, Phys. Rev. B **52**, 8150 (1995).

[130] P. Pfeffer and W. Zawadzki, Phys. Rev. B **53**, 12813 (1996).

[131] D. C. Hutchings and J. M. Arnold, Phys. Rev. B **56**, 4056 (1997).

[132] R. Winkler, *Spin-orbit coupling effects in two-dimensional electron and hole systems*, vol. 191 of *Springer tracts in modern physics* (Springer, Berlin, 2003).

[133] W. H. Lau, J. T. Olesberg, and M. E. Flatté, Phys. Rev. B **64**, 161301 (2001).

[134] W. H. Lau, J. T. Olesberg, and M. E. Flatté (2004), `cond-mat/0406201`.

[135] P.-O. Löwdin, J. Chem. Phys. **19**, 1396 (1951).

[136] M. Cardona, F. H. Pollak, and J. G. Broerman, Phys. Lett. **19**, 276 (1965).

[137] M. Cardona, N. Christensen, and G. Fasol, Phys. Rev. B **38**, 1806 (1988).

[138] P. Enders, A. Bärwolff, M. Woerner, and D. Suisky, Phys. Rev. B **51**, 16695 (1995).

[139] W. H. Press, S. A. Teukolsky, W. T. Vetterling, and B. P. Flannery, *Numerical Recipes in C: The Art of Scientific Computing* (Cambridge University Press, Cambridge, 2002), 2nd ed.

[140] A. Baldereschi and N. O. Lipari, Phys. Rev. B **8**, 2697 (1973).

[141] F. Nastos, private communication.

[142] M. D. Dvorak, W. A. Schroeder, D. R. Anderson, A. L. Smirl, and B. S. Wherrett, IEEE J. Quant. Electron. **30**, 256 (1994).

[143] D. C. Hutchings and B. S. Wherrett, J. Modern Optics **41**, 1141 (1994).

[144] M. Murayama and T. Nakayama, Phys. Rev. B **52**, 4986 (1995).

[145] G. Dresselhaus, Phys. Rev. **100**, 580 (1955).

[146] G. E. Pikus, V. A. Marushchak, and A. N. Titkov, Sov. Phys. Semicond. **22**, 115 (1988).

[147] M. I. Bell, in *Electronic density of states*, edited by L. H. Bennett (U.S. GPO, Washington, D.C., 1971), vol. 323 of *Natl. Bur. Std. (U.S.) Spec. Publ.*, p. 757.

[148] D. J. Moss, J. E. Sipe, and H. M. van Driel, Phys. Rev. B **36**, 9708 (1987).

[149] E. Ghahramani, D. J. Moss, and J. E. Sipe, Phys. Rev. B **43**, 9700 (1991).

[150] M.-Z. Huang and W. Y. Ching, Phys. Rev. B **47**, 9464 (1993).

[151] L. C. Lew Yan Voon and L. R. Ram-Mohan, Phys. Rev. B **50**, 14421 (1994).

[152] J. L. P. Hughes and J. E. Sipe, Phys. Rev. B **53**, 10751 (1996).

[153] B. Adolph and F. Bechstedt, Phys. Rev. B **57**, 6519 (1998).

[154] P. L. Kelley, J. Phys. Chem. Solids **24**, 607 (1963).

[155] P. L. Kelley, J. Phys. Chem. Solids **24**, 1113 (1963).

[156] K. C. Rustagi, J. Phys. Chem. Solids **30**, 2547 (1969).

[157] M. I. Bell, Phys. Rev. B **6**, 516 (1972).

[158] S. S. Jha and J. J. Wynne, Phys. Rev. B **5**, 4867 (1972).

[159] D. E. Aspnes, Phys. Rev. B **6**, 4648 (1972).

[160] H. P. Wagner, M. Kühnelt, W. Langbein, and J. M. Hvam, Phys. Rev. B **58**, 10494 (1998).

[161] T. Maruyama, E. L. Garwin, R. Prepost, G. H. Zapalac, J. S. Smith, and J. D. Walker, Phys. Rev. Lett **66**, 2376 (1991).

[162] T. Omori, Y. Kurihara, T. Nakanishi, H. Aoyagi, T. Baba, T. Furuya, K. Itoga, M. Mizuta, S. Nakamura, Y. Takeuchi, et al., Phys. Rev. Lett **67**, 3294 (1991).

[163] F. Ciccaci, E. Molinari, and N. E. Christensen, Solid State Commun. **62**, 1 (1987).

[164] S.-H. Wei and A. Zunger, Appl. Phys. Lett. **64**, 1676 (1994).

[165] A. Janotti and S.-H. Wei, Appl. Phys. Lett. **81**, 3957 (2002).

[166] A. M. Danishevskii, Sov. Phys. Solid State **20**, 1818 (1978).

[167] A. M. Danishevskii, Sov. Phys. Solid State **29**, 575 (1987).

[168] M. S. Bresler, O. B. Gusev, and I. A. Merkulov, Sov. Phys. JETP **66**, 1179 (1987).

[169] M. S. Bresler, O. B. Gusev, and I. A. Merkulov, Sov. Phys. Solid State **30**, 99 (1988).

[170] A. M. Danishevskii, E. L. Ivchenko, S. F. Kochegarov, and M. I. Stepanova, JETP Lett. **16**, 440 (1972).

[171] S. B. Arifzhanov and E. L. Ivchenko, Sov. Phys. Solid State **17**, 46 (1975).

[172] J. P. van der Ziel, Phys. Rev. B **16**, 2775 (1977).

[173] I. M. Catalano, A. Cingolani, and M. Lepore, Phys. Rev. B **33**, 7270 (1986).

[174] C. C. Lee and H. Y. Fan, Phys. Rev. B **9**, 3502 (1974).

[175] V. I. Bredikhin, M. D. Galanin, and V. N. Genkin, Soviet Phys. Uspekhi **16**, 299 (1973).

[176] G. D. Mahan, Phys. Rev. **170**, 825 (1968).

[177] A. Baldereschi and N. O. Lipari, Phys. Rev. Lett **25**, 373 (1970).

[178] A. Baldereschi and N. O. Lipari, Phys. Rev. B **3**, 439 (1971).

[179] N. O. Lipari and A. Baldereschi, Phys. Rev. Lett **25**, 1660 (1970).

[180] K. J. Vahala and P. C. Sercel, Phys. Rev. Lett **65**, 239 (1990).

[181] F. H. Pollak, C. W. Higginbotham, and M. Cardona, J. Phys. Soc. Jpn. Suppl. **21**, 20 (1966).

[182] I. Gorczyca, P. Pfeffer, and W. Zawadzki, Semicond. Sci. Technol. **6**, 963 (1991).

[183] R. Loudon, Proc. Phys. Soc. (London) **80**, 952 (1962).

[184] K. C. Rustagi, F. Pradere, and A. Mysyrowicz, Phys. Rev. B **8**, 2721 (1973).

[185] E. Doni, G. P. Parravicini, and R. Girlanda, Solid State Commun. **14**, 873 (1974).

[186] M. Sondergeld, phys. stat. sol. (b) **81**, 451 (1977).

[187] G. L. Bir, A. G. Aronov, and G. E. Pikus, Sov. Phys. JETP **42**, 705 (1976).

[188] U. Rössler, phys. stat. sol. (b) **234**, 385 (2002).

[189] R. D. R. Bhat, F. Nastos, A. Najmaie, and J. E. Sipe (2004), `cond-mat/0404066 version 1`, URL `http://arxiv.org/abs/cond-mat/0404066v1`.

[190] S. F. Alvarado, H. Riechert, and N. E. Christensen, Phys. Rev. Lett **55**, 2716 (1985).

[191] G. E. Pikus and G. L. Bir, Sov. Phys. Solid State **1**, 1502 (1959).

[192] I. Vurgaftman, J. R. Meyer, and L. R. Ram-Mohan, J. Appl. Phys. **89**, 5815 (2001).

[193] B. Koopmans, P. V. Santos, and M. Cardona, phys. stat. sol. (b) **205**, 419 (1998).

[194] D. Bertho, J.-M. Jancu, and C. Jouanin, Phys. Rev. B **50**, 16956 (1994).

[195] A. Blacha, H. Presting, and M. Cardona, phys. stat. sol. (b) **126**, 11 (1984).

[196] P. Etchegoin and M. Cardona, Solid State Commun. **82**, 655 (1992).

[197] V. V. Belkov, S. D. Ganichev, P. Schneider, C. Back, M. Oestreich, J. Rudolph, D. Hagele, L. E. Golub, W. Wegscheider, and W. Prettl, Solid State Commun. **128**, 283 (2003).

[198] N. Laman, A. I. Shkrebtii, J. E. Sipe, and H. M. van Driel, Appl. Phys. Lett. **75**, 2581 (1999).

[199] Y. B. Lyanda-Geller and G. E. Pikus, Sov. Phys. Solid State **31**, 2068 (1989).

[200] M. Shapiro, J. W. Hepburn, and P. Brumer, Chem. Phys. Lett. **149**, 451 (1988).

[201] M. Shapiro and P. Brumer, *Principles of the Quantum Control of Molecular Processes* (Wiley, New York, 2003).

[202] L. Zhu, V. Kleiman, X. Li, S. P. Lu, K. Trentelman, and R. J. Gordon, Science **270**, 77 (1995).

[203] T. Seideman, J. Chem. Phys. **108**, 1915 (1998).

[204] T. Seideman, J. Chem. Phys. **111**, 9168 (1999).

[205] N. B. Baranova, A. N. Chudinov, and B. Y. Zel'dovich, Opt. Commun. **79**, 116 (1990).

[206] V. A. Pazdzersky and V. I. Usachenko, J. Phys. B **30**, 3387 (1997).

[207] S. Albrecht, L. Reining, R. Del Sole, and G. Onida, Phys. Rev. Lett **80**, 4510 (1998).

[208] L. X. Benedict, E. L. Shirley, and R. B. Bohn, Phys. Rev. Lett **80**, 4514 (1998).

[209] L. X. Benedict, E. L. Shirley, and R. B. Bohn, Phys. Rev. B **57**, R9385 (1998).

[210] M. Rohlfing and S. G. Louie, Phys. Rev. Lett **81**, 2312 (1998).

[211] M. Rohlfing and S. G. Louie, Phys. Rev. B **62**, 4927 (2000).

[212] R. J. Elliott, Phys. Rev. B **108**, 1384 (1957).

[213] V. I. Shelest and M. V. Éntin, Sov. Phys. Semicond. **13**, 1353 (1979).

[214] D. F. Blossey, Phys. Rev. B **2**, 3976 (1970).

[215] A. K. Ganguly and J. L. Birman, Phys. Rev. B **162**, 806 (1967).

[216] R. M. Martin, Phys. Rev. B **4**, 3676 (1971).

[217] A. García-Cristóbal, A. Cantarero, C. Trallero-Giner, and M. Cardona, Phys. Rev. B **49**, 13430 (1994).

[218] A. García-Cristóbal, A. Cantarero, C. Trallero-Giner, and M. Cardona, Phys. Rev. B **58**, 10443 (1998).

[219] M. A. Kolber and J. D. Dow, Phys. Rev. B **18**, 5499 (1978).

[220] M. Sheik-Bahae, J. Wang, and E. W. V. Stryland, IEEE J. Quantum Electron. **30**, 249 (1994).

[221] D. W. Schumacher and P. H. Bucksbaum, Phys. Rev. A **54**, 4271 (1996).

[222] J. O. Dimmock (Academic Press, New York, 1967), vol. 3 of *Semiconductors and Semimetals*, Chap. 7, p. 259.

[223] V. Nathan, A. H. Guenther, and S. S. Mitra, J. Opt. Soc. B **2**, 294 (1985).

[224] F. Bassani and G. P. Parravicini, *Electronic States and Optical Transitions in Solids* (Pergamon Press, Oxford, 1975), Chap. 6.

[225] G. Breit and H. A. Bethe, Phys. Rev. B **93**, 888 (1954).

[226] J. R. Taylor, *Scattering Theory* (Wiley, New York, 1972).

[227] L. I. Schiff, *Quantum Mechanics* (McGraw-Hill, New York, 1955), p. 119, 2nd ed.

[228] J. M. Luttinger and W. Kohn, Phys. Rev. B **97**, 869 (1955).

[229] G. Dresselhaus, J. Phys. Chem. Solids **1**, 14 (1956).

[230] M. Sondergeld, phys. stat. sol. (b) **81**, 253 (1977).

[231] H. A. Bethe and E. E. Salpeter, *Quantum Mechanics of One- and Two-electron Atoms* (Plenum, New York, 1977).

[232] O. Madelung, ed., *Semiconductors—Basic Data* (Springer-Verlag, Berlin, 1996), 2nd ed.

[233] D. D. Sell, Phys. Rev. B **6**, 3750 (1972).

[234] M. D. Sturge, Phys. Rev. B **127**, 768 (1962).

[235] M. H. Weiler, Solid State Commun. **39**, 937 (1981).

[236] J. E. Sipe, A. I. Shkrebtii, and O. Pulci, phys. stat. sol. (a) **170**, 431 (1998).

[237] T. Meier and S. Koch, private communication.

[238] F. Wang, G. Dukovic, L. E. Brus, and T. F. Heinz, Science **308**, 838 (2005).

[239] E. J. Mele, P. Kral, and D. Tomanek, Phys. Rev. B **61**, 7669 (2000).

[240] E. Y. Sherman, A. Najmaie, and J. E. Sipe, Appl. Phys. Lett. **86**, 122103 (2005).

[241] J. D. Jackson, *Classical Electrodynamics* (John Wiley & Sons, New York, 1975), 2nd ed.

[242] E. O. Kane, J. Phys. Chem. Solids **1**, 82 (1956).

[243] M. Cardona and F. H. Pollak, Phys. Rev. B **142**, 530 (1966).

[244] T. B. Bahder, Phys. Rev. B **41**, 11992 (1990).

[245] T. E. Ostromek, Phys. Rev. B **54**, 14467 (1996).

[246] K. Suzuki and J. C. Hensel, Phys. Rev. B **9**, 4184 (1974).

[247] H.-R. Trebin, U. Rössler, and R. Ranvaud, Phys. Rev. B **20**, 686 (1979).